UNIVERSITY OF SOUTHAMPTON

FACULTY OF NATURAL AND ENVIRONMENTAL SCIENCES

Chemistry

The Manipulation of the Microstructure of Functional Metal Oxides using Aerosol Assisted Chemical Vapour Deposition

by

Karl M Kaye

Thesis for the degree of Doctor of Philosophy

January 2016

UNIVERSITY OF SOUTHAMPTON

ABSTRACT

FACULTY OF NATURAL AND ENVIRONMENTAL SCIENCES

Chemistry

Thesis for the degree of Doctor of Philosophy

THE MANIPULATION OF THE MICROSTRUCTURE OF FUNCTIONAL METAL OXIDES USING AEROSOL ASSISTED CHEMICAL VAPOUR DEPOSITION

Karl M. Kaye

The presence of organic ionic additives during aerosol assisted chemical vapour deposition of zinc oxide has a profound influence on the microstructure of the resulting films. Growth of crystallites can be controlled to grow a range of shapes, including irregular shaped clusters, individual hexagonal plates and stacks of plates growing perpendicular to the substrate.

During testing of organic additives in the deposition of zinc oxide via aerosol assisted chemical vapour deposition, urea was found to result in the formation of zinc carbodiimide. By adjusting the parameters it was determined that a temperature of 450 °C and a molar ratio of 3:1 of urea:zinc acetate are ideal conditions to form uniform films of zinc carbodiimide. This is the first example of the formation of a thin film of zinc carbodiimide.

By using a mixed solution of zinc acetate and titanium (IV) isopropoxide, it is possible to deposit mixed phase films of zinc oxide, titanium dioxide and various zinc titanate phases. Stepwise treatment of these films with dilute acid and hydrogen results in the leeching of the zinc phases. The resulting films are composed of porous titanium dioxide which exhibits greater photocatalytic activity than dense films of titanium dioxide.

By using a solution of tetrakis (diethylamido) titanium in hexane or toluene, it is possible to deposit a thin film of titanium nitride onto float glass in a single step at temperatures as low as 350 °C. Introduction of ethyl acetate results in the formation of thin films comprised of phases of both titanium nitride and titanium dioxide.

Table of Contents

List of Tables

List of Figures

DECLARATION OF AUTHORSHIP

I, Karl Kaye declare that the thesis entitled 'The Manipulation of the Microstructure of Functional Metal Oxides using Aerosol Assisted Chemical Vapour Deposition' and the work presented in it are my own and has been generated by me as the result of my own original research.

I confirm that:

1. This work was done wholly or mainly while in candidature for a research degree at this University;
2. Where any part of this thesis has previously been submitted for a degree or any other qualification at this University or any other institution, this has been clearly stated;
3. Where I have consulted the published work of others, this is always clearly attributed;
4. Where I have quoted from the work of others, the source is always given. With the exception of such quotations, this thesis is entirely my own work;
5. I have acknowledged all main sources of help;
6. Where the thesis is based on work done by myself jointly with others, I have made clear exactly what was done by others and what I have contributed myself;
7. Parts of this work have been published as:

   (1) Kaye, K.; Turner, D.; McKenna, D.; Cackett, A.; Hyett, G. *Physics Procedia* **2013**, *46*, 21.

   (2) Kaye, K. M.; Grantham, W.; Hyett, G. *Chem. Vap. Deposition* **2015**, *21*, 281.

   (3) Kaye, K. ; Hyett, G. *J. Nanosci. Nanotechnol*. In Press

Signed: .....

Date:.....

Acknowledgements

There are many people who have played a role in my PhD either directly or indirectly. First and foremost I need to thank my supervisor Dr Geoff Hyett for his support and wealth of knowledge throughout the entire project. His assistance helped me find direction during the times it felt like I'd reached a dead-end. I would also like to thank the X-ray staff at the University of Southampton; powder X-ray diffraction was such an important technique that it would not have been possible without their help. Dr Shuncai Wang in Southampton and the LEMAS facility in Leeds were pivotal in the collection of SEM images by providing both access to and assisting with the operation of the microscopes. Dr Alex Kulac in Leeds for the collection of some of the high-resolution SEM images featured in this thesis and Dr Robert Palgrave in UCL for XPS analysis. Two fantastic project students, William Grantham and Nathanya Platt both of whom carried out work which contributed to this thesis. I would also like to thank the other members of the Hyett group along with every member of the Reid/Levason group over the last three years for the company, the tea breaks and the distractions away from CVD. My family and friends for their moral support, and of course, Jenny, thank you so much.

Definitions and Abbreviations

AACVD – Aerosol Assisted Chemical Vapour Deposition

APCVD – Atmospheric Pressure Chemical Vapour Deposition

NH_4SO_4 – Ammonium Sulphate

AZO – Aluminium-Doped Zinc Oxide

BBG – Brilliant Blue G

CTAB – Cetyltrimethylammonium Bromide

D12D1AB – Didodecyldimethylammonium Bromide

DCIP – Dichloroindophenol Sodium Salt

DMAPS – 3-(N,N-Dimethylmyristylammonio)propanesulphonate

DTAB – Decyltrimethylammonium Bromide

EtAc – Ethyl Acetate

ITO – Tin Doped Indium Oxide

LPCVD – Low Pressure Chemical Vapour Deposition

Mol. Eq. – Mole Equivalents

$NaMeSO_4$ – Methyl Sulphate Sodium Salt

PECVD – Plasma Enhanced Chemical Vapour Deposition

S3S – Sodium 1- Propanesulphonate

S5S – Sodium 1-Pentanesulphonate

S7S – Sodium 1-Heptanesulphonate

SDS – Sodium Dodecyl Sulphate

T10AB – Tetrakis (Decyl) Ammonium Bromide

T1AB – Tetramethylammonium Bromide

T2AB – Tetraethylammonium Bromide

T4AB – Tetrabutylammonium Bromide

T6AB – Tetrahexylammonium Bromide

TCO – Transparent Conductive Oxide

TDEAT – Tetrakis (Diethylamido) Titanium (IV)

TOAB – Tetramethylammonium Bromide

XPS – X-Ray Photoelectron Spectroscopy

XRD – X-Ray Diffraction

Chapter 1: Introduction

1.1 Thin Films

Thin films are thin layers of a material on a substrate; they can vary in thickness from single monolayers of atoms such as atomic layers of graphene[1] to multiple microns thick such as the surface coatings used for mirror backings. Thin films have been incorporated into many systems, for instance in the development of dye-sensitised photosensors,[2] catalysis[3] and in the manufacturing of new battery technology. One such example of the latter is the deposition of alternating layers of graphene with amorphous silicon films to develop a promising platform for modern battery technology.[4]

A large sector which takes advantage of thin films is the window coatings industry. Transparent thin films have the ability to imbue particular effects to the window, for instance self-cleaning glass. The main way in which this is carried out is through the deposition of hydrophilic semi-conducting materials such as titanium dioxide. TiO_2 can act as a photocatalyst for the decomposition of organic matter, thus resulting in a self-cleaning window,[5] a process which will be discussed in more detail below (see Porous Titania Films, page 111). A second process which could potentially be used involves super-hydrophobic coatings which cause water droplets to roll down the surface, the action of which transports dirt down the material. One such example of this was shown by Lau *et al* who deposited a 2 μm thick film of carbon nanotubes which was then coated with PTFE and was able to achieve water contact angles of up to 170°.[6]

Research has been carried out to investigate potential coatings to create smart windows; vanadium dioxide is a pioneering material in this area. [7-9] Vanadium dioxide exists in two common phases, a monoclinic phase and a rutile phase.[10] The monoclinic phase exists at room temperature and is a semi-conductor which transmits light within the infrared region whereas the rutile phase exists at higher temperatures (> 68 °C) and is metallic and reflects a large percentage of infrared light present within the solar spectrum. This transition makes VO_2 an ideal candidate for window coatings. By introducing small amounts of dopant materials such as tungsten and fluorine,[8,11,12] or strain within the crystal lattice, it has been possible to lower the temperature at which this transition occurs thus increasing the possibility of it being used as an energy efficient method of regulating building temperature within hot conditions.

Thin films are formed using a wide variety of techniques, one such technique is electrodeposition. This is a method in which precursors are dissolved within an electrolyte solution and deposition occurs at electrodes once a potential difference is passed across the system. One of the materials deposited using this technique were silicate films by Collinson *et al* who investigated the influence of electrolyte solution on the deposition of silicate films using alkoxysilanes as

precursors.[13] In 2005, Dong *et al* reported the growth of thin films of ferrous sulphide on tin-doped indium oxide using electrodeposition.[14] Valade *et al* reported the formation of conductive films based on molecular deposition via electrodeposition, for instance, a thin film of $Ni(tmdt)_2$ where tmdt = trimethylene-tetrathiafulvalenedithiolate was conductive and exhibited metallic character.[15] A disadvantage of this technique however is that both the substrate and the film being deposited are required to exhibit reasonable conductivity for deposition to occur and be maintained.[16]

Another method used to deposit thin films is physical vapour deposition (PVD), this is a technique in which precursors are vaporised, for instance using low pressure or increased temperature and then coated on a suitable substrate. This is a procedure which has been used to deposit electrolyte layers for solid oxide fuel cells.[17] It has also seen success in the deposition of thin films of organic materials which can be used as chemical sensors for gases or liquids.[18] However, a disadvantage of PVD is that it is a process which requires a line of site between the material source and the substrate, as a result of this, depositing on irregular surfaces becomes more of a challenge.[19]

A deposition technique which overcomes both of the disadvantages of electrodeposition and PVD is chemical vapour deposition.

1.2 Chemical Vapour Deposition

One of the most widely used techniques in the formation of thin films is chemical vapour deposition (CVD). Chemical vapour deposition differs from physical vapour deposition in that during the process a chemical change occurs. One of the first applications of CVD in an industrial sense dates back to Alexander de Lodyguine and his patent on the deposition of tungsten onto carbon and platinum filaments using vaporised WCl_6 and reducing it with hydrogen gas in the presence of the heated filament in the production of incandescent lamps.[20,21]

There are many techniques and variations upon chemical vapour deposition; however, they all function using the same principles. Traditional CVD always begins with the generation of vapour from the precursors, this vapour is then transported to a chamber in which it undergoes a chemical change, either through thermal decomposition, or reaction with other gas phase species at which point it is deposited onto a substrate.[19,21] The main sources of variation are in the method used to vaporise the precursor and the technique employed to heat the reaction chamber or instigate the reaction. The deposition chambers themselves can be split into two broad groups, hot-wall and cold-wall reactors. In a hot-wall reactor, the heat source surrounds the reaction vessel, for example, a tube furnace. Within this system the substrate is heated indirectly and there is generally a uniform temperature within the entire reactor, as a result of this, deposition often occurs on both the substrates and the inside walls of the chamber, reducing efficiency. Inside a cold-wall reactor, the substrate is heated directly, this results in the walls of the chamber being cold in comparison. This causes the deposition to occur preferentially on the substrate, reducing the amount of deposition which occurs on the walls of the reactor. However, a drawback to this is that because of the temperature gradient within the system, thermal convection can create a concentration gradient and cause uneven coatings of the substrates.[19] These thermal effects will be discussed in more detail below (see Aerosol Assisted Chemical Vapour Deposition, page 5).

A common technique used to vaporise precursors is low pressure chemical vapour deposition (LPCVD). A simple example of a LPCVD set up is shown below (see Figure 1-1). This exploits the use of volatile precursors, for example, LPCVD has been used to great effect to deposit thin films of titanium dioxide from the precursor titanium isopropoxide (TTiP).[22,23] LPCVD is a technique which was used extensively in the formation of thin films of silicon.[24,25] Copper films have also been formed using LPCVD, for example, in 2013, Krisyuk *et al* reported the formation of new copper (II) complexes which were shown to be viable candidates for the deposition of thin films of copper metal.[26]

One variation on LPCVD introduces plasma to reduce deposition temperature; this variation is commonly referred to as plasma enhanced chemical vapour deposition (PECVD).[24,27] PECVD works by supplying a gas at low pressure with electrical power. This then causes the gas to breakdown into electrons and ions. These species then ionise the reactants and stimulate the

chemical reactions and formation of the intended material in the vicinity of the heated substrate where it is subsequently deposited.[19] An example of this technique is demonstrated by Kato and Ito who deposited thin films of aluminium using trimethylaluminium and small amounts of hydrogen gas. Using these conditions, they succeeded in forming uniform layers of aluminium at temperatures below 100 °C.[27]

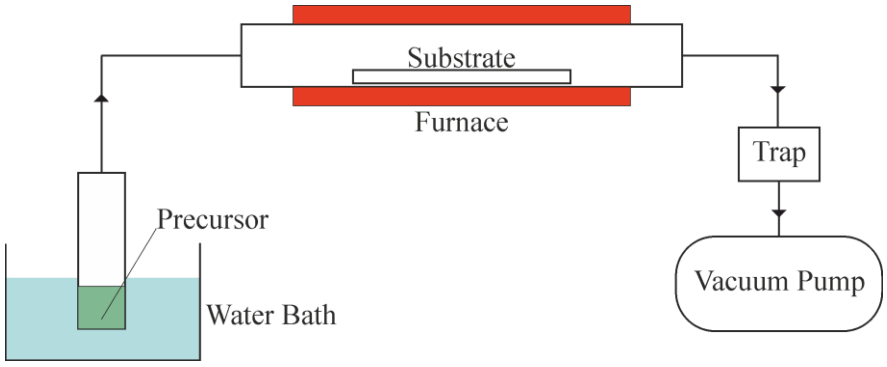

Figure 1-1 – Example of a simple LPCVD set up within a tube furnace

As an alternative to low pressures, carrier gases can be used to transport precursors to the deposition chamber.[19,21] These systems operate at ambient pressure and as a result, they are often referred to as atmospheric pressure chemical vapour deposition (APCVD). Similar to LPCVD, APCVD requires the use of volatile or gaseous precursors, for instance, methane, a precursor employed by Chen *et al* in their recent work on the deposition of graphene onto molten glass.[28] Another recent report of APCVD was carried out by Vernardou *et al*. In their work they successfully deposited thin films of vanadium dioxide using nitrogen as a carrier gas and the precursor vanadyl (V) triisopropoxide onto tin oxide coated glass.[29] In 2010, Thomas *et al* reported the deposition of titanium arsenide thin films at temperatures between 450 and 550 °C. These films were formed via APCVD using the precursors $TiCl_4$ and *t*$BuAsH_2$ supplied by a dual source system.[30]

1.3 Aerosol Assisted Chemical Vapour Deposition

The principle technique used in the deposition of thin films during this project was aerosol assisted chemical vapour deposition (AACVD). AACVD is a variation upon APCVD in which depositions are carried out at atmospheric pressure and a carrier gas is used to transport the precursors into the deposition chamber. The difference lies in the method of vaporising the precursor; instead of requiring volatile precursors AACVD simply requires the precursor to be soluble within a solvent. The solvents used are commonly organic solvents with a high boiling point.[19,21] The solutions are then converted into an aerosol by a number of techniques including electrospray. The method used for AACVD within this work is via the use of a piezoelectric humidifier. This functions by using ultrasound to generate aerosol droplets from the solution which can then be transported by the carrier gas. One of the main advantages to AACVD is that it is often a one-pot system which allows for fine control over the quantity of additives and precursors within the system which can be used as, for example, dopants[31-33] or additives which can be used to control microstructure[34,35] (see The use of Organic Additives to Control Microstructure and Surface Morphology of Zinc Oxide Thin Films, page 25).

AACVD has seen a large amount of success in the formation of an array of materials, for example, in 2003, Cross *et al* deposited tungsten oxides using AACVD from tungsten hexaaryloxide complexes in solutions of toluene and acetone.[36] $SrTiO_3$ thin films were deposited using AACVD by Peña *et al* in 1997.[37] These films were formed from solutions of strontium and titanium oxide bisdipavaloylmethanate in ethanol. Another example of AACVD being used was reported by Kiri *et al*. Their work involved forming thin films of fluorine doped vanadium dioxide onto glass substrates. This was achieved from solutions of vanadyl acetylacetonate and trifluoroacetic acid in ethanol.[8] One more example of thin film formation using AACVD is shown in the report by Qadri *et al* in 2011. In this work they detailed the formation of tungsten oxide layers doped with nanoparticles of gold from a solution of $W(OPh)_6$ and $HAuCl_4.3H_2O$ in a solvent mixture of acetone and methanol.[38]

One of the challenges facing AACVD comes when using in a cold-wall reactor. As mentioned above, these reactors possess a temperature gradient which results in thermal convection within the chamber which can cause concentration gradients within the gas (see Chemical Vapour Deposition, page 3). In the context of aerosol assisted CVD, it poses an additional problem due to the precursors being located within solvent droplets. As the aerosol droplets travel through the reactor they are influenced by three main forces operating perpendicular to the substrate (Figure 1-2). These are gravity, buoyancy and thermophoresis. The droplets are constantly under the influence of gravity and will be pulled downwards as a result; droplets with more mass will be affected by gravity more than small droplets. Buoyancy is caused by the resistance the droplet experiences as it moves downwards and increases with surface area, similar to gravity, larger

droplets will experience this effect more than small droplets. Finally, thermophoresis is caused by the thermal convection within the reactor. Two main factors influence the magnitude of this effect; these are droplet size and temperature. Droplets with a larger surface area will be subject to the upwards motion from the convection greater than smaller droplets, similarly, higher temperatures will increase the magnitude of the thermophoresis effect.[39,40] There is a positive correlation between surface tension and size of droplets when generated using an ultrasonic humidifier, this is represented by the following equation (Equation 1-1). As a result of this, in cold-wall reactors while using AACVD, it is desirable to use solvents with a low surface tension, to reduce droplet size, and low temperatures to maximise the quantity of precursor which reaches the substrate rather than the upper surfaces of the reaction chamber.

$$D = 0.34\left(\frac{8\pi T}{\rho F^2}\right)^{\frac{1}{3}}$$

Equation 1-1 – Equation representing the relationship between surface tension and droplet size. D is the droplet size, T is the surface tension, ρ is the liquid density and F is the exciting sound frequency.[41]

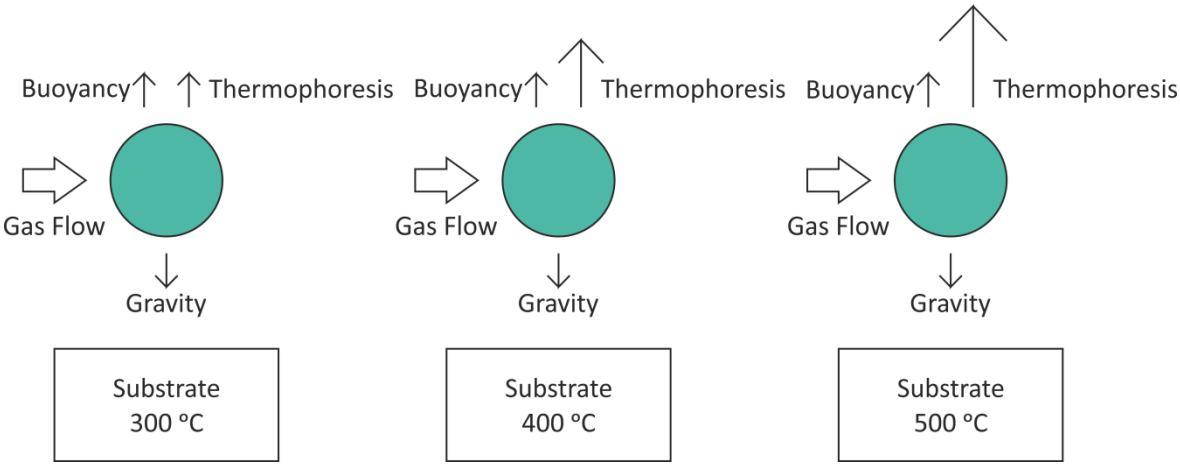

Figure 1-2 – Figure showing thermophoresis effects on a liquid droplet (Not to scale)

There are other factors which need to be taken into consideration when choosing a solvent for use during AACVD. One of these is the vapour pressure at the temperature in which the solution will be used. The reason why this is an important factor to consider is that during the process, the carrier gas will be passing across the solution; therefore a solvent with a high vapour pressure will be subject to a high level of evaporation. This evaporation will cause the solution to become more concentrated, potentially causing super saturation and eventually for the precursors to begin to precipitate out of solution reducing the efficiency of the system. Another important factor to take into consideration when choosing solvents is viscosity. This is particularly important when a piezoelectric humidifier is the method chosen to generate the aerosol. It was discovered during experiments that solvents with high viscosity reduces the piezoelectric humidifiers effectiveness at generating an aerosol. Some common solvents and their physical properties are shown in the table

below (Table 1-1). Methanol is a solvent which is used extensively during this project as it is fits the criteria for an ideal solvent as listed above. The table below shows that the vapour pressure of methanol is relatively low (16.9 kPa at 25 °C) which results in little evaporation during the deposition process, the viscosity shows that the solvent is a good candidate for aerosol generation using piezoelectric humidifiers and finally, the low surface tension (22.1 mN m^{-1} at 25 °C) will result in small droplets which are idea in cold wall reactors. Conversely, diethyl ether, propan-2-ol and water are not ideal solvents due the their high vapour pressure, viscosity and surface tension respectively.

Table 1-1 – Table showing properties of common solvents. Data taken from Handbook of Chemistry and Physics.[42]

Solvent	**Boiling Point / °C**	**Vapour Pressure at 25 ° / kPa**	**Viscosity at 25 °C / mPa s**	**Surface Tension at 25 °C / mN m^{-1}**
Acetone	56.1	30.8	0.306	23.5
Acetonitrile	81.7	11.8	0.369	28.7
Diethyl Ether	34.5	71.7	0.224	16.7
Ethanol	78.3	7.87	1.07	22.0
Hexane	68.7	20.2	0.300	17.9
Methanol	64.6	16.9	0.544	22.1
Propan-2-ol	82.3	2.76	2.04	20.9
Toluene	111	3.79	0.560	27.9
Water	100	3.17	0.890	72.0

1.4 Experimental

Aerosol assisted chemical vapour deposition was carried out inside a cold-wall reactor which was equipped with a carbon block heated by a Watlow cartridge in which the temperature was regulated by two chromel alumel thermocouples, an example of which is shown below (Figure 1-3). Unless specified otherwise, the exhaust of the reaction chamber was open to air. Deposition was typically carried out onto barrier coated float glass which had been cleaned prior to use by initially rinsing with deionised water, followed by acetone and finally by polishing using a dry paper towel and isopropyl alcohol. A second piece of float glass was suspended parallel c.a. 10 mm above the substrate which was used to maintain a laminar flow through the reaction chamber. Before depositions were carried out the reaction chamber was first heated to the desired temperature (350 °C unless stated otherwise) under a low flow of argon. Due to the exhaust being open to air, back diffusion of oxygen potentially occurred in the system, irrespective of the positive pressure of argon within the chamber.[43] The base of the dispersion chamber was positioned at a fixed height above the tip of the piezoelectric humidifier (20 mm unless stated otherwise) to maintain consistency between experiments. Once heated, the solution was made up and added to the dispersion chamber, the piezoelectric humidifier (Maplin, Mini Fogger Mist Generator, L38AK, 1.7 MHz) was then switched on and adjusted to achieve the maximum evolution of mist possible. The taps were then repositioned to direct the argon flow through the dispersion chamber and then the deposition chamber. Once all of the solution has been transported through the system the piezoelectric humidifier was switched off and the deposition chamber was allowed to cool to ambient temperature under a low flow of argon. Analysis of the films was carried out in air. Purities and suppliers of all chemicals used are provided in Appendix A.

Variations on the deposition technique include the substitution of the dispersion chamber for a 100 cm^3 3-necked round bottom flask (supplied by fisher). In this situation, the flask is lowered until the very bottom is level with the tip of the piezoelectric humidifier to maintain a consistent height among all samples run using this method. The other variation involves the use of a tube furnace as opposed to a cold walled reactor. In this set up the substrate is seated on a stainless steel block which aids in heat transfer to the substrate. In all depositions in which the tube furnace was used, a three neck round bottom flask is used as the dispersion chamber.

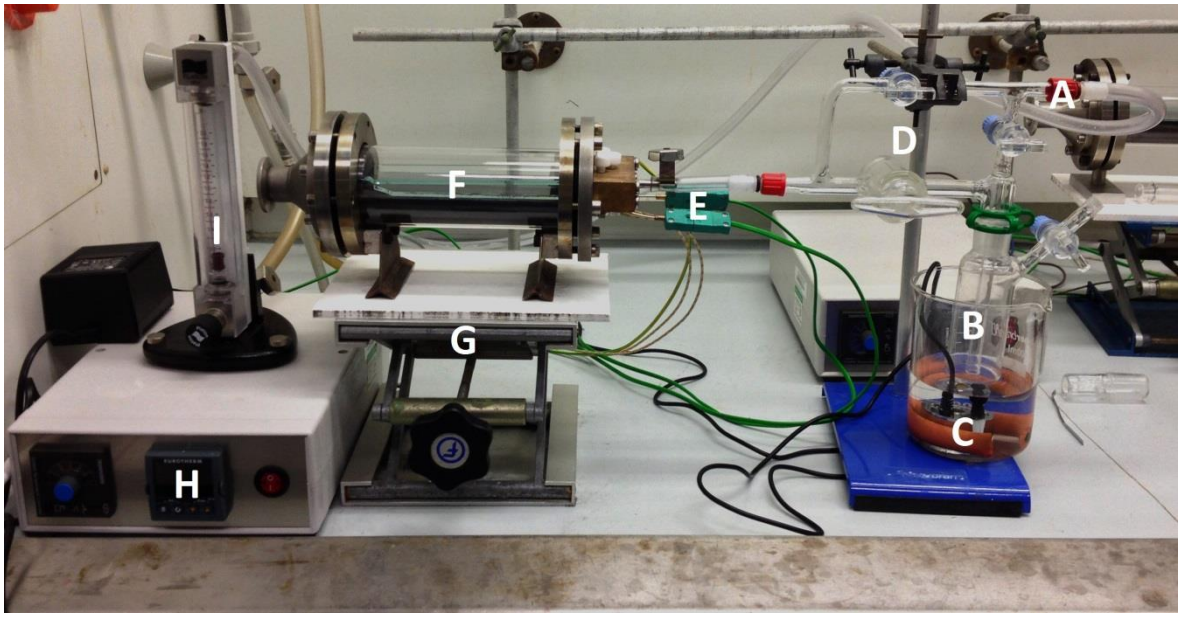

Figure 1-3 – Picture of Reactor with an example set up

Key:
A – Gas Flow Inlet
B – Dispersion Chamber
C – Piezoelectric Humidifier
D – Gas Flow Bypass
E – Thermocouples
F – Deposition Chamber
G – Adjustable Stand with Heatproof Plate
H – Temperature Controls
I – Gas Rotameter

1.5 Analytical Techniques

1.5.1 UV-Vis-NIR

1.5.1.1 Theory

As light reaches the interface between air and a transparent thin film mounted onto a glass substrate, some light is reflected off of the surface, the remaining light is refracted due to the change in refractive index. The light then carries on travelling until it reaches the thin-film and glass interface. At this point some of the light is then reflected back into the material, the remainder is refracted further as it enters the glass substrate. Once the light which is reflected travels through the air-thin film interface it begins to interfere with the light which was reflected initially. This interference will be dependent upon the film thickness and the wavelength of light. Constructive and destructive inference will occur depending on coherence between the light reflected from the surface and that reflected from the glass-thin film interface. This is the effect exploited by the Swanepoel method to determine the film thickness (see 1.5.1.3, page 12).

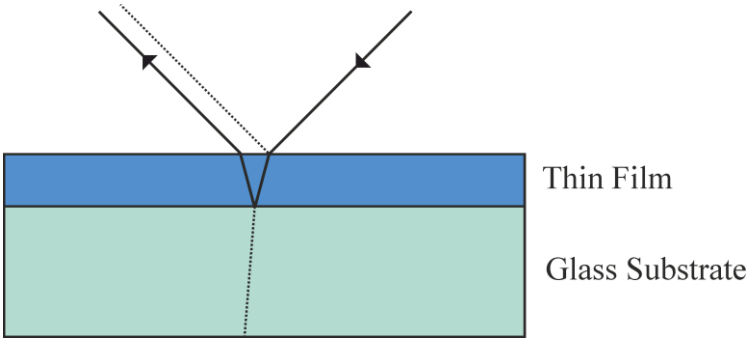

Figure 1-4 – Figure showing the source of interference patterns on transparent thin films

Conductivity within solid state materials is dictated by interaction between valence bands and conduction bands (Figure 1-5).

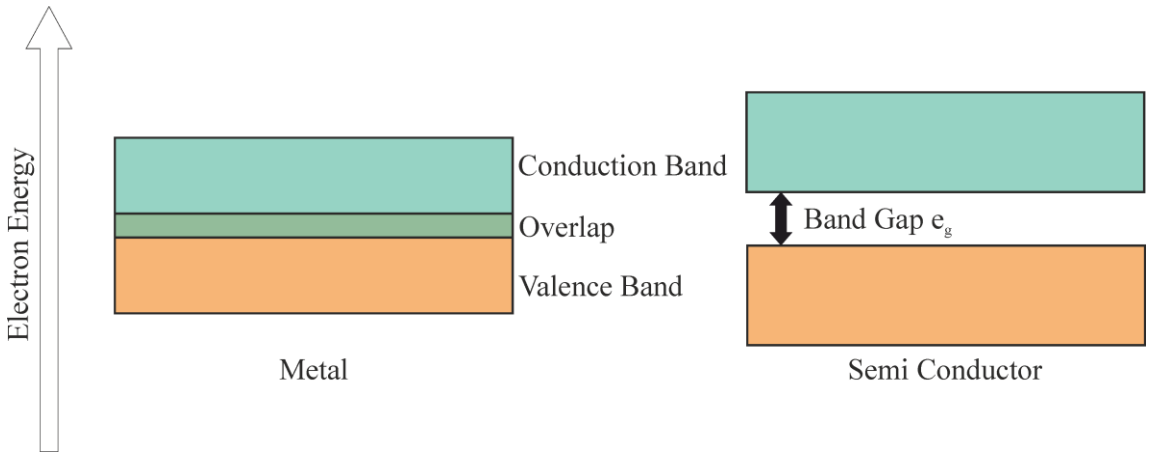

Figure 1-5 – Simplified diagram showing difference in conductivity between metals and semiconductors

In metals, there is an overlap between the filled valence and vacant conduction bands which results in free mobility of charge carriers within the material. However, in semiconductors, the valence and conduction bands are separated by an energy gap. For the material to conduct, charge carriers must first be excited to the conduction band. The energy required for this excitation to occur is known as the band gap.[44]

Conductivity within a material is shown by the following equation (Equation 1-2).

$$\sigma = ne\mu$$

Equation 1-2 – Equation to calculate conductivity. n is the number of charge carriers, e is the charge of the carriers and μ is the mobility of the carriers

Where the number of carriers is expressed by the following equation (Equation 1-3)

$$n = n_0 e^{\frac{-E}{kT}}$$

Equation 1-3 – Equation showing the number of charge carriers. n_0 is a constant and is the total number of electrons within the material, E is the promotion energy, k is the Boltzmann constant and T is the temperature.

1.5.1.2 Sample Preparation

A small strip from the substrate was cut with a width of c.a. 10 mm. No other preparation was carried out. Analysis was carried out on a Perkin Elmer UV-Vis-NIR Spectrometer Lambda 19 by measuring the absorbance between 250-2750 nm. The background was taken by running the same scan on a blank section of glass and subtracting from the sample data. Processing was carried out using a combination of Microsoft Excel and Origin. The film thickness was calculated using the Swanepoel method[45] (See 1.5.1.3, Page 12). The band gap was calculated using the Tauc method[46] (See 1.5.1.4, Page 13). UV-Vis-NIR was only carried out on thin films of zinc oxide due to the transparency of the films, as well as the particular interest in potential changes in the band gap. However, due to a malfunction within the machine rendering it unusable, only early samples were examined using UV-Vis-NIR spectroscopy.

1.5.1.3 Swanepoel Method

The Swanepoel method is a technique which can be used to calculate the thickness of thin films based upon the refractive index of the material and the wavelength of the interference effects.[45] The refractive index for zinc oxide films at each wavelength is calculated using the following equation.

$$n = \sqrt{2.81418 + \frac{0.87968\lambda^2}{\lambda^2 - 0.3042^2} - 0.00711\lambda^2}$$

Equation 1-4 - Dispersion Formula to Calculate Refractive Index

Where *n* is the refractive index, λ is the wavelength and the values are parameters obtained experimentally.[47] The wavelengths of the maximum and minimum points of the interference bands are recorded and the refractive index is calculated at each point using the equation above. An example spectrum featuring the interference effects is shown below (Figure 1-6). Theoretical order numbers (*l/2*) are then assigned to the values, beginning at 0 for the values at the highest wavelength increasing in half integers. A graph is then plot of $\frac{n}{\lambda}$ vs *l/2*. This produces a straight line graph with the standard form of $y = mx + c$ where *c* is the y-intercept and represents the negative value of the initial order number. This value is then assigned to each value starting with the highest wavelength and increasing in half integers. The thickness is then calculated using the equation.

$$d = \frac{m\lambda}{2n}$$

Equation 1-5 – Equation to Calculate Film Thickness

Where *d* is the thickness and *m* is the order number. This equation is used for each value obtained from the interference effects and an average value is recorded as the thickness of the film.

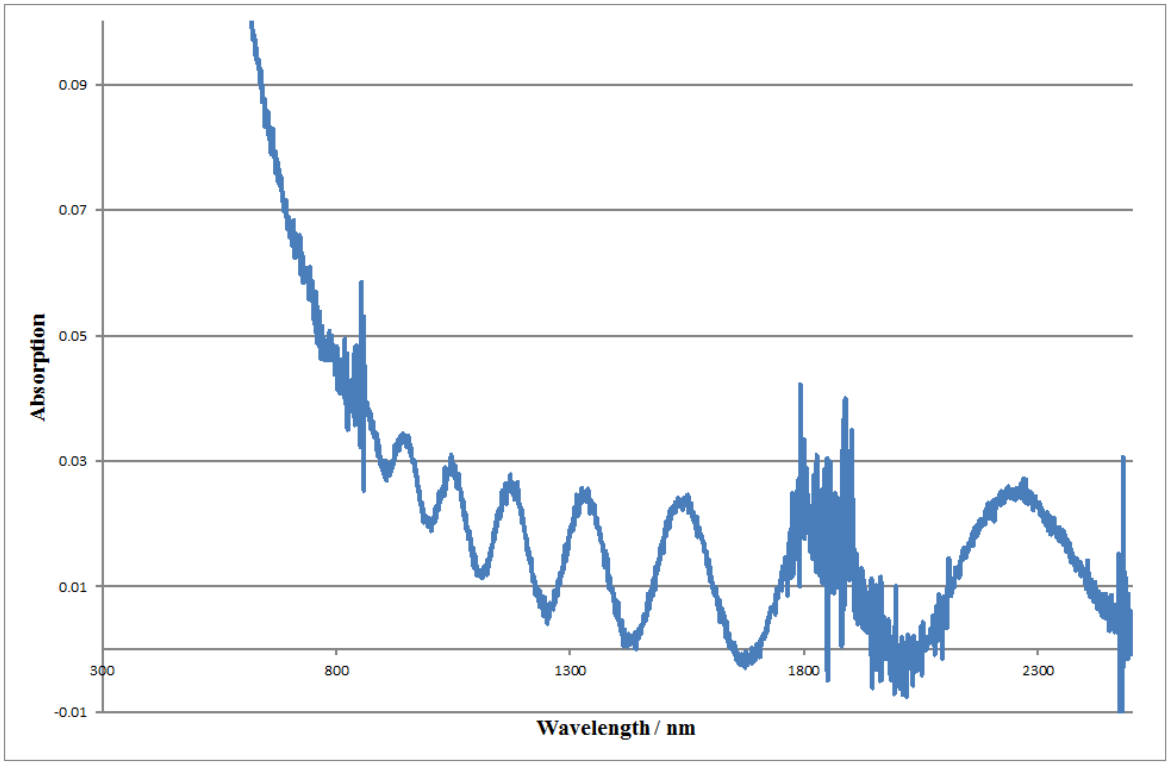

Figure 1-6 – UV-Vis-NIR Spectrum of Example Zinc Oxide film Featuring Interference bands

1.5.1.4 Tauc Method

Developed by Tauc, it is a method which can be used to calculate the band gap of materials.[46,48] The absorbance data that was recorded is first converted into transmission using the following equation.

$$T = 10^{-A}$$

Equation 1-6 - Equation used to convert Absorbance into Transmission

Where T is transmission and A is absorbance. For each data point the attenuation coefficient is calculated using the following equation.

$$\alpha = \frac{-\ln(T)}{d}$$

Equation 1-7 - Equation used to Calculate Attenuation Coefficient

Where α is the attenuation coefficient and d is the thickness of the film calculated from the Swanepoel Method. A Tauc plot of $(\alpha h\nu)^2$ vs $h\nu$ is composed, where hν is the energy of the photon. An example is shown below (Figure 1-7).

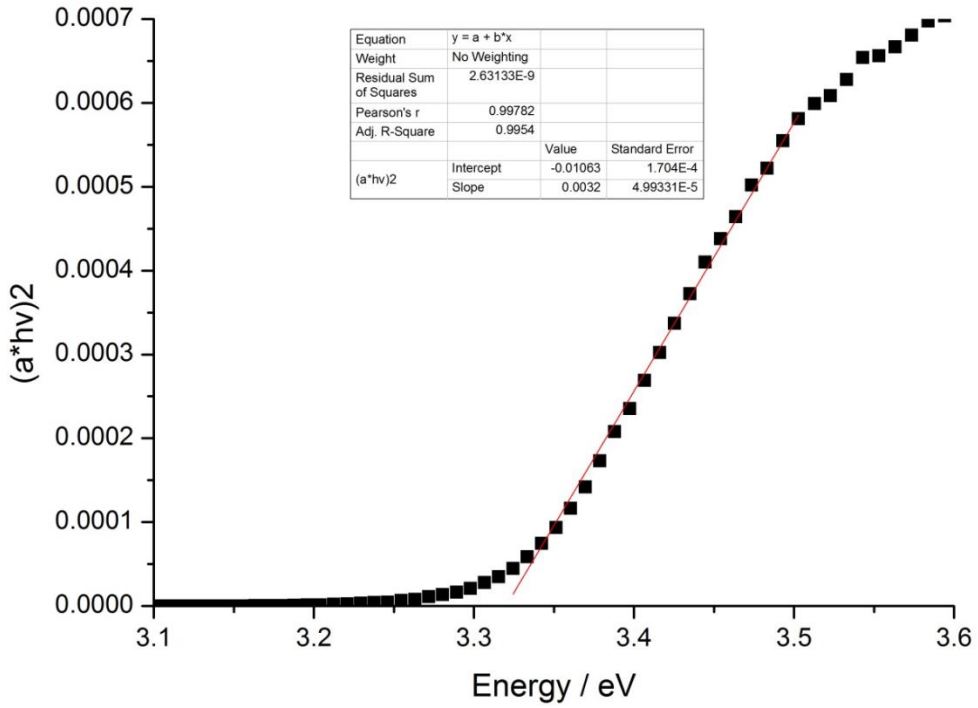

Figure 1-7 – Example of a Tauc Plot

A linear line of best fit is plotted using the values in the linear section which denotes the onset of the absorbance. The band gap is represented by the x-axis intercept of the line of best fit. The error associated with calculation of the band gap is governed by the line of best fit represented by the points at the onset of absorption. With respect to the sample data within the thesis, this error is ± 0.1 eV to 1 decimal place. As a result of this, individual errors are not reported throughout.

1.5.2 Powder X-Ray Diffraction

1.5.2.1 Theory

When X-rays are directed into a single crystal of a substance, the photons are reflected off crystal planes in a regular way producing a sequence of spots which can be interpreted to determine crystal structures. These spots are caused when the incident X-rays refracting off of crystal planes interfere in a positive manner. For positive interference to occur the Bragg law must be followed (Figure 1-8), this states the relationship between the perpendicular crystallographic plane distance, the angle of incidence and the wavelength of the X-ray (Equation 1-8).[49]

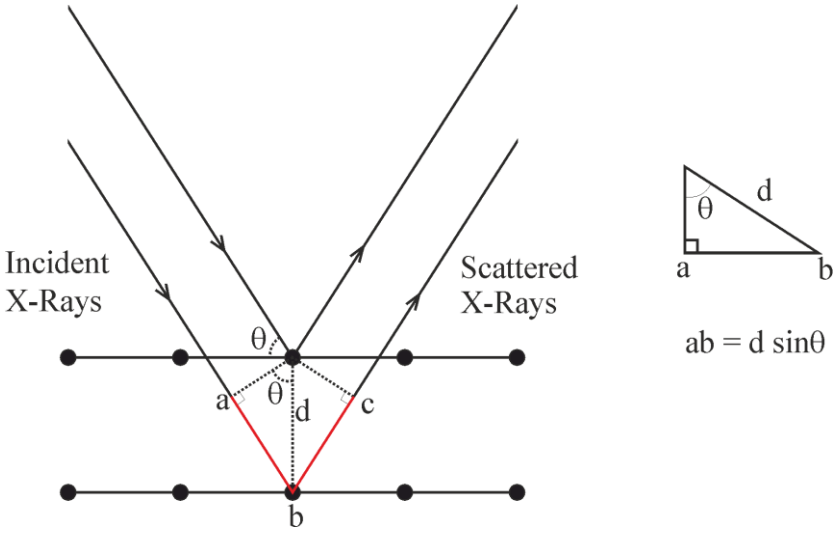

Figure 1-8 - Diagram showing the derivation of the Bragg Law. The red line indicates the extra distance travelled by the photon reflecting off of the bottom plane. The diagram on the right shows the relationship between the angle and the lengths of the sides in the right angled triangle.

$$n\lambda = 2d \sin\theta$$

Equation 1-8 – Bragg Law. Where n is a positive integer, λ is the wavelength of the incident X-ray, d is the crystallographic plane distance and θ is the angle of the incident X-ray.

In a perfectly homogenised powder sample, the random orientation of crystal environments causes the spots to form concentric cones. Integration of these circles results in a diffraction pattern which is characteristic of the crystalline material being analysed. In the case of thin films these crystal environments are rarely homogenous, and often display some preferred orientation, in this situation, the circles may be broken, this can make accurate integration more challenging as very few instruments integrate across the whole circle (Figure 1-9).

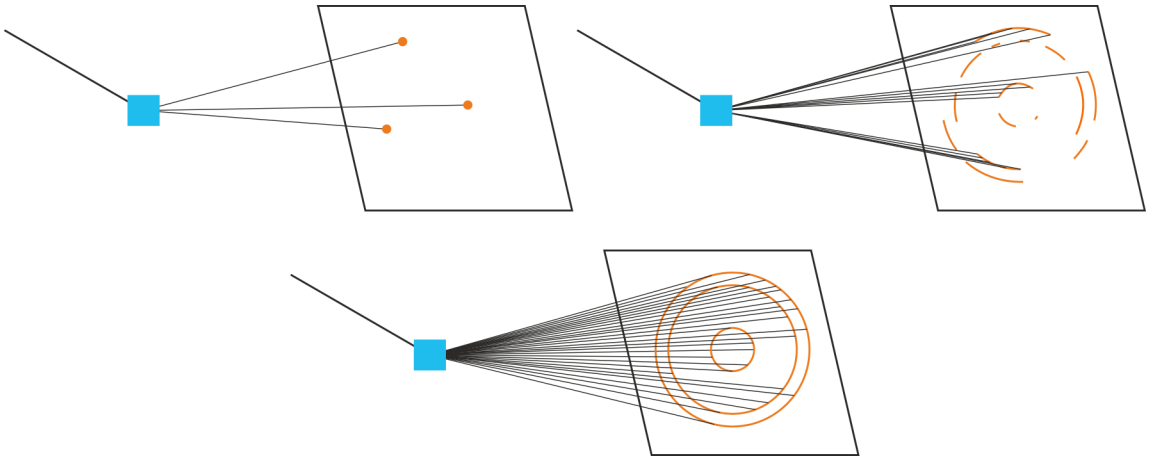

Figure 1-9 – Diagram showing the difference in results for a different powdered states of one material. Top left shows the discreet spots visible from a single crystal, top right shows the broken diffraction rings obtained from a poorly homogenised powder or a thin film and the bottom shows the full diffraction rings obtained from a perfect powder.

The typical method used for collecting powder X-ray diffraction patterns is to use a symmetrical scan. This is a technique in which the angle of the X-ray source is moved vertically in an arc at the same rate as the detection arm. This allows for collection of a diffraction pattern covering a wide 2θ range. However, this technique is often not possible when collecting an X-ray diffraction pattern of a thin film. As a result of the thin nature of the sample, penetration into the substrate of the incident X-ray can occur, reducing the diffraction caused by the sample, this effect is more pronounced at higher angles. Therefore, grazing incidence is often chosen as the preferred method when analysing thin films. Grazing incidence is a technique in which the incident X-ray angle remains fixed and the detector arm moves in a vertical arc. The advantage of this is that it limits the amount of penetration into the substrate by using a low angle to increase the distance the X-ray has to travel through the substrate before reaching the substrate. However, this technique has the disadvantage that the diffraction vector tilts as the detector arm moves in an arc (Figure 1-10).

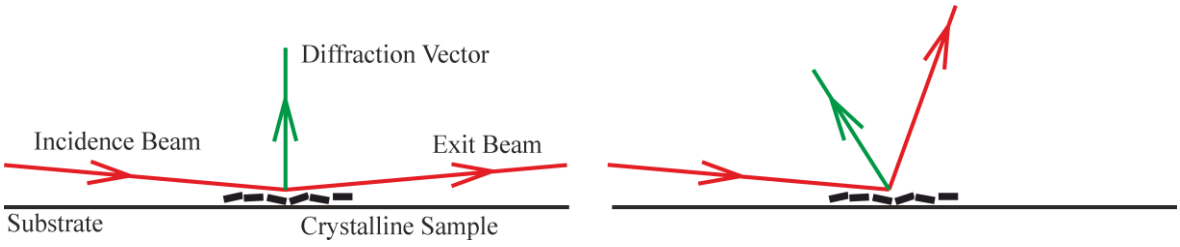

Figure 1-10 – Figure showing the change in diffraction vector as the detector moves. When the incident and exit beams are at the same angle (left) and when the detector moves during grazing incidence (right).

The above figure demonstrates how the diffraction vector is influenced by the position of the incident and exit X-rays. When the beams are at equal angles from the substrate, the diffraction

vector is positioned perpendicular to the surface of the substrate and so samples crystallographic planes which are lying parallel to the surface. Crystallographic faces can only be sampled when they are lying perpendicular to the diffraction vector. As a result of this, as the vector tilts in one direction, it is unable to measure the crystallographic faces unless they are lying in the correct orientation. This can cause issues in samples which exhibit a large degree of preferred orientation, as unless they are arranged perpendicular to the diffraction vector at the appropriate 2θ, they will not be detected.

1.5.2.2 Sample Preparation and Equipment

No prior preparation necessary, however, unless stated otherwise, the same strip which was cut for UV-Vis-Near IR was re-used for XRD. Analyses of the diffraction patterns were performed using the GSAS software. The main parameters which were refined were peak shape, peak position and unit cell parameters, these were all refined as part of a Rietveld refinement. Another parameter which was looked at was the preferred orientation of the samples, this was quantified using the Spherical Harmonic Preferred Orientation model as part of a Rietveld refinement.[50] Due to the samples being analysed through the use of grazing incidence, the preferred orientation represented by the texture index (*J*) is relative to the tilting diffraction vector (Figure 1-10). Due to the method being semi-quantitative, texture index values (*J*) are only reported to 1 decimal place, errors are assumed to be ± 0.1 and so are not reported. Data was collected using either a Bruker GADDS C2 diffractometer or a Rigaku Smartlab diffractometer, using a grazing incidence technique with an incidence angle set between 1 and 5°. Due to the films being deposited onto glass, many of the samples exhibited a broad feature in the X-Ray diffraction patterns between 2θ of 10 and 30, this is a result of the amorphous substrate.

1.5.2.3 Rietveld Refinement

Developed by H.M. Rietveld, the refinement procedure is used to confirm structural models for powder diffraction patterns.[50-52] The method works by modelling each individual data point using a number of factors including instrumental factors and peak profile to achieve the best fit between the observed (y_i) and the calculated data point (y_{ci}). Due to a model being required before refinement, the method cannot be used to solve a structure. The intensity at point *i* can be calculated by taking into account all the Bragg reflections within a fixed range using the following equation.

$$y_{ci} = y_{bi} + s \sum_{K} L_K {F_K}^2 \phi\,(2\theta_i - 2\theta_K) P_K A$$

Equation 1-9 - Rietveld Equation

Where y_{bi} is the background intensity, s is the scale factor, *K* is the Miller Indices of the Bragg Reflection, L_K is the Lorentz polarisation and multiplicity factors, F_K is the structure factor for the

Kth Bragg reflection, φ is the reflection profile function, P_K is the preferred orientation and A is the absorption. A Least Squares analysis can be used during refinement to determine the quality of the fit. During refinement the sum of the squares of the difference between the observed and the calculated data points is minimised and expressed as a χ^2 value. This is defined in the following equation.

$$\chi^2 = \left(\frac{R_{wp}}{R_{exp}}\right)^2$$

Equation 1-10 - Least Squares Equation

Where R_{wp} is the weighted profile and R_{exp} is the expected profile, equations of these are expressed below.

$$R_{wp} = 100\sqrt{\left[\frac{\sum_i w_i|{y_i}^{obs} - {y_i}^{calc}|^2}{\sum_i w_i|{y_i}^{obs}|^2}\right]}$$

Equation 1-11 - Weighted Profile Reliability Factor

$$R_{exp} = 100\sqrt{\left[\frac{(N-P+C)}{\sum_i w_i|{y_i}^{obs}|^2}\right]}$$

Equation 1-12 - Expected Profile Reliability Factor

Where $w_i = \frac{1}{{y_i}^{obs}}$ and is the weighted parameter on the data, N is the number of data points, P is the number of refinable parameters, C is the number of constraints and ${y_i}^{obs}$ and ${y_i}^{calc}$ are the observed and calculated data points. When combined with the least squares equation it becomes.

$$\chi^2 = \frac{\sum_i w_i\left({y_i}^{obs} - {y_i}^{calc}\right)^2}{N-P+C}$$

Equation 1-13 - Substituted Least Squares Equation

During refinement χ^2 is the value which is being minimised and as such tends towards 0 as the fit is improved.

1.5.3 Scanning Electron Microscopy

1.5.3.1 Theory

When a beam of electrons is directed at a sample, a sequence of interactions occurs within a droplet shape, the size of this shape increases with accelerating voltage (Figure 1-11). These interactions are caused by the electrons losing energy through scattering and absorption within the sample. Two of these interactions are typically used to image samples. The first of these are the secondary electrons, these are low in energy (<50 eV) and are the electrons which are emitted from the k-shell of atoms through inelastic scattering.[53] As a result of the low energy, they originate from near the surface of the sample and are used for imaging the surface of a sample during this project (Figure 1-11).

The next source which can be used for imaging are the backscattered electrons. These originate from the electron beam and are a result of reflection or elastic scattering on or within the sample. Backscattered electrons are higher in energy than secondary electrons and so can originate from deeper within the sample.[53]

Certain scanning electron microscopes can also be used to carry out elemental analysis on samples. When a high energy electron from the electron beam interacts with an atom within the sample, there is a chance that an electron from an inner shell of the atom will be excited and ejected resulting in an electron hole; this can then be filled by an electron from an outer shell. The outer shell electrons are higher in energy than those of the inner shells; as a result of this, the excess energy is emitted as a photon. By detecting the energies of the emitted photons, it is possible to determine the elemental composition of the sample. This is a technique commonly referred to as energy dispersive X-ray spectroscopy (EDX).[53]

The final two droplet shapes shown below (Figure 1-11) are continuum X-rays and Fluorescent X-rays. Continuum X-rays are caused by the deceleration of the high energy electron beam and are released as emission as the electrons lose energy within the sample. Fluorescent X-rays are the result of further interaction in the sample from the continuum X-rays and the characteristic X-rays.

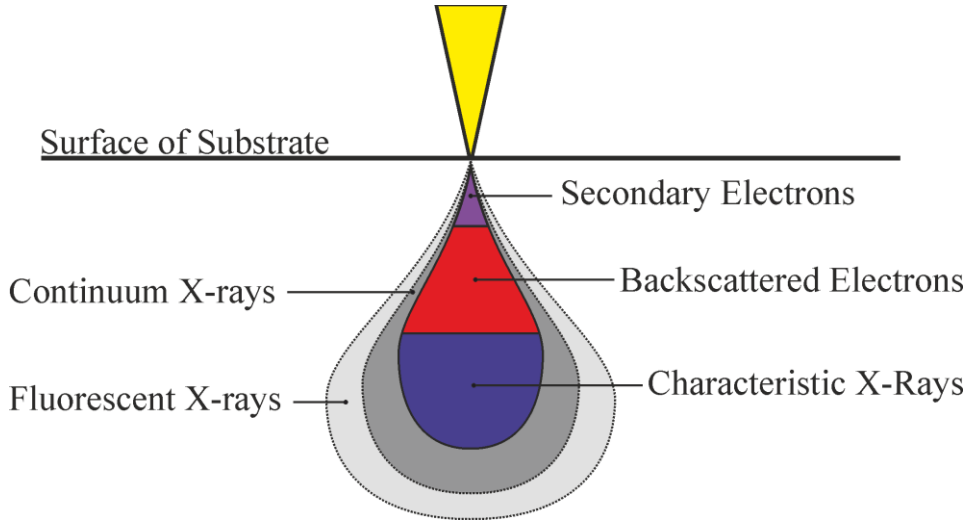

Figure 1-11 - Diagram showing the interactions between the electron beam and the sample

1.5.3.2 Sample Preparation

A small square c.a. 10 mm x 10 mm was cut. This square was secured onto stubs using carbon tape. This was then coated with a layer of gold (Hummer 6.2 Sputtering System coating for 1 minute). The edges were then coated with carbon paint to create a conductive pathway from the gold covered surface to the metal base.

Some samples were coated with platinum/palladium (5 nm) instead of gold; however, unless stated otherwise, the sample was coated with gold.

Unless stated otherwise, scanning electron microscopy was carried out using a JEOL JSM 6500 scanning electron microscope. Energy dispersive X-ray spectroscopy was carried out using a Philips FEI XL30SEM environmental scanning electron microscope.

1.6 Aims

The main aims of this project were to expand the scope of aerosol assisted chemical vapour deposition in the following ways:

- The initial aim of the project was to build up a library of zinc oxide films with varying crystallite structures. This was to be achieved by varying factors in the synthesis of ZnO such as using a range of different additives, in various mole ratios, adjusting the substrate temperature and the flow rate of the carrier gas. These films were to be characterised primarily using XRD and SEM.
- Another aim was to branch into other metal oxides, focussing primarily on titanium dioxide. The objective was to form hybrid films of zinc and titanium oxides which could be reduced to potentially form porous TiO_2 films.
- As an extension to the titanium dioxide work, one aim was to form titanium nitride using aerosol assisted chemical vapour deposition in the absence of ammonia. Once achieved this would carried on by doping in small amounts of an oxygen source in an attempt to form titanium oxynitride.

1.7 References

(1) Novoselov, K. S.; Geim, A. K.; Morozov, S. V.; Jiang, D.; Zhang, Y.; Dubonos, S. V.; Crigorieva, I. V.; Firsov, A. A. *Science* **2004**, *306*, 666.

(2) O'Regan, B.; Schwartz, D. T.; Zakeeruddin, S. M.; Grätzel, M. *Adv. Mater.* **2000**, *12*, 1263.

(3) Strunk, J.; Kähler, K.; Xia, X.; Muhler, M. *Surf. Sci.* **2009**, *603*, 1776.

(4) Ji, L.; Zheng, H.; Ismach, A.; Tan, Z.; Xun, S.; Lin, E.; Battaglia, V.; Srinivasan, V.; Zhang, Y. *Nano Energy* **2012**, *1*, 164.

(5) Parkin, I. P.; Palgrave, R. G. *J. Mater. Chem.* **2005**, *15*, 1689.

(6) Lau, K. K. S.; Bico, J.; Teo, K. B. K.; Chhowalla, M.; Amaratunga, G. A. J.; Milne, W. I.; McKinley, G. H.; Gleason, K. K. *Nano Lett.* **2003**, *3*, 1701.

(7) Li, S. Y.; Niklasson, G. A.; Granqvist, C. G. *Thin Solid Films* **2012**, *520*, 3823.

(8) Kiri, P.; Warwick, M. E. A.; Ridley, I.; Binions, R. *Thin Solid Films* **2011**, *520*, 1363.

(9) Granqvist, C. G. *Adv. Mater. (Weinheim, Ger.)* **2003**, *15*, 1789.

(10) Rogers, K. D. *Powder Diffr.* **1993**, *8*, 240.

(11) Piccirillo, C.; Binions, R.; Parkin, I. P. *Thin Solid Films* **2008**, *516*, 1992.

(12) Warwick, M. E. A.; Ridley, I.; Binions, R. *Surf. Coat. Technol.* **2013**, *230*, 163.

(13) Collinson, M. M.; Higgins, D. A.; Kommidi, R.; Campbell-Rance, D. *Anal. Chem.* **2008**, *80*, 651.

(14) Dong, Y.; Zheng, Y.; Zhang, X.; Duan, H.; Sun, Y.; Chen, Y. *Sci. China, Ser. E: Eng. Mater. Sci.* **2005**, *48*, 601.

(15) Valade, L.; de Caro, D.; Savy, J. P.; Malfant, I.; Faulmann, C.; Almeida, M.; Fraxedas, J.; Brooks, J. S. *J. Low Temp. Phys.* **2006**, *142*, 393.

(16) Hodes, G. *Electrochemistry of Nanomaterials*; Wiley, 2008.

(17) Coddet, P.; Liao, H.-l.; Coddet, C. *Adv. Manuf.* **2014**, *2*, 212.

(18) Tonezzer, M.; Maggioni, G. *Physical vapour deposition techniques for producing advanced organic chemical sensors*; InTech, 2011.

(19) Choy, K. L. *Prog. Mater Sci.* **2003**, *48*, 57.

(20) De Lodyguine, A. *Illuminant For Incandescent Lamps*; US 575668 A; 1897.

(21) Pierson, H. O. *Handbook of Chemical Vapor Deposition*; 2nd Ed. ed.; William Andrew Publishing/Noyes, 1999.

(22) Yamauchi, S.; Yamamoto, K.; Hatakeyama, S. *J. Mater. Sci. Chem. Eng.* **2015**, *3*, 28.

(23) Yamauchi, S.; Saiki, S.; Ishibashi, K.; Nakagawa, A.; Hatakeyama, S. *J. Cryst. Process Technol.* **2014**, *4*, 79.

(24) Hitchman, M. L.; Ahmed, W. *Vacuum* **1984**, *34*, 979.

(25) Hitchman, M. L. *Vacuum* **1984**, *34*, 377.

(26) Krisyuk, V. V.; Sysoev, S. V.; Rumyantsev, Y. M.; Prokhorova, S. A.; Maximovskiy, E. V.; Kosinova, M. L.; Igumenov, I. K. *Phys. Procedia* **2013**, *46*, 174.

(27) Kato, T.; Ito, T.; Maeda, M. *J. Electrochem. Soc.* **1988**, *135*, 455.

(28) Chen, Y.; Sun, J.; Gao, J.; Du, F.; Han, Q.; Nie, Y.; Chen, Z.; Bachmatiuk, A.; Priydarshi, M. K.; Ma, D.; Song, X.; Wu, X.; Xiong, C.; Ruemmeli, M. H.; Ding, F.; Zhang, Y.; Liu, Z. *Adv. Mater.* **2015**, *27*, 7839.

(29) Vernardou, D.; Louloudakis, D.; Spanakis, E.; Katsarakis, N.; Koudoumas, E. *Adv. Mater. Lett.* **2015**, *6*, 660.

(30) Thomas, T.; Blackman, C. S.; Parkin, I. P.; Carmalt, C. J. *Eur. J. Inorg. Chem.* **2010**, 5629.

(31) Bhachu, D. S.; Sankar, G.; Parkin, I. P. *Chem. Mater.* **2012**, *24*, 4704.

(32) Noor, N.; Parkin, I. P. *Thin Solid Films* **2013**, *532*, 26.

(33) Qin, X.; Han, S.; Zhao, L.; Zuo, H.; Song, S. *Wuji Cailiao Xuebao* **2011**, *26*, 607.

(34) McNally, C. S.; Turner, D. P.; Kulak, A. N.; Meldrum, F. C.; Hyett, G. *Chem. Commun.* **2012**, *48*, 1490.

(35) Kaye, K.; Turner, D.; McKenna, D.; Cackett, A.; Hyett, G. *Phys. Procedia* **2013**, *46*, 21.

(36) Cross, W. B.; Parkin, I. P.; O'Neill, S. A.; Williams, P. A.; Mahon, M. F.; Molloy, K. C. *Chem. Mater.* **2003**, *15*, 2786.

(37) Peña, J.; Martínez, A.; Conde, F.; González-Calbet, J. M.; Vallet-Regí, M. *Solid State Ionics* **1997**, *101–103, Part 1*, 183.

(38) Qadri, M. U.; Stoycheva, T.; Pujol, M. C.; Llobet, E.; Correig, X.; Borull, J. F.; Aguiló, M.; Díaz, F. *Procedia Eng.* **2011**, *25*, 761.

(39) Zhao, L.; Qin, X. J.; Shao, G. J.; Wang, N. *Chem. Vap. Deposition* **2012**, *18*, 256.

(40) Qin, X. J.; Zhao, L.; Shao, G. J.; Wang, N. *Thin Solid Films* **2013**, *542*, 144.

(41) Lang, R. J. *J. Acous. Soc. Am.* **1962**, *34*, 6.

(42) Lide, D. R. *CRC Handbook of Chemistry and Physics, 84th Edition*; Taylor & Francis, 2003.

(43) Verma, N. K.; Haider, A. M.; Shadman, F. *J. Electrochem. Soc.* **1993**, *140*, 1459.

(44) West, A. R. *Basic solid state chemistry*; John Wiley & Sons, 1999.

(45) Swanepoel, R. *J. Phys. E. Sci. Instrumen.* **1983**, *16*, 1214.

(46) López, R.; Gómez, R. *J. Sol-Gel Sci. Technol.* **2012**, *61*, 1.

(47) Bass, M.; DeCusatis, C.; Enoch, J.; Lakshminarayanan, V.; Li, G.; MacDonald, C.; Mahajan, V.; Van Stryland, E. *Handbook of Optics Volume 2*; McGraw-Hill, 1994; Vol. 2.

(48) Buchholz, D. B.; Liu, J.; Marks, T. J.; Zhang, M.; Chang, R. P. H. *ACS Appl. Mater. Interfaces* **2009**, *1*, 2147.

(49) Ladd, M.; Palmer, R. *Structure Determination by X-Ray Crystallography*; 5 ed.; Springer US, 2013.

(50) Von Dreele, R. B. *J. Appl. Crystallogr.* **1997**, *30*, 517.

(51) Rietveld, H. M. *Acta Crystallogr.* **1967**, *22*, 151.

(52) Liu, X.; Wankeu, M. A.; Lueken, H.; Dronskowski, R. *Z. Naturforsch., B: Chem. Sci.* **2005**, *60*, 593.

(53) Goldstein, J. *Scanning Electron Microscopy and X-ray Microanalysis: Third Edition*; Springer US, 2003.

Chapter 2: The use of Organic Additives to Control Microstructure and Surface Morphology of Zinc Oxide Thin Films

2.1 Introduction

In recent years there has been an increased interest in zinc oxide materials, with many groups publishing work detailing synthesis and applications as well as reviews discussing recent discoveries.[1-5] As a material zinc oxide is a semi-conductor with a wide direct band gap of 3.37 eV[6] and a large exciton binding energy of 60 meV.[1,7] It has been shown to be a promising candidate for gas sensors[2,8] and dye sensitised solar cells.[9] It has also been investigated as a potential self-cleaning coating and for use in photocatalytic devices.[10,11]

Zinc oxide exists in two common crystallographic phases, hexagonal wurtzite structure[12] and the cubic zincblende structure.[13] There is also a high pressure polymorph in which the zinc oxide adopts a cubic rock salt structure where the zinc and oxygen centres are situated in octahedral geometries, as opposed to the tetrahedral geometries which exist in wurtzite and zincblende.[14] The most common phase is the wurtzite structure (Figure 2-2). The unit cell is hexagonal, with the space group $P6_3mc$ and cell lengths of a = 3.249(8) and c = 5.206(6) nm. For crystals with hexagonal unit cells, it is convenient to express the lattice planes using Bravais-Miller indices (*h k i l)* which incorporate the additional index *i*. This additional index is governed by the restraint $h+k+i=0$ (Figure 2-1).

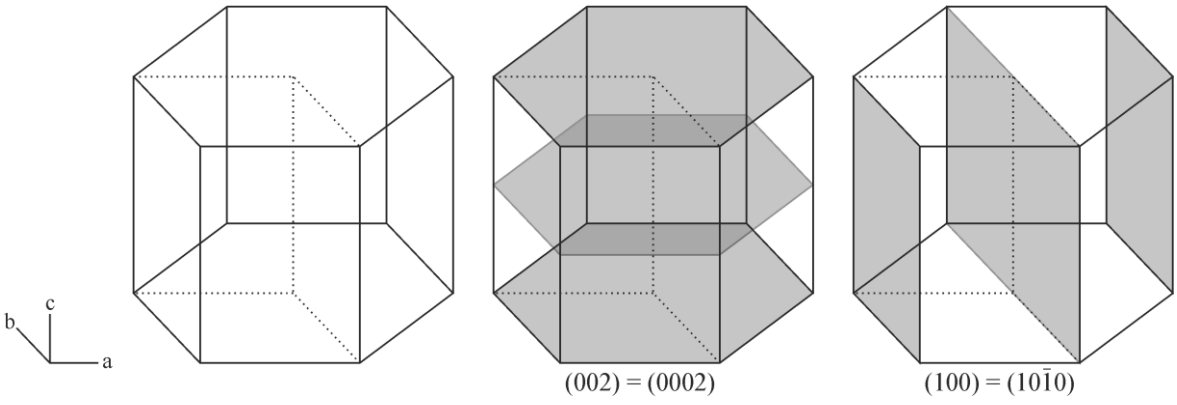

Figure 2-1 – Representation of Bravais-Miller indices in a hexagonal unit cell with two examples of lattice planes. Dotted line represents unit cell.

Aerosol assisted chemical vapour deposition has been used as a technique to deposit thin films of zinc oxide, for example, in 2012, Bhachu et al reported the synthesis of highly conductive and transparent zinc oxide.[15] This was carried out by using a solution of diethyl zinc in toluene with a

dual source of methanol at 450 °C. Their investigation involved doping the ZnO films with small quantities of aluminium or fluorine, to achieve this, they introduced ααα-trifluorotoluene or trimethylaluminium into the diethyl zinc solution prior to carrying out deposition. Using this technique the group was able to synthesise ZnO films with sheet resistance as low as 4.5 $\Omega\ \square^{-1}$.

There has been much interest in manipulating the structure of zinc oxide crystals, this is often as a way to increase the available surface area which will improve the materials interaction with gaseous and liquid phase species; however, it has also been manipulated as a way of increasing the exposure of certain crystallographic faces. For instance, the (0002) face of zinc oxide has been shown to have a 10 fold increase in activity in a dye sensitised solar cell as opposed to randomly oriented zinc oxide.[16] The conversion of CO_2 to methanol was also found to occur at a faster rate in samples of zinc oxide which had a larger surface area of the exposed (0002) face.[17] There has been a large amount of success in using solution based techniques to form zinc oxide with controlled microstructure, for instance, Verges *et al* synthesised a range of microstructures, including prismatic and needle like structures by varying certain conditions such as pH and temperature through hydrolysis of zinc nitrate and zinc chloride solutions.[18] A simple experiment carried out by Al-Harbi *et al* demonstrated the formation of zinc oxide nanorods from a reaction between zinc powder and deionised water at 110 °C.[19] In 2011, Hu *et al* used a self-assembly method to synthesise hollow microspheres composed entirely of zinc oxide nanorods from a solution of zinc acetate and water in glycerol.[20]

There has also been success at controlling the microstructure of zinc oxide through chemical vapour techniques, such as through ethanol assisted vaporisation of zinc oxide powder to form ZnO nanorods carried out by Miyamoto *et al*,[21] or the similar formation of ZnO nanorods using vaporised zinc oxide powder carried out by Yang *et al*.[22] One of the main drawbacks to these methods is the need for high temperatures or low pressures as well as seed layers or expensive precursors such as sapphire or silicon to direct crystal growth.[23-25]

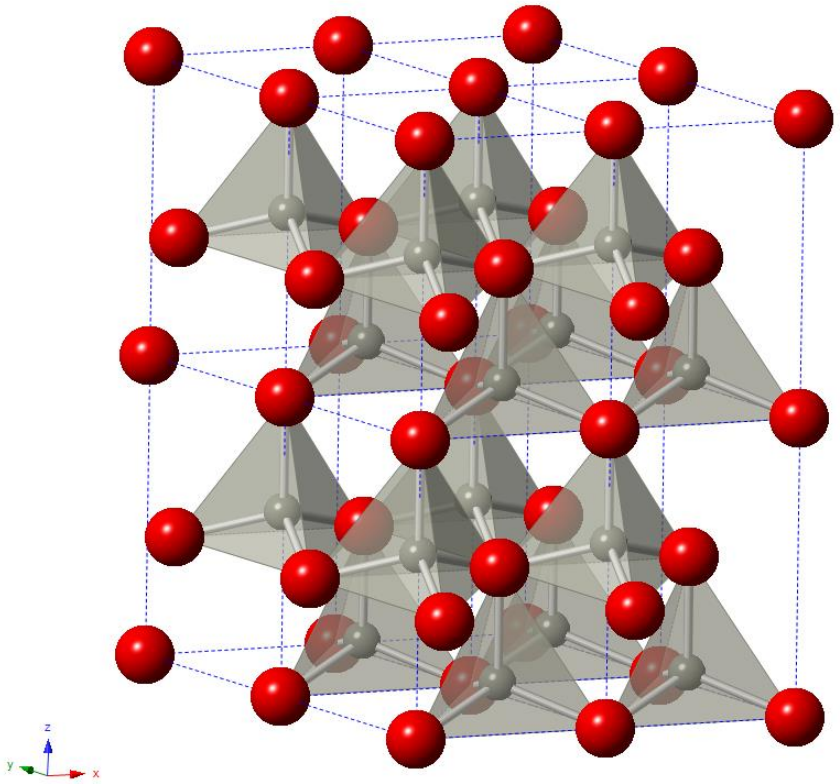

Figure 2-2 – Crystal structure of the wurtzite structure of zinc oxide

One of the most successful methods at controlling the morphology of zinc oxide has been through the use of additives to direct the crystal growth. These behave by attaching to a crystallographic face, capping that area and preventing growth in that direction. A wide range of additives have been used to accomplish this, such as sodium dodecyl sulphate (SDS) being used during electrodeposition of zinc oxide to form a hybrid ZnO:SDS lamellar structure with layers of smooth ZnO plates separated by layers of pillared SDS molecules.[26,27] Qin *et al* employed octylphenol-ethoxylate during electrodeposition of zinc oxide, in this situation the ZnO crystallites grew as tightly packed spheres of uniform size.[28] Zhang *et al* managed to achieve a range of structures including, flowerlike, discs and hexagonal prisms by using ammonia, citric acid and poly (vinyl alcohol) respectively using a hydrothermal synthesis method.[29]

Previous work within the group has demonstrated the use of cetyltrimethylammonium bromide (CTAB) in varying concentrations as an additive during the AACVD synthesis of zinc oxide.[30] The experiments showed that as the mole equivalent of CTAB was increased in respect to the zinc acetate precursor, the resulting structure of zinc oxide changed from being randomly oriented, irregular shaped platelets in the absence of CTAB to regular sized hexagonal plates which aligned parallel to the surface of the substrate in the presence of 0.05 mole equivalents of CTAB or above. These plates were then shown to increase in thickness as the concentration of CTAB was increased to 2 mole equivalents (Figure 2-3).

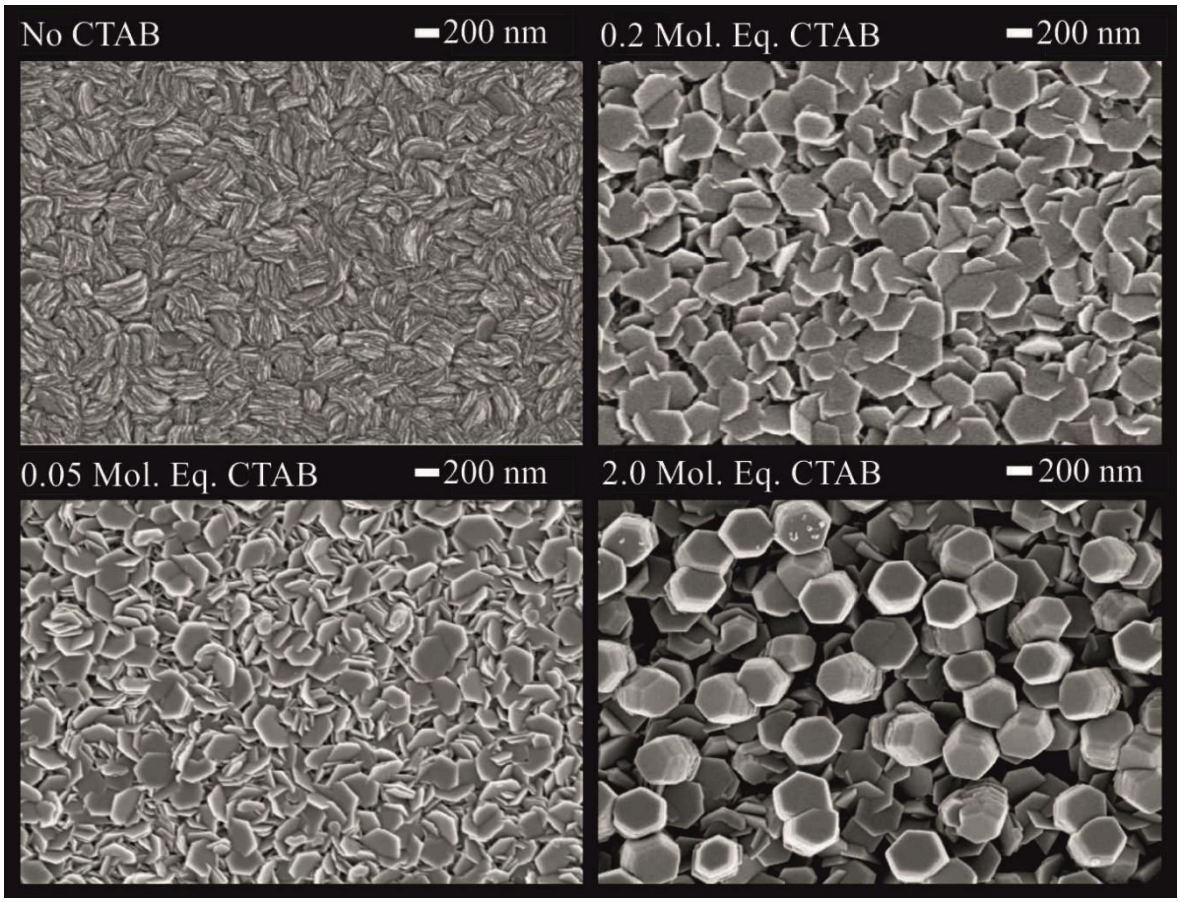

Figure 2-3 – SEM images of ZnO formed in the presence of CTAB, taken from McNally *et al*

During the deposition, thermal decomposition of the zinc acetate precursor will be occurring with the final product being zinc oxide. A study carried out by Chih-Cheng and Yuan-Yao into the formation of zinc oxide from zinc acetate discovered that decomposition begins to occur above 150 °C.[31] Through the use of mass spectrometry they were able to determine that decomposition mostly occurs via the following chemical reactions (Equation 2-1).

Equation 2-1 – Equations outlining the main chemical reactions for the decomposition of zinc acetate into ZnO

$$4Zn(CH_3COO)_2+2H_2O \rightarrow Zn_4O(CH_3COO)_6+2CH_3COOH$$

$$Zn_4O(CH_3COO)_6+3H_2O \rightarrow 4ZnO+6CH_3COOH$$

$$Zn_4O(CH_3COO)_6 \rightarrow 4ZnO+3CH_3COCH_3+3CO_2$$

However, the system also contains methanol. In 1934, Fletcher reported the investigation on the thermal decomposition of methanol in an inert atmosphere. They discovered that under these conditions, methanol begins to thermally decompose at 650 °C into carbon monoxide and hydrogen via the following steps (Equation 2-2).[32]

Equation 2-2 – Reaction equations for the anaerobic decomposition of methanol

$$CH_3OH \rightarrow H_2CO + H_2$$

$$H_2CO \rightarrow CO + H_2$$

During the first step, the methanol decomposes into formaldehyde and hydrogen, this is followed by a rapid further decomposition into carbon monoxide and hydrogen. This reaction was found to occur at much lower temperatures in the presence of zinc oxide by Dohse.[33] In their report, they discovered that ZnO catalyses the decomposition of methanol into carbon monoxide and hydrogen at temperatures around 300 °C. As a result of these reports, it can be postulated that as a solution of zinc acetate in methanol is passed into the decomposition chamber, initially only decomposition of zinc acetate occurs due to the temperature being too low to decompose methanol. However, once a film of zinc oxide begins to build up, methanol will begin to decompose catalytically on the surface. There is potential for these decomposition processes to interact, complicating the steps, without analysing the gases present in the exhaust of the reactor, this cannot be confirmed.

This decomposition is complicated even further upon the introduction of additives. Goworek *et al* reported the thermal decomposition of CTAB in a hydrogen rich environment in 2009.[34] During their investigation, they discovered that at temperatures above 150 °C, trimethylamine is formed along with 1-hexadecene and N,N-dimethylhexadecylamine. Above 300 °C this become more complicated, as three separate isomers of hexadecene and two amines, N,N-dihexadecylamine and N,N,N-trihexadecylamine begin to be observed. Due to the structure of the quaternary ammonium bromides being related, it is possible that decomposition occurs in a similar fashion with loss of a chain to form a tertiary amines and alkenes at low temperatures, and formation of isomers of the longer alkene chains and mixtures of secondary and tertiary amines at higher temperatures.

The aim of this chapter is to build up a library of zinc oxide microstructures by using a range of precursors, primarily quaternary ammonium bromides; however, it will also include anionic sulphates, zwitterions and neutral additives. This will include investigating the effects of temperature and additive concentrations on film thickness, surface morphology and preferred orientation. It will also attempt to shed light upon the mechanism by which the structure is directed by the additives during film growth, whether this is during the solution phase, gaseous phase or on the surface of the growing crystallites.

2.2 Zinc Oxide with No Additive

Films of zinc oxide were analysed using three methods, UV-Vis-NIR, powder X-ray Diffraction and scanning electron microscopy. UV-Vis-NIR spectroscopy data was processed using the Swanepoel method[35] to determine film thickness (see Swanepoel Method, page 12) followed by the Tauc method[36] (see Tauc Method, page 13) to calculate the band gap. Analysis of X-ray diffraction data was carried out using a Rietveld refinement[37] (see Rietveld Refinement, page 17) using the GSAS software, the parameters which were refined were the peak position relating to sample alignment caused by height variations, peak shape using a Gaussian profile, the unit cell parameter, primarily cell lengths. Finally, the preferred orientation is refined as part of a spherical harmonic model to account for preferential growth of certain crystallographic faces within the film. Emphasis is placed upon the preferred orientation of the film due to interest in increasing the exposure of particular crystallographic faces, for instance the (0002) because of its increased activity in certain catalytic processes.[17]

2.2.1 Initial Deposition of Zinc Oxide with No Additive

To compare films of zinc oxide made in the presence of additives, it was necessary to first form zinc oxide films with no other species present. A deposition was carried out following the procedures outlined above (see Experimental, page 8) at 350 °C, with a dispersion chamber height of 0 mm and an argon flow rate of 0.84 l min^{-1}. The solution used was zinc acetate (0.5 g, 2.72 mmol). Supplier and purity information for chemicals used are provided in Appendix A. The resulting film was a transparent coating displaying interference bands. Analysis of the UV-Vis-NIR data showed a film thickness of 499 ± 14 nm and a band gap of 3.3 eV. The XRD data was collected on a Bruker GADDS C2 diffractometer. Data from the XRD showed formation of zinc oxide within a wurtzite phase with no visible signs of contamination. However, the low quality of the obtained data resulted in difficulties in refinement; therefore no lattice data was obtained (Figure 2-4). This is a result of a combination of artefacts within the data caused by filaments within the detector and low intensity of the peaks with respect to the amorphous glass substrate. SEM analysis showed that the crystallites were too small to resolve on the microscope and so observations into the microstructure cannot be made.

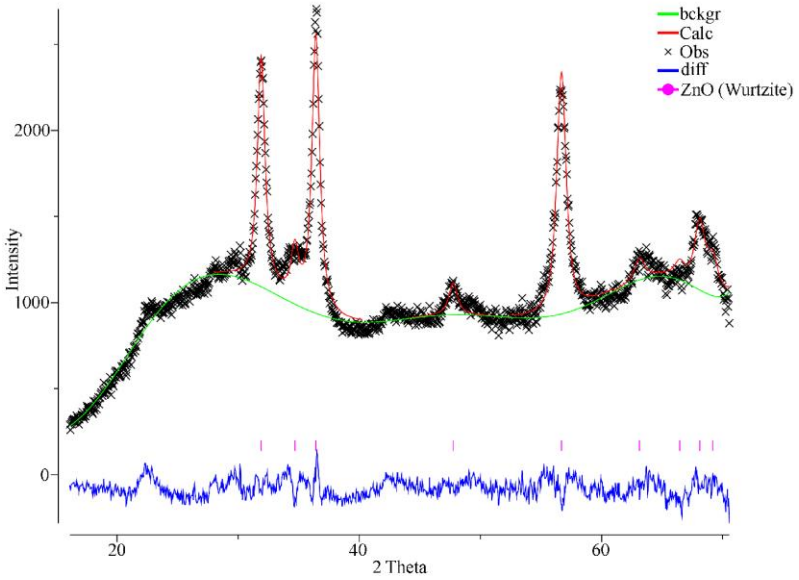

Figure 2-4 – X-ray diffraction pattern of initial deposition of ZnO

2.2.2 Slow Deposition of Zinc Oxide with no Additives

Upon comparison to the methods and results obtained previously by McNally *et al*,[30] it was evident that the zinc oxide crystallites were much smaller than in previous work. It was decided that the main reason for this difference could be caused by the much faster deposition times in the work above (c.a. 30 minutes as opposed to c.a. 120 minutes). To solve this issue the deposition rate was slowed down by increasing the distance between the piezoelectric humidifier and the dispersion chamber along with slowing down the rate of argon flow. A second deposition was carried out following the conditions outlined above (see Experimental, page 8) using a flow rate of 0.42 l min^{-1} argon, a dispersion chamber height of 20 mm and a solution of zinc acetate (0.5 g, 2.72 mmol). Deposition took c.a. 120 minutes and the resulting film once again was transparent and exhibited interference bands. Analysis of the UV-Vis-NIR data revealed a film thickness of 2382 ± 29 nm and a band gap of 3.3 eV. X-ray data was collected on a Bruker GADDS C2 diffractometer, the peaks present were broad, resulting in much overlap, however, refinement showed a cell size of a = 3.248(2) Å and c = 5.243(4) Å and a texture index of J = 1.2, suggesting a very low amount of preferred orientation (Figure 2-6). The broad peaks suggest that the sample is composed of small crystallites of ZnO. The SEM image is shown below (Figure 2-5).

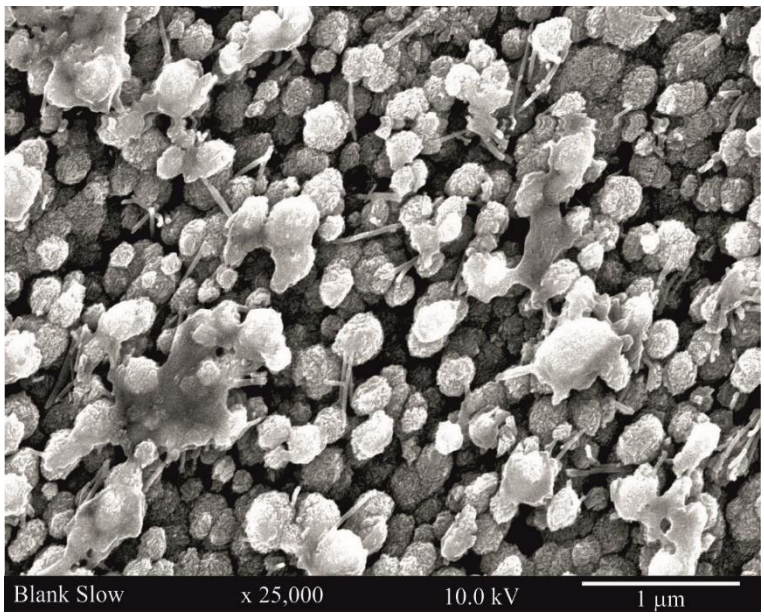

Figure 2-5 – SEM Image of ZnO formed in the absence of any additives

The zinc oxide crystallites have grown into randomly arranged clusters composed of what appears to be irregular shaped plates. The more amorphous coating is possibly a greasy organic material which has contaminated the surface of the film since formation.

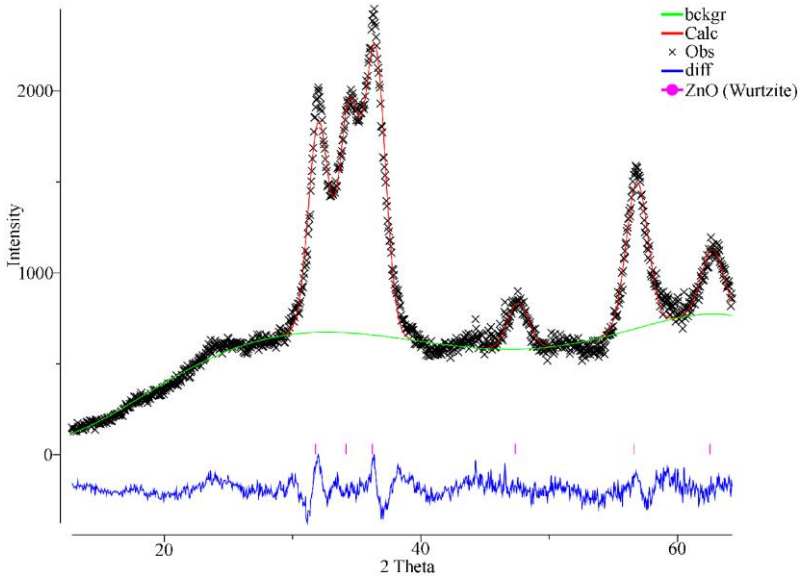

Figure 2-6 – X-ray diffraction data for ZnO formed using the slow deposition technique

2.2.3 Investigation into the Effect of Temperature on the Deposition of Zinc Oxide

To investigate the growth of zinc oxide films with changing temperature, a sequence of depositions was carried out using the same procedure as before, however, the temperature was adjusted between 300 and 500 °C in 25 °C increments. Analysis was carried out with a UV-Vis-NIR spectrometer and a Bruker GADDS C2 diffractometer. A plot of film thickness vs temperature is shown below (Figure 2-7).

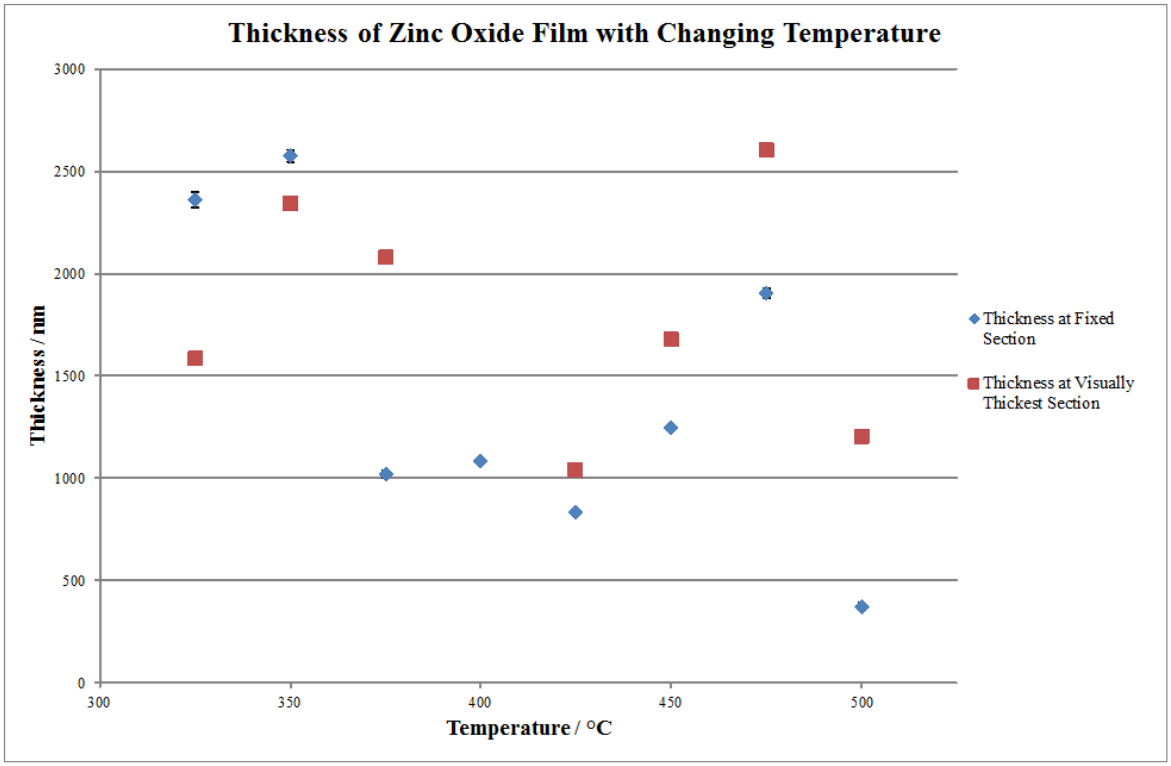

Figure 2-7 – Graph showing the thickness of a zinc oxide film grown at different temperatures

Two points were analysed on each film, the first was at the point which was judged to be the thickest by eye, based on the colour of the interference pattern, and the second point was at a fixed position on each film at 5 cm in from the leading edge of the substrate. As can be seen from the plot, the maximum thickness was reached at the temperatures of 350 °C and 475 °C, however, at 475 °C there is a brown-black deposit within the film, most likely a result of carbon contamination from the decomposition of the acetate ligands and methanol. As a result of this, 350 °C was decided to be the optimal temperature to deposit zinc oxide from a solution of zinc acetate in methanol. To determine how the relevance of the thickness values, the data was used to calculate the refractive index of the films, samples that have a lower refractive index will be less dense, this is a result of porosity or cavities present in the sample. To calculate the refractive index for the sample, T_s must first be determined, this is the %T of the sample when the maxima in the spectrum plateau (Figure 2-8). Due to the transmission of each sample dipping between c.a. 900 and 1500 nm the resulting values of refractive index are subject to a high degree of error. Refractive index (s) is then calculated using the following equation (Equation 2-3).

Equation 2-3 – Equation used to calculate refractive index

$$s = \frac{1}{T_s} + \sqrt{\frac{1}{T_s} - 1}$$

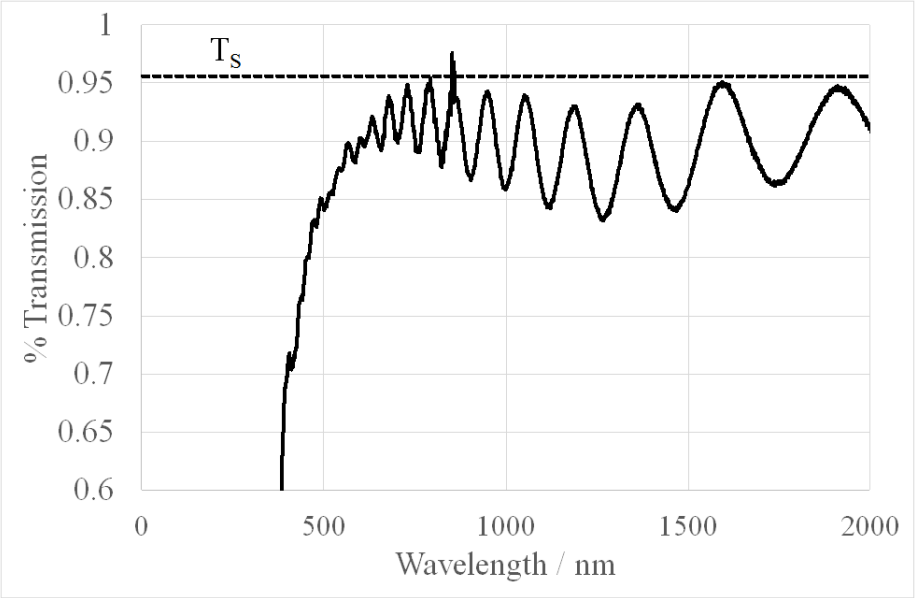

Figure 2-8 – Example transmission spectrum of ZnO to demonstrate T_s. Sample 350 °C at visually thickest point.

The refractive indices are shown in the table below (Table 2-1). The literature value for the refractive index of zinc oxide is 1.92, this is higher than the refractive index for each sample, this suggests that the thin films have a low density. The lowest refractive index was obtained for samples formed at 350 °C, this sample also has the highest thickness, suggesting that this thickness value is not entirely representative of the overall quantity of material deposited.

Table 2-1 – Table outlining the refractive index for each sample of ZnO formed at different temperatures

	Fixed Section		**Visually Thickest**	
Temperature	**T_s**	**Refractive Index**	**T_s**	**Refractive Index**
325	0.94	1.41	0.94	1.44
350	0.95	1.40	0.95	1.36
375	0.92	1.50	0.91	1.57
400	0.91	1.54	Too thin to calculate	
425	0.93	1.45	0.92	1.49
450	0.93	1.48	0.92	1.51
475	0.90	1.60	0.88	1.68
500	0.90	1.59	0.86	1.76

The X-ray data is summarised in the table below (Table 2-2).

Table 2-2 – Table summarising the refined XRD Data for the ZnO deposited at different temperatures

Temperature / °C	**a / Å**	**c / Å**	**Volume / Å^3**	***J***	**χ^2**
300	3.247(6)	5.211(6)	47.6(0)	1.2	3.1
325	3.240(5)	5.232(8)	47.5(8)	1.0	8.6
350	3.249(6)	5.245(2)	47.9(7)	1.1	4.0
375	3.247(0)	5.239(1)	47.8(3)	1.1	7.7
400	3.257(1)	5.225(7)	48.0(1)	1.0	7.7
425	3.256(8)	5.223(0)	47.7(9)	3.0	4.3
450	3.251(9)	5.217(4)	47.7(8)	4.5	4.5
475	3.256(4)	5.220(1)	47.9(4)	2.4	6.8
500	3.248(7)	5.214(3)	47.6(6)	1.8	2.1

Films formed at temperatures of 400 °C and below exhibit little to no preferred orientation, which shows that the crystallites have grown in random configurations. At 425 °C and above this changes and the films show much more preferred orientation with *J* values of 3.0 and 4.5, this is demonstrated in the diffraction patterns with a reduction of intensity in the $10\bar{1}0$ peak, suggesting that as temperature increases, growth in this crystallographic plane becomes less preferential. A plot of the unit cell length with change in temperature (Figure 2-9) shows a trend in the cell length a in which it increases as the temperature approaches 400 °C, at which point it begins to decrease. This pattern is also observed with the unit cell length c, with the maximum cell length observed at 350 °C. This alteration shows that the crystal strain alters direction depending on temperature. A waterfall plot of the XRD patterns is shown below (Figure 2-10).

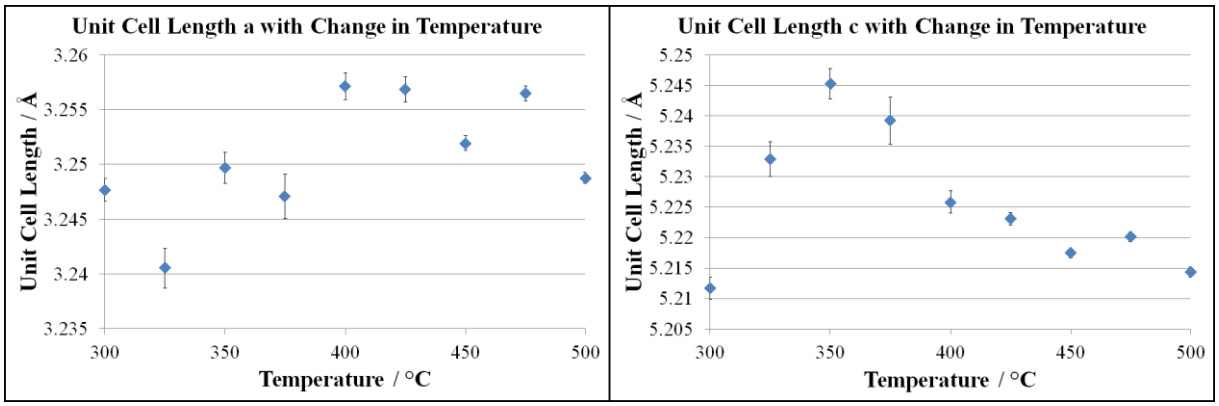

Figure 2-9 – Plots of unit cell lengths vs temperature. a (left), c (right)

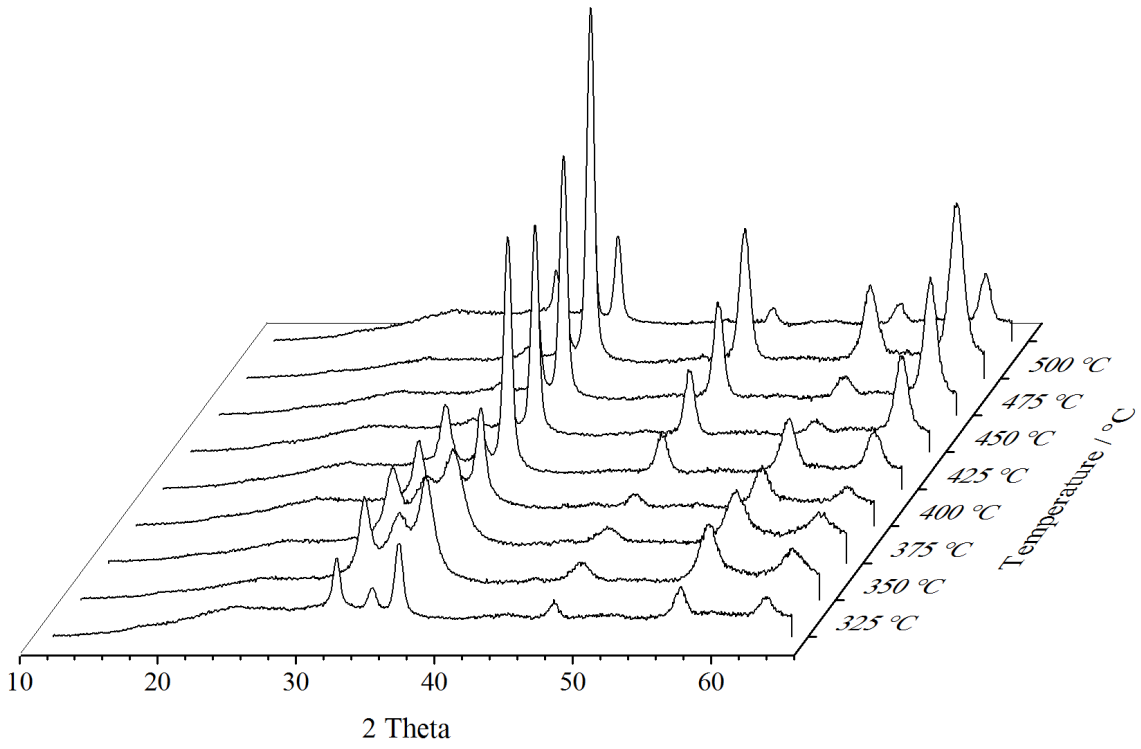

Figure 2-10 – X-ray diffraction patterns for ZnO deposited at different temperatures

2.2.4 Exclusion of Air during the Deposition of Zinc Oxide

A final deposition was carried out using no additive, this time investigating the effect of small amounts of air within the reaction chamber. Previous experiments have been carried out with the exhaust of the deposition chamber being open to air; therefore, a final deposition was carried out using no additive, this time investigating the effect of a completely sealed reaction chamber. A back bubbler of silicone oil was attached to the exhaust and a Teflon gasket was placed between the manifold and the front plate of the deposition chamber to seal any leaks in the metal on metal interface. A temperature of 350 °C was used with an argon flow rate of 0.42 l min^{-1} and a solution of zinc acetate (0.183 g / 1 mmol) in methanol (40 cm^3). The resulting film was transparent and exhibited interference bands. The film was analysed using a Rigaku Smartlab X-ray Diffractometer and a JEOL Field Emission Scanning Electron Microscope. The results from the X-ray diffraction data revealed unit cell lengths of a = 3.240(9) and c = 5.214(0) Å. The texture index gave a value of J = 1.0, showing that the film has little to no preferred orientation (Figure 2-19). The SEM image is shown below (Figure 2-11).

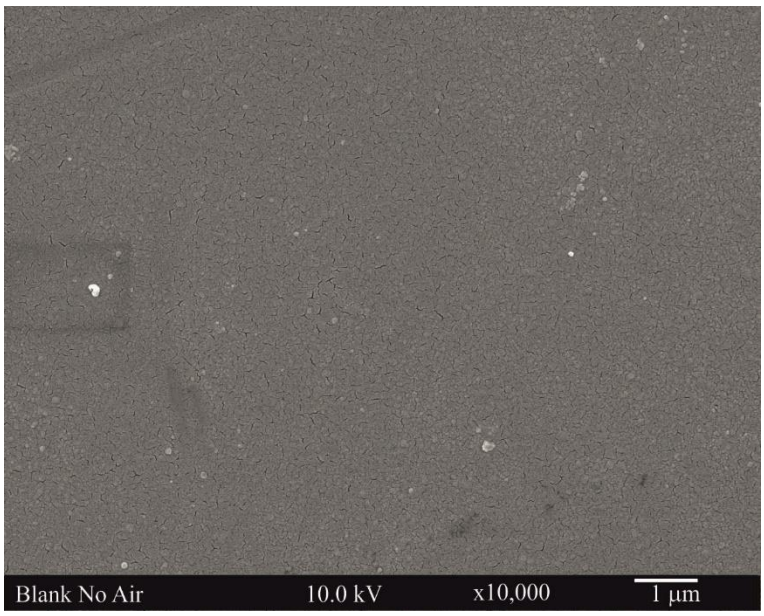

Figure 2-11 – SEM image of zinc oxide formed in the absence of oxygen

The SEM image shows that the zinc oxide crystallites are too small to resolve, however, it does appear as if the crystallites are growing in an irregular arrangement with no particular structure. The lack of contrast suggests that the surface is uniformly flat. The reduction in size of crystallites between the previous experiment (Figure 2-5) could be a result of the lower quantity of zinc acetate used in this deposition, the lower quantity means that there is less overall precursor present, and therefore the growth of the film is inhibited.

2.3 Quaternary Ammonium Bromides to Control Microstructure

2.3.1 Cetyltrimethylammonium Bromide and Investigation into the Mechanism

2.3.1.1 Fast Deposition of ZnO in the Presence of CTAB

Due to the slight differences in methodology between this work and previous experiments[30] it was decided that a comparison should be carried out using cetyltrimethylammonium bromide (CTAB) as an additive in ZnO deposition. The initial sequence of experiments involved using CTAB in a 1:1 mole ratio with zinc acetate in varying concentrations and delivery methods. Each deposition was carried out at 350 °C using a flow rate of 0.84 l min^{-1} and a dispersion chamber height of 0 mm above the piezoelectric humidifier. In each reaction, zinc acetate (0.5 g / 2.72 mmol) and CTAB (0.992 g / 2.72 mmol) were used and the quantity of methanol used was varied as outlined in the following table (Table 2-3). For each run that used aliquots, the full aliquot was allowed to run through the chamber completely before the next was added.

Table 2-3 – Table outlining initial ZnO depositions using CTAB as an additive

Run	**MeOH / cm^3**	**Method**	**Band Gap / eV**	**Texture Index / *J***	**χ^2**
1	40	1 x 40 cm^3	3.3	Low intensity of peaks	
2	80	2 x 40 cm^3	3.3	1.8	7.0
3	80	16 x 5 cm^3	3.3	2.1	1.5

The resulting films were transparent and exhibited interference bands similar to the samples formed in the absence of additive, however, the films formed with CTAB were noticeably thinner, suggesting that the presence of CTAB inhibits film growth of zinc oxide. The reason for this is unclear; however it could possibly be a result of CTAB binding to crystallographic faces of the growing zinc oxide a phenomenon which has been observed in solution phase chemistry, this in turn could be inhibiting the growth of the zinc oxide crystallites. The samples were analysed using UV-Vis-NIR spectroscopy; however, the films were too thin to calculate the film thickness due to the absence of interference bands within the spectrum. The band gaps were calculated using an estimated value for film thickness and so have a large error margin. It was not possible to fully refine the X-ray diffraction data for the sample formed from Run 1; this is due to a combination of the low peak intensity and artefacts within the pattern caused by the filaments within the detector of the Bruker GADDS C2 diffractometer. Run 2 and 3 exhibit texture indexes of 1.8 and 2.1 respectively; this preferred orientation was along the [0002] axis. SEM images of the films are shown below (Figure 2-12).

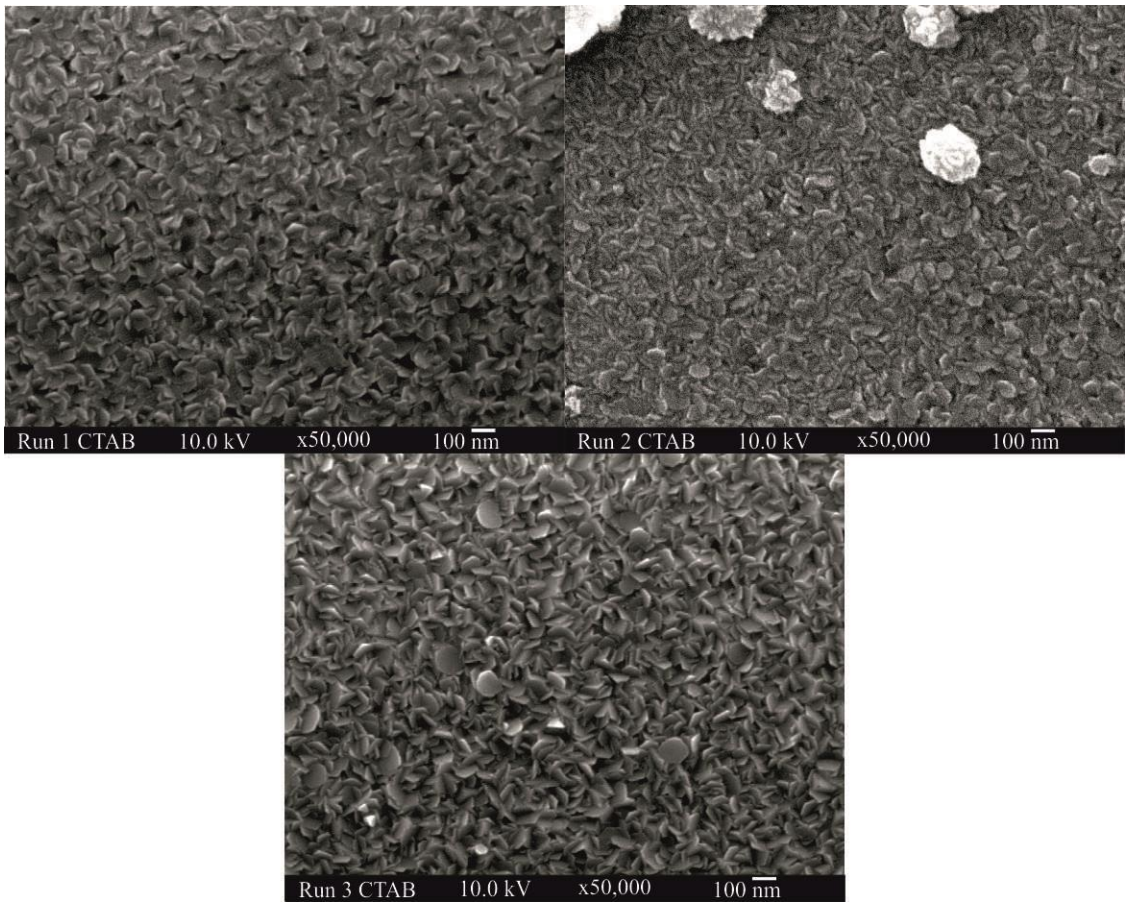

Figure 2-12 – SEM images of initial depositions of ZnO in the presence of CTAB

The SEM images show the formation of hexagonal plates; this is in line with observations made by McNally *et al* in previous studies;[30] however the plate size is smaller, c.a. 100 nm as opposed to c.a. 200 nm. This is potentially a result of the shorter deposition times recorded in this set of experiments, c.a. 30 minutes compared to c.a. 120 minutes.

2.3.1.2 Slow Deposition of ZnO in the presence of CTAB

As a result of the deposition times being shorter than previous experiments, an investigation was carried out in which the deposition was slowed down. To achieve this, two parameters were changed, the first of which was the dispersion chamber height, this was raised to 20 mm above the piezoelectric humidifier. The reason for this is to reduce the efficiency of the aerosol generation and therefore to slow down the rate at which the solution is converted into a mist. The second parameter which was changed was the argon flow rate, this was reduced to 0.42 l min^{-1}, the effect of this would be to lower the rate at which the generated aerosol was transported into the deposition chamber. By lowering the flow rate it was speculated that the precursors would spend more time within the deposition chamber, thus increasing the time in which they are exposed to the high temperature, this was desirable as it would result in more decomposition and therefore more deposition onto the substrate.

A deposition was carried out following the procedure outlined above (see Experimental, page 8) at a temperature of 350 °C, dispersion height of 20 mm and an argon flow rate of 0.42 l min^{-1} using a solution of zinc acetate (0.5 g / 2.72 mmol) and CTAB (0.992 g / 2.72 mmol) in methanol (40 cm^3). The film was analysed using UV-Vis-NIR spectroscopy, X-ray diffraction and scanning electron microscopy. The UV-Vis-NIR data showed that the film had a thickness of 233 ± 15 nm and a band gap of 3.3 eV. This is thicker than the previous films formed in the presence of CTAB, most likely a result of the slower deposition times used allowing more deposition to occur. The X-ray data was collected on the Bruker GADDS C2 diffractometer. Rietveld refinement of the data yielded a goodness of fit index $\chi^2 = 3.4$ and showed a texture index of $J = 4.5$, this shows that the film formed has a high preferred orientation which is found to be along the (0002) plane when compared to the diffraction pattern (Figure 2-13). The SEM of the sample (Figure 2-14) showed the formation of hexagonal plates, many of which appear to be aligned roughly parallel to the surface of the substrate, confirming the high texture index found during refinement of the X-ray data. The plates formed are c.a. 200 nm in diameter, larger than in the previous sample (Figure 2-12). This matches the observations made from the UV-Vis-NIR results. The combination of lower rate of aerosol generation and reduced flow rate has caused the deposition of zinc oxide to be increased, both in terms of film thickness and in crystallite size.

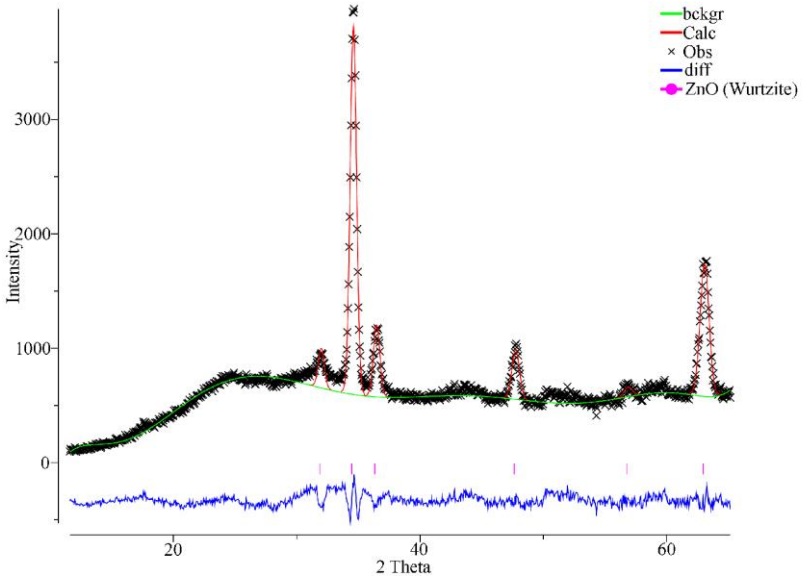

Figure 2-13 – X-ray diffraction pattern of ZnO formed in the presence of CTAB via slow deposition

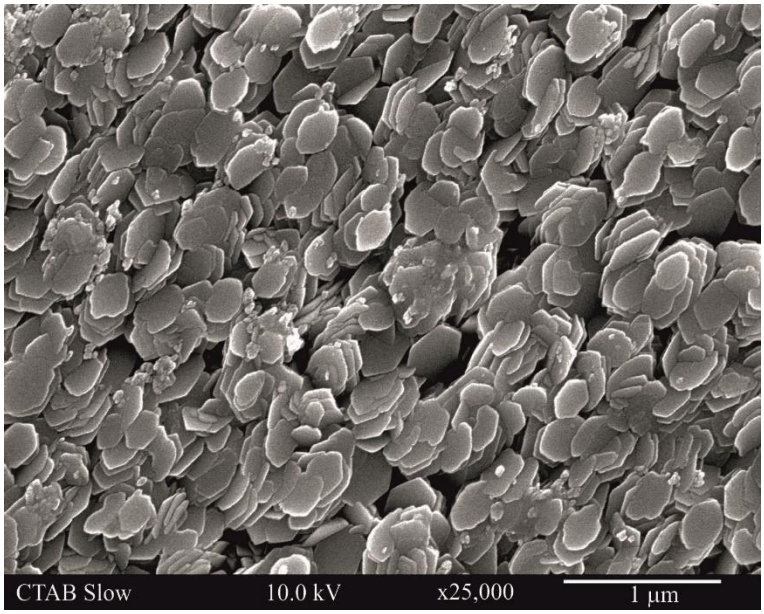

Figure 2-14 – SEM image of ZnO film formed in the presence of CTAB using slower deposition conditions

2.3.1.3 Investigation into the Mechanism of Additive Interaction of the Formation of Thin Films of Zinc Oxide

It was decided to use cetyltrimethylammonium bromide as the additive during an investigation into the mechanism in which the additive interacts with the growing zinc oxide film. The potential areas are within the solution phase as either the bulk solution or inside the aerosol droplets, the vapour phase after the droplets have evaporated within the deposition chamber and finally on the surface of the substrate. A deposition was carried out which utilised separate solutions of precursor and additive which only began to mix within the vapour phase. A schematic of the setup is shown below (Figure 2-15).

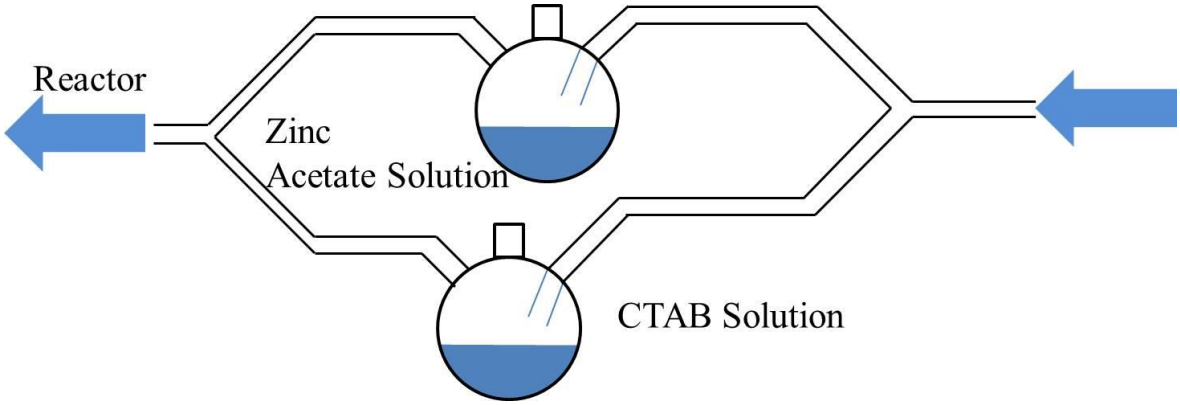

Figure 2-15 – Schematic of the separate precursor and additive deposition

The deposition chamber was set to 350 °C and the argon flow rate was set to 0.84 l min^{-1} of argon, this was to ensure that the flow rate through each solution was 0.42 l min^{-1}. The precursor solution was composed of zinc acetate (0.5 g / 2.72 mmol) in methanol (40 cm^3) while the additive solution was CTAB (0.992 g / 2.72 mmol) in methanol (40 cm^3). Both flasks were positioned at 0 mm above their respective piezoelectric humidifiers. The resulting film was analysed using scanning electron microscopy (Figure 2-16).

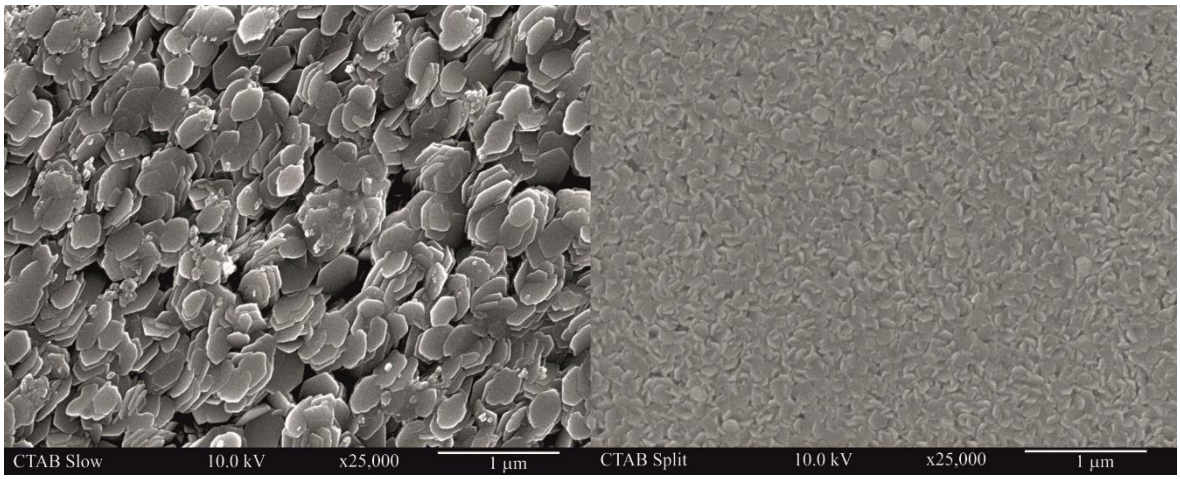

Figure 2-16 – Comparison between ZnO films grown in the presence of CTAB. Single source (left) and dual source (right)

The dual source deposition exhibits the characteristic hexagonal plates which are present within the single source deposition. This suggests that the interaction between the CTAB and the growing zinc oxide film occurs on the surface of the substrate due to the species being separate during the solution phases. However, there could be some interaction occurring between the decomposing zinc acetate and the CTAB within the vapour phase. The decrease in crystallite size in the dual source reaction is most likely a result of the decrease in deposition time for this experiment and the higher flow rate of argon through the deposition chamber. This is the same as the change seen when transitioning between the fast and slow deposition methods. X-ray diffraction was not carried out on this sample.

A deposition was carried out to investigate whether the structure directing effect of the CTAB would continue after the source of additive had run out, to do this a film was formed using the conditions above (see Experimental, page 8) at 350 °C using a flow rate of 0.42 l min^{-1} and a dispersion chamber height of 20 mm and the following solutions.

- First step – Zinc acetate (0.125 g / 0.68 mmol) and CTAB (0.248 g / 0.68 mmol) in methanol (40 cm^3)
- Second step – Zinc acetate (0.375 g / 2.04 mmol) in methanol (40 cm^3)

Both steps were run to completion. This method was used so that the total mass of precursor used was the same as previous experiments while the additive was only present in the solution during the initial stages of film growth. UV-Vis-NIR analysis showed that the film had a thickness of 2095 ± 26 nm and a band gap of 3.3 eV, this result is comparable to the thickness values obtained for films formed in the absence of an additive such as CTAB. Refinement of the X-ray data yielded a goodness of fit index of $\chi^2 = 2.7$ and a texture index of $J = 1.0$ (Figure 2-17), demonstrating that the film has little to no preferred orientation, a result that is once again suggesting that the film has formed in a similar way to that of zinc acetate deposited in the absence of additive. Finally, observations from scanning electron microscopy further reinforce these results. As is shown in the image (Figure 2-18), the zinc oxide has grown into randomly arranged clusters in the same way as was seen in previous zinc oxide depositions (Figure 2-5). These results show that while the CTAB interacts with the growing zinc oxide film on the surface, without a constantly replenishing source of the additive it will not continue to direct the crystallite growth. A possible explanation for this is the high temperature at the surface decomposing the CTAB, preventing it from binding to the crystallographic faces indefinitely, therefore once all of the present CTAB is removed, the film reverts to growing in random configurations with no preference to particular crystallographic faces.

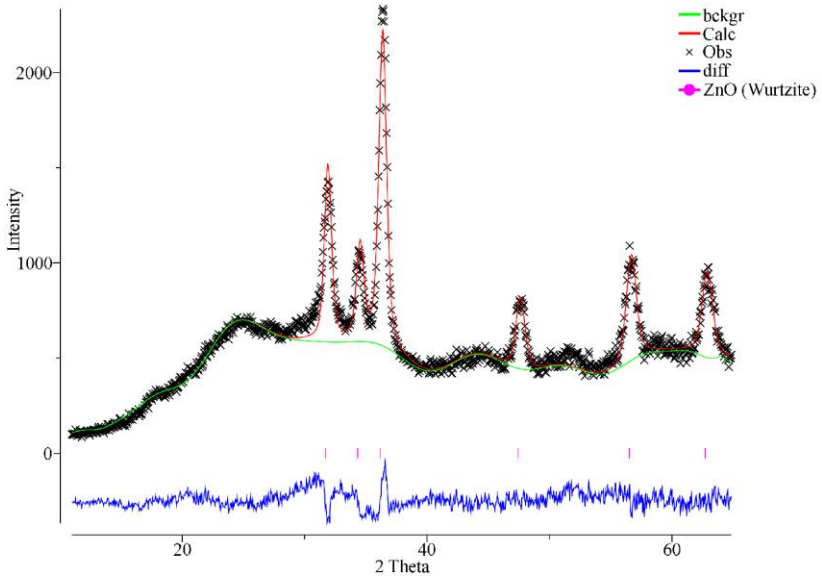

Figure 2-17 – X-ray diffraction pattern of ZnO formed with seed growth in the presence of CTAB

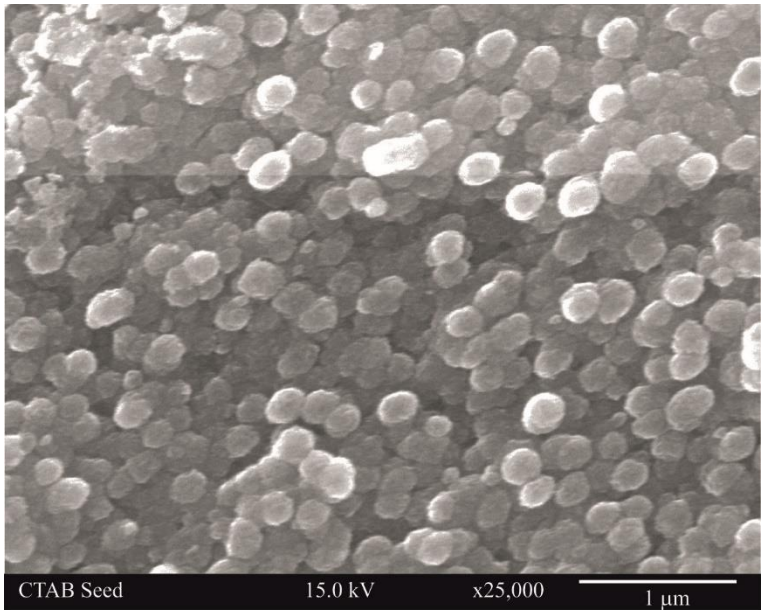

Figure 2-18 – SEM image of ZnO film formed with a seed layer of CTAB

2.3.1.4 Exclusion of Air from the Deposition of Zinc Oxide in the Presence of CTAB

The final deposition of zinc oxide formed in the presence of CTAB looked at the effect of exclusion of oxygen from the system. This was carried out following the procedure outlined above (see Experimental, page 8) at a temperature of 350 °C using a flow rate of 0.42 l min^{-1} of argon, a dispersion chamber height of 20 mm and a solution of zinc acetate (0.183 g / 1 mmol) and cetyltrimethylammonium bromide (0.364 g / 1 mmol) in methanol (40 cm^3). The reactor had been sealed by the insertion of a Teflon gasket between the manifold and the front plate and the addition of a silicone oil bubbler attached to the exhaust, the same conditions used for the sample formed with no additives (see 2.2.4 Exclusion of Air during the Deposition of Zinc Oxide, page 37). The

X-ray data (collected on a Rigaku Smartlab diffractometer) showed a texture index of J = 1.9, suggesting that the film has some preferred orientation; this is revealed to be along the [0002] axis when compared to the diffraction pattern. The X-ray diffraction pattern is shown below, with a comparison to the diffraction pattern from ZnO formed in the absence of any additives, this demonstrates the difference between a texture index of J = 1.0 and 1.9 (Figure 2-19). Scanning electron microscopy showed a film composed of hexagonal plates (Figure 2-20), the same as are observed in previous experiments with CTAB. The crystallite shape is similar to that formed in the previous experiment; however, the plate size is smaller (Figure 2-14). This is most likely a result of the lower quantity of zinc precursor present in this deposition.

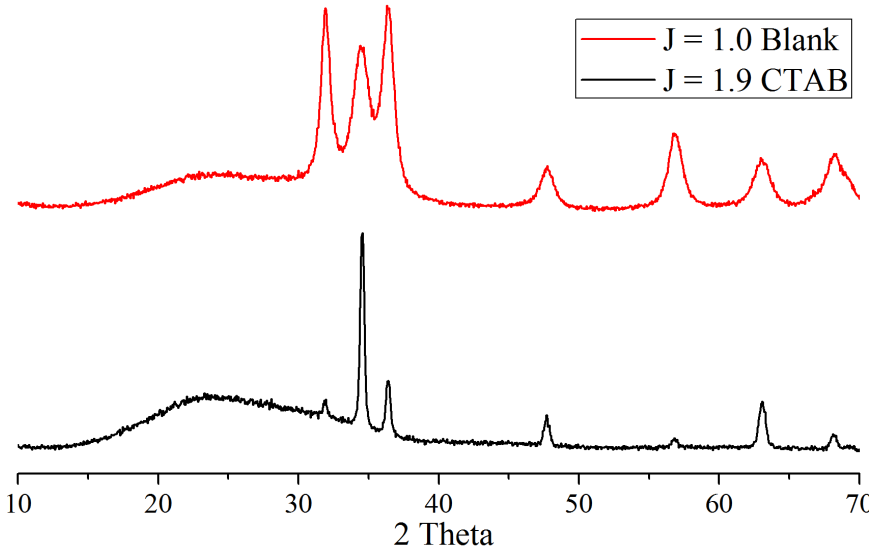

Figure 2-19 – Comparison of ZnO with different texture index. No preferred orientation, taken from data for Chapter 2.2.4 (top), some preferred orientation, taken from sample deposited in the presence of CTAB (bottom).

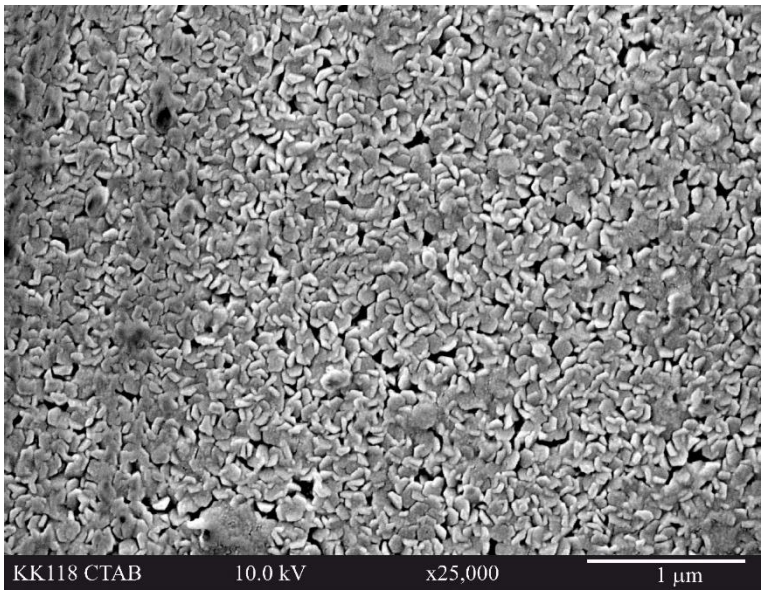

Figure 2-20 – SEM image of ZnO formed in the presence of CTAB in the absence of air

2.3.2 Tetraoctylammonium Bromide

2.3.2.1 Fast Deposition of ZnO in the Presence of TOAB

One of the additives which was tested extensively was tetraoctylammonium bromide (TOAB), like CTAB, it is a quaternary ammonium bromide. The initial experiment carried out was a sequence using a varying mole ratio of TOAB with respect to the zinc acetate precursor. The depositions were carried out as outlined above (see Experimental, page 8) at a temperature of 350 °C, a dispersion chamber height of 0 mm and an argon flow rate of 0.84 l min^{-1}. In each sample, the solution used was zinc acetate (0.5 g / 2.72 mmol) in methanol (40 cm^3) with a quantity of TOAB as outlined in the following table (Table 2-4).

Table 2-4 – Table detailing the runs within the initial TOAB experiment with summaries of UV-Vis-NIR and XRD data

Run	TOAB / g	TOAB / Mol Eq.	Thickness / nm	Band Gap / eV	χ^2	Texture index / *J*
1	0.0094	0.006	264 ± 3	3.3	6.5	1.1
2	0.0472	0.032	218 ± 9	3.3	6.4	1.1
3	0.0945	0.063	222 ± 27	3.3	Incomplete data	
4	0.189	0.126	246 ±4	3.3	1.5	2.0
5	0.472	0.316	299 ± 4	3.3	9.3	4.3
6	0.945	0.632	156 ± 11	3.3	Incomplete data	
7	1.890	1.26	Too Thin		2.2	3.5

Even with only small amounts of TOAB present, the thickness of the resulting zinc oxide films is reduced when compared to the formation of zinc oxide in the absence of any additive (see Zinc Oxide with No Additive, page 30), however, as is the case with CTAB, there is no discernible change in the band gap. Films of zinc oxide formed in the presence of TOAB mirror the results formed in the presence of CTAB, in which the films become progressively thinner as the mole ratio increases suggesting that the additive is inhibiting the growth of the zinc oxide film. This trend is also observed in the texture index for the films, with the samples displaying more preferred orientation along the [0002] axis as the quantity of additive increases. An exemplar fit of XRD data is shown below (Figure 2-21).

The SEM images (Figure 2-22) show that there is a progression within the microstructure as the mole ratio of TOAB increases. At 0.316 mole equivalents of TOAB, the film is composed of randomly orientated clusters of plates, as the ratio increases to 0.632 mole equivalents this microstructure starts to become more organised, with some of the stacks beginning to align parallel to the substrate. At 1.26 mole equivalents of TOAB the microstructure has changed dramatically, it is now composed of hexagonal plates aligned parallel to the substrate, all growing within stacks perpendicular to the surface of the glass. When compared to the high preferred orientation along [0002] visible within the X-ray diffraction data, it suggests that these plates are a physical manifestation of the (0002) crystallographic plane.

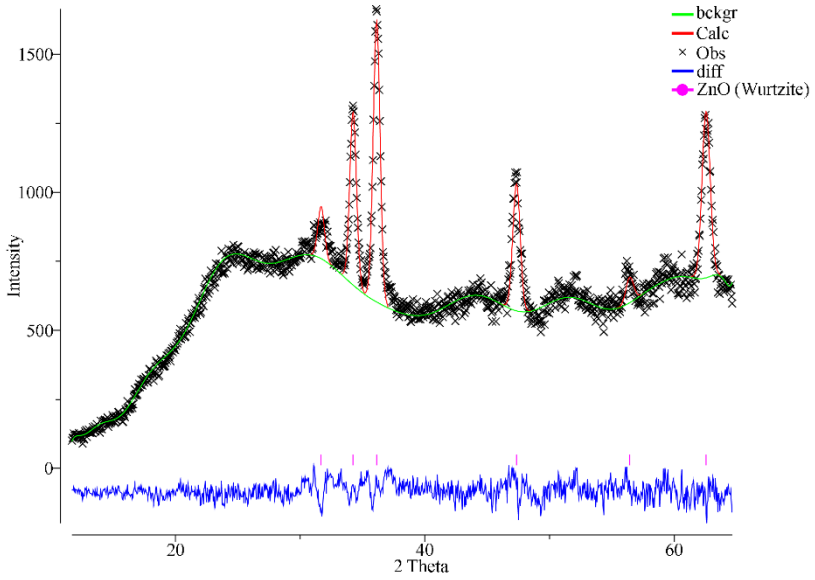

Figure 2-21 – Exemplar X-ray diffraction pattern for initial ZnO formation in the presence of TOAB. Data taken from Run 4, using 0.126 mole equivalents of TOAB.

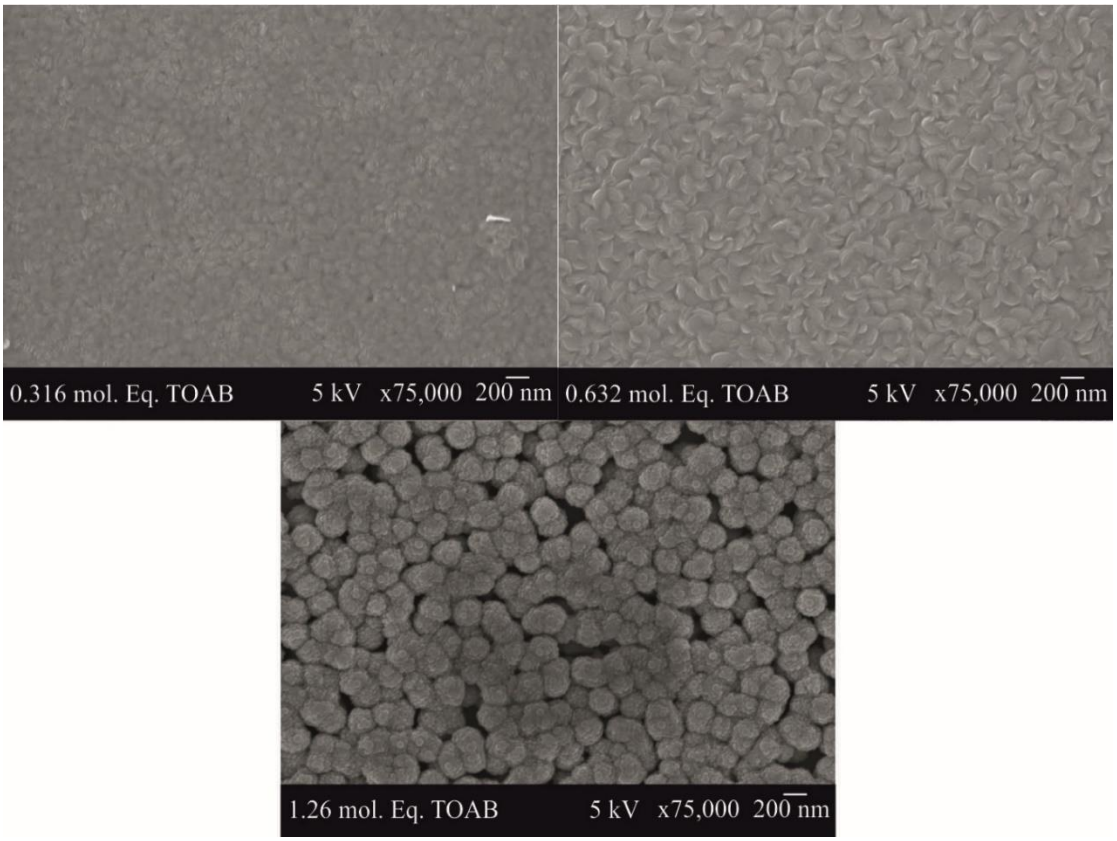

Figure 2-22 – SEM images of ZNO films formed in the presence of TOAB. 0.316 mole equivalents (top left), 0.632 mole equivalents (top right), 1.26 mole equivalents (bottom)

2.3.2.2 Slow Deposition of ZnO in the Presence of TOAB

An investigation was carried out using TOAB to determine whether slowing the deposition down would lead to an increase in film thickness and crystallite size similar to the observation seen when

forming thin films of ZnO in the absence of additive and in the presence of CTAB. Two depositions were carried out to investigate this; both were carried out according to the outline above (see Experimental, page 8) at 350 °C using an argon flow rate of 0.42 l min^{-1} and a dispersion chamber height of 20 mm. Each sample used a solution of zinc acetate (0.5 g / 2.72 mmol) in methanol (40 cm^3) and a quantity of TOAB as described in the table below (Table 2-5).

Table 2-5 – Table outlining slower ZnO depositions with TOAB and summary of UV-Vis-NIR and XRD results

Run	**TOAB / Mass**	**TOAB / Mol Eq**	**Thickness / nm**	**Band Gap / eV**	χ^2	**Texture Index / *J***
1	0.945	0.632	568 ± 13	3.3	3.2	3.8
2	1.890	1.26	Too Thin		2.2	1.4

The results show an increase in film thickness for the sample with 0.632 mol. eq of TOAB when compared to the previous experiment. The sample deposited using 1.26 mole equivalents of TOAB is still too thin to calculate the film thickness. There was no change in preferred orientation for the sample using 0.632 mole equivalents of TOAB, however, when this is increased to 1.26 mole equivalents the texture index drops to $J = 1.4$, this is much lower than the films formed using the faster deposition conditions.

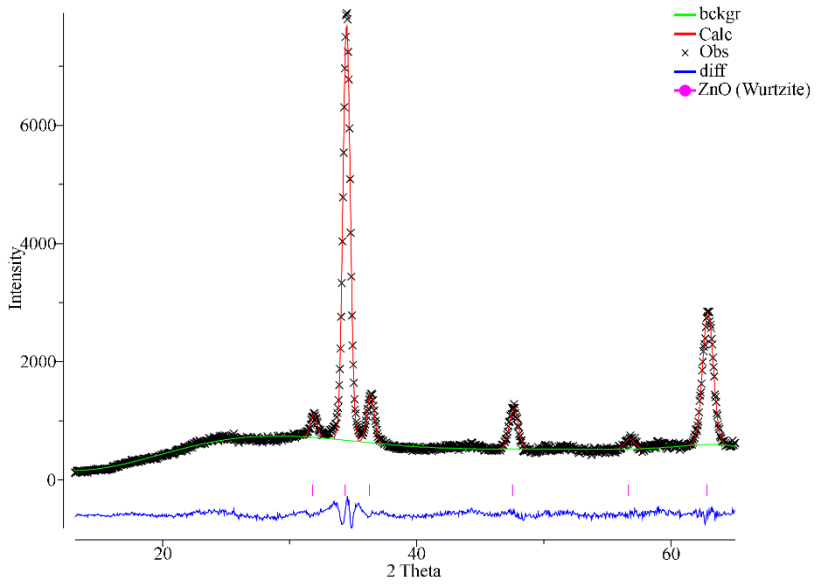

Figure 2-23 – Exemplar fit of X-ray diffraction data for ZnO formed in the presence of TOAB. Data taken from Run 1, with 0.632 mole equivalents of TOAB.

The SEM image for the sample deposited using 0.632 mole equivalents TOAB displays irregular shaped plates arranged in randomly orientated clusters similar to the sample formed using the same mole ratio in the quicker deposition conditions; however, there appears to be less alignment parallel to the surface. At 1.26 mole equivalents of TOAB the ZnO is beginning to form tall stacks growing perpendicular to the substrate composed of hexagonal plates which lay parallel to the glass surface.

The reason for the large spacing between the stacks could be a result of competitive growth, a process in which the stacks that are aligned perpendicular to the substrate grow away from the surface faster than stacks growing at an angle. These stacks then out-compete the others for more material, causing deposition to occur there. This is a process that has been observed by Olson *et al* during the formation of zinc oxide nanowires from a randomly orientated surface.[38]

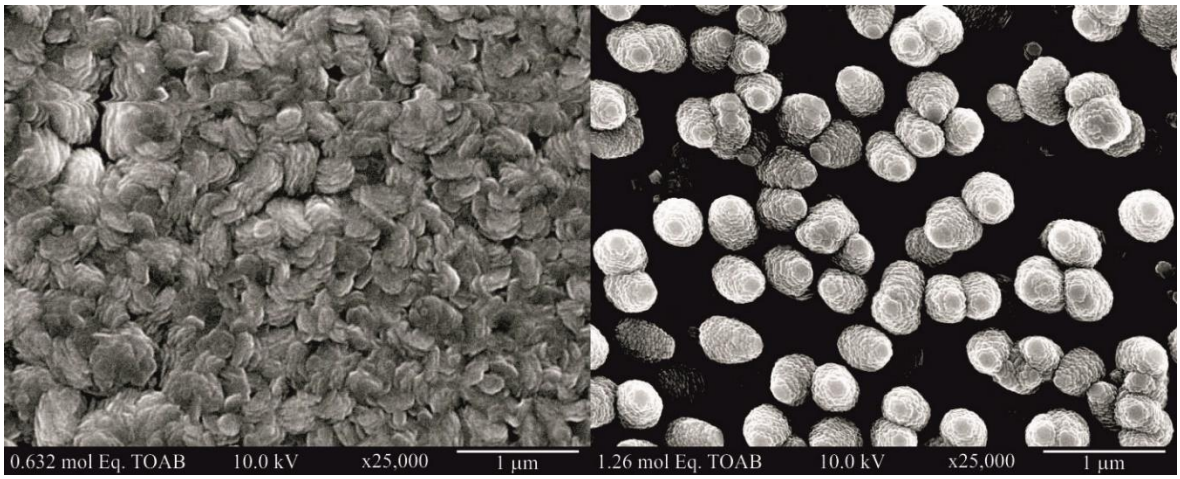

Figure 2-24 – SEM images for samples of ZnO formed in the presence of TOAB. 0.632 mole equivalent (left), 1.26 mole equivalents (right)

2.3.2.3 Further Investigation into the Effect of Mole Equivalents of TOAB on the Deposition of Zinc Oxide

Another set of experiments investigating the mole ratio of TOAB was carried out, focusing on either side of 1.0 mole equivalents of additive to zinc acetate. This was to further explore the change in microstructure that occurs as the ratio increases from 0.632 to 1.26. These depositions were carried out following the procedure outlined above (see Experimental, page 8) at a temperature of 350 °C using an argon flow rate of 0.42 l min^{-1} and a dispersion chamber height of 20 mm. A solution of zinc acetate (0.5 g / 2.72 mmol) in methanol (40 cm^3) was used in each run with a quantity of tetraoctylammonium bromide as outlined in the following table (Table 2-6).

Table 2-6 – Table showing the quantities of TOAB used in the deposition of ZnO and summarising the results from UV-Vis-NIR and XRD analysis

Run	**TOAB / g**	**TOAB / Mol Eq**	**Thickness / nm**	**Band Gap / eV**	**Texture Index / *J***	χ^2
1	1.192	0.8	453 ± 6	3.3	2.9	4.1
2	1.490	1.0	498 ± 19	3.3	2.1	6.9
3	1.788	1.2	674 ± 45	3.3	3.0	6.9

There appears to be a slight increase in film thickness of the ZnO film as the mole ratio of TOAB increases, this is a counter intuitive route as previous experiments have shown that the presence of additive inhibits films growth. This increase could be an artefact of variation of film thickness across the surface of the substrate. Each sample to be analysed was taken from the same section on each substrate, the increasing quantities of TOAB could be causing growth to occur further along the substrate, thus pushing the thickest section of the film closer to the position which was analysed. The X-ray diffraction results (Figure 2-25) show the formation of ZnO with a high level of preferred orientation (J > 2.1) along the [0002] axis. This is reminiscent of the previous results of ZnO deposition in the presence of CTAB and TOAB.

The SEM images (Figure 2-26) show that at 0.8 mole equivalents of TOAB, the ZnO crystallites are growing as roughly hexagonal plates arranged in small clusters, many of these are aligned approximately parallel to the surface of the substrate. As this increases to 1.0 mole equivalent, the plates lose their hexagonal structure, however they grow into larger clusters. At 1.2 mole equivalents of TOAB this structure reverts back to being composed of hexagonal plates which are no longer forming aggregated clusters. The change and difference between this sample and the sample formed from 1.26 mole equivalents of TOAB (see 2.3.2.2, page 49) could be related to position along the substrate. As you move further down the substrate there could be a change in various stages of decomposition for the zinc acetate and tetraoctylammonium bromide, these decomposition products may affect the microstructure in different ways.

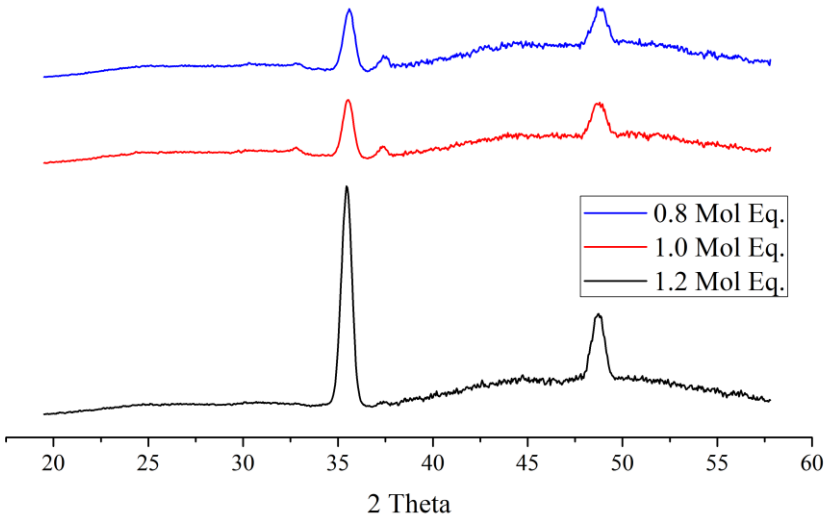

Figure 2-25 – X-ray diffraction patterns of ZnO formed in the presence of TOAB

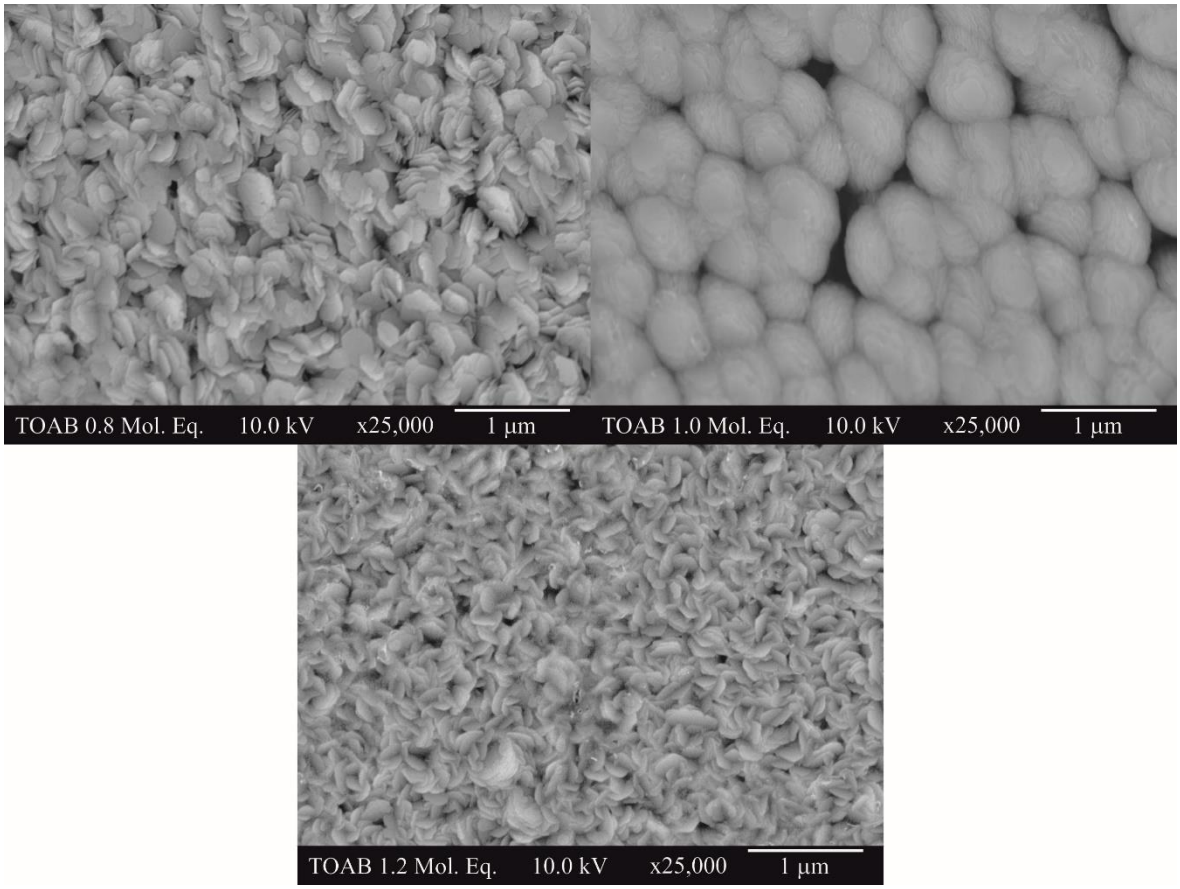

Figure 2-26 – SEM Images of ZnO films grown using varying quantities of TOAB. 0.8 mole equivalents (top left), 1.0 mole equivalents (top right) and 1.2 mole equivalents (bottom)

2.3.2.4 Exclusion of Air on the Deposition of ZnO in the Presence of TOAB

One final film of zinc oxide was formed in the presence of tetraoctylammonium bromide, this time the reactor would be completely sealed to ensure no air is present within the system. To carry this out the reactor was sealed by inserting a Teflon gasket in between the manifold and the front plate, and attaching a silicone oil bubbler onto the exhaust of the deposition chamber. This is the same set-up used above (see 2.2.4, page 37). The deposition was carried out using the procedure above (see Experimental, page 8) at a temperature of 350 °C, an argon flow rate of 0.42 l min^{-1} and a dispersion height of 20 mm. A solution of zinc acetate (0.183 g / 1 mmol) and TOAB (0.543 g / 1 mmol) in methanol (40 cm^3) was used for the deposition.

Once processed, the X-ray diffraction data for the resulting film had a texture index of $J = 1.9$ and a goodness of fit index of $\chi^2 = 1.7$ (Figure 2-27). This is a value similar to that of the film formed using the conditions in which the exhaust of the chamber was open to air (see 2.3.2.3, page 52). The SEM image shows that the film is composed of hexagonal plates of zinc oxide which are forming small clusters, many of which are orientated parallel to the surface of the substrate (Figure 2-28). The structure is reminiscent of the film formed using 1.26 mole equivalents of TOAB (see 2.3.2.2, page 49) and could represent a similar microstructure at an earlier stage. If the film was allowed to grow further, the stacks present in previous samples (Figure 2-24) could be visible in films grown under the same conditions. The reason for it being at an earlier stage is most likely caused by the lower amount of precursor and additive present in this deposition. These results suggest that the presence of air resulting from back diffusion into the reactor has no apparent effect on the deposition of zinc oxide thin films.

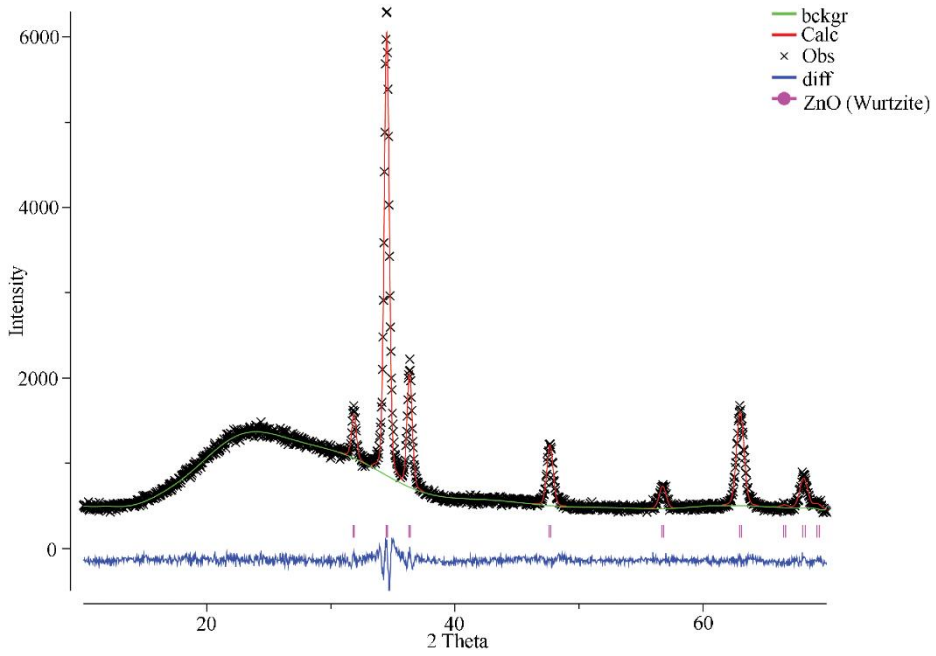

Figure 2-27 – X-ray diffraction pattern of ZnO formed in the presence of TOAB in a sealed reactor

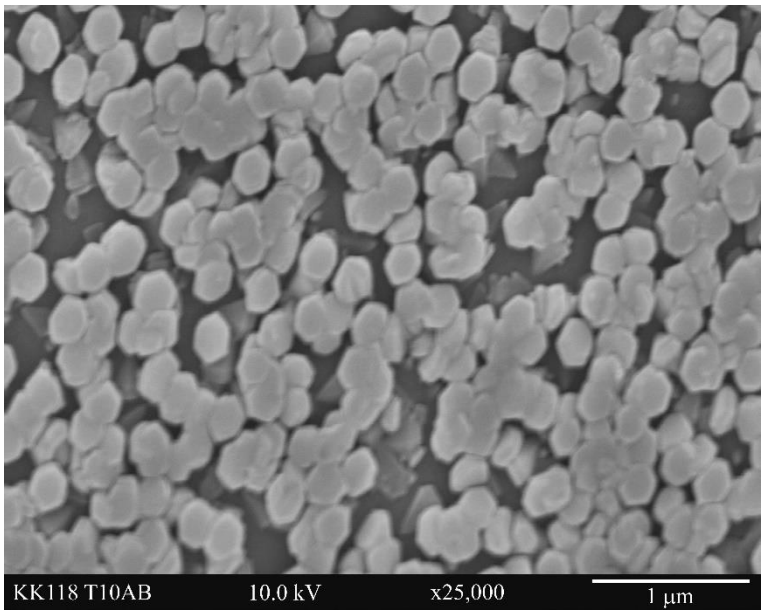

Figure 2-28 – SEM image of ZnO formed in the presence of TOAB in the absence of air

2.3.3 Altering the Chain Length of the Quaternary Ammonium Bromide

2.3.3.1 Fast Deposition of ZnO in the Presence of Various Additives

It was decided that an investigation into the effect of chain length of the quaternary ammonium bromide on the deposition of zinc oxide thin films would be of interest. The quaternary ammonium bromides chosen for this all have equivalent alkyl chains and are shown in the diagram below (Figure 2-29).

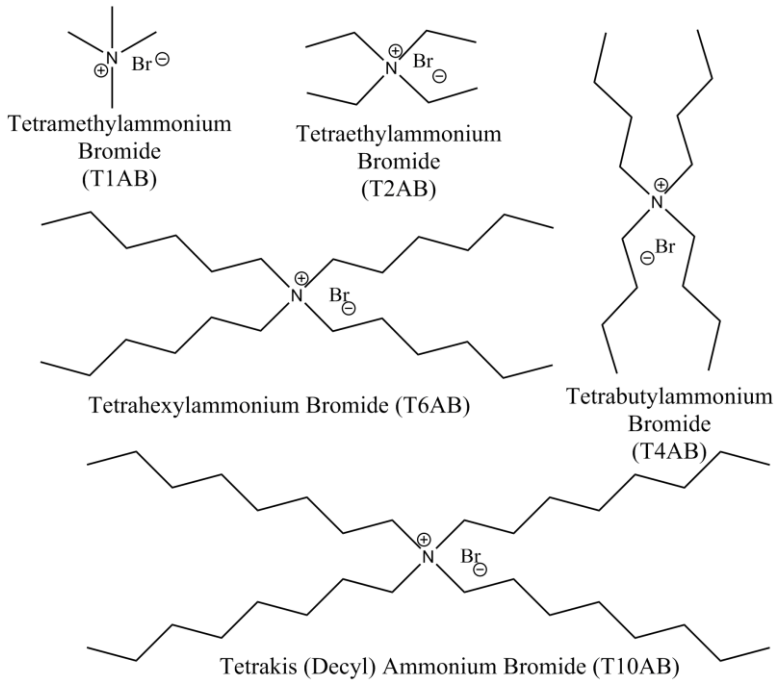

Figure 2-29 - Diagrams of additives used with abbreviations

Each deposition was carried out following the procedure outlined above (see Experimental, page 8) at 350 °C, using an argon flow rate of 0.84 l min^{-1} and a dispersion chamber height of 0 mm. A solution of zinc acetate (0.5 g / 2.72 mmol) and additive (2.72 mmol, 1 mole equivalent) in methanol (40 cm^3) was used for each deposition. The results are summarised in the table below (Table 2-7).

Table 2-7 – Table summarising the results for ZnO films formed in the presence of a range of additives

Additive	**Thickness / nm**	**Band Gap / eV**	**Texture Index / *J***	**χ^2**
T1AB	Too Thin		1.0	4.1
T2AB	Too Thin		1.9	2.4
T4AB	367 ± 3	3.3	4.9	2.3
T6AB	424 ± 7	3.3	2.1	3.0
T10AB	Too Thin		1.0	4.1

The only films which were thick enough to process using the Swanepoel method were the samples formed in the presence of tetrabutylammonium bromide (T4AB) and tetrahexylammonium bromide

(T6AB), therefore it is not possible to determine whether there is a relationship between chain length and the thickness of the resulting zinc oxide film. There does appear to be a trend in texture index however, with the preferred orientation increasing as the chain length increases from methyl to butyl followed by a decrease as the chain length approaches decyl. There is no data available for a film made under these conditions with 1 mole equivalent of tetraoctylammonium bromide; therefore it cannot be included in this sequence as a comparison. The SEM images (Figure 2-30) show that for the sample in the presence of tetramethylammonium bromide (T1AB) the crystallites are growing as irregular shaped plates in randomly orientated clusters. The sample formed using T4AB as an additive exhibits hexagonal shaped plates forming small clusters with many of the plates aligned roughly parallel to the surface of the substrate. The high texture index for this sample suggests that this alignment is representative of the (0002) face of the zinc oxide crystallites. With T6AB as an additive the film is composed of what appear to be irregular shaped stacks. With T10AB as an additive the zinc oxide is growing into randomly orientated clusters composed of plates, similar to the film formed using T1AB as an additive. It was not possible to resolve the detail in the sample with tetraethylammonium bromide (T2AB) as an additive.

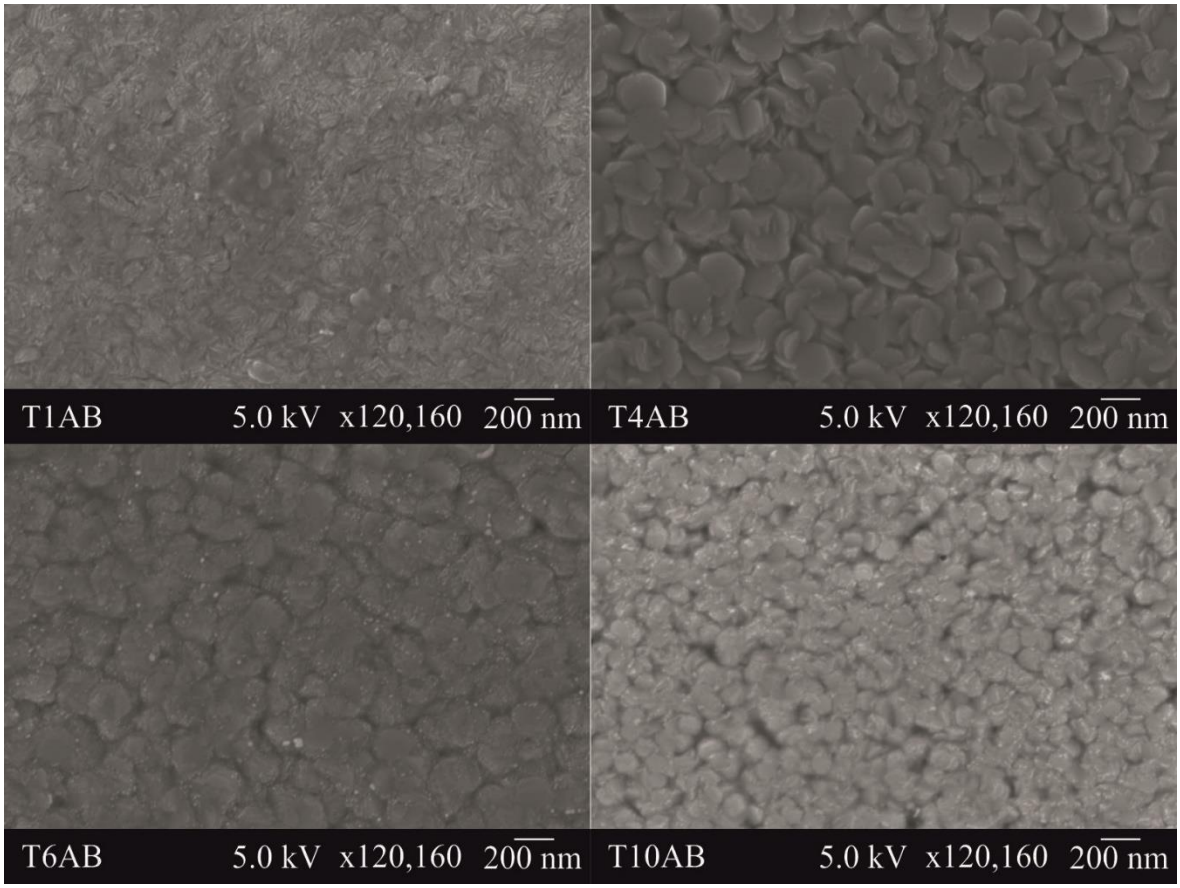

Figure 2-30 – SEM images for ZnO films formed in the presence of various quaternary ammonium bromides. T1AB (top left), T4AB (top right), T6AB (bottom left) and T10AB (bottom right)

2.3.3.2 Slow Deposition of ZnO in the Presence of a Variety of Additives

This sequence of additives was repeated using the slower deposition conditions. Films were formed using the procedure outlined above (see Experimental, page 8) at 350 °C with an argon flow rate of 0.42 l min^{-1} and a dispersion chamber height of 20 mm. Results are outlined in the table below (Table 2-8).

Table 2-8 – Table summarising the results from a sequence of ZnO films formed with a range of additives formed using the slow deposition method

Additive	Film Thickness / nm	Band Gap / eV	Texture Index / *J*	χ^2
T1AB	No Data		1.9	1.7
T2AB	207 ± 22	3.3	2.6	3.4
T4AB	585 ±12	3.3	3.2	6.3
T6AB	802 ± 7	3.3	3.0	9.6
T10AB	342 ± 18	3.3	3.0	3.8

The results for the X-ray diffraction (Figure 2-31) show an increase in preferred orientation as the chain length increases to butyl groups, above this the value seems to hold at a constant value. For all the samples the preferred orientation is along the [0002] axis, as has been the case for other films formed using quaternary ammonium bromides so far. There appears to be a trend in the film thickness as the length of the alkyl chain increases, this is shown in the plot below (Figure 2-32). The thickness value for tetraoctylammonium bromide formed under the same conditions has been included in the figure to complete the series.

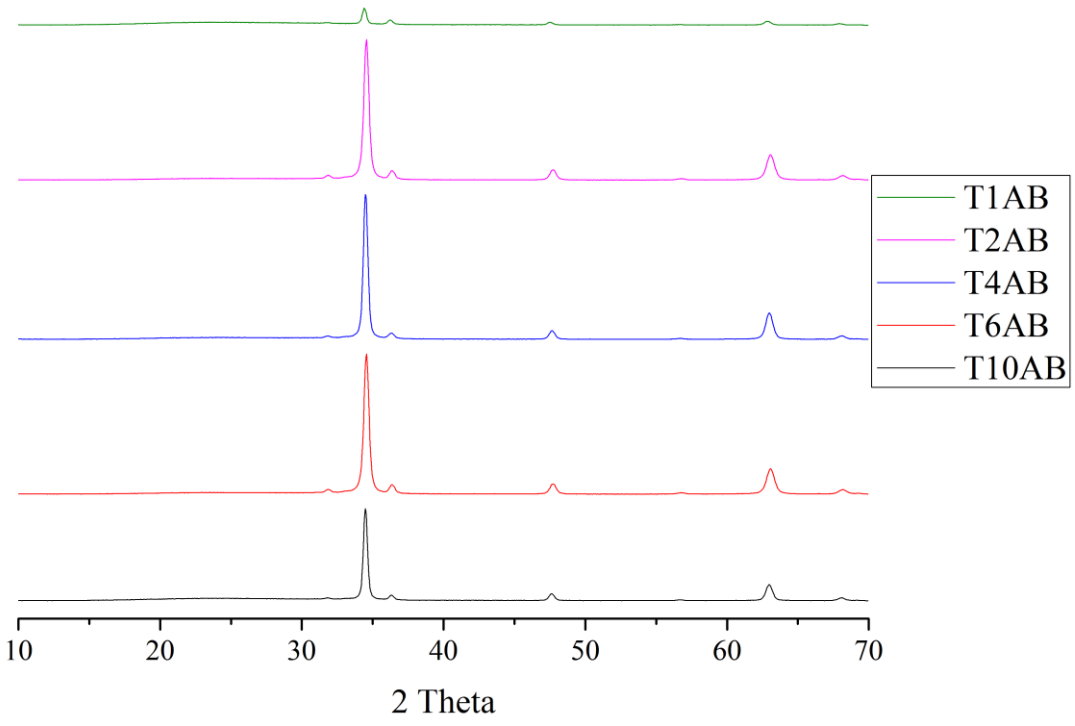

Figure 2-31 – X-ray diffraction patterns of ZnO formed in the presence of the different additives

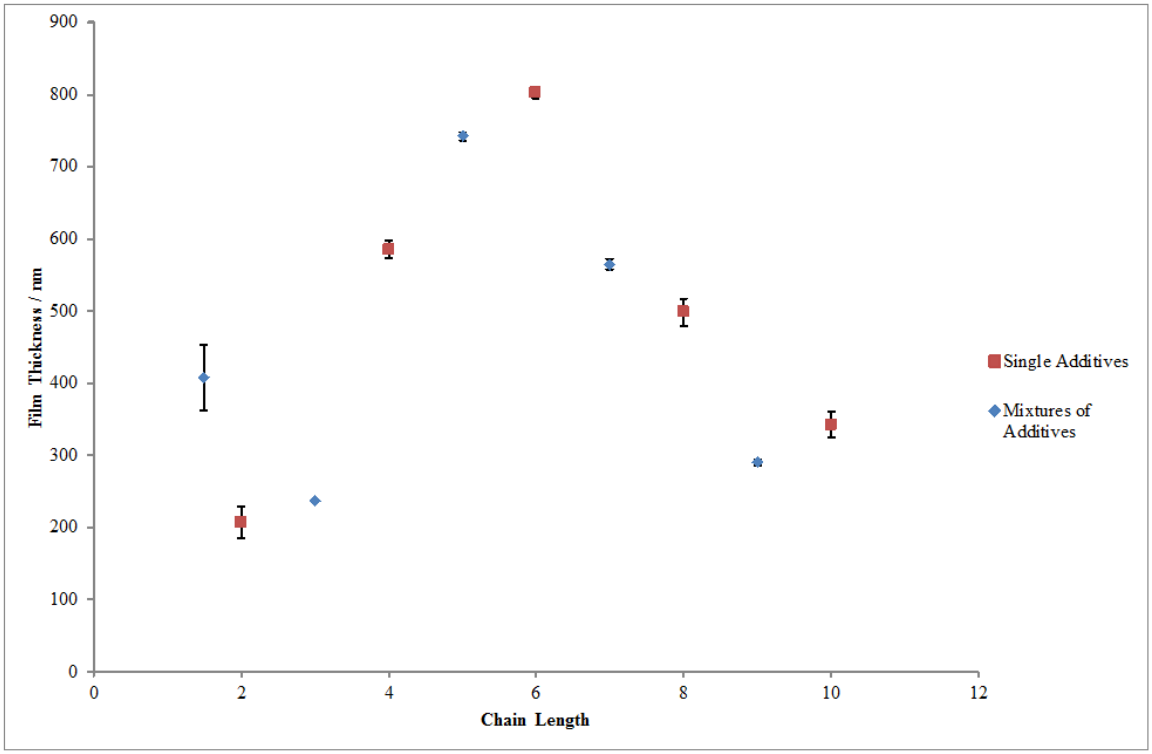

Figure 2-32 - Plot showing the change in ZnO film thickness as the length of the additive chain length increases

The film thickness increases as the chain length of the additive approaches hexyl groups and then decreases as the chain length increases further. This trend is noticed in the SEM images for the same samples (Figure 2-33).

Between T1AB and T4AB there is a progression in the microstructure as the zinc oxide film changes from being composed of well-defined individual hexagonal plates (T1AB) to being formed of irregular shaped plates in small stacks (T4AB) with T2AB demonstrating an intermediate between the two. This trend continues for T6AB with the zinc oxide growing as very irregular shaped plates in large stacks. For TOAB (taken from 2.3.2.3, page 52), this trend begins to reverse as the plates begin to show some hexagonal character and the stacks are formed of fewer plates. Finally, at T10AB the trend has completely reversed and the zinc oxide thin film is composed entirely of well-defined hexagonal plates, many of which are individual. Between tetramethylammonium bromide and tetrahexylammonium bromide the reason for the trend observable in both the film thickness and the microstructure could be related to the lengthening alkyl chains providing better shielding for the cationic ammonium centre of the additive. On the other hand, it is unclear why the trend is reversed for tetraoctylammonium bromide and tetrakis (decyl) ammonium bromide.

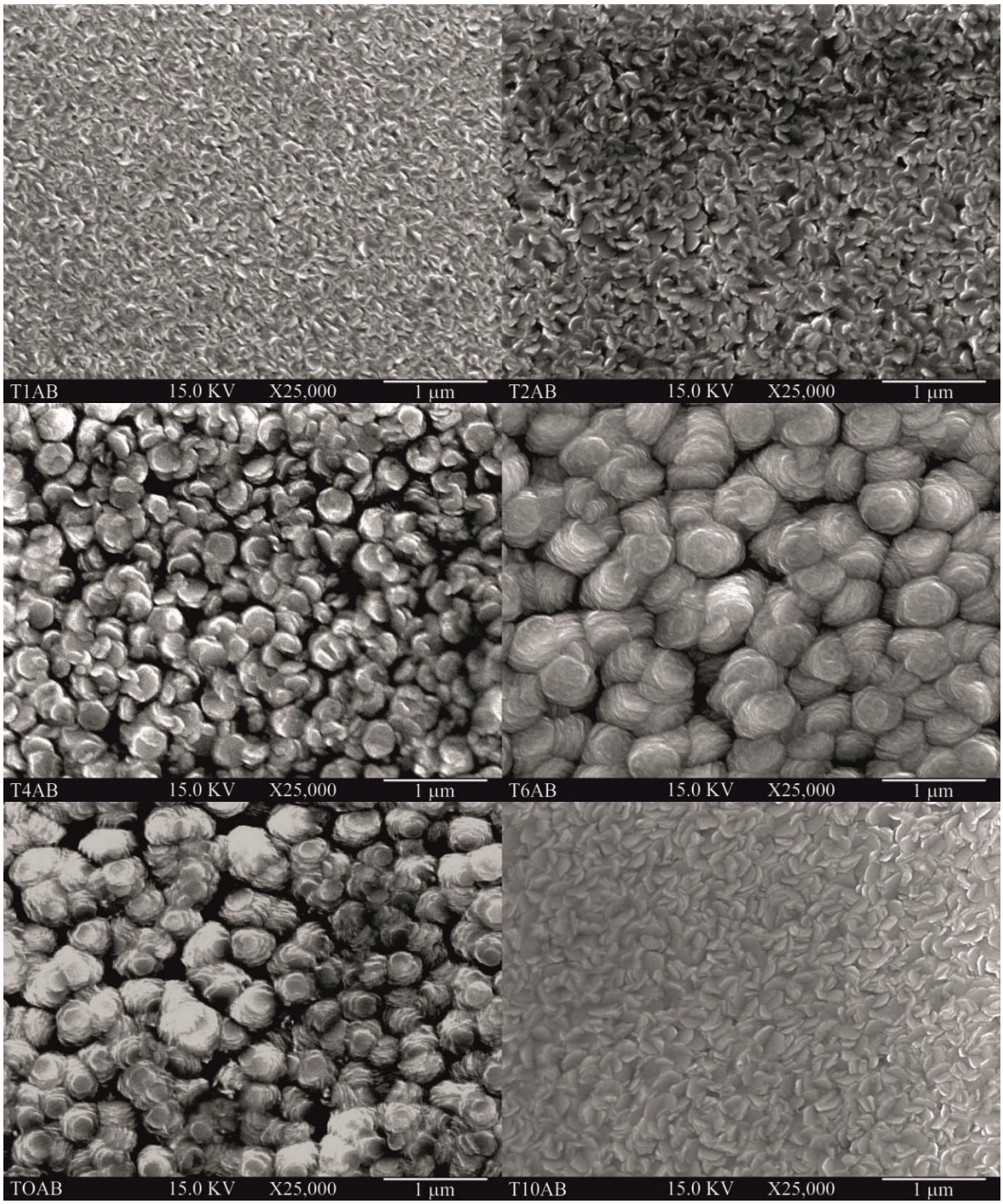

Figure 2-33 - SEM images for ZnO films grown in the presence of a range of quaternary ammonium bromides. T1AB (top left), T2AB (top right), T4AB (middle left), T6AB (middle right), TOAB (bottom left) and T10AB (bottom right)

2.3.3.3 Deposition of Zinc Oxide in the Presence of Mixtures of Additives

A sequence of depositions were carried out using mixtures of consecutive additives to investigate the respective influence each one has on the deposition of zinc oxide thin films. These depositions were carried out following the procedure above (see Experimental, page 8) at a temperature of 350 °C with an argon flow rate of 0.42 l min^{-1} and a dispersion chamber height of 20 mm. A solution of zinc acetate (0.5 g / 2.72 mmol) in methanol was used for each run. The additives were present in equal mole quantities (1.36 mmol) so that the total additive to precursor ratio was 1:1 with respect to zinc acetate. The additives present are shown in the table below (Table 2-9).

Table 2-9 – Table outlining the additives used in each deposition and summarising the UV-Vis-NIR and X-ray diffraction results

Shorthand Sample Name	**Additive 1**	**Additive 2**	**Thickness / nm**	**Texture Index / *J***	**χ^2**
T‘1.5’AB	T1AB	T2AB	407 ± 46	2.0	2.1
T‘3’AB	T2AB	T4AB	237 ± 1	2.8	1.8
T‘5’AB	T4AB	T6AB	742 ± 6	2.9	8.9
T‘7’AB	T6AB	TOAB	564 ± 7	3.5	12.9
T‘9’AB	TOAB	T10AB	290 ± 4	2.8	2.3

The thickness results follow the same pattern as seen with the additives when used singularly (Figure 2-32), with the thinnest films being formed using tetramethylammonium bromide and tetrakis (decyl) ammonium bromide while the thickest are formed in the presence of tetrahexylammonium bromide. The result for the mixture of T2AB and T4AB does not fit into this trend, the reason for this is unclear, however, it could be related to variations in sample thickness across the surface of the substrate. The X-ray diffraction data shows that each sample exhibits preferred orientation along the (0002) axis (Figure 2-34).

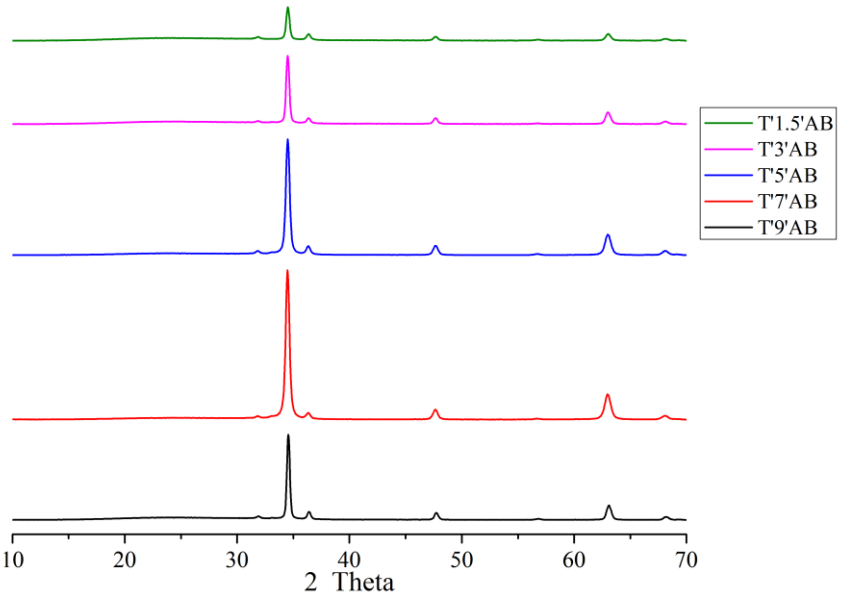

Figure 2-34 – X-ray diffraction patterns of ZnO formed in the presence of mixtures of additives

The SEM results (Figure 2-35) also follow the same trend as observed in the additives used singularly (see 2.3.3.2, page 58). Samples T‘1.5’AB and T‘3’AB show well defined hexagonal plates, with some stacking of the plates visible in T‘3’AB. T‘5’AB exhibits hexagonal plates, however the definition is much less pronounced and they are aggregating into much larger stacks. There are signs of a layering system present, with the lower layer showing stacks of plates with random orientations and the top layer showing preferential growth perpendicular to the substrate. The sample T‘7’AB is composed of irregular stacks in large clusters with random orientations. The hexagonal shape of the plates has been completely lost. Finally, the sample T‘9’AB shows that the structure of the zinc oxide has reverted back to being composed of hexagonal pates in small clusters. The SEM images show that the microstructure for each sample exhibits an intermediate structure between the individual additives, showing that each additive influences the structure of the film to an equal degree.

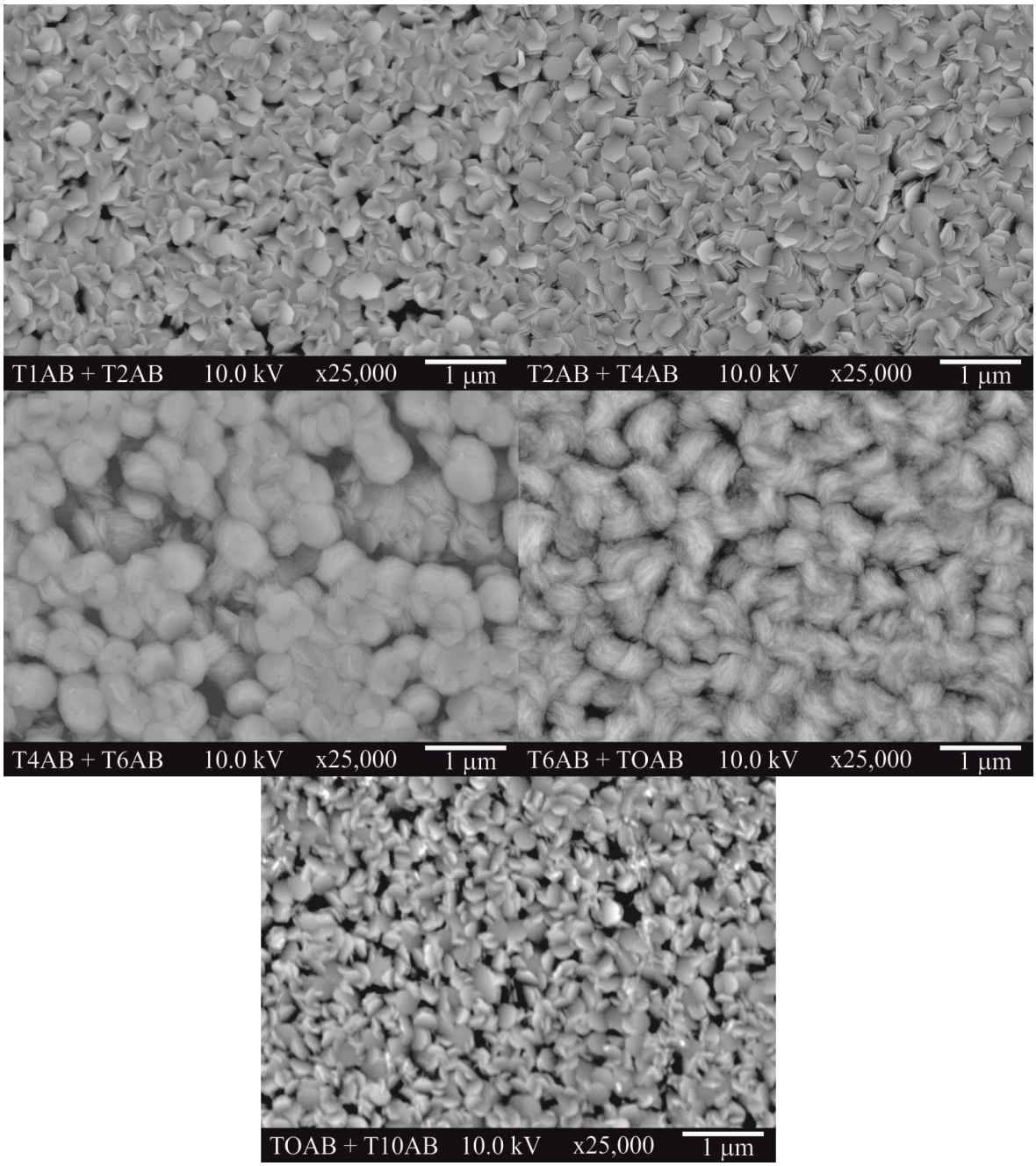

Figure 2-35 – SEM images of ZnO films formed in the presence of mixtures of additives. T‘1.5’AB (top left), T‘3’AB (top right), T ‘5’AB (middle left), T‘7’AB (middle right) and T‘9’AB (bottom)

2.3.4 Other Quaternary Ammonium Bromides on the Deposition of Zinc Oxide

2.3.4.1 Didodecyldimethylammonium Bromide.

Two depositions were carried out using didodecyldimethylammonium bromide (D12D1AB). Both depositions were carried out following the procedure outlined above (see Experimental, page 8) at 350 °C using a solution of zinc acetate (0.5 g / 2.72 mmol) and D12D1AB (1.261 g / 2.72 mmol) in methanol (40 cm^3). The first experiment (Run 1) was carried out following the fast deposition method using a dispersion chamber height of 0 mm and an argon flow rate of 0.84 l $min^{-1,}$ whilst the second deposition (Run 2) was carried out following the slow deposition method, using a sample height of 20 mm and an argon flow rate of 0.42 l min^{-1}.

Run 1 was too thin to calculate the film thickness or band gap using UV-Vis-NIR and the peaks were of too low intensity to acquire meaningful results from the X-ray diffraction data. However, the film formed using the slow method had a thickness of 300 ± 7 nm and a band gap of 3.3 eV. The processing of the X-ray data for the sample formed under slow conditions revealed a texture index of $J = 2.3$ with a goodness of fit index of $\chi^2 = 2.8$ (Figure 2-37).

The microstructure for both samples is composed of thin hexagonal plates of zinc oxide (Figure 2-36), most of which are individual; however, some of the plates are in very small stacks comprised of two or three plates. Overall the structure is similar to the films formed in the presence of CTAB (see 2.3.1, page 39). The difference between the two D12D1AB samples is plate size, with the slow deposition sample plates being c.a. 250 nm in diameter as opposed to c.a. 100 nm, this increase in size is due to the slower conditions causing the mist passing through the reaction chamber to be less dense, reducing insulating and cooling effects from the aerosol droplets, along with the slower gas flow through the chamber increasing the time the aerosol takes to travel across the heated substrate, increasing the proportion which thermally decomposes.

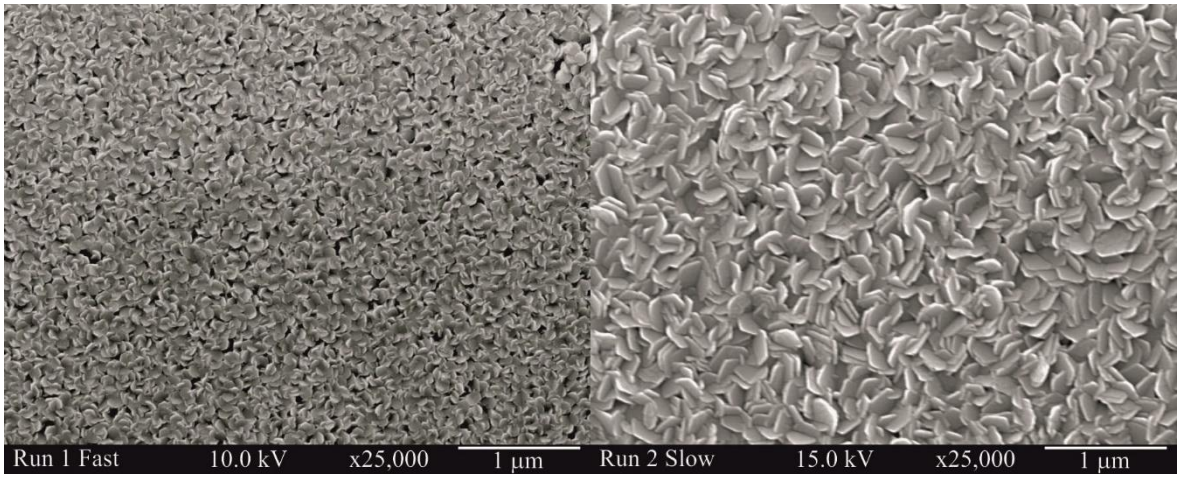

Figure 2-36 – SEM images showing the structure of ZnO films grown in the presence of didodecyldimethylammonium bromide. Fast (left) and slow (right)

2.3.4.2 Decyltrimethylammonium Bromide

Decyltrimethylammonium bromide (DTAB) is similar in structure to CTAB; both additives are quaternary ammonium bromides composed of a central nitrogen atom bonded to three methyl groups and one longer alkyl chain. The difference between the two lies in the length of this longer alkyl chain, for CTAB this chain is 16 carbons in length whereas for DTAB it is only 10. An investigation was carried out to determine whether this small change would have any impact on the deposition of zinc oxide.

Two depositions were carried out using decyltrimethylammonium bromide (DTAB) as an additive during the formation of zinc oxide films via AACVD. Both depositions were carried out following the procedure outlined above (see Experimental, page 8) at 350 °C using a solution of zinc acetate (0.5 g / 2.72 mmol) and DTAB (0.762 g / 2.72 mmol) in methanol (40 cm^3). The first experiment (Run 1) was carried out following the fast deposition method using a dispersion chamber height of 0 mm and an argon flow rate of 0.84 l $min^{-1,}$ whilst the second deposition (Run 2) was carried out following the slow deposition method, using a sample height of 20 mm and an argon flow rate of 0.42 l min^{-1}.

The UV-Vis-NIR data for Run 1 shows that the sample is too thin to analyse using the Swanepoel method and subsequently the Tauc method so no results are available for film thickness or band gap for this sample. However, Run 2 was shown to have a measurable film thickness of 190 ± 17 nm and a band gap of 3.3 eV.

The X-ray diffraction data showed that for Run 1 the texture index was J = 1.4 whereas for Run 2 it had increased to J = 2.0 (Figure 2-37). This increase could be a result of the slower deposition for Run 2 allowing more growth to occur along the [0002] axis.

The SEM images (Figure 2-38) show that the ZnO films are forming the same microstructure as the films formed in the presence of CTAB (see 2.3.1, page 39). This shows that the small change in structure of the additive has had no impact on its effect on the growth of zinc oxide thin films. The only visible difference between the films formed during the fast and slow techniques is the plate size, with it being larger in Run 2. This increase will be a result of the slower deposition conditions allowing more decomposition of the precursor to occur and thus more growth on the substrate.

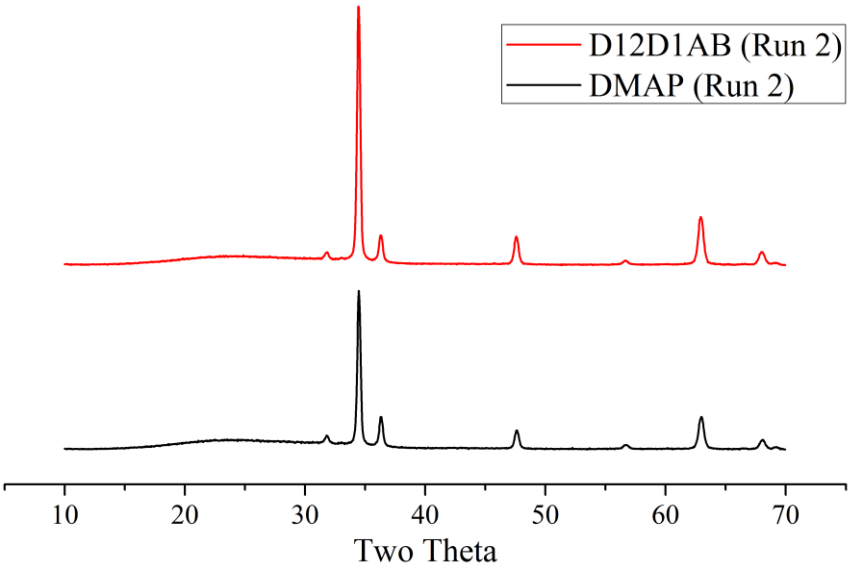

Figure 2-37 - X-ray diffraction pattern of ZnO formed in the presence of D12D1AB (top) DMAP (bottom)

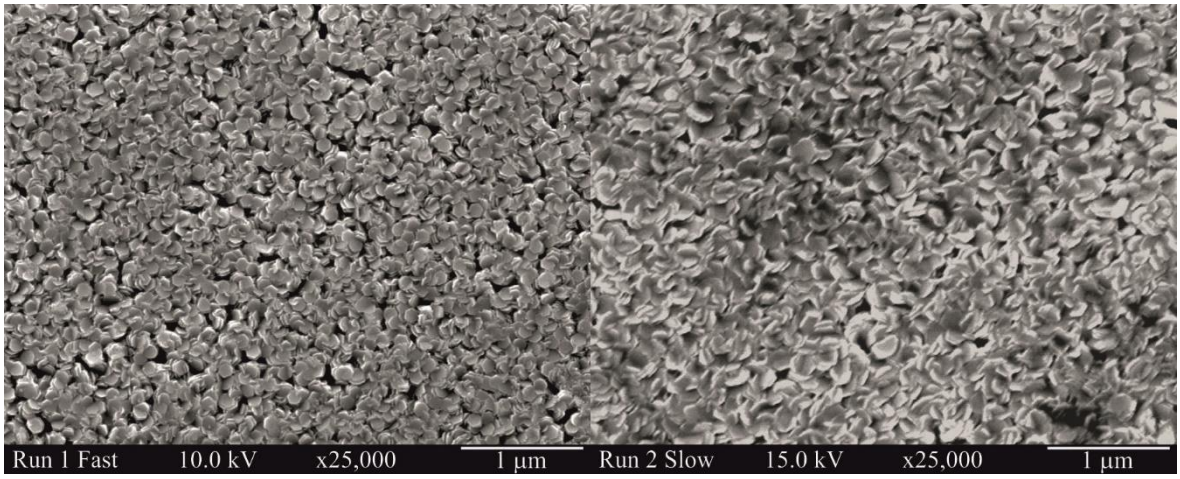

Figure 2-38 – SEM images of ZnO films formed in the presence of decyltrimethylammonium bromide. Fast (left) and slow (right)

2.4 Sulphates to Control Microstructure

2.4.1 Fast Deposition of ZnO in the Presence of Sulphates as Additives

Three depositions were carried out following the procedure outlined above (see Experimental, page 8) at 350 °C with an argon flow rate of 0.84 l min^{-1} and a dispersion chamber height of 0 mm. A solution of zinc acetate (0.5 g / 2.72 mmol) in methanol (40 cm^3) was used for each deposition with an additive added as outlined in the following table (Table 2-10). The mole amount of each additive used was 2.72 mmol so as to keep the mole ratio between additive and zinc acetate to 1:1.

Table 2-10 – Table showing the additives used and summarising the UV-Vis-NIR and X-ray diffraction results

Additive	**Mass / g**	**Thickness / nm**	**Band Gap / eV**	**Texture Index / *J***	**χ^2**
Sodium Dodecyl Sulphate	0.785	779 ± 2	3.3	2.7	11.1
Ammonium Sulphate	0.36	Too Thin		Low Intensity	
Methyl Sulphate Sodium Salt	0.365	1165 ± 17	3.3	1.5	6.7

The results for the UV-Vis-NIR show that the films thickness for the zinc oxide formed in the presence of sodium dodecyl sulphate (SDS) and methyl sulphate sodium salt ($NaMeSO_4$) is comparable to that formed in the absence of any additive (see 2.2.1, page 30). On the other hand, in the presence of ammonium sulphate (NH_4SO_4) the formation of zinc oxide is greatly diminished. The X-ray diffraction data shows that the films deposited in the presence of $NaMeSO_4$ and SDS exhibit preferred orientation, this is more pronounced in the sample formed in the presence of SDS (Figure 2-40). This preferred orientation is along the [0002] axis, as is the case with the films formed in the presence of some of the quaternary ammonium bromides (see 2.3, page 39), this is reflected in preferred orientation along the $[10\bar{1}3]$ axis. Due to a combination of low peak intensity and artefacts present within the X-ray diffraction data it was not possible to process the data for the film formed in the presence of NH_4SO_4 in a way to provide meaningful results. For films of zinc oxide formed in the presence of SDS and $NaMeSO_4$, the fate of the sodium is unclear. Once the solution enters the deposition chamber, the solvent evaporates and the precursors begin to decompose. At this stage there are two main possibilities for the sodium ions, either they are incorporated into the zinc oxide film, or thermophoresis causes it to be deposited onto the top plate as either sodium oxide or sodium hydroxide. XRD patterns of these films showed no evidence of a ternary zinc oxide with sodium, therefore any incorporation of sodium will exist as doping of the existing ZnO. No elemental analysis was carried out on the films, therefore conclusions as to the fate of the sodium cannot be drawn.

The increase in peak intensity representing preferred growth along the [10$\bar{1}$3] is most likely a side effect of the increase in preferred orientation along [0002], this is demonstrated in the figure below (Figure 2-39). This is caused by the diffraction vector tilting during grazing incidence scans (see Figure 1-10). For this to be the case, the difference in angle between the planes (0002) and (10$\bar{1}$3) must equal the difference in 2θ between the peaks representing the planes. Using lattice parameters of a single crystal of ZnO (a = 3.249 and c = 5.206 Å)[12] it can be calculated that the angle between the two planes is 28.1°. This value is comparable to the difference between the 2θ angles between the peaks (28.2°) demonstrating that the increase in intensity is related to the increase in preferred orientation observed for (0002).

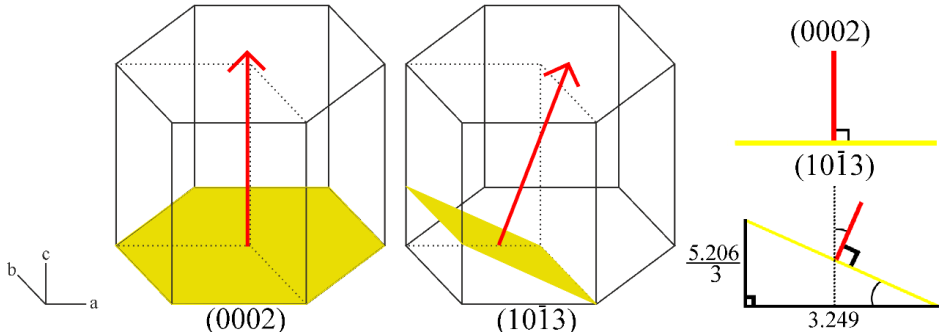

Figure 2-39 – Figure showing the representative lattice planes and the diffraction vector required to sample them within a single crystal of ZnO

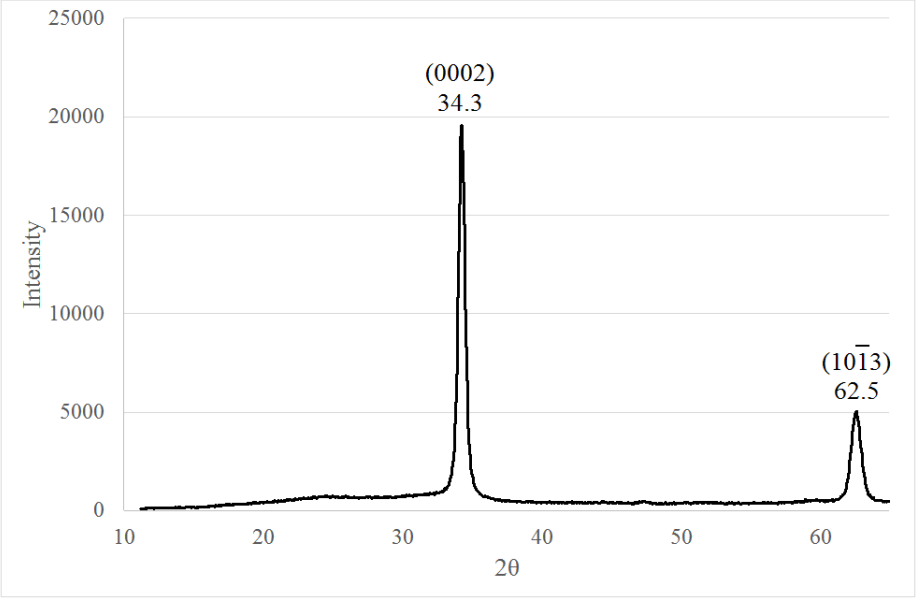

Figure 2-40 – X-ray diffraction pattern of ZnO formed in the presence of SDS using the fast conditions

The SEM images (Figure 2-41) show that the film formed in the presence of SDS has grown in hexagonal plates which appear to have a tendency to be orientated roughly parallel to the surface

of the substrate. NH_4SO_4 appears to be influencing the ZnO to grow into hexagonal plates; however, in this case the plates appear to be aligned randomly. Zinc oxide grown in the presence of $NaMeSO_4$ appear to grow in irregular shapes clusters, in a similar way to how ZnO grows in the absence of any additive, suggesting that the additive is having no influence on the microstructure. This is an unexpected result as the X-ray diffraction data shows that the film has preferred orientation, suggesting that the additive is in fact interacting with the growing ZnO film.

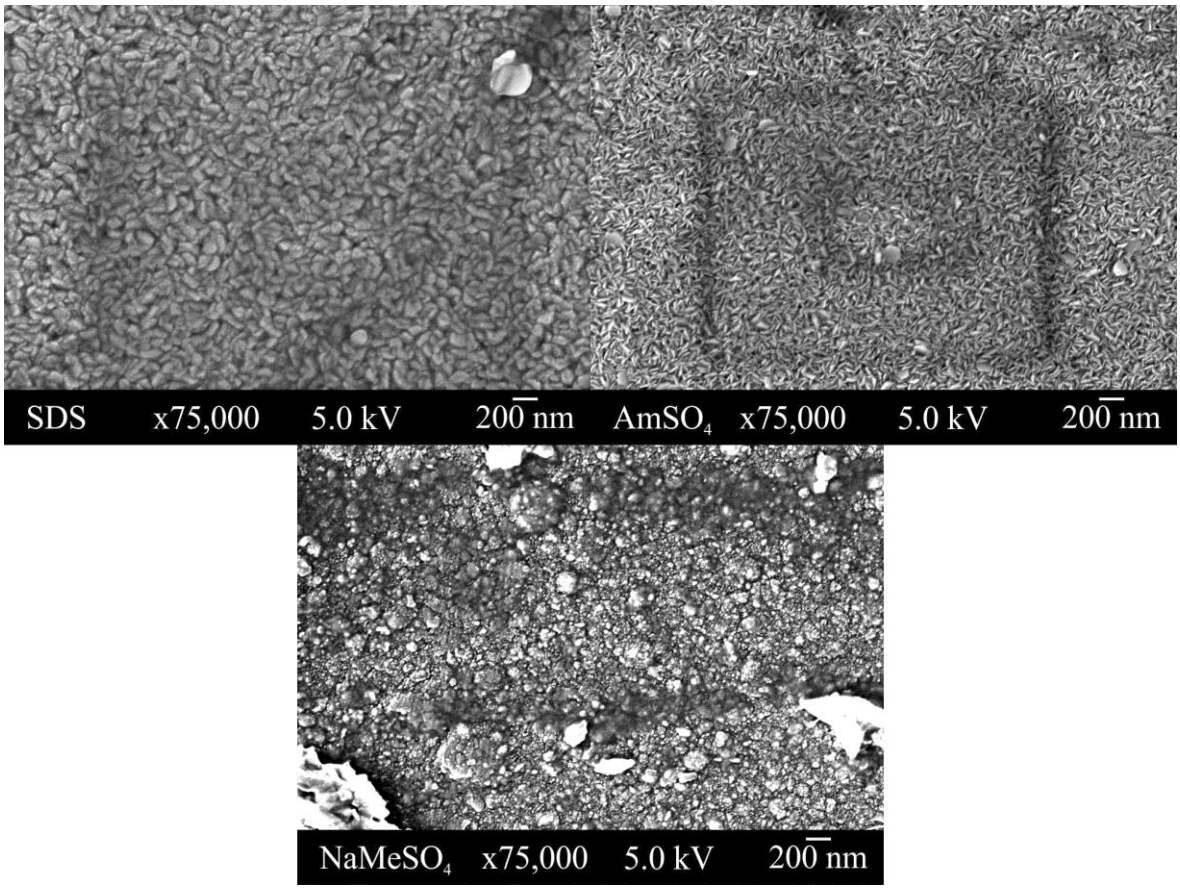

Figure 2-41 – SEM images of the ZnO films formed under the presence of sulphates.SDS (top left), NH_4SO_4 (top right) and $NaMeSO_4$ (bottom)

2.4.2 Investigation into Mole Ratio on Zinc Oxide Deposition in the Presence of Methyl Sulphate Sodium Salt

A set of experiments was carried out to investigate the effect of changing mole ratios of methyl sulphate sodium salt on the deposition of zinc oxide. The depositions were carried out following the procedure outlined above (see Experimental, page 8) at a temperature of 350 °C, an argon flow rate of 0.42 l min^{-1} and a dispersion chamber height of 15 mm. A solution of zinc acetate (0.183 g / 1 mmol) in methanol (40 cm^3) was used in each run. An amount of $NaMeSO_4$ was added according to the following table (Table 2-11).

Table 2-11 – Table outlining the quantities of $NaMeSO_4$ used and summary of X-ray data

Run	**$NaMeSO_4$ / g**	**$NaMeSO_4$ / mole equivalent**	**Texture Index / *J***	**χ^2**
1	0.067	0.5	1.2 (front)	9.4 (front)
			1.1 (back)	6.6 (back)
2	0.134	1.0	3.8	21.0
3	0.201	1.5	1.2	7.1

The X-ray diffraction patterns (Figure 2-42) show that with 0.5 and 1.5 mole equivalents there is little to no preferred orientation within the zinc oxide film, however, the sample formed in the presence of 1.0 mole equivalents of $NaMeSO_4$ has a texture index of $J = 3.8$. As was the case with SDS, the preferred orientation was present along the [0002] and [$10\bar{1}3$] axes. Two positions were analysed with the sample formed in the presence of 0.5 mole equivalent, this was due to a visible tide mark across the substrate approximately 6 cm away from the leading edge. The X-ray diffraction patterns are the same for both positions.

The SEM images (Figure 2-43) show that at 0.5 and 1.5 mole equivalents of $NaMeSO_4$ the zinc oxide grows in irregular clusters, similar to what was observed for ZnO grown in the absence of any additive. Whereas, in the presence of 1.0 mole equivalents, the zinc oxide grows into more discrete structures which potentially lowers the density of the film due to porosity, however, due to the small size of these it was not possible to resolve the fine detail, therefore further comments on the microstructure cannot be made.

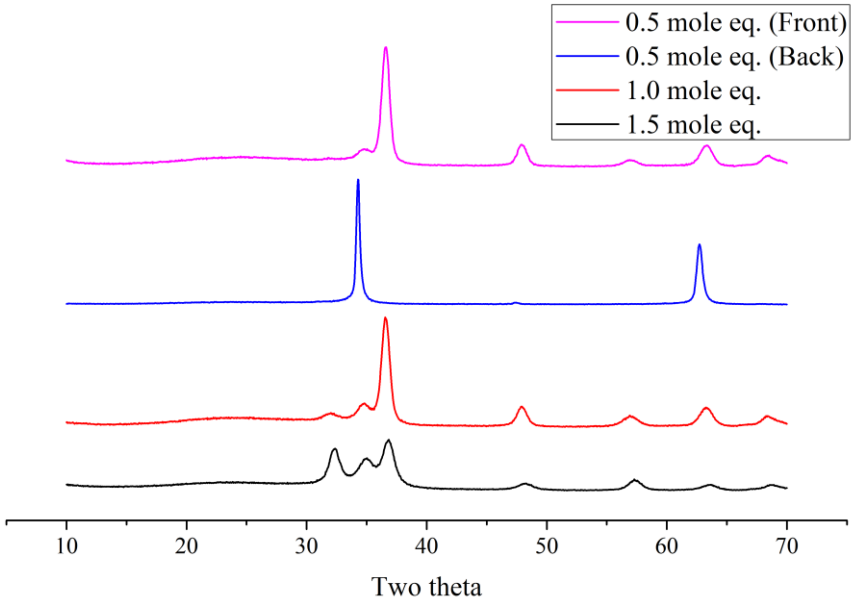

Figure 2-42 – X-ray diffraction patterns of ZnO formed in the presence of varying quantities of $NaMeSO_4$

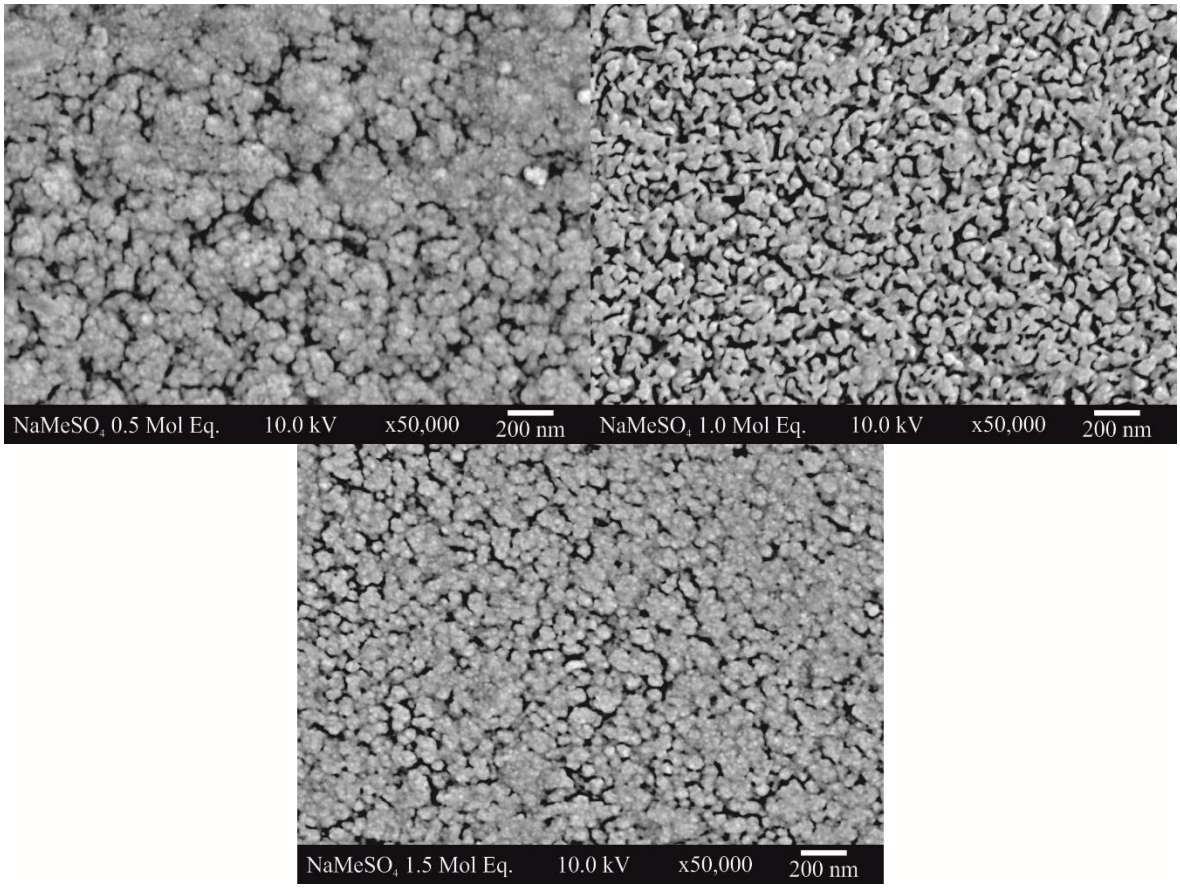

Figure 2-43 – SEM images showing ZnO formed under varying amounts of $NaMeSO_4$. 0.5 mole equivalents (top left), 1.0 mole equivalents (top right) and 1.5 mole equivalents (bottom)

2.4.3 Increasing the Chain length of the Sulphate Additive

A sequence of experiments was carried out using sulphates as additives, looking into the effect of changing alkyl chain length on the deposition of zinc oxide. The depositions were carried out following the procedure outlined above (see Experimental, page 8) at 350 °C with an argon flow rate of 0.42 l min^{-1}. A three-necked round bottom flask (100 cm^3) was used as the dispersion chamber and the height was set to 0 mm above the piezoelectric humidifier. A solution of zinc acetate (0.183 g / 1 mmol) in methanol was used. Each deposition used 1 mmol of additive to ensure a 1:1 mole ratio between additive and precursor in each reaction. The additives used are described in the following table (Table 2-12).

Table 2-12 – Table outlining the sulphates used as additives and summarising the X-ray results

Additive	**Mass / g**	**Texture Index / *J***	χ^2
Sodium 1-Propanesulphonate monohydrate	0.164	1.3	27.5
Sodium 1-Pentanesulphonate	0.174	1.2	4.0
Sodium 1-Heptanesulphonate	0.202	1.1	4.5
Sodium Dodecyl Sulphate	0.288	1.0 (front)	4.6 (front)
		3.7 (back	68.0 (back)

The X-ray data shows that for sodium 1-propanesulphonate monohydrate (S3S), sodium 1-pentanesulphonate (S5S) and sodium 1-heptanesulphonate (S7S) there is very little preferred orientation within the zinc oxide films, and that the peaks are very broad, suggesting low crystallinity, results which are similar to those obtained for zinc oxide formed in the absence of any additive. The film formed in the presence of SDS was transparent along the whole substrate except for a colourless translucent band roughly half way along. The sections were analysed separately and labelled depending on their location relative to the end of the substrate closest to the front of the reactor. The front section shows no preferred orientation and exhibits broad peaks, the same as the results for the other sulphates. On the other hand, the back section shows a large degree of preferred orientation along the [0002] and [$10\bar{1}3$] axes and much sharper peaks with more intensity (Figure 2-44).

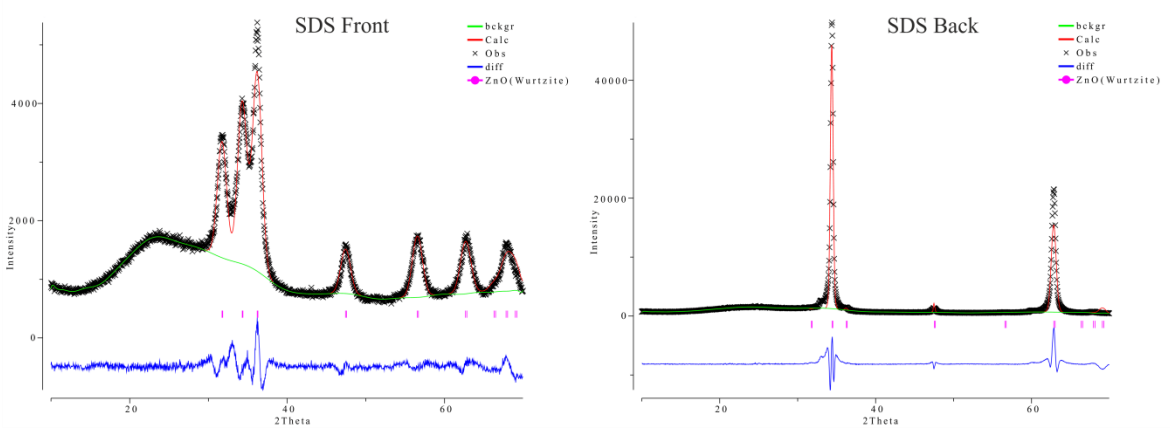

Figure 2-44 – X-ray diffraction patterns for the ZnO film formed in the presence of SDS. Front section of substrate (left) and back section of substrate (right)

The scanning electron microscopy images (Figure 2-45) show that the microstructure for each of the samples is composed of irregular shaped crystallites c.a. 10 nm. Due to the small size it is difficult to make further comments about the microstructure.

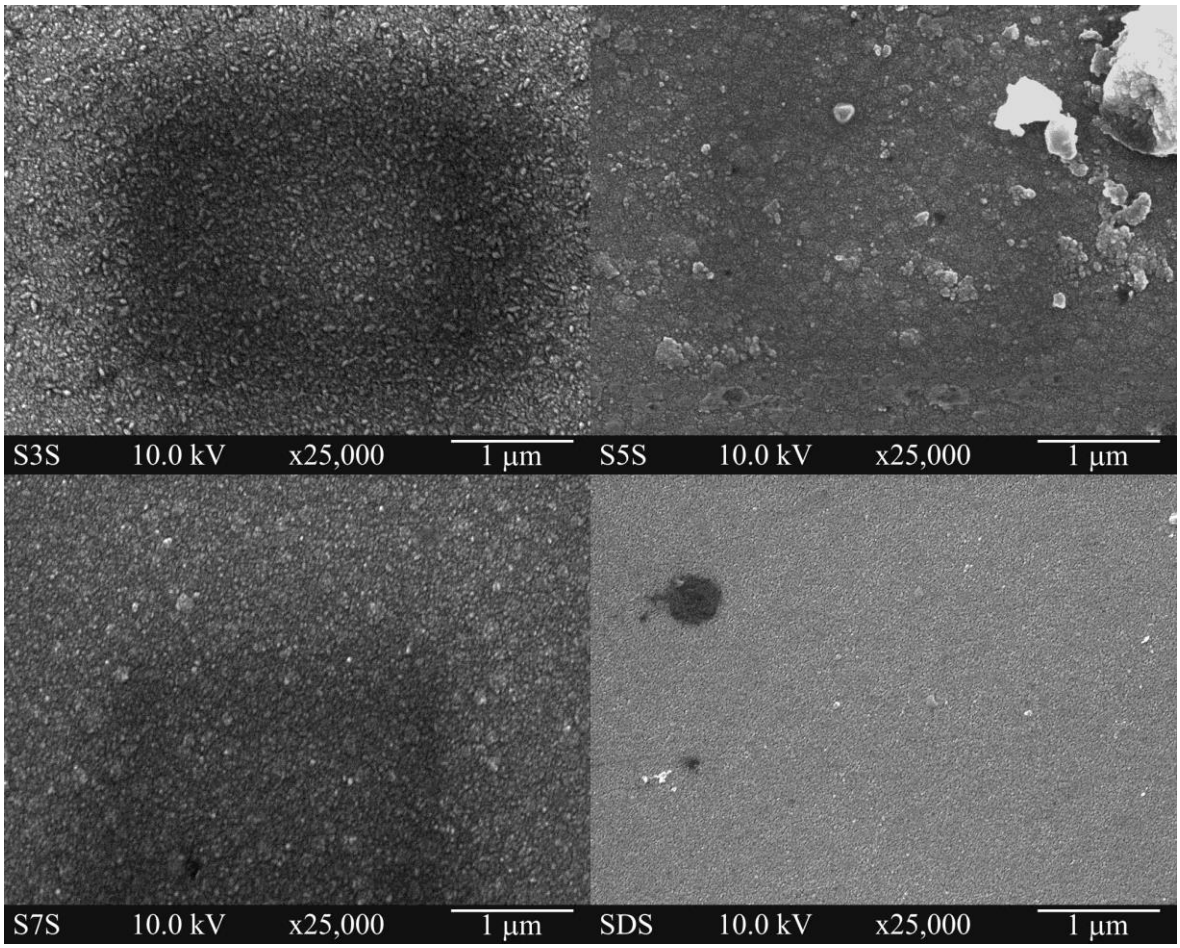

Figure 2-45 – SEM images of ZnO formed in the presence of different sulphate additives. Sodium propanesulphonate (top left), sodium pentanesulphonate (top right), sodium heptanesulphonate (bottom left) and sodium dodecyl sulphate (bottom right)

2.5 Other Additives to Control Microstructure

2.5.1 The Effect of Dye Molecules on the Deposition of Zinc Oxide

A test was carried out on the effect of two dye molecules on the deposition of zinc oxide thin films. The depositions were carried out following the procedure outlined above (see Experimental, page 8) at 300 °C with an argon flow rate of 0.25 l min^{-1} and a dispersion chamber height of 20 mm. A Drechsel bottle filled with water was attached to the exhaust of the reactor to dissolve any dye which was not decomposed inside the decomposition chamber. For each deposition a solution was made up in methanol (40 cm^3). The dyes used were dichloroindophenol sodium salt (DCIP) and Brilliant Blue G (BBG), the structure of which is shown below (Figure 2-46) and the quantities are outlined in the table below (Table 2-13).

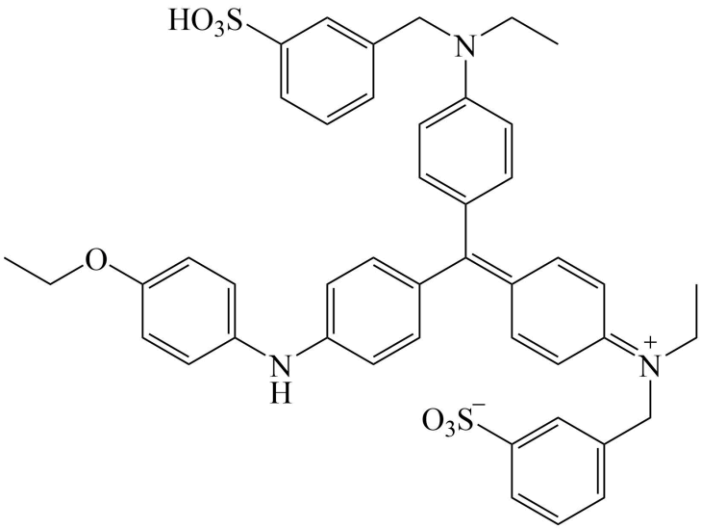

Figure 2-46 – Structure of Brilliant Blue G

Table 2-13 – Table outlining the dyes used and summarising the X-ray diffraction results

Run	Zinc Acetate / g	Dye	Dye / g	Mole Ratio Zn:Dye	Texture Index / *J*	X^2
1	0.0917	DCIP	0.0268	5:1	1.0	1.9
2	0.0269	BBG	0.0854	3:2	No peaks present	
3	0.0917	BBG	0.0427	10:1	1.1	5.2

The X-ray diffraction patterns (Figure 2-47) show that the dyes used do not cause any preferred orientation within the zinc oxide thin films in the mole ratios in which they were used. The reason there are no peaks present for Run 2 could be a result of the small quantity of precursor used. The resulting film could be composed of a very small amount of crystalline material; this will cause the peaks to be too low in intensity to be distinguishable from the baseline.

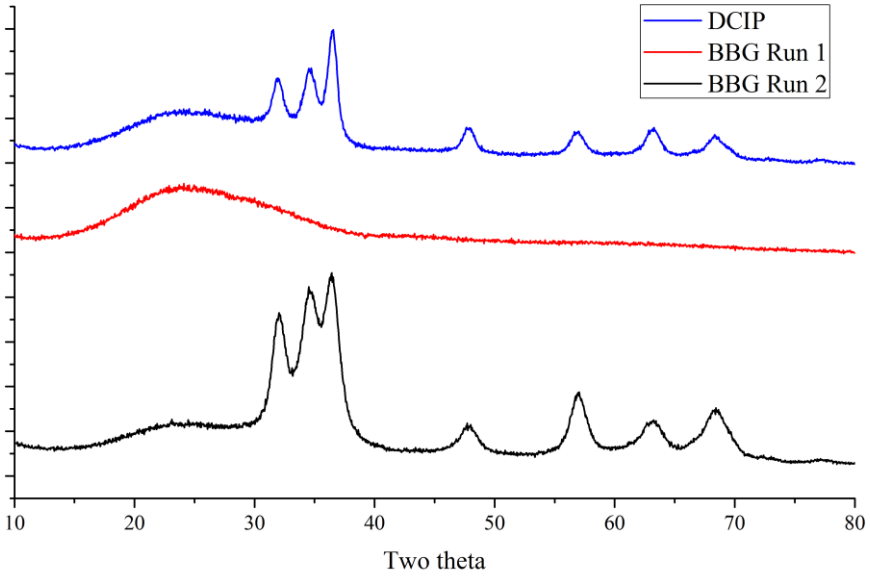

Figure 2-47 – X-ray diffraction patterns of ZnO formed in the presence of dyes

The SEM images (Figure 2-48) show that the zinc oxide is growing in irregular shaped clusters for Run 1 and Run 3, this suggests that the dyes are having no influence on the microstructure of the film, however, it could be a result of the low mole ratios used; the image for Run 2 suggests that this could be the case. The SEM image shows that the zinc oxide seems to be growing in hexagonal plates, however, the plates are too small to allow for accurate resolution and so this observation cannot be confirmed. The small crystallite size will be a result of the small amount of zinc oxide precursor available.

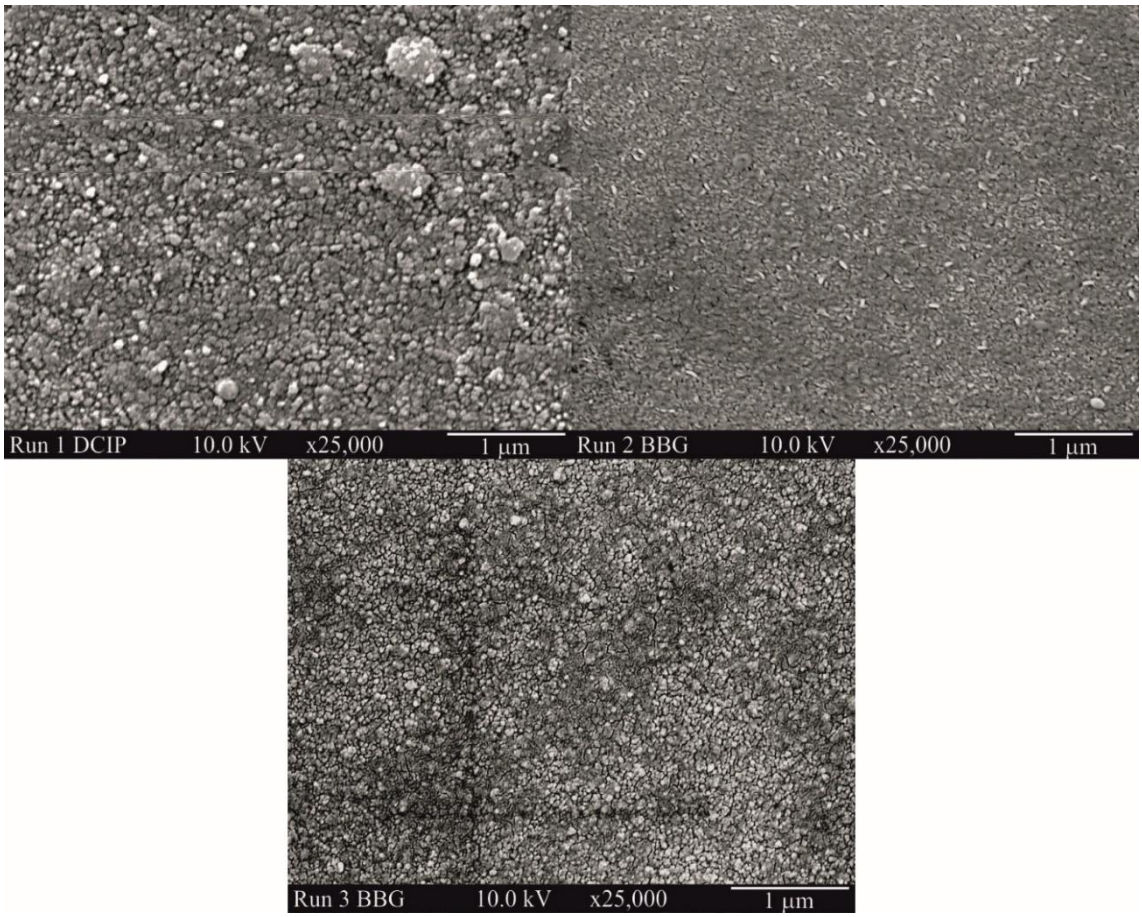

Figure 2-48 – SEM images of zinc oxide formed in the presence of dyes DCIP (top left), 3:2 ratio of ZnAc to BBG (top right) and 10:1 ratio ZnAc to BBG (bottom)

2.5.2 3-(N,N-Dimethylmyristylammonio)propanesulphonate

A sequence of reactions was carried out investigating the effect of the additive 3-(N,N-dimethylmyristylammonio)propanesulphonate (DMAPS) on the deposition of zinc oxide. A diagram of the additive is shown below (Figure 2-49). This additive was chosen as it is a zwitterion composed of both a quaternary ammonium centre and a sulphate centre, both of which have been key features of previous additives tested.

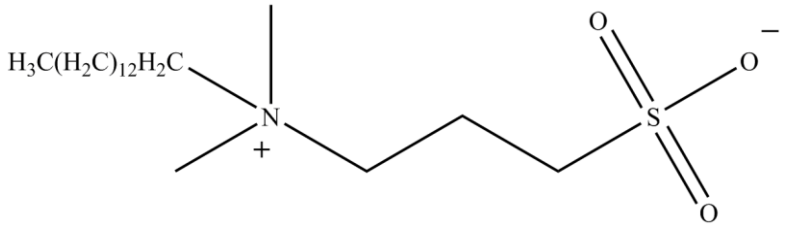

Figure 2-49 – Diagram of the additive 3-(N,N-Dimethylmyristylammonio)propanesulphonate (DMAPS)

Depositions were carried out following the procedure outlined above (see Experimental, page 8) at a temperature of 350 °C using an argon flow rate of 0.42 l min^{-1} and a dispersion chamber height of 20 mm. A solution of zinc acetate (0.183 g / 1 mmol) in methanol (40 cm^3) is used in each deposition with a quantity of DMAPS added as described in the following table (Table 2-14).

Table 2-14 – Table outlining the quantities of DMAPS used and summarising the results from X-ray diffraction

Run	**DMAPS / g**	**DMAPS / mmol**	**Texture Index / *J***	χ^2
1	0.036	0.1	1.1	5.4
2	0.073	0.2	1.0	6.7
3	0.182	0.5	1.0	6.2
4	0.364	1.0	1.1	1.9
5	0.727	2.0	1.3	1.3

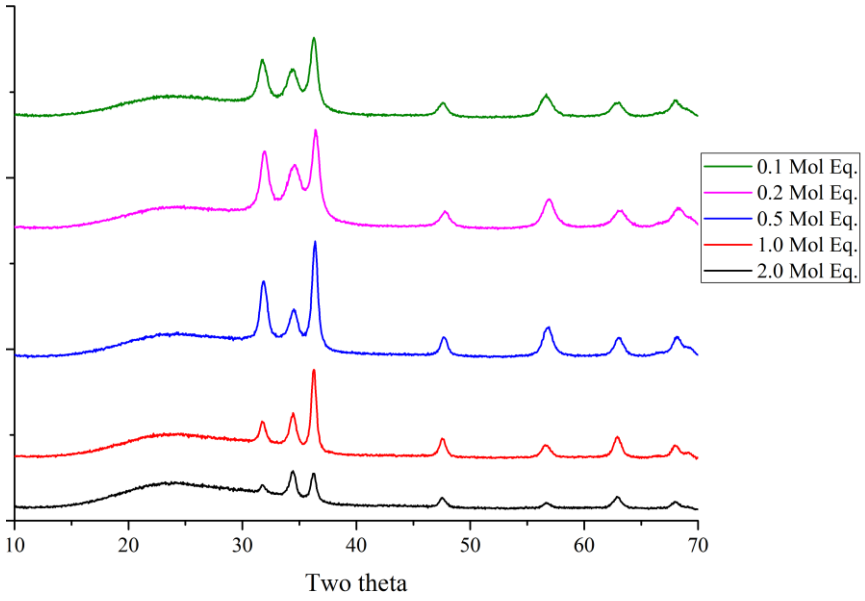

Figure 2-50 – X-ray diffraction patterns for ZnO formed in the presence of DMAPS

The X-ray diffraction results (Figure 2-50) show that the zinc oxide films have little to no preferred orientation regardless of the quantity of DMAPS used. On the other hand, as the quantity increased to 1 mole equivalent, the peaks became sharper, resulting in less overlap between the 0002 and $10\bar{1}1$ peaks which is reflected in the χ^2 values decreasing because of better fit caused by the shapes being fit to discrete peaks. The SEM images (Figure 2-51) show that there does not appear to be any change in the microstructure of the zinc oxide films as the quantity of DMAPS changes, however, due to the small size of the crystallites, it was not possible to fully resolve the microstructure therefore further comments cannot be made.

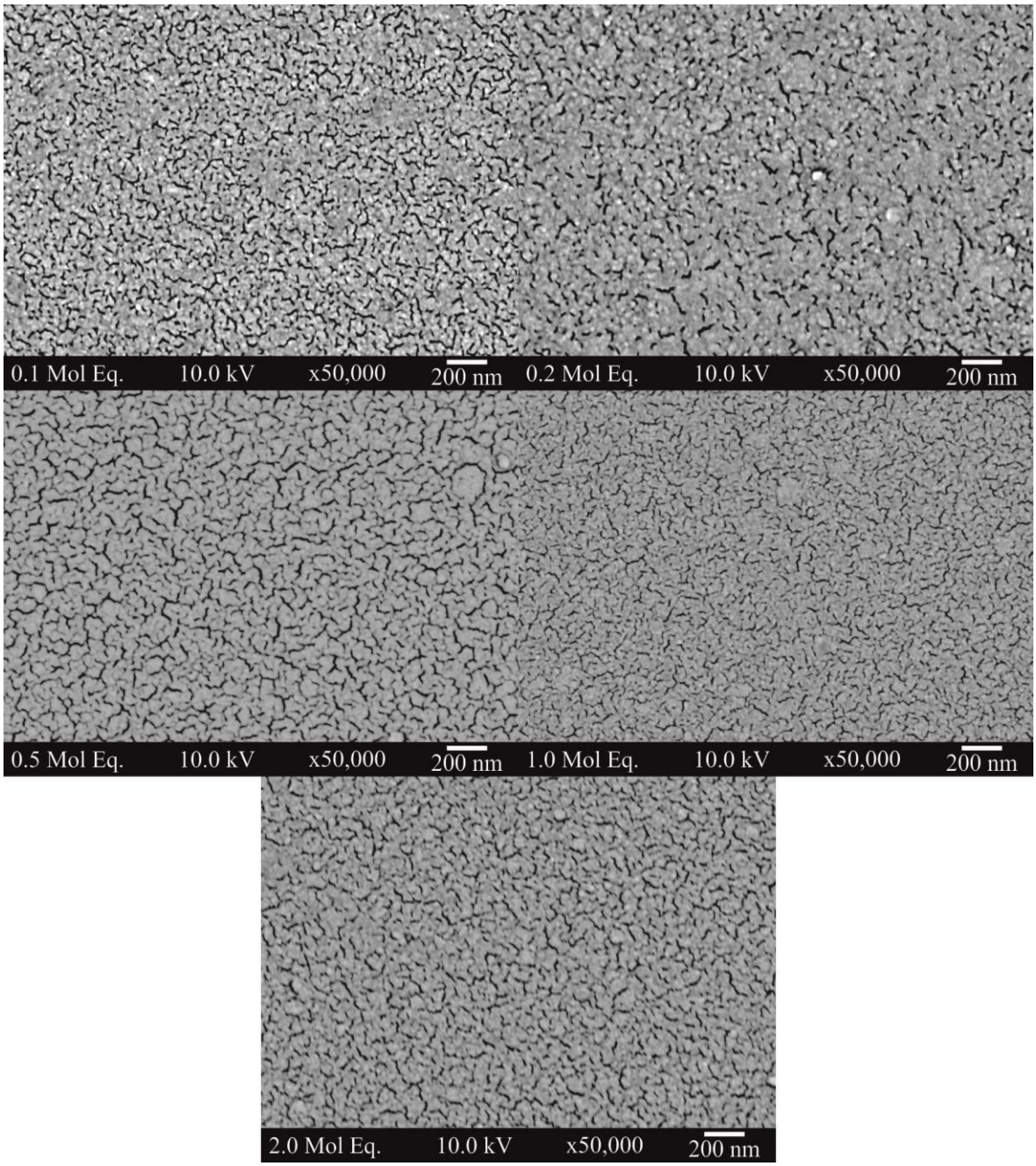

Figure 2-51 – SEM images showing the ZnO films formed in the presence of DMAPS. 0.1 mole equivalent (top left), 0.2 mole equivalent (top right), 0.5 mole equivalent (middle left), 1.0 mole equivalent (middle right) and 2.0 mole equivalent (bottom)

2.6 Conclusions

This chapter has demonstrated that it is possible to grow thin films of zinc oxide into a range of microstructures simply by introducing additives into the precursor solution. It has also shown that the ideal temperature for film growth is 350 °C to maximise film thickness and minimise the amount of carbon contamination.

The results have shown that the use of various quaternary ammonium bromides can influence the microstructure of zinc oxide films in different ways. There appears to be a trend amongst them resulting in the possibility of grouping the additives based on exposure of the cationic ammonium centre. 1 mole equivalent of additives with a higher degree of exposure, resulting from short alkyl chains, for example, CTAB, D12D1AB, T1AB and DTAB cause the zinc oxide to grow into hexagonal plates with some preferred orientation. These samples also suffer from a highly reduced thickness of the resulting film. As the alkyl chains increase in length and shield the cationic centre more, the microstructure shows less hexagonal character but growth of the zinc oxide into stacks, i.e. as seen with T4AB, T6AB and to a lesser degree TOAB, the film thickness also increases with this trend. The reason for the subsequent reversal of this trend with the additive T10AB, which begins with TOAB, is unclear. However, thermal stabilities of the additives could be playing a factor in this. It is possible that these additives could decompose with loss of alkyl chains (a process observed with CTAB[34]) at a faster rate than T6AB for example. This could result in an increased exposure of the cationic centre. To confirm this, a study into the decomposition of methanol solutions of each of the additives would have to be carried out, focusing on the additives T6AB, TOAB and T10AB.

The investigation into the mechanism shows that the interaction between the precursor and additive occurs at the surface of the substrate. It has also been shown that due to thermal decomposition, a constant supply of the additive is required to maintain the directing effect.

It has been shown that sulphates interact with the growing zinc oxide thin film in a different manner to quaternary ammonium bromides. In general the results have shown that they cause preferred orientation within the sample along the [0002] axis similar to quaternary ammonium bromides, with a more pronounced related increase in growth along the $[10\bar{1}3]$ axis. It is not possible to make comments about the microstructure due to the small crystallites of ZnO. A way to compensate for this could be to repeat the experiments using a larger quantity of precursor. A potential experiment to carry out would be the use of SDS in the synthesis of zinc oxide films carried out at lower temperatures. The reason for this would be to investigate whether it is possible to form lamellar like structures using AACVD similar to those seen in solution phase chemistry.[27,39] To do this it may be necessary to change to a different zinc oxide precursor with a lower decomposition temperature to zinc acetate.

The results from DMAPS suggest that the presence of both a cationic and an anionic centre prevents the additive from having an influence on the growing zinc oxide film. The reason for this is possibly due to electrostatic effects within the additive preventing the molecule from binding to crystallographic faces of the growing film.

There is a vast library of potential additives still remaining; however, it would not be possible to investigate them all. Some additives which could prove of interest are further anionic molecules, such as alkyl phosphates, for example trimethyl phosphate. Alkyl phosphates would provide a direct comparison to the quaternary ammonium bromides investigated in this chapter. Some other potentially interesting additives are neutral or further zwitterions such as natural occurring amino acids. An issue facing amino acids is their solubility in non-aqueous mediums. A possible solution to this could be solvent mixtures using a minimum quantity of water as possible to reduce thermophoresis effects caused by the larger droplets (see Aerosol Assisted Chemical Vapour Deposition, page 5).

2.7 References

(1) Schmidt-Mende, L.; MacManus-Driscoll, J. L. *Mater. Today* **2007**, *10*, 40.

(2) Norton, D. P.; Heo, Y. W.; Ivill, M. P.; Ip, K.; Pearton, S. J.; Chisholm, M. F.; Steiner, T. *Mater. Today* **2004**, *7*, 34.

(3) Pearton, S. J.; Norton, D. P.; Ip, K.; Heo, Y. W.; Steiner, T. *Prog. Mater Sci.* **2005**, *50*, 293.

(4) Özgür, Ü.; Alivov, Y. I.; Liu, C.; Teke, A.; Reshchikov, M. A.; Doğan, S.; Avrutin, V.; Cho, S.-J.; Morkoç, H. *J. Appl. Phys.* **2005**, *98*, 041301.

(5) Heo, Y. W.; Norton, D. P.; Tien, L. C.; Kwon, Y.; Kang, B. S.; Ren, F.; Pearton, S. J.; LaRoche, J. R. *Mater. Sci. Eng., R* **2004**, *47*, 1.

(6) Zhang, T.; Dong, W.; Keeter-Brewer, M.; Konar, S.; Njabon, R. N.; Tian, Z. R. *J. Am. Chem. Soc.* **2006**, *128*, 10960.

(7) Li, W.-M.; Yin, P.-G.; Guo, L. *Res. Chem. Intermed.* **2011**, *37*, 125.

(8) O'Brien, S.; Nolan, M. G.; Çopuroglu, M.; Hamilton, J. A.; Povey, I.; Pereira, L.; Martins, R.; Fortunato, E.; Pemble, M. *Thin Solid Films* **2010**, *518*, 4515.

(9) O'Regan, B.; Sklover, V.; Gratzel, M. *J. Electrochem. Soc.* **2001**, *148*, C498.

(10) Barreca, D.; Gasparotto, A.; Maccato, C.; Tondello, E.; Lavrencic, S. U.; Patil, S. R. *Surf. Coat. Technol.* **2009**, *203*, 2041.

(11) Parkin, I. P.; Palgrave, R. G. *J. Mater. Chem.* **2005**, *15*, 1689.

(12) Abrahams, S. C.; Bernstein, J. L. *Acta Crystallogr., Sect. B: Struct. Sci., Cryst. Eng. Mater.* **1969**, *25*, 1233.

(13) Bragg, W. L.; Darbyshire, J. A. *Trans. Faraday Society* **1932**, *28*, 522.

(14) Bates, C. H.; White, W. B.; Roy, R. *Science* **1962**, *137*, 993.

(15) Bhachu, D. S.; Sankar, G.; Parkin, I. P. *Chem. Mater.* **2012**, *24*, 4704.

(16) Zhang, R.; Kumar, S.; Zou, S.; Kerr, L. L. *Cryst. Growth Des.* **2008**, *8*, 381.

(17) French, S. A.; Sokol, A. A.; Bromley, S. T.; Catlow, C. R. A.; Rogers, S. C.; King, F.; Sherwood, P. *Angew. Chem. Int. Ed.* **2001**, *40*, 4437.

(18) Verges, M. A.; Mifsud, A.; Serna, C. J. *J. Chem. Soc., Faraday Trans.* **1990**, *86*, 959.

(19) Al-Harbi, L. M.; El-Mossalamy, E. H.; Arafa, H. M.; Al-Owais, A.; Shah, M. A. *Mod. Appl. Sci.* **2011**, *5*, 87.

(20) Hu, P.; Zhang, X.; Han, N.; Xiang, W.; Cao, Y.; Yuan, F. *Cryst. Growth Des.* **2011**, *11*, 1520.

(21) Miyamoto, S.; Hasegawa, T.; Takahashi, H.; Yonezawa, T.; Kiyono, H.; Yanase, T.; Nagahama, T.; Shimada, T. *Bull. Chem. Soc. Jpn.* **2012**, *85*, 1287.

(22) Yang, P.; Yan, H.; Mao, S.; Russo, R.; Johnson, J.; Saykally, R.; Morris, N.; Pham, J.; He, R.; Choi, H. J. *Adv. Funct. Mater.* **2002**, *12*, 323.

(23) Wang, X.; Summers, C. J.; Wang, Z. L. *Nano Lett.* **2004**, *4*, 423.

(24) Wang, X.; Song, J.; Li, P.; Ryou, J. H.; Dupuis, R. D.; Summers, C. J.; Wang, Z. L. *J. Am. Chem. Soc.* **2005**, *127*, 7920.

(25) Ramgir, N. S.; Late, D. J.; Bhise, A. B.; More, M. A.; Mulla, I. S.; Joag, D. S.; Vijayamohanan, K. *J. Phys. Chem. B* **2006**, *110*, 18236.

(26) Usui, H. *Electrochim. Acta* **2011**, *56*, 3934.

(27) Gan, X.; Gao, X.; Qiu, J.; Li, X. *Appl. Surf. Sci.* **2008**, *254*, 3839.

(28) Qin, X.; Shao, G.; Zhao, L. *Mater. Sci. Eng., B* **2012**, *177*, 1678.

(29) Zhang, H.; Yang, D.; Li, D.; Ma, X.; Li, S.; Que, D. *Cryst. Growth Des.* **2005**, *5*, 547.

(30) McNally, C. S.; Turner, D. P.; Kulak, A. N.; Meldrum, F. C.; Hyett, G. *Chem. Commun.* **2012**, *48*, 1490.

(31) Lin, C.-C.; Li, Y.-Y. *Mater. Chem. Phys.* **2009**, *113*, 334.

(32) Fletcher, C. J. M. *Proc. R. Soc. London, Ser. A* **1934**, *147*, 119.

(33) Dohse, H. *Z. Physik. Chem.* **1930**, *8*, 159.

(34) Goworek, J.; Kierys, A.; Gac, W.; Borówka, A.; Kusak, R. *J. Therm. Anal. Calorim.* **2009**, *96*, 375.

(35) Swanepoel, R. *J. Phys. E. Sci. Instrumen.* **1983**, *16*, 1214.

(36) López, R.; Gómez, R. *J. Sol-Gel Sci. Technol.* **2012**, *61*, 1.

(37) Von Dreele, R. B. *J. Appl. Crystallogr.* **1997**, *30*, 517.

(38) Olson, T. Y.; Chernov, A. A.; Drabek, B. A.; Satcher, J. H.; Han, T. Y.-J. *Chem. Mater.* **2013**, *25*, 1363.

(39) Pauporte, T.; Rathousky, J. *Microporous Mesoporous Mater.* **2009**, *117*, 380.

Chapter 3: Formation of Zinc Carbodiimide

3.1 Introduction

Attempts to use urea as an additive to control microstructure of zinc oxide thin films (Chapter 2, page 25) lead to an unexpected result. After analysis of the X-ray diffraction pattern it was ascertained that zinc carbodiimide had been formed in place of the oxide. This chapter will provide evidence on the formation of the material and investigate how the conditions affect the formation of zinc carbodiimide and attempt to provide an optimum set of conditions to maximise crystallinity and substrate coverage. It will then briefly move on to investigating some potential applications of these films through thermal degradation.

The full decomposition pathway of urea which occurs in this system is unclear, however, a study into the decomposition of urea in an open vessel was carried out by Schaber *et al*.[1] Their results show that decomposition begins to occur at temperatures in excess of 150 °C, at this temperature the urea begins to decompose into ammonium cyanate (NH_4NCO) which then further decomposes into ammonia and cyanic acid (HNCO). This cyanic acid then reacts with urea to generate biuret ($NH_2CONHCONH_2$). Cyanamide was not isolated by Schaber et al during this experiment, however, small quantities of melamine was detected. One of the possible pathways for melamine formation is the trimerisation of cyanamide (H_2NCN). Three potential routes to cyanamide were proposed by the group, these are shown in the image below (Figure 3-1).

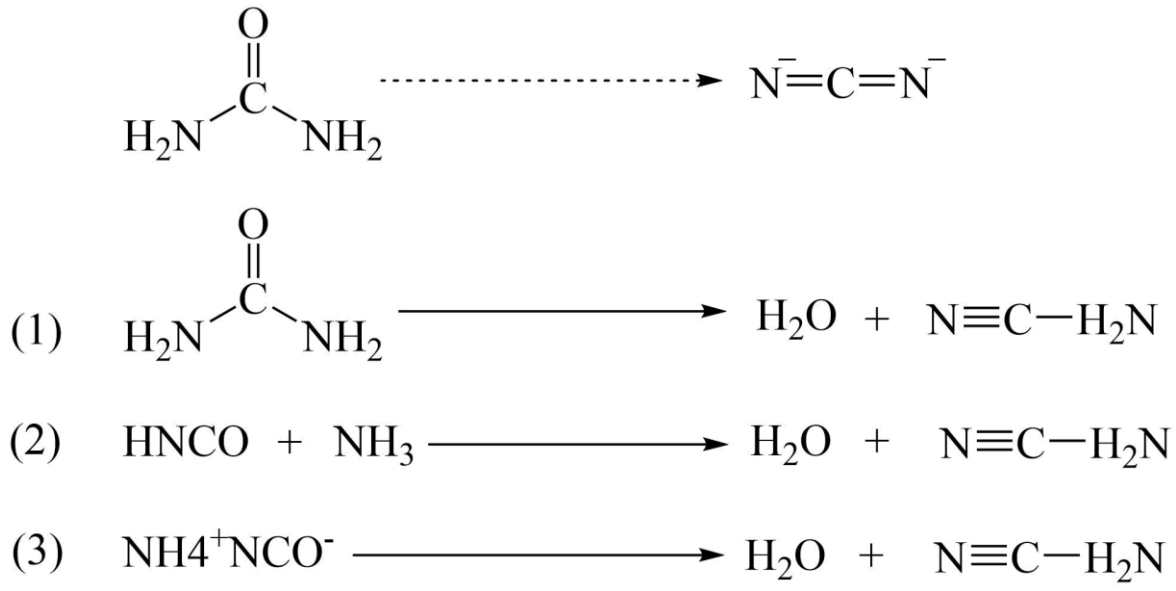

Figure 3-1 – Figure depicting the overall reaction with three proposed pathways to cyanamide

There has been much recent interest in forming metal carbodiimides and cyanamides,[2,3] for instance, in 2010 Krings *et al* synthesised Sr(NCN) via a salt metathesis reaction between SrI_2 and Zn(NCN) at 570 °C,[4] and in 2002 Liu *et al* characterised a new polymorph of mercury cyanamide through the reaction of mercury chloride and cyanamide in the presence of aqueous ammonia.[5] In 2005, the same group synthesised and characterised the first known example of a magnetic transition metal carbodiimide, MnNCN.[6]

Metal carbodiimides and cyanamides have many potentially useful properties, such as cobalt carbodiimide being a promising water oxidation catalyst.[7] The chromium carbodiimide $Cr_2(NCN)_3$ has been shown to be ferromagnetic, this is in contrast to other known transitional metal carbodiimides as well as Cr_2O_3 which is antiferromagnetic.[8] However, some cyanamides have been found to be unstable, such is the case with silver cyanamide which is known to be explosive, and as such has been the subject of a transmission electron microscopy study into the early stages of thermal decomposition of explosive crystals including the products liberated during thermal breakdown.[9] Silver cyanamide was also used alongside various other metal cyanamides such as thallous cyanamide, mercurous cyanamide and cuprous cyanamide in studies into the decomposition of the compounds through heating and irradiation with UV-visible light.[10] There has also been work into non-metal carbodiimides, for instance, Riedel *et al* synthesised a polymeric inorganic silicon carbodiimide through the reaction of $SiCl_4$ with bis(trimethylsilyl)carbodiimide.[11]

The difference in nomenclature between metal cyanamides and metal carbodiimides stems from the symmetry present within the NCN linker. Cyanamides are asymmetric, with it formally being composed of one single and one double CN bond. On the other hand, carbodiimides are symmetrical, with the bonds being of equal lengths within the NCN group. Zinc carbodiimide has historically been referred to as zinc cyanamide, and was first reported in the literature in 1932 through the reaction of cyanogen on zinc oxide.[12] More recent studies on the structure have determined that this nomenclature is inaccurate due to the symmetrical NCN linkage depicting carbodiimide formation.[13] A number of techniques to form zinc carbodiimide have been reported in the literature, all of which involve the production of bulk powders or single crystals. Some of these techniques include a salt metathesis reaction between zinc sulphate and sodium cyanamide,[14] a reaction between zinc chloride, cyanamide (H_2NCN) in the presence of a base[15,16] and the reaction of zinc oxide with three equivalents of urea at 135 °C.[17] Although the compound has been known since the 1930s, the crystal structure was only reported in 2001 by Becker and Jansen.[13] The crystal structure has a tetragonal unit cell and is in the space group $I\bar{4}_2d$. The zinc atoms are arranged in corner sharing ZN_4 tetrahedra; with slightly bent carbodiimide linkages bridging gaps within the structure with equal bond lengths between the central carbon and the adjoining nitrogens.[13] It was described as being related to the zinc silicate structure Willemite (Zn_2SiO_4) with substitution of nitrogen for oxygen, removal of silicon and insertion of carbon to form the bridge between nitrogen atoms (Figure 3-2).[18]

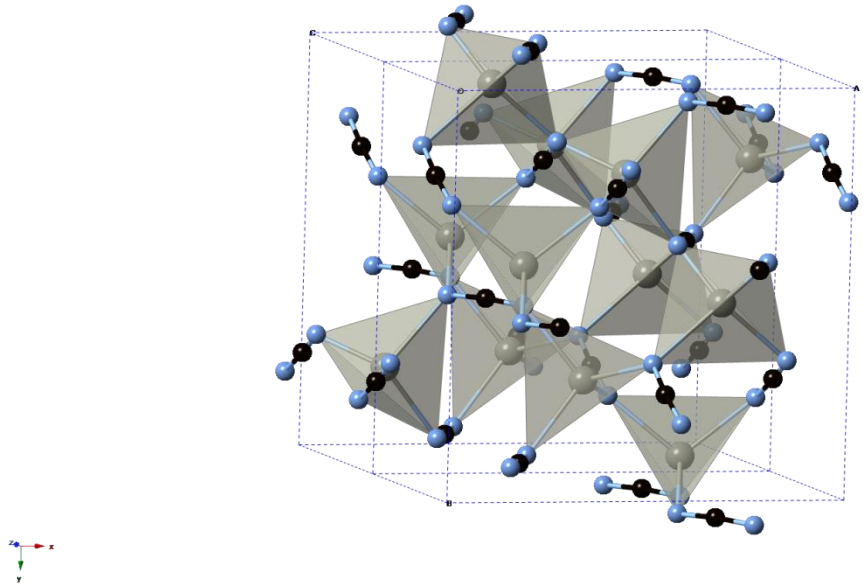

Figure 3-2 – Crystal structure of zinc carbodiimide

Many of the applications of zinc carbodiimide focus on its properties as a non-corrosive white pigment[13] and for mirror coatings.[19] It has also been proposed as a rust prevention coating through the calcination of a mixture of nitrogen containing organic compound with zinc cyanurate.[20] Decomposition experiments showed that between 150 and 530 °C in air, zinc carbodiimide decomposes into zinc oxide and carbon dioxide.[21] However, in an inert atmosphere, zinc carbodiimide has been shown to be stable up to 800 °C.[15] At 1120 °C, decomposition into bamboo-like carbon nanotubes and release of zinc vapour occurs.[22]

3.2 Formation of Zinc Carbodiimide Films

3.2.1 Initial Formation of Zinc Carbodiimide

Initial formation of zinc carbodiimide occurred during the investigation of using urea as an additive during zinc oxide deposition. Following the procedure outlined above (see Experimental, page 8) using a temperature of 500 °C and an argon flow rate of 0.42 l min^{-1} in reactor A with the dispersion chamber set to a height of 0 cm above the tip of the piezoelectric humidifier. Zinc acetate (0.5 g, 2.72 mmol) and urea (0.2 g, 3.33 mmol) were dissolved in methanol (40 cm^3) and this solution was used in the AACVD process. The resulting film was composed of a small section of white, translucent material followed by a transparent coating featuring interference bands along the remainder of the substrate. XRD analysis was carried out on the translucent spot of coating using a Bruker GADDS C2 diffractometer. Upon processing the data, it was discovered that instead of the expected zinc oxide, the deposited material was zinc carbodiimide (Figure 3-3).

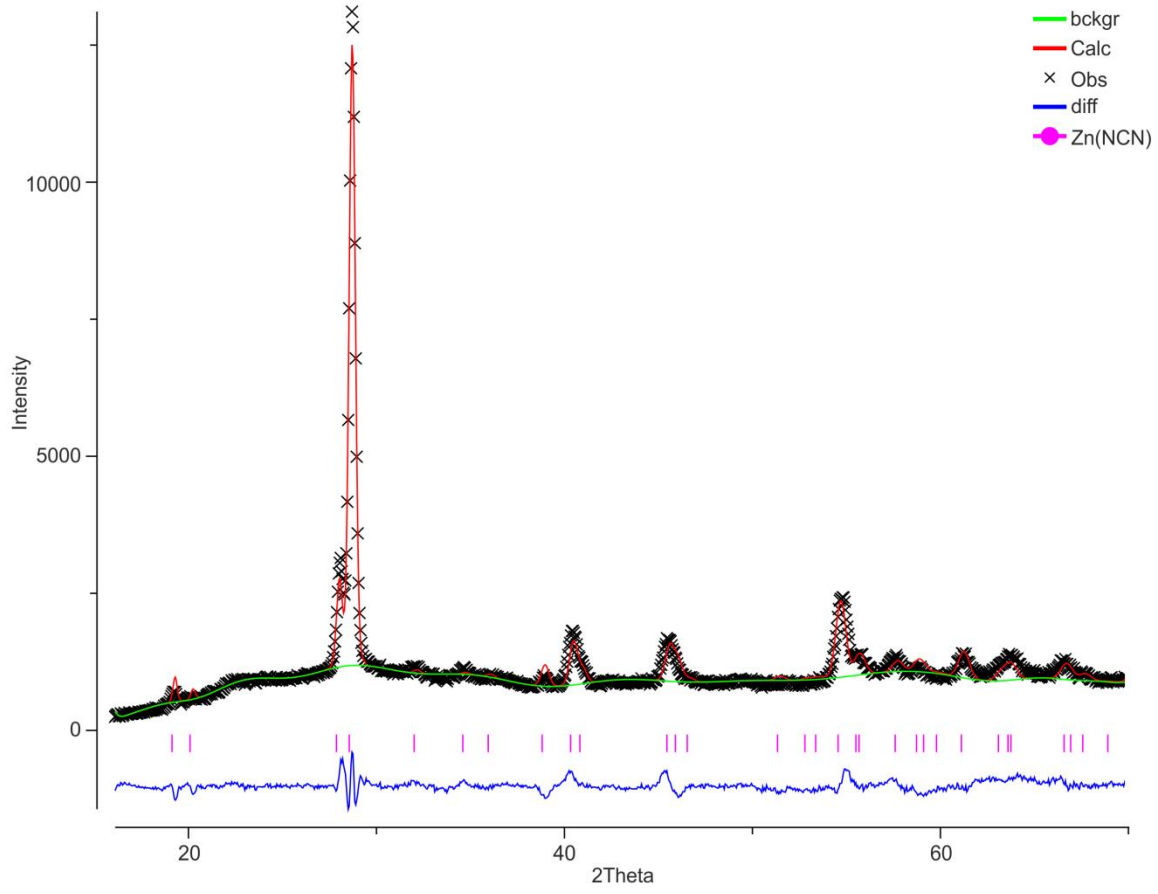

Figure 3-3 - Diffraction pattern of Zn(NCN) from initial deposition

To try and increase the coverage of the translucent section another deposition was carried out, this time doubling all of the quantities of the solution and using aliquots (20 cm^3), allowing each aliquot to transfer completely before the next was added. Aliquots were used as the piezoelectric

humidifiers are unable to generate an aerosol in the dispersion chamber through 80 cm^3 of methanol. The flow rate was increased slightly to 1.0 l min^{-1} while all other conditions remained unchanged. XRD patterns were collected at 10 points on the resulting substrate spaced 1 cm apart, beginning from c.a. 1 cm in from the front edge of the glass. A waterfall graph shows that there is a transition from zinc carbodiimide to zinc oxide (see Figure 3-4) between 4 and 6 cm across the substrate from the leading edge.

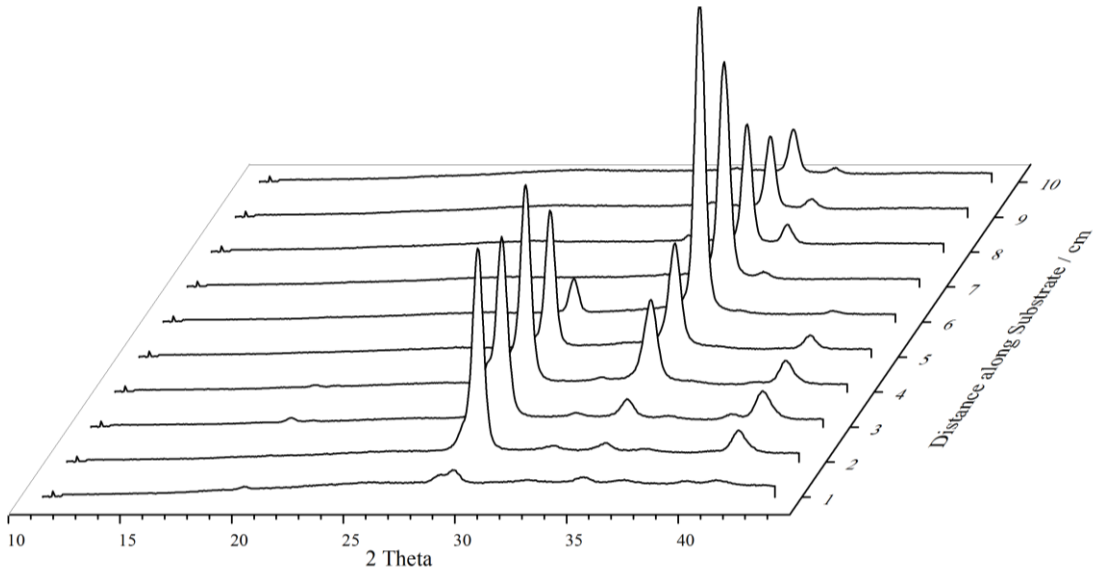

Figure 3-4 – Image showing waterfall graph of X-ray diffraction patterns taken at regular intervals across the sample. Sharp peaks at c.a. 29 2θ for positions 1-6 correspond to the (220) face of zinc carbodiimide. The peaks at c.a. 35 2θ for positions 4-10 correspond to the (0002) face of ZnO.

3.2.2 Initial Investigation into Conditions Affecting Zinc Carbodiimide Formation

Chapter 3.2.2 is a summary of work carried out by William Grantham, a project student under my supervision. This work serves as an intermediate between Chapter 3.2.1 and Chapter 3.2.3

Work was carried out to determine the influence of various conditions on the deposition of the zinc carbodiimide films. The analysis was initially carried out visually; this is due in part to the large difference between appearance of zinc oxide and zinc carbodiimide, the former of which is a transparent coating with noticeable interference effects and the latter being an off-white translucent coating, this is a characteristic that can be used to visually differentiate between the two phases prior to running the sample on the diffractometer. The parameters adjusted included the flow rate, temperature, zinc precursor amount and ratio to urea along with the solvent used (full results are included in Appendix B). During the investigation it was discovered that the flow rate had no appreciable influence on the composition of the produced film, however, it did affect the coverage. Low flow rates caused most deposition to occur at the preceding edge of the substrates, resulting in only the initial section of the glass being coated with the carbodiimide. An ideal rate was found to be 1.5 l min^{-1}, however, the flow rate had less of an impact than the temperature of the reactor. Carbodiimide films formed at temperatures above 450 °C were found to deposit mostly in the beginning section of the substrate, irrespective of the flow rate used. Films formed at temperatures below 400 °C were found to often be non-crystalline when analysed using X-ray diffraction. The quantity of zinc acetate used was found to only impact the thickness and coverage of the resulting films. With quantities above 2 mmol, small amounts of delamination often occurred. It was discovered that by using 1.36 mmol of zinc acetate it is possible to achieve a good coverage of the substrate with no delamination. The results for adjusting precursor to urea ratios showed that at ratios lower than 1:2, there is a large amount of zinc oxide present within the produced film; however, both phases rarely appear within the same section of substrate. There is always a transition moving from the front edge with zinc carbodiimide generally forming at the leading edge then being replaced by zinc oxide, this is a trend observable in both the diffraction patterns and by visible observation, with the transition manifesting as a ‘tide mark’ on the surface of the coating. Above 1:3, the film appears to solely consist of zinc carbodiimide.

3.2.3 Optimising the Temperature of Deposition

The above results were used to optimise the conditions with respect to the temperature and zinc acetate to urea ratios. This sequence was broken in to two strands, the first of which investigate the impact varying the temperature has on the system. To carry this out, a solution of zinc acetate (0.25 g / 1.36 mmol) and urea (0.245 g / 4.08 mmol) in methanol (40 cm^3) is used for each experiment. The depositions were carried out using the procedure outlined above (see Experimental page 8) with a flow rate of 0.84 l min^{-1} of argon, a dispersion chamber height of 0 cm and temperature varied according to the following table (Table 3-1). X-ray analysis was carried out on two diffractometers; initial data was run at 10 points along the surface of each substrate, beginning at 1 cm from the preceding edge with each subsequent point being spaced 1 cm away along a line. This was collected on a Bruker GADDS C2 diffractometer (see Appendix B) and a more detailed scan was carried out at c.a. 5 cm on each sample using a Rigaku Smartlab diffractometer (Figure 3-5).

Table 3-1 - Summary of results in change of temperature on zinc carbodiimide formation

Run (KK058)	**Temperature / °C**	**Visual Observation**	**XRD Summary**
1	375	No visible deposition at front of substrate, some deposition after initial c.a. 5 cm	Very low intensity Zn(NCN) in second half of substrate
2	400	Most of substrate covered by translucent coating	Low intensity Zn(NCN) across whole substrate
3	425	Most of substrate covered by translucent coating	Sharp by low intensity Zn(NCN) across whole substrate
4	450	Most of substrate covered by translucent coating	High intensity Zn(NCN) across first half of substrate
5	475	Slightly uneven deposition, mostly at start of substrate	Low intensity Zn(NCN) in first half of substrate
6	500	Poor coverage, most deposition at beginning of substrate	Low intensity Zn(NCN) in first half of substrate

The sequence shows that below 400 °C, the temperature is not high enough to deposit uniform films of crystalline zinc carbodiimide. Above 450 °C the reaction occurred within the first few centimetres of the reaction chamber, resulting in only forming the zinc carbodiimide along the first half of the substrate. The samples also showed low intensity in the XRD, this could be due to further decomposition of the urea molecule causing carbon contamination reducing the formation of zinc carbodiimide, another possibility is that due to the furnace heating from the bottom and the presence of a temperature gradient above the surface of the substrate, thermophoresis effects (see Aerosol Assisted Chemical Vapour Deposition page 5) are causing the aerosol droplets to rise upon entering the chamber, and resulting in an increase in deposition on the top plate.[23,24] Due to the coverage and intensity (Figure 3-5) it was decided that 450 °C is the optimal temperature to deposit zinc carbodiimide.

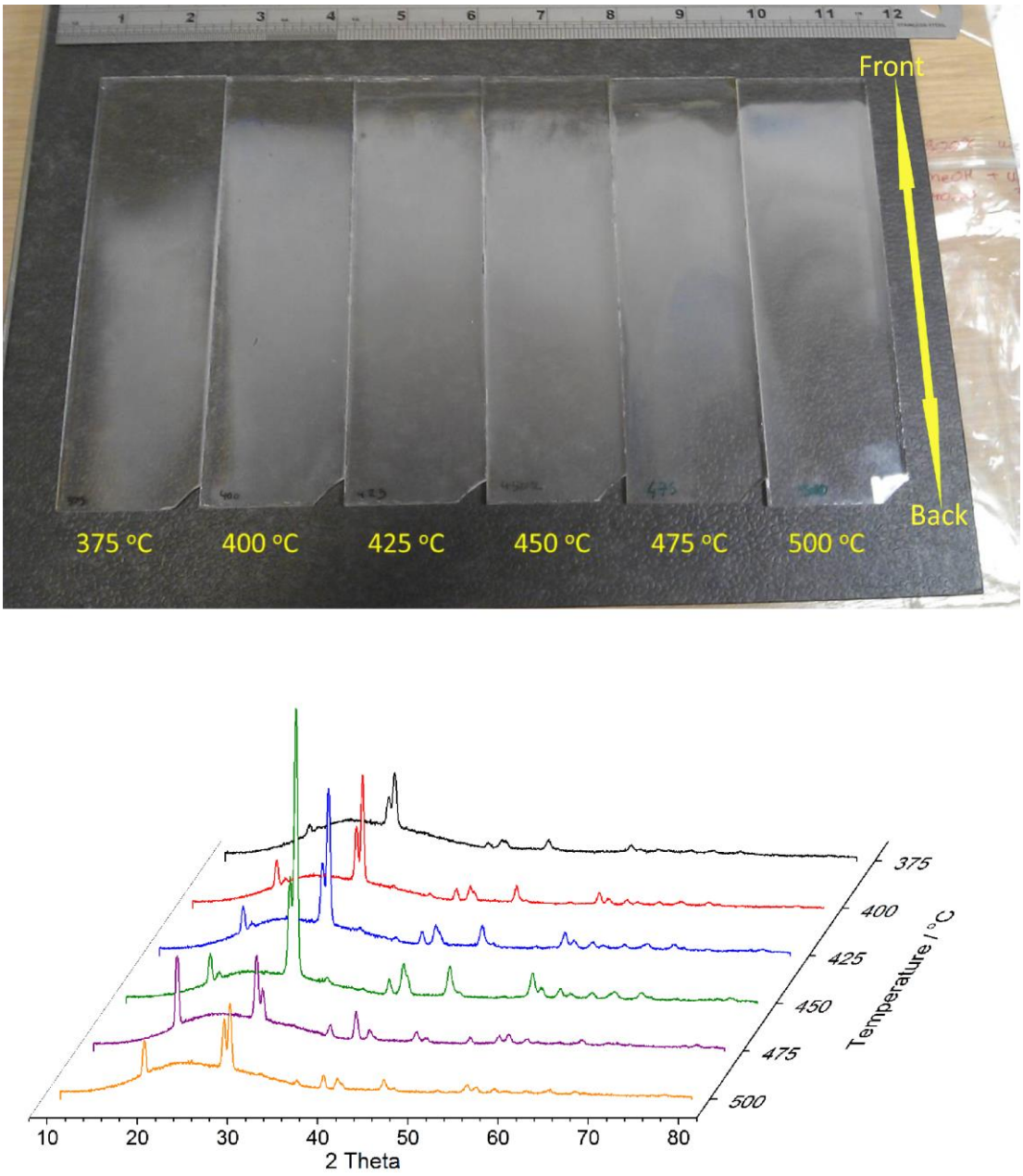

Figure 3-5 – Photograph of the films within the sequence (top) and waterfall graph of associated XRD patterns (bottom). Sharpest and most intense peaks for zinc carbodiimide obtained for sample deposited at 450 °C.

3.2.4 Optimising the Mole Ratios of Zinc Acetate and Urea

Following the above results, a set of experiments were carried out in which the mole ratio of zinc acetate and urea was varied. The depositions were carried out according to the outline above (see Experimental page 8) using a temperature of 450 °C, an argon flow rate of 0.84 l min^{-1} and a dispersion chamber height of 0 cm. A solution of zinc acetate (0.25 g, 1.36 mmol) in methanol (40 cm^3) was used in each experiment and to each of these; a varying quantity of urea was added as shown in the following diagram (Figure 3-6). X-ray analysis was carried out on two diffractometers; initial data run at 10 points along the surface of each substrate was collected on Bruker GADDS C2 (see Appendix B) and a more detailed scan was carried out at c.a. 5 cm on each sample using a Rigaku Smartlab diffractometer (Figure 3-7).

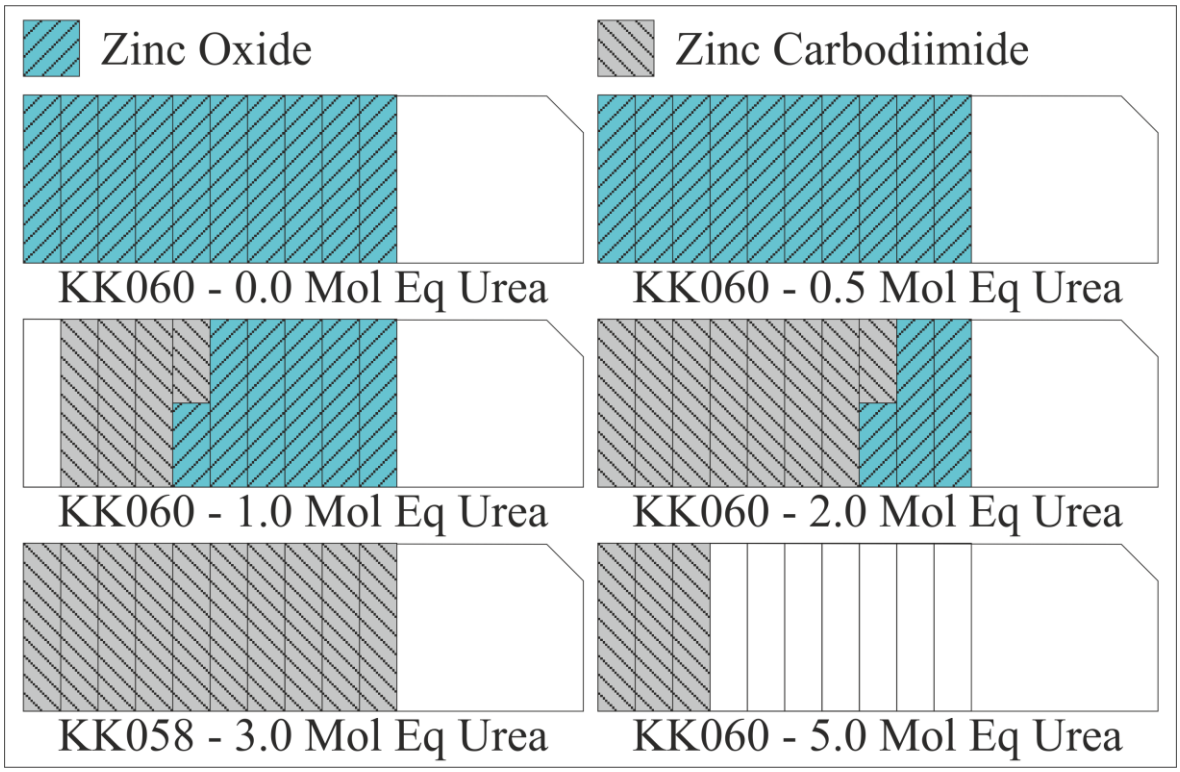

Figure 3-6 – Diagram showing experiments in this set and a pictorial representation of XRD results

The sequence shows that below 1 mole equivalents of urea, there is no formation of zinc carbodiimide visible in the X-ray diffraction patterns. At 1 mole equivalent, some of the zinc oxide towards the beginning of the substrate begins to be replaced by zinc carbodiimide. As this is increased to 2 mole equivalents of urea, there is no longer evidence of zinc oxide within the X-ray diffraction patterns; however, this is accompanied by a visible 'tide mark' present c.a. 7 cm along the substrate itself (Figure 3-7). This could suggest that after this point, there is a small amount of zinc oxide forming; however, due to the conditions it is poorly crystalline and so is not having an impact on the X-ray diffraction pattern. The sample for 3.0 mole equivalents, which is drawn from the previous set of experiments, there is no evidence of zinc oxide within the film. The X-ray diffraction pattern shows zinc carbodiimide across the entire sample, visual inspection of substrate

itself shows a white translucent coating across the entire surface. Once the mole ratio of zinc acetate to urea reaches 1:5, the X-ray diffraction data shows only zinc carbodiimide with a low intensity across the initial 4 cm of the substrate; this is reflected in the physical appearance of the sample, with the white translucent coating only being visible within the first c.a. 5 cm of the glass.

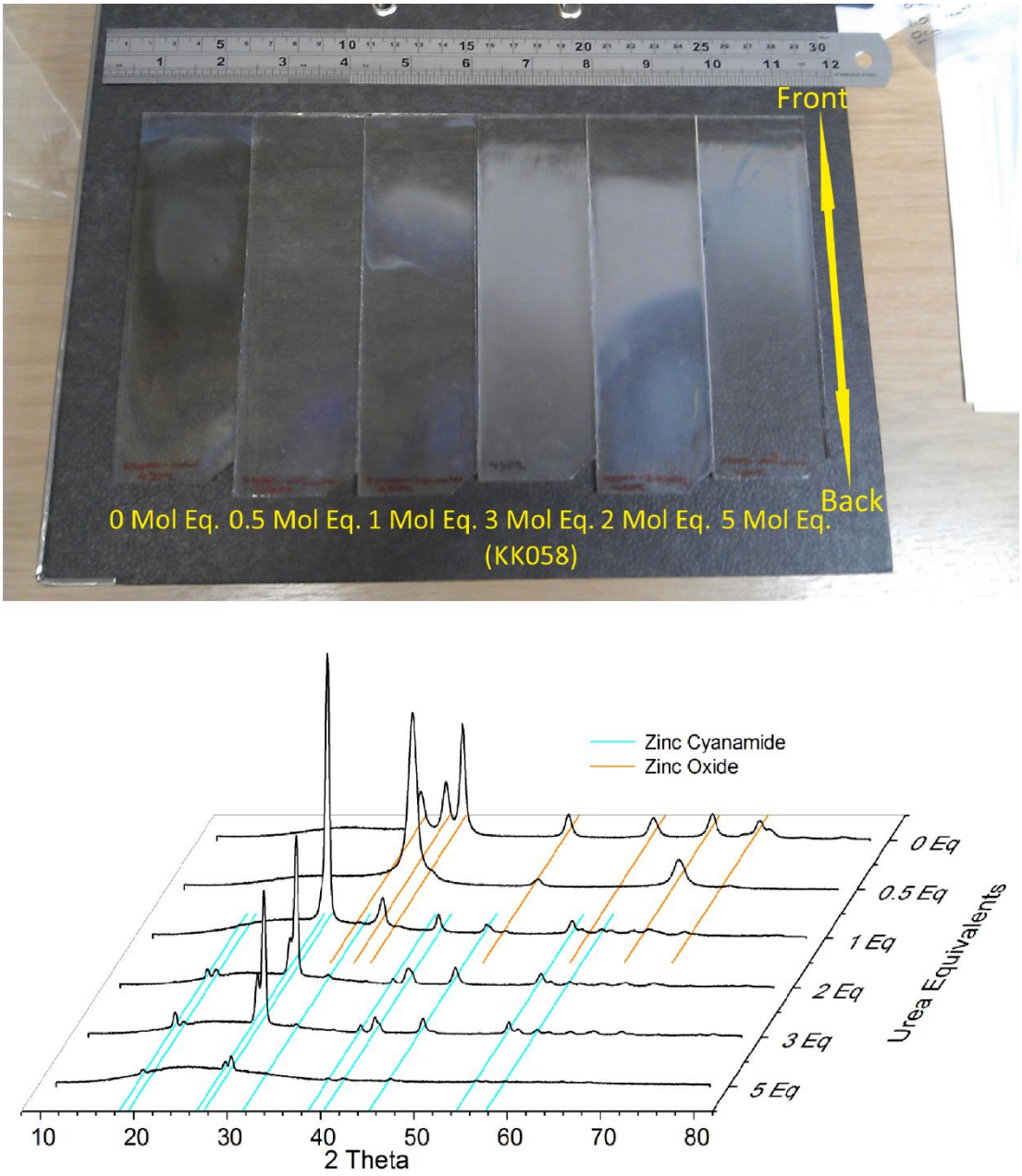

Figure 3-7 – Photograph of films within sequence (top) and waterfall graph of associated XRD patterns (bottom)

These findings suggest that using aerosol assisted chemical vapour deposition with zinc acetate, methanol and urea, the idea conditions for optimal coverage and crystallinity of zinc carbodiimide is a temperature of 450 °C and a zinc acetate to urea ratio of 1:3.

3.3 Analysis of Zinc Carbodiimide Films

3.3.1 X-Ray Diffraction Refinement

The X-ray diffraction data collected for the sequences above (See 3.2.3 and 3.2.4) were analysed using Rietveld refinement to determine how the growth of the films in the conditions used affected the lattice parameters. The reference data used in the Rietveld refinement was the crystallographic information file provided by Becker and Jansen as part of their zinc carbodiimide characterisation.[13] An exemplar fit is shown below (Figure 3-8). The main parameters which were refined during the process are sample height which is to take into account slight shifts in peak positions present during the collecting of the diffraction pattern. Peak shape was also refined, using both Gaussian and Lorentzian parameters. Due to the samples being thin films, growth on the substrate may have resulted in growth along particular crystallographic faces to become more preferential, to take this into account, the preferred orientation was refined as part of a spherical harmonic function. Finally, the unit cell was refined, this revolved primarily around refining the unit cell lengths; however, atom positions and thermal parameters were adjusted in an attempt to more accurately fit the pattern to the reference data and to account for any variation brought about by lattice strain within the sample. The lattice parameters for zinc carbodiimide are summarised in the table below (Table 3-2). X-ray diffraction patterns are shown above (Figure 3-5 and Figure 3-7).

Table 3-2 – Table summarising the XRD data for samples containing zinc carbodiimide

Experiment	Urea / Mol Eq.	Temperature / °C	Cell Volume / Å^3	Texture Index	χ^2
KK058_375	3.0	375	417.8 ± 0.3	1.2	3.0
KK058_400	3.0	400	415.2 ± 0.0	1.2	3.9
KK058_425	3.0	425	418.2 ± 0.1	1.2	3.9
KK058_450	3.0	450	417.5 ± 0.1	1.3	4.8
KK058_475	3.0	475	417.1 ± 0.1	1.1	2.9
KK058_500	3.0	500	416.5 ± 0.1	1.0	3.1
KK060_10	1.0	450	417.4 ± 0.2	1.4	23.1
KK060_20	2.0	450	417.0 ± 0.1	1.5	6.4
KK060_50	5.0	450	417.4 ± 0.3	1.1	2.4

The data for KK060_00 and KK060_05 were omitted from the table due to the XRD containing no evidence of zinc carbodiimide and being solely composed of zinc oxide. The diffraction pattern for KK060_05 showed peak broadening for ZnO with respect to the sample with no urea present, there is also a large amount of preferred orientation (J = 4.2) along [0002] plane. This suggests that the small amount of urea present is influencing the crystallite growth of ZnO by inducing preferential growth along [0002] plane, in a similar way to the effects seen with CTAB (see Quaternary Ammonium Bromides to Control Microstructure, page 39). Sample KK060_10 has a small amount of ZnO present in the diffraction pattern (2.77 wt%), the ZnO present exhibited broad peaks,

resulting in the pattern being more challenging to fit, this is reflected in the high χ^2 value (23.1). All of the samples showed texture indexes between 1 and 1.5, this shows that there is very little preferred orientation present within the zinc carbodiimide films. All of the samples show a unit cell volume lower than the quoted literature value of 421.17 Å^3, this is less than a 1% difference, but it is systematic, this is most likely due to crystal strain induced through the growth of the zinc carbodiimide on the glass substrate. Williamson-Hall analysis was carried out on the diffraction patterns. This takes into account the peak broadening caused by strain and crystallite size in such a way that a plot of sin θ vs B cos θ, where B is the full width half maximum of the peaks, gives a straight line in which the intercept in inversely proportional to the crystallite size and the gradient is proportional to lattice strain.[25] Analysis was carried out using the *fityk* curve fitting software using a pseudo voigt function to model the peaks and determine their width.[26] The Williamson-Hall analysis determined that the average crystallite size within the samples was 34(7) ± 11(4) nm with a lattice strain of 0.39(7) ± 0.30(2)%. The strain present explains the systematic reduction in the unit cell size for each of the samples.

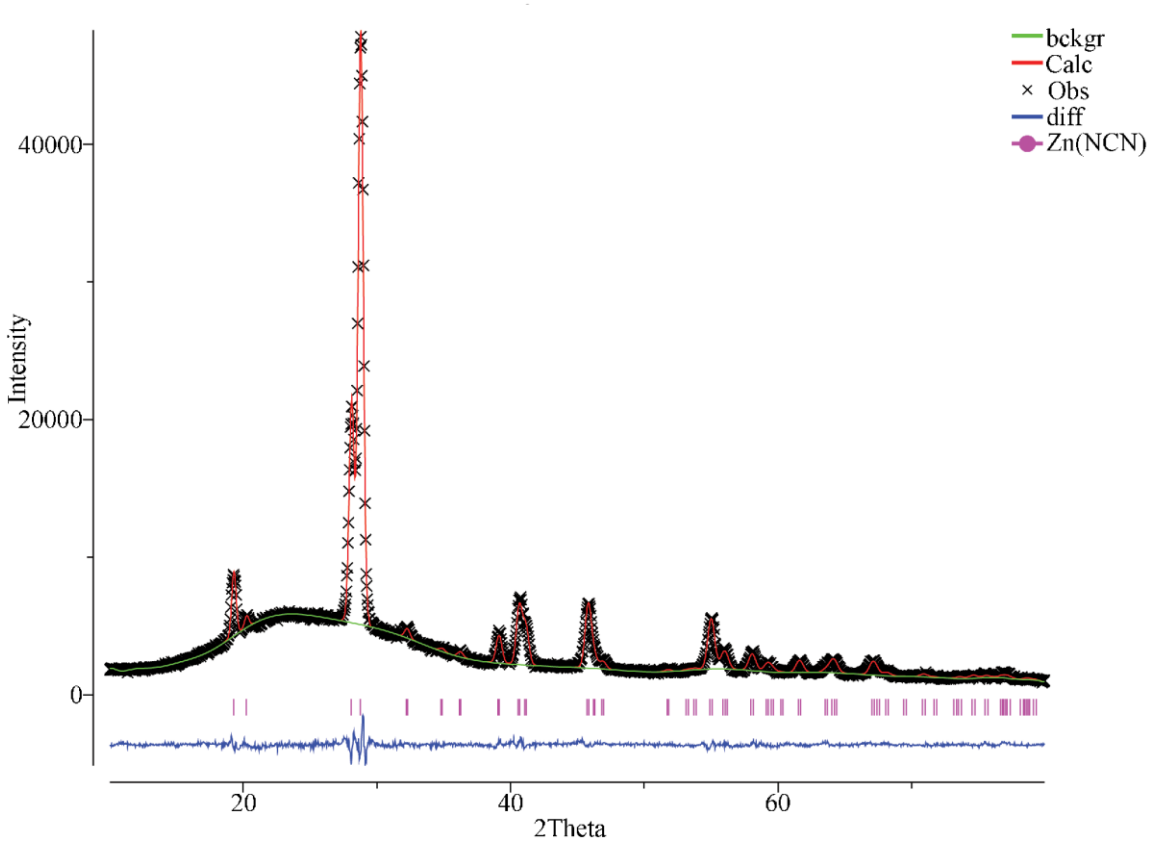

Figure 3-8 – Exemplar fit of X-ray diffraction data. Data set KK058_450.

3.3.2 Scanning Electron Microscopy

Scanning electron microscopy was carried out on a sequence of samples at a range of temperatures to investigate whether there is a progression in crystallite sizes (Figure 3-9). The square analysed was taken from the same position on each sample, this was 5 cm from the leading edge, each sample was coated on the top surface with gold to create a conductive pathway to the base during microscopy.

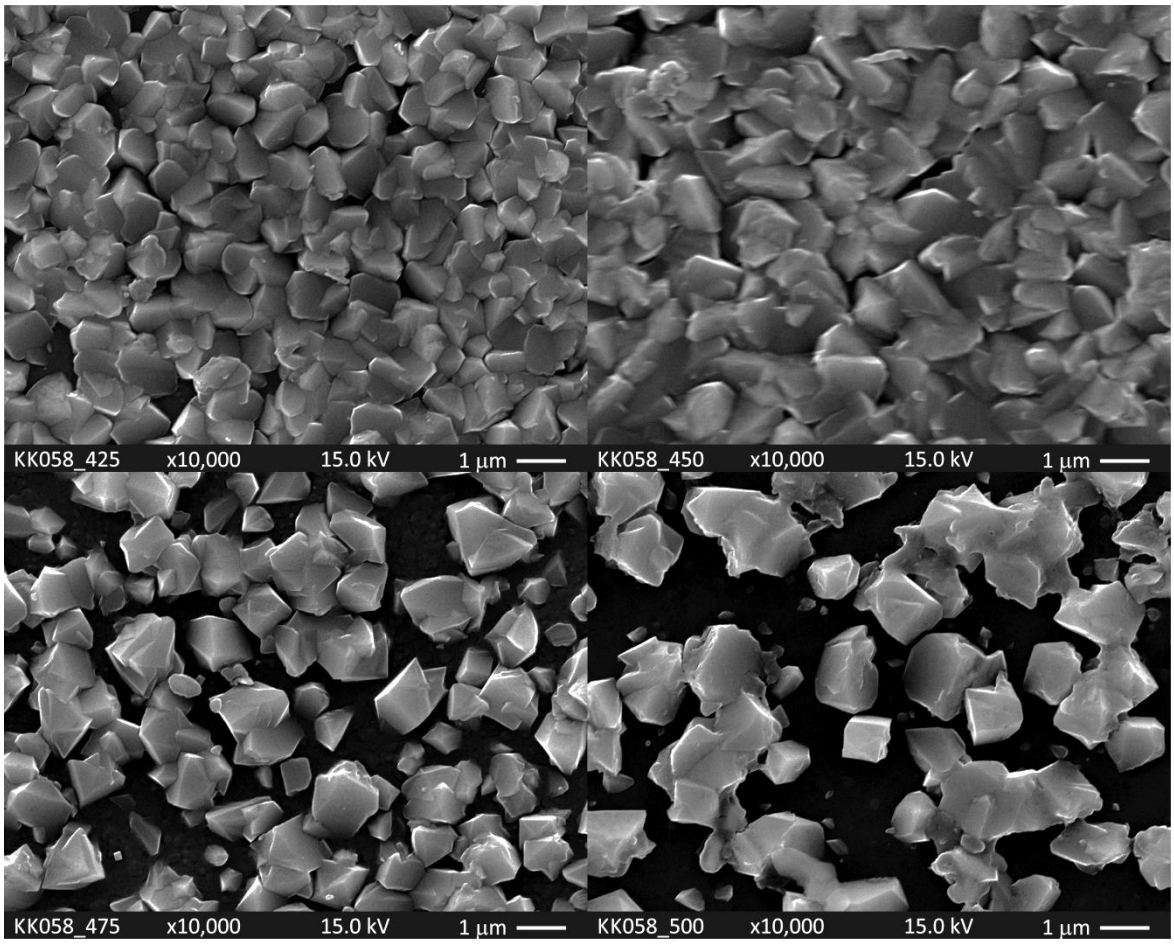

Figure 3-9 – SEM Images of Zinc Carbodiimide at Various Temperatures from 425-500 °C

As the temperature increases from 425 to 450 °C, there is an increase in particle size, from c.a. 1 µm to c.a. 1.5 µm. Above 450 °C the particle size does not appear to grow any further, however, there is an increase in porosity with particles being separated by seemingly empty spaces, this continues into the sample at 500 °C, with the spacing growing even larger. These observations reflect what was seen in the XRD for these samples (Figure 3-5), with 450 °C exhibiting the most intense peaks with samples grown at 475 and 500 °C being less intense. This can be explained simply by there being less crystalline material present to diffract X-rays. However, this is most likely an artefact caused by the samples for electron microscopy being taken from the trailing edge of the coating. The results from the Williamson-Hall analysis suggests that the crystallite size is c.a. 35 nm, this is much lower that the apparent size of the particles on the substrate, this potentially

shows that each of the particles present are polycrystalline and are composed of many aggregated crystallites. However, no standard was run so the function will assume that all peak broadening is a result of the peak width and lattice strain, therefore there is a possibility that the value for crystallite size is being underestimated due to it not taking into account instrument broadening. When compared to the photographs of the samples (Figure 3-5), the position 8 cm away from the leading edge of the sample at 500 °C is where the thickness of the zinc carbodiimide film appears to be reducing. This could explain why there are open voids within the SEM images while the particle size is remaining constant. The large particle size could explain why the films have a white translucent appearance, this could be due to Mie Scattering occurring within the particles which have diameters comparable to that of visible light.[27,28] The white translucent appearance of the films could also be a result of diffuse reflectance occurring, in which partial reflection is occurring between the interface between the particles, this will be more pronounce in samples in which there are voids between the particles resulting in a change in refractive index at the interfaces.[28]

Side-on SEM was also carried out on the samples to provide a value for film thickness. Microscopy was carried out on the same samples as shown above (Figure 3-9). There is a clear distinction between the glass of the substrate and the thin film deposited on top; this can be used to determine film thickness as shown in the example below (Figure 3-10). The thickness for the sample at 450 °C using 3 mole equivalents of urea is approximately 1 μm. This was the case for each of the samples measured, suggesting that there are factors preventing the films growing thicker than this. One possibility is that while crystallites are growing initially, they are spaced out, with large gaps between them, as shown in the SEM image for the sample grown at 500 °C. As the crystallites begin to reach a limiting size, growth begins to occur in the empty spaces, demonstrated by the denser packing featured in the films grown at 425 and 450 °C (Figure 3-9). It may be of interest to carry out an investigation on this by depositing a zinc carbodiimide film at 450 °C using 3 mole equivalents of urea, except using a larger quantity of zinc acetate. This would determine whether there is a maximum thickness for films of zinc carbodiimide formed under these conditions. Another suggestion would be to run the deposition as outlined above multiple times, interrupting it after a different length of time with each run; this would provide a sequence of samples which when examined on the SEM would depict growth of the zinc carbodiimide films in stages.

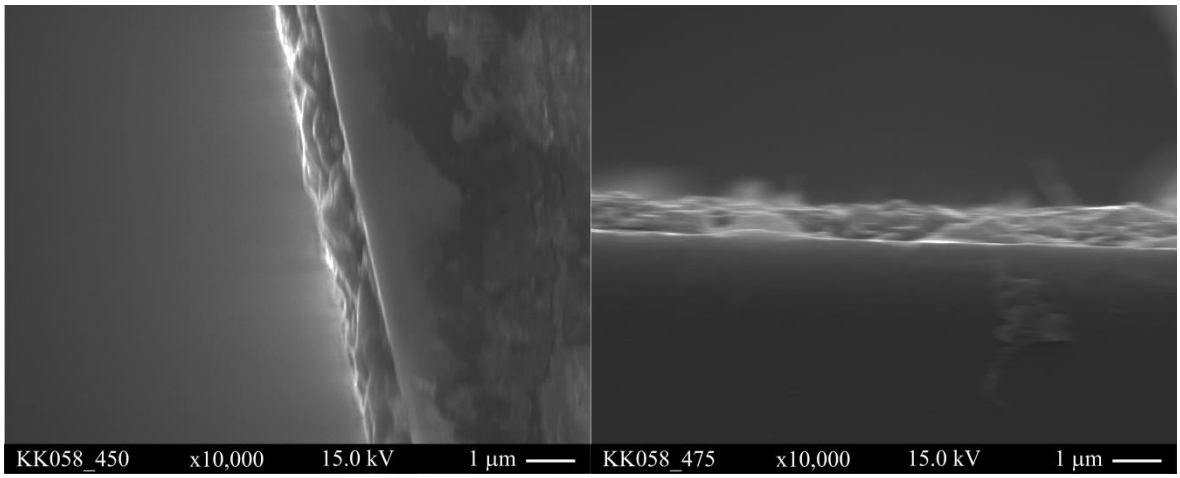

Figure 3-10 – Side on SEM image of zinc cyanamide formed at 450 °C (left) and at 475 °C (right)

3.3.3 Elemental Analysis and FTIR

Elemental analysis of the films came from energy dispersive X-ray spectroscopy (EDX). The results are summarised in the table below (Table 3-3).

Table 3-3 – Table showing summary of EDX Results

Experiment	Run	Zn / at%	C / at%	N / at%	Si / at%	O / at%	Mg / at%	Al / at%
KK058_425	1	28.8	25.8	39.4	2.2	3.8	0.0	0.0
	2	28.9	25.5	39.5	2.3	3.8	0.0	0.0
KK058_450	1	27.8	29.7	39.9	1.2	3.8	0.0	0.7
	2	28.4	28.6	38.4	0.9	3.3	0.0	0.4
	3	17.3	17.4	20.8	15.9	27.6	0.8	0.2
	4	17.1	17.4	20.6	16.0	27.8	0.9	0.3
KK058_475	1	21.5	25.1	26.8	10.0	16.0	0.3	0.3
	2	21.6	24.5	26.9	10.2	16.1	0.4	0.3
KK058_500	1	16.3	22.4	17.5	15.5	27.1	0.9	0.4
	2	16.9	21.6	18.1	15.6	26.7	0.8	0.3

From the results it can be shown that penetration into the glass substrate is occurring, as is evidenced by the silicon content present. This also accommodates the presence of high levels of oxygen, for instance, in run 3 of experiment KK058_450. The traces of magnesium and aluminium could likewise be attributed to penetration into the glass substrate; however, they may also be from contaminants on the surface of the film. When taking the average at% while discounting elements present as glass or contaminants, the average formula is $ZnC_{1.08}N_{1.26}$. This severely underestimates the nitrogen content; however, due to the lack of internal standards, quantification of light elements including carbon and nitrogen will suffer from inaccuracies. This underestimation of nitrogen could also be explained by one of the limitations of EDX being accurate measurement of rough samples. The SEM images (Figure 3-9) show that the samples used are composed of interlocking crystallites, all of which increase the sample roughness, this can prevent the X-rays emitted escaping the sample to reach the detector, this is particularly pronounced with lower energy X-rays, as is the case with carbon and nitrogen. The EDX supports the interpretation of the X-ray diffraction, in that the main elements present are zinc, carbon and nitrogen.

Final analysis of the films came from FTIR analysis. The only peaks present other than those exhibited by the glass substrate are the asymmetric vibration ν_{as}(NCN) = 2029 cm^{-1} and the deformation vibration δ(NCN) = 675 cm^{-1} peak (Figure 3-11). This is in agreement with other work into metal carbodiimides such as manganese.[6] The peak which would be present for an asymmetric cyanamide group is absent, this being the symmetric vibration ν_s which would be situated at around 1200 cm^{-1}, providing evidence of the NCN group existing in the symmetrical carbodiimide configuration.

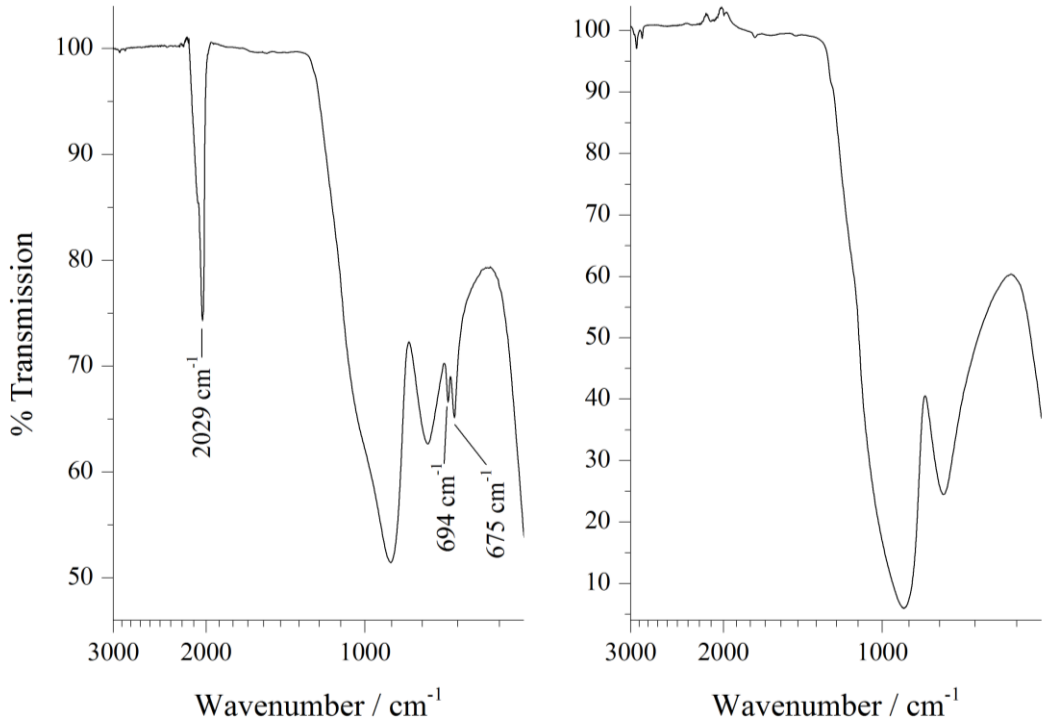

Figure 3-11 – FTIR Spectra of zinc carbodiimide (left) and just glass (right)

3.4 Investigation into Treatment of Zinc Carbodiimide Thin Films

Due to the findings from Becker in which they heated zinc carbodiimide powder under an inert atmosphere and discovered the formation of C-N nanotubes[13,22] it was determined that this would be an interesting phenomenon to test with thin films. To test this, zinc carbodiimide was grown on quartz following the procedure outlined above (See Experimental, page 8) using a temperature of 450°C, an argon flow of 0.42 l min^{-1} and a solution of zinc acetate (0.25 g, 1.36 mmol) and urea (0.425 g / 4.08 mmol) in methanol (40 cm^3). Once completed, the quartz was cut into 4 equal pieces (2.5 x 2.5 cm^2). The XRD was collected on one of the pieces to confirm the formation of zinc carbodiimide and to obtain a pre-treatment reference.

Three of the pieces were returned to the reactor and were coated with titanium dioxide following the procedure outlined above (see Experimental page 8), a temperature of 450 °C, an argon flow rate of 0.5 l min^{-1} and a solution of titanium isopropoxide (0.25 cm^3, 0.84 mmol) in ethanol (10 cm^3). This was part of an investigation to determine whether it would be possible to insert the zinc which is liberated during decomposition into TiO_2 to form zinc doped titanium dioxide. A schematic of the possibility is shown below (Figure 3-12). The XRD of one of these samples was collected and was found to consist of solely zinc carbodiimide and titanium dioxide in the anatase phase.

One of the dual coated pieces was placed inside a tube furnace under air where it was heated to 600 °C at 5 °C min^{-1} followed by an increase to 800 at 2 °C min^{-1} before finally increasing to 1150 at a rate of 0.2 °C min^{-1}. At this point it was held at 1150 °C for 1 hour before cooling to 800 °C at a rate no faster than 0.2 °C min^{-1} and finally down to ambient temperature at an uncontrolled rate. This ramping rate was chosen so that as the temperature approached the point at which decomposition starts to occur it would increase very gradually in an attempt to allow the system to remain at equilibrium while the temperature was increasing.

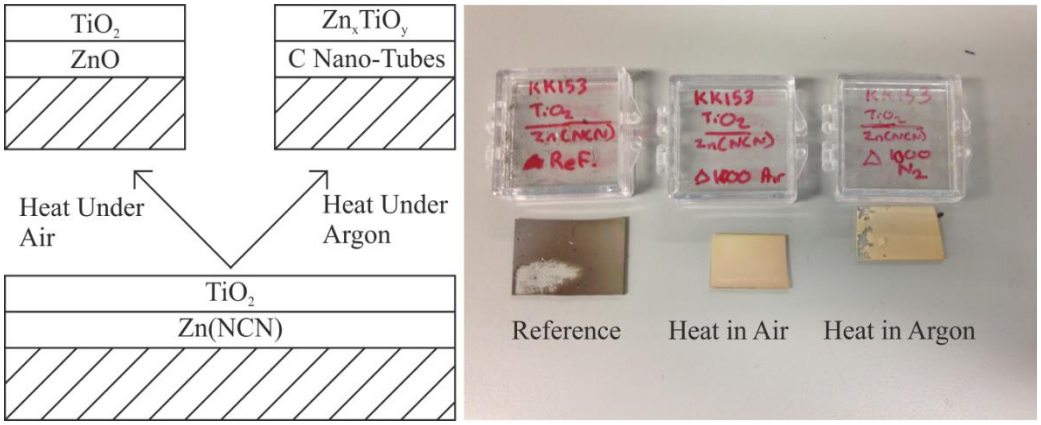

Figure 3-12 – Schematic showing the plan for the investigation into potential applications for a thin film of zinc carbodiimide (left). Picture of films formed during heating (right)

The other dual coated piece was placed inside the tube furnace under a flow of argon gas and heated using the same programme as outlined for the sample heated in air. The appearance of both samples had changed after heating. The initial dual coated sample was grey in colour, however, upon removal, both samples had an off white, opaque appearance. A picture of the films before and after heating is shown above (Figure 3-12). Both samples were then analysed on the Rigaku Smartlab and the processed diffraction patterns are shown below (Figure 3-13).

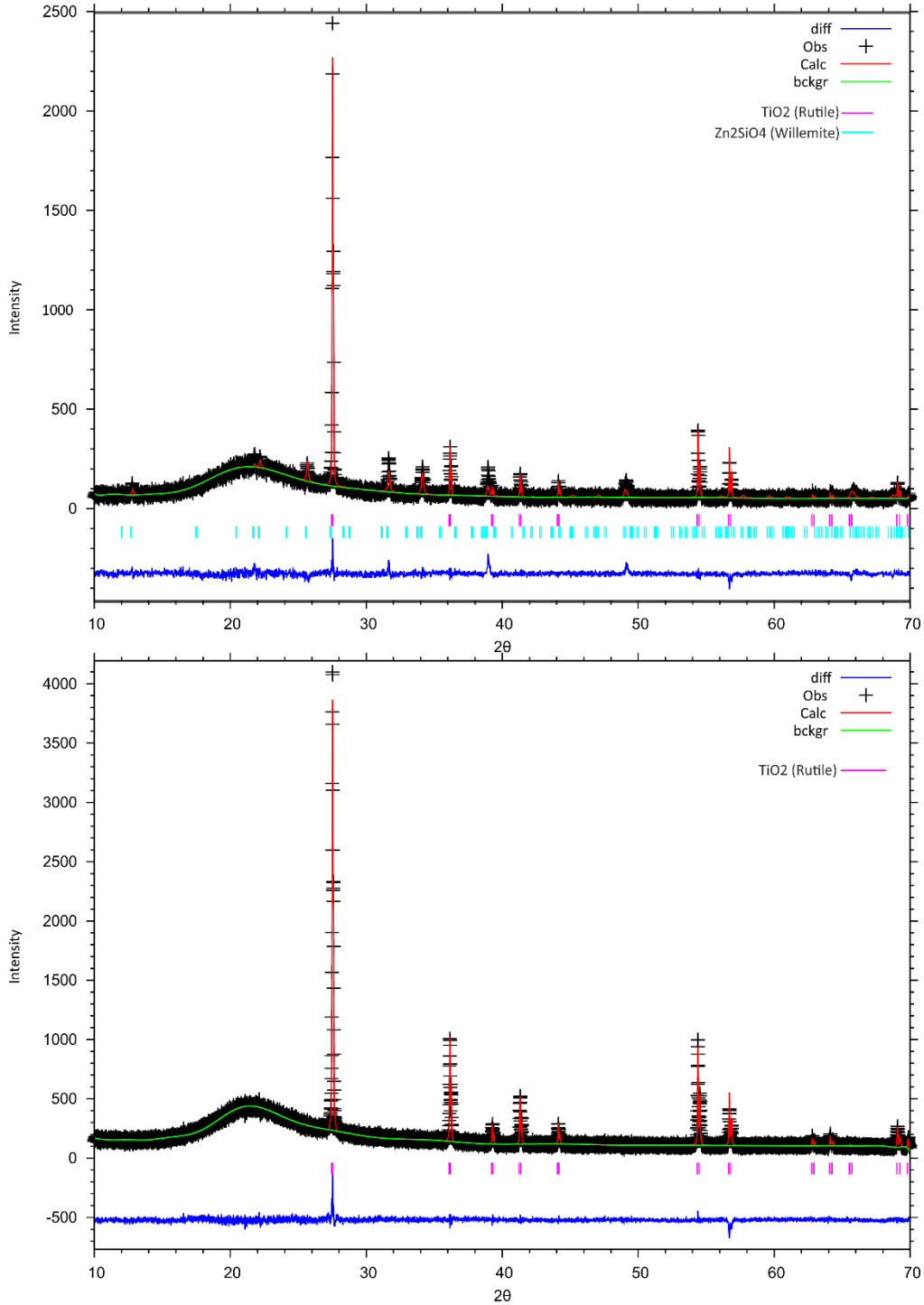

Figure 3-13 – XRD Patterns for the sample treated in air (top) and the sample treated under argon (bottom)

The diffraction pattern for the sample treated in air shows the presence of two phases, TiO_2 in the rutile phase, and Zn_2SiO_4 in the willemite phase. The formation of the zinc silicate was an unexpected result; it suggests that at the temperatures used, the zinc oxide forming from the decomposition of the zinc carbodiimide reacted with the silica substrate to form willemite. It may be of interest to repeat this experiment using a more inert substrate, such as alumina, that way, it may be possible to isolate a sample with a layer of zinc oxide underneath titanium dioxide; however, due to the possibility of forming zinc oxide directly then coating it with titanium dioxide, this would be a very inefficient and energy intensive route to such a sample.

As can be seen in the XRD pattern for the sample heated under argon, the only phase present in the sample is TiO_2 which is entirely in the rutile phase. This is opposed to the anatase phase it was adopting before heating, showing that a phase change has occurred. There is no evidence of any zinc containing species within the diffraction pattern, a possible explanation is that the zinc carbodiimide has decomposed according to Becker's observations and zinc has been removed as zinc vapour during the heating process; this is supported by the grey residue on the inside of the quartz tube after it was removed from the tube furnace. This suggests that there is a possibility that the remaining sample is TiO_2 mounted onto a carbon-nitrogen framework. This framework would have no diffraction peaks due to either poor crystallinity or very low molecular density and so would be difficult to analyse. EDX would be of little use in confirming presence of a framework due to its location underneath a layer of titanium dioxide. Penetration into the sample can occur, however, this can be limited and so the spectrum will be dominated by the presence of titanium and oxygen, however, EDX could show whether or not there has been any incorporation of zinc atoms into the titanium dioxide phase to form a Zn-Doped TiO_2. The film is poorly adhered to the substrate, and requires very little force to remove. This could potentially be used as a method to remove metal oxides from the surface of a substrate; however, it suffers from the large disadvantage of being very intensive, in both time and energy.

SEM images of the samples show that there is a change in morphology after the samples are heated (Figure 3-14). The sample of TiO_2 deposited onto Zn(NCN) is composed of hexagonal plates, arranged in clusters. Comparison to SEM images of thin films of Zn(NCN) (Figure 3-9) suggest that the titanium dioxide has grown into hexagonal plates following the crystallites formed from the zinc carbodiimide base layer. Upon heating, the hexagonal character of the plates is lost. The morphology present within the sample heated under argon shows smooth crystallites of varying sizes (c.a. 500-2000 nm in diameter). The surface appears to be very porous. The SEM image for the sample heated in air once again shows smooth crystallites, however, they are of a much larger size than those present in the sample heated under argon (c.a. 1000-4000 nm in diameter). This increase in crystallite size could be a result of the change in the base layers. When heated under argon, X-ray diffraction suggests that the base layer has decomposed entirely, removing all crystalline material, this could have resulted in cavities beneath the titanium dioxide

top layer which collapsed during the heating process. This was not the case with the sample heated under air, the decomposing base layer of zinc carbodiimide reacted with the silica substrate to form willemite during the heating process. As a result of this, a base layer was present during the entire reaction.

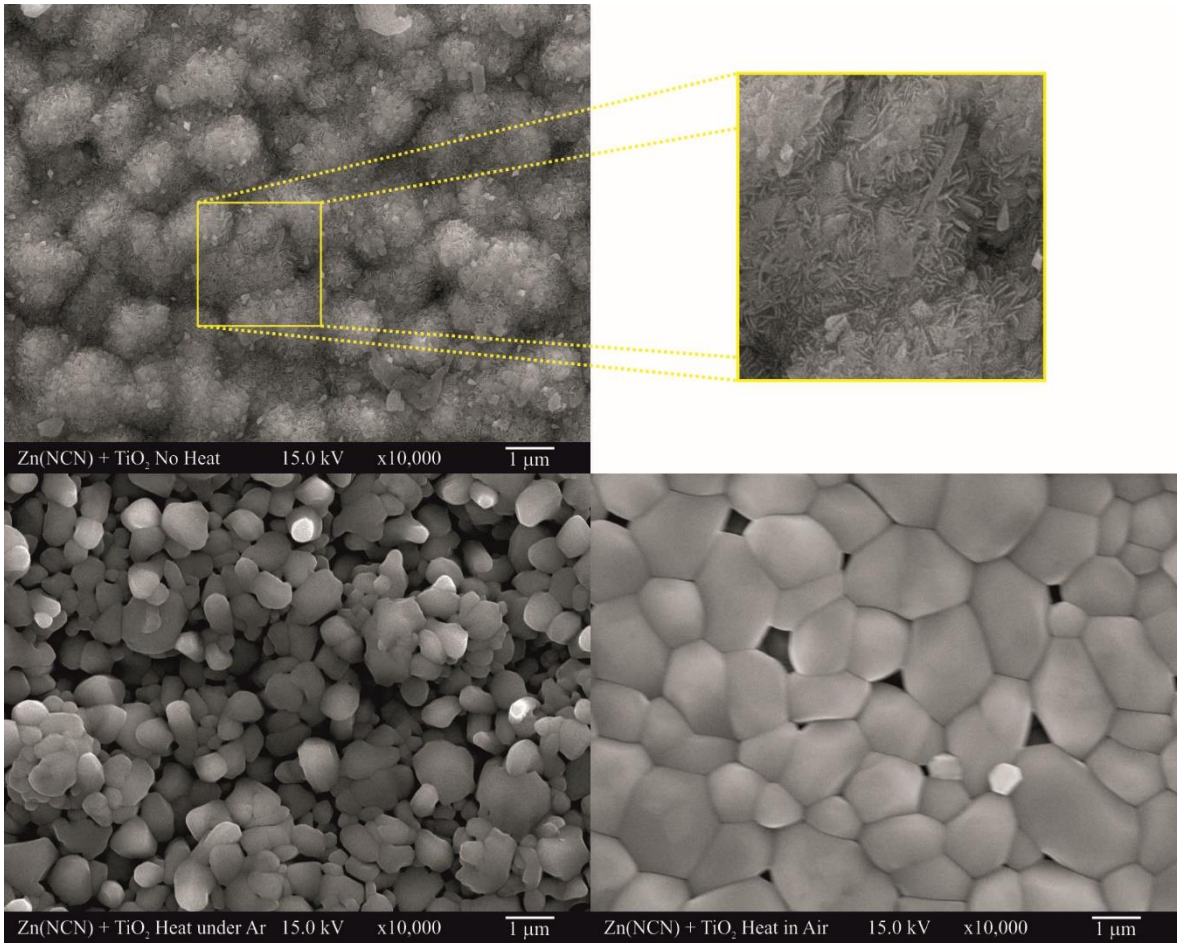

Figure 3-14 – SEM images of samples of Zn(NCN) and TiO_2 before and after heat treatment. Before heat treatment, with expansion (top), sample heated in argon (bottom left) and sample heated in air (bottom right).

Finally, the sample of just zinc carbodiimide on quartz was heated under argon inside a tube furnace using the same heating programme as shown above. Once removed the substrate was completely transparent and showed no visible signs of film presence. This is a drastic change to the translucent white coating of the zinc carbodiimide before it was heated. This sample was coated with a layer of gold (c.a. 10 nm) to provide a conductive pathway and then analysed using scanning electron microscopy. The image shows a mostly smooth surface with small islands of tubular and globular structures scattered across the substrate (Figure 3-15). Following the observations by Becker, it is possible that these islands are in fact carbon-nitrogen nanotubes; however, this cannot be confirmed due to a lack of elemental analysis. The coating of gold limits the use of EDX, this is because the heavy gold atoms present will dominate the spectrum making analysis difficult. A method for confirming this could be to repeat this process using a conductive substrate with a high

melting point; a potential candidate could be titanium. This would remove the need to coat the sample before analysing via SEM and could therefore result in EDX being a useful technique in characterising the material. However, this still may not solve the issue, due to the low density of the C-N nanotubes there could be a large degree of penetration into the substrate, causing the spectrum to be dominated by the titanium peaks.

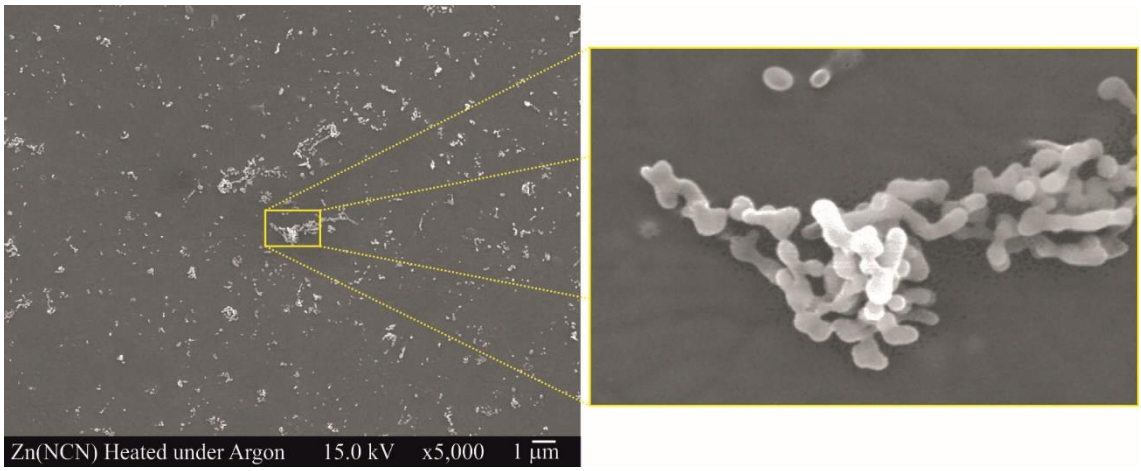

Figure 3-15 – SEM image of zinc carbodiimide heated under argon

3.5 Conclusions

The set of experiments has shown that it is possible to form thin films of zinc carbodiimide using aerosol assisted chemical vapour deposition from a precursor solution of zinc acetate and urea in methanol. The optimal set of conditions for this were to use a temperature of 450 °C, an argon flow rate of 0.84 l min^{-1} and a zinc acetate to urea ratio of 1:3. These conditions provide a thin film of zinc carbodiimide with no detectable impurities of zinc oxide, along with providing an even coating across the majority of the substrate. XRD refinement has confirmed the phase present, and has shown the presence of a small amount of lattice strain, it has also revealed that films have a surprisingly low level of preferred orientation for thin films ($1.0 < J < 1.5$). Through EDX it has been shown that the films are composed of zinc, carbon and nitrogen and the FTIR has confirmed that the carbodiimide linkage NCN is present within the structure. Together, these conclusively prove the formation of thin films of zinc carbodiimide.

The results from the treatment of zinc carbodiimide films have shown that it is possible to decompose the zinc carbodiimide thin film while it is part of a layered system. The decomposition under argon opens the possibility of using this as a method by which to remove thermally stable films from a substrate. The change in morphology between the pre-heated and post-heated samples suggests that the photocatalytic activity of the films would be an interesting property to analyse. This is particularly the case for the pre-heated layer of TiO_2 on Zn(NCN) and the sample heated under argon, the former film being composed of many plates arranged on an irregular surface and the latter being composed of a seemingly porous array of smooth crystallites.

The SEM results for the heating of zinc carbodiimide under argon suggest that it could be possible to form C-N nanotubes on top of a quartz substrate, however, further characterisation is required to definitively show that this is the case.

3.6 References

(1) Schaber, P. M.; Colson, J.; Higgins, S.; Thielen, D.; Anspach, B.; Brauer, J. *Thermochim. Acta* **2004**, *424*, 131.

(2) Ulrich, H. *Chemistry and Technology of Carbodiimides*; Wiley: Hoboken, NJ, USA, 2008.

(3) Launay, M.; Dronskowski, R. *Z. Naturforsch., B: Chem. Sci.* **2005**, *60*, 437.

(4) Krings, M.; Wessel, M.; Wilsmann, W.; Müller, P.; Dronskowski, R. *Inorg. Chem.* **2010**, *49*, 2267.

(5) Liu, X.; Müller, P.; Kroll, P.; Dronskowski, R. *Inorg. Chem.* **2002**, *41*, 4259.

(6) Liu, X.; Krott, M.; Müller, P.; Hu, C.; Lueken, H.; Dronskowski, R. *Inorg. Chem.* **2005**, *44*, 3001.

(7) Ressnig, D.; Shalom, M.; Patscheider, J.; More, R.; Evangelisti, F.; Antonietti, M.; Patzke, G. R. *J. Mater. Chem. A* **2015**, *3*, 5072.

(8) Tang, X.; Xiang, H.; Liu, X.; Speldrich, M.; Dronskowski, R. *Angew. Chem. Int. Ed.* **2010**, *49*, 4738.

(9) Bowden, F. P.; Montagu-Pollock, H. M. *Nature* **1961**, *191*, 556.

(10) Deb, S. K.; Yoffe, A. D. *Trans. Faraday Society* **1959**, *55*, 106.

(11) Riedel, R.; Greiner, A.; Miehe, G.; Dressler, W.; Fuess, H.; Bill, J.; Aldinger, F. *Angew. Chem. Int. Ed.* **1997**, *36*, 603.

(12) Bernheim, G. *Bull. Soc. Chim. Fr.* **1932**, *51*, 1388.

(13) Becker, M.; Jansen, M. *Acta Crystallogr. Sect. C: Cryst. Struct. Commun.* **2001**, *57*, 347.

(14) Hughes, Z. J.; Torgussen, O. G.; Google Patents: 1994.

(15) Morita, K.; Mera, G.; Yoshida, K.; Ikuhara, Y.; Klein, A.; Kleebe, H.-J.; Riedel, R. *Solid State Sci.* **2013**, *23*, 50.

(16) Krott, M.; Liu, X.; Fokwa, B. P. T.; Speldrich, M.; Lueken, H.; Dronskowski, R. *Inorg. Chem.* **2007**, *46*, 2204.

(17) Sokolov, N. A.; Pavlov, A. M.; Golov, V. S.; Dergunov, Y. I. *Tr. Khim. Khim. Tekhnol.* **1973**, 24.

(18) Marumo, F.; Syono, Y. *Acta Crystallogr., Sect. B: Struct. Sci., Cryst. Eng. Mater.* **1971**, *27*, 1868.

(19) Yao, S. *Salt free, oxidation-resistant zinc cyanamide anticorrosive pigments for environment-friendly mirror back coatings and preparation method thereof*; WO2010133119A1; 2010.

(20) Ota, I.; Oiwamoto, M. *Method for producing zinc cyanamide*; AN 2015:1007833; 2015.

(21) Bernard, M. A.; Chemin, A. *Compt. Rend.* **1964**, *258*, 3041.

(22) Becker, M.; Bender, H.; Jansen, M.; Kienle, L.; Assenmacher, W. *J. Phys. Chem. Solids* **2001**, *62*, 1431.

(23) Zhao, L.; Qin, X. J.; Shao, G. J.; Wang, N. *Chem. Vap. Deposition* **2012**, *18*, 256.

(24) Qin, X. J.; Zhao, L.; Shao, G. J.; Wang, N. *Thin Solid Films* **2013**, *542*, 144.

(25) Williamson, G. K.; Hall, W. H. *Acta Metall.* **1953**, *1*, 22.

(26) Wojdyr, M. *J. Appl. Crystallogr.* **2010**, *43*, 1126.

(27) Stratton, J. A.; Antennas, I.; Society, P. *Electromagnetic Theory*; Wiley, 2007.

(28) Kortüm, G. *Reflectance Spectroscopy*; 1 ed.; Springer-Verlag Berlin Heidelberg, 1969.

Chapter 4: Porous Titania Films

4.1 Introduction

Titanium dioxide (titania) exists naturally in four phases, the tetragonal anatase phase with the space group $I4_1/amd$,[1] the also tetragonal phase rutile with the space group $P4_2/mnm$ (Figure 4-1),[2] orthorhombic brookite with the space group *Pbca*[3] and finally as the monoclinic TiO_2 with the space group $C2/m$.[2] The most common phases are anatase and rutile.

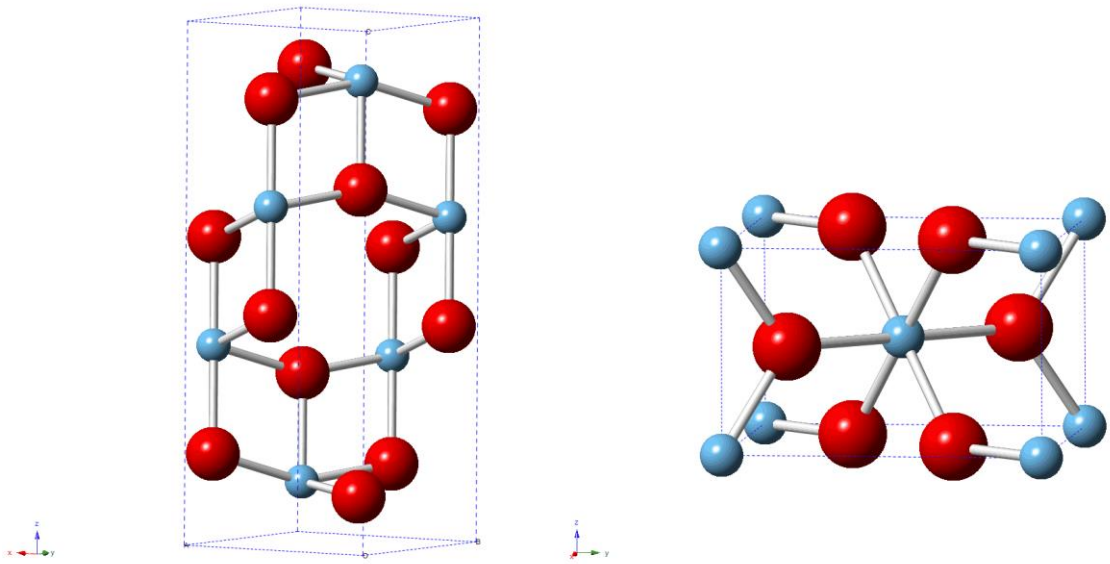

Figure 4-1 – Crystal structures of two common phases of TiO_2. Anatase (left) and rutile (right).

Titanium dioxide is an effective photocatalyst with a band gap of 3.02 eV.[4-7] It is implemented as a self-cleaning coating for windows,[8,9] for instance, in the commercially available Activ™ range of self-cleaning glass from Pilkington. When titanium dioxide is irradiated using ultra-violet light ($\lambda \leq 388$ nm) an electron is promoted from the valence band to the conduction band, resulting in the formation of a hole in the valence band. Once this occurs, recombination of the electron and hole often follows, however, it is possible for both species to migrate to the surface of the material. Once at the surface the electron can reduce an electron acceptor, for example atmospheric oxygen, in this case forming the superoxide O_2^-. This can be further reduced to H_2O. The holes on the other hand can oxidise ^-OH groups which are adsorbed to the surface, this results in the formation of the hydroxyl radical $^\bullet OH$ which can then oxidise a range of organic molecules to simple molecules such as CO_2 and H_2O.[10,11] These can remove surface grease and other organic contaminants. Another application of titanium dioxide includes the use as a gas sensor, for instance, in the detection of ethanol and methanol.[12] TiO_2 also shows promise as a protective layer in AC plasma display panels[13] and the photocatalytic decomposition of gas phase organic pollutants.[14]

Thin films of titania have been studied extensively by many different groups using a variety of different techniques, for instance, in 2013, Gupta *et al* reported the e-beam physical vapour deposition of crystalline TiO_2 thin films in the rutile phase.[15] RF magnetron sputtering has also been implemented in the formation of thin films of titania such as the deposition of TiO_2 on indium tin oxide coated glass from titanium in an Ar/O_2 atmosphere carried out by Sung and Kim.[16] Chemical vapour deposition has also been employed to synthesise thin films of TiO_2, an example of which was demonstrated by Yang and Wolden who used titanium isopropoxide in the presence of oxygen during plasma-enhanced chemical vapour deposition to form amorphous thin films of TiO_2.[17] In 2010, Hyett *et al* reported the synthesis of thin films of TiO_2 onto glass and titanium substrates through the use of APCVD from $TiCl_4$ and ethyl acetate at 660 °C as part of an investigation into the effects of film thickness on photocatalytic activity of titania films.[7] Aerosol assisted CVD has also been used previously to deposit thin films of TiO_2, for instance, in 2014 Lim *et al* reported the synthesis of thin films of TiO_2 on ITO substrates using a solution of TTiP in methanol.[18]

As is outlined above, the photocatalytic decomposition of organic molecules occurs at the surface of the titania, as a result of this it is preferable to increase the surface area of the material. One method of achieving this is to introduce porosity into the TiO_2. For example, in 1999, Saadoun *et al* synthesised a high surface area powder of TiO_2 via the hydrolysis of 1,2-diolate titanium compounds under microwave radiation.[19] One method used to synthesise a porous thin film of titanium dioxide is demonstrated by Huang *et al* who used polyethylene glycol as a templating reagent to synthesise porous TiO_2 films using sol-gel process from a mixture of titanium (IV) butoxide, deionised water, acetylacetone and HCl with ethanol as the solvent.[20] In 1999, Huang *et al* reported the deposition of titania onto a porous ceramic substrate using atmospheric pressure CVD utilising titanium (IV) isopropoxide as a precursor.[21] They discovered that at a temperature of 300 °C, they were achieving pore sizes of c.a. 64 nm with good adhesion between the titania and the ceramic substrate. A similar technique was used by Lei *et al* to deposit thin films of TiO_2 onto porous alumina.[22] The alumina was crushed into small particles c.a. 1 mm in diameter and have pore sizes ranging from 6-3000 nm. This was used under reduced pressure in MOCVD using TTiP as the precursor. The calculated surface area of the resulting material was found to be 165 $m^2 g^{-1}$, a 12% reduction on the initial alumina. This is much higher than the surface area of commercial Degussa P25 TiO_2 powder (40-60 $m^2 g^{-1}$). During testing they found that the synthesised material had a lower activity as a photocatalyst than the Degussa P25 powder, however, due to the granular nature of the alumina, it can easily be recovered from the mixture by filtration and then recycled.

In 2006, Toberer *et al* reported the synthesis of hierarchically porous titania via the leaching of zinc out of zinc titanate phases.[23] This was achieved by mixing TiO_2 and ZnO and forming a pellet. This was then heated in a crucible to 1200 °C for 12 hours in a Zn rich atmosphere, maintained by the presence of powdered ZnO within the crucible. The resulting material consisted

of Zn_2TiO_4 and ZnO. The excess ZnO was removed by immersing the pellet in a dilute acid solution to dissolve the wurtzite-structured ZnO. The now macroporous pellet was then heated to 800 °C under a flow of H_2 (5% in N_2). During this process zinc is reduced to its elemental state and carried as a vapour where it is deposited on the walls of the furnace once it is outside the hot-zone. The resulting pellet was composed of highly crystalline rutile titania which exhibited hierarchical porosity.

Zinc titanate, in particular Zn_2TiO_4 has been shown to be a useful material for low-temperature sintering dielectrics. Other applications of zinc titanate involve being used as a regenerable catalyst and a good sorbent for the removal of sulphur containing compounds at high temperatures.[24]

Following on from the work by Toberer *et al*, the main aim of this chapter is to produce a thin film of hierarchically porous titanium dioxide. The first step of this project is to synthesis a thin film with a mixture of zinc oxide and mixed Zn and Ti phases such as zinc titanate (Zn_2TiO_4). This film will then be separated into 4 sections. Each section will then be treated differently. The first section will be left untreated to serve as a reference. The second section will be treated by being soaked in a dilute HCl solution. The third section will be heated under an atmosphere of H_2 (5% in N_2). The final section will be subjected to both treatments, first the acid washing, followed by the hydrogen reduction to leach the remaining zinc out of the system.

4.2 Initial Formation of Mixed Phase

Prelimary work for this chapter was carried out by Nathanya Platt, a project student under my supervision. The work carried out by Nathanya is described in chapters 4.2-4.4.

4.2.1 Initial Exploration of Molar Ratio between Precursors

Depositions were carried out following the procedure outlined above (see Experimental, page 8) inside the tube furnace at 450 °C using an argon flow rate of 0.8 l min^{-1}. A solution of titanium isopropoxide (TTiP) and zinc acetate (ZnAc) in methanol (40 cm^3) was used for each deposition. The quantities of each precursor used are outlined below (Table 4-1). Deposition of all initial films was carried out on float glass.

Table 4-1 – Table outlining the molar ratios of zinc acetate and titanium isopropoxide used in the initial film formation

Zn:Ti Molar Ratio	ZnAc / mmol	TTiP / mmol
1:1	1.13	1.13
1.5:1	0.785	0.524
2:1	0.87	0.43
3:1	1.39	0.46
4:1	1.84	0.46
5:1	2.3	0.46

The films were analysed by collecting X-ray diffraction data using a Rigaku Smartlab diffractometer and the results are shown in the following table (Table 4-2). X-ray data was collected from two spots on each sample, the first was c.a. 6 cm away from the leading edge of the substrate, labelled front, and the second was c.a. 12 cm from the leading edge, labelled back.

Table 4-2 – Table summarising the X-ray diffraction data. Black spots represent the primary phase present at that point on the substrate. The blue squares represent the secondary phase, if present.

Ratio	ZnO		Zn_2TiO_4		$ZnTiO_3$		Pseudo Brookite		TiO_2	
	Front	Back	Front	Back	Front	Back	Front	Back	Front	Back
1:1				●			●			
1.5:1	●		■			■				●
2:1			●	●						
3:1		●	■	■	●					
4:1		●	●	■						
5:1	●	●	■							

As the table shows, as more zinc acetate is introduced into the reaction mixture, the more ZnO is present in the film produced, up to 5:1 where it is the dominant phase across the entire substrate,

with only a small amount of zinc titanate (Zn_2TiO_4) present. Using a ratio of 1:1 resulted in a film with a visible blue colour and a zinc titanate compound with a diffraction pattern which did not match any previously reported patterns. Further investigation into this compound was carried out (see Further Analysis of Psuedo-Brookite). The film formed using a 2:1 ratio appears to be the most consistent, with the sample being composed of Zn_2TiO_4 across the entire substrate. The X-ray diffraction pattern for this sample is shown below (Figure 4-2).

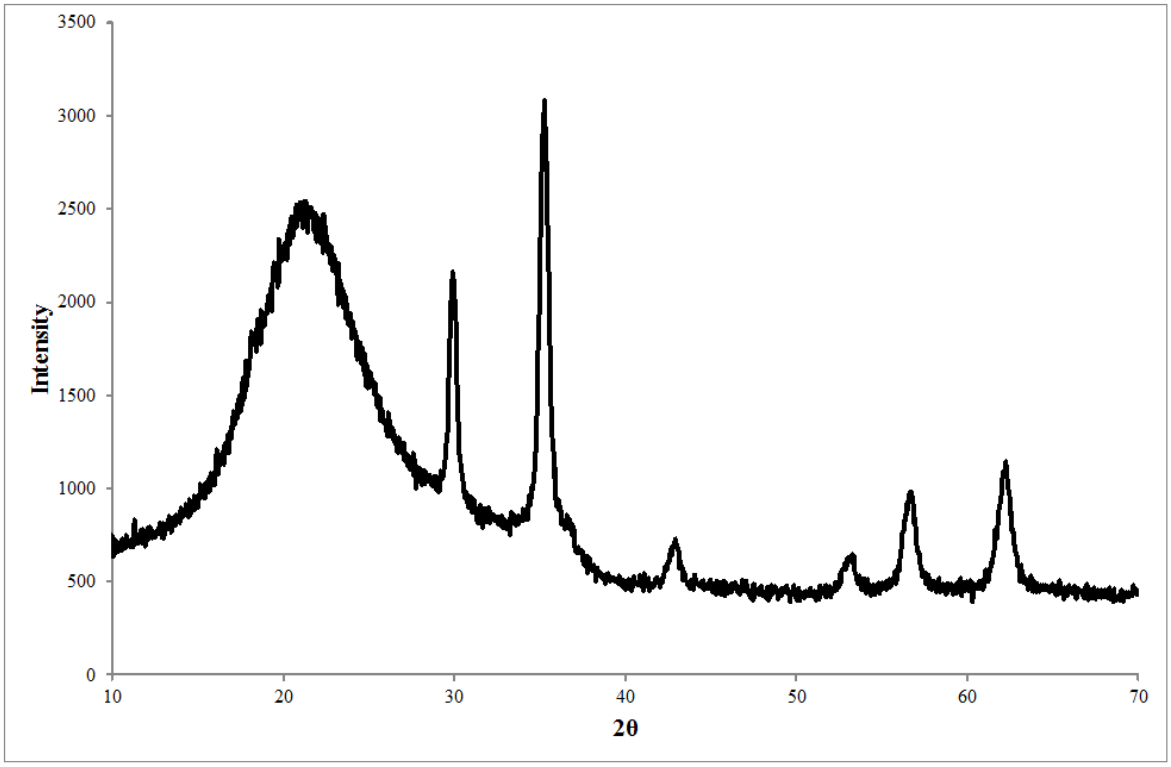

Figure 4-2 – X-ray diffraction pattern of film formed with a 2:1 Zn:Ti ratio

The sample formed from a solution of 2:1 ZnAc:TTiP was chosen for reduction testing to remove the zinc in an attempt to leave hierarchically porous titania (see Removal of Zinc Phases).

4.2.2 Further Analysis of Psuedo-Brookite

The results obtained from the 1:1 sample were particularly interesting. The surface of the film was visibly divided into 4 sections, differentiated by a change in colour; this is shown in the diagram below (Figure 4-3).

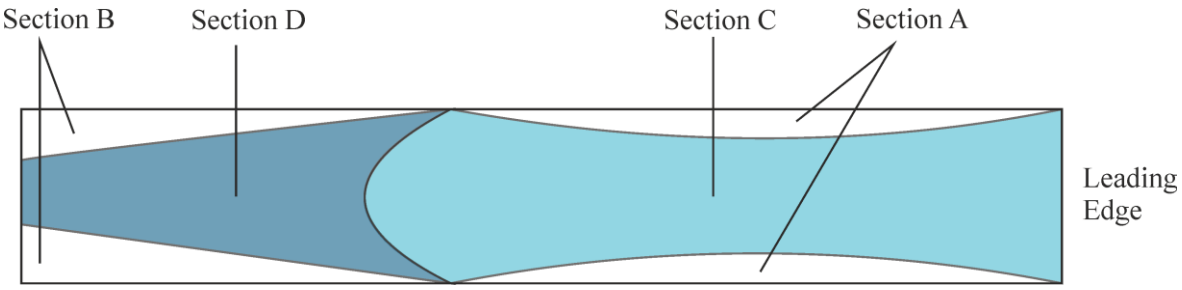

Figure 4-3 – Diagram of colour change in film formed from a ratio of 1:1 of ZnAc:TTiP

Section A corresponds to the side section of the substrate. X-ray diffraction revealed the phase to be predominantly TiO_2 (rutile) with a small amount of TiO_2 (anatase). The peak intensity of this section is low; this is most likely a result of less deposition occurring along the outside edge of the substrate.

Section B was characterised by the lack of colour and increased transparency when compared to the rest of the substrate. X-ray diffraction shows that the section is predominantly composed of Zn_2TiO_4.

Sections C and D are more crystalline than A and B. X-ray diffraction shows the dominant phase to be pseudo-brookite phase with the space group *CmCm*. The pattern was very similar to $FeTi_2O_5$, another pseudo-brookite phase,[25] using this as the reference it was possible to refine the obtained pseudo-brookite (Figure 4-4). The lattice parameters were a = 3.721(4), b = 9.763(6) and c = 10.058(9). The sample was analysed using X-ray photoelectron spectroscopy (XPS) by Dr Robert Palgrave at University College London. The results show that the composition of the phase is $Zn_{0.66}Ti_{2.33}O_5$, a zinc-doped phase. This is of potential interest as a zinc-doped pseudo-brookite has not been reported as a thin film elsewhere in the literature. Recent work has been published by Perry *et al* in which they outline the bulk phase synthesis of ternary pseudo-brookite with the formula $Zn_xTi_{3-x}O_{5-\delta}$ where x = 0.6.[26] The sample was analysed using UV-Vis-NIR spectrometry (Figure 4-5), upon processing using the Tauc method, it was discovered that the material had a band gap of 3.9 eV.

Further characterisation of this phase is ongoing within the group.

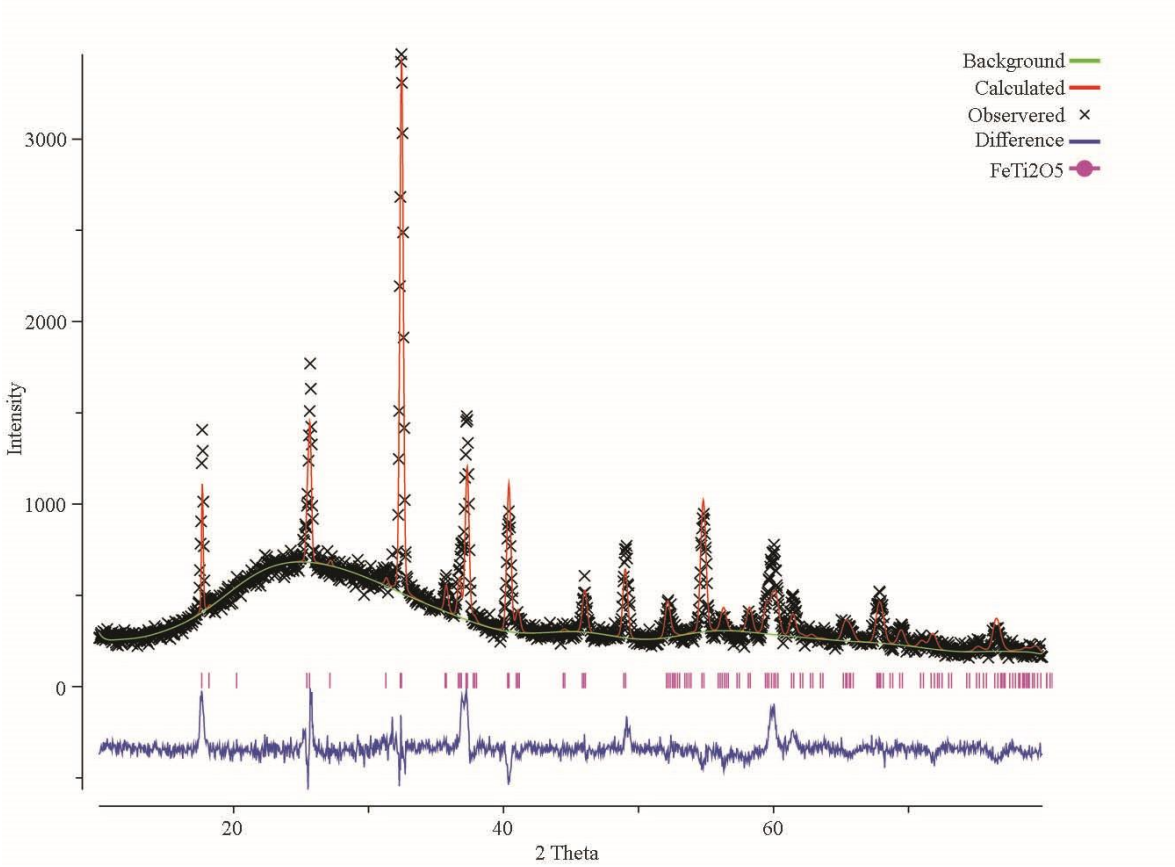

Figure 4-4 – Powder X-ray diffraction pattern for section D of the Zn:Ti ratio of 1:1

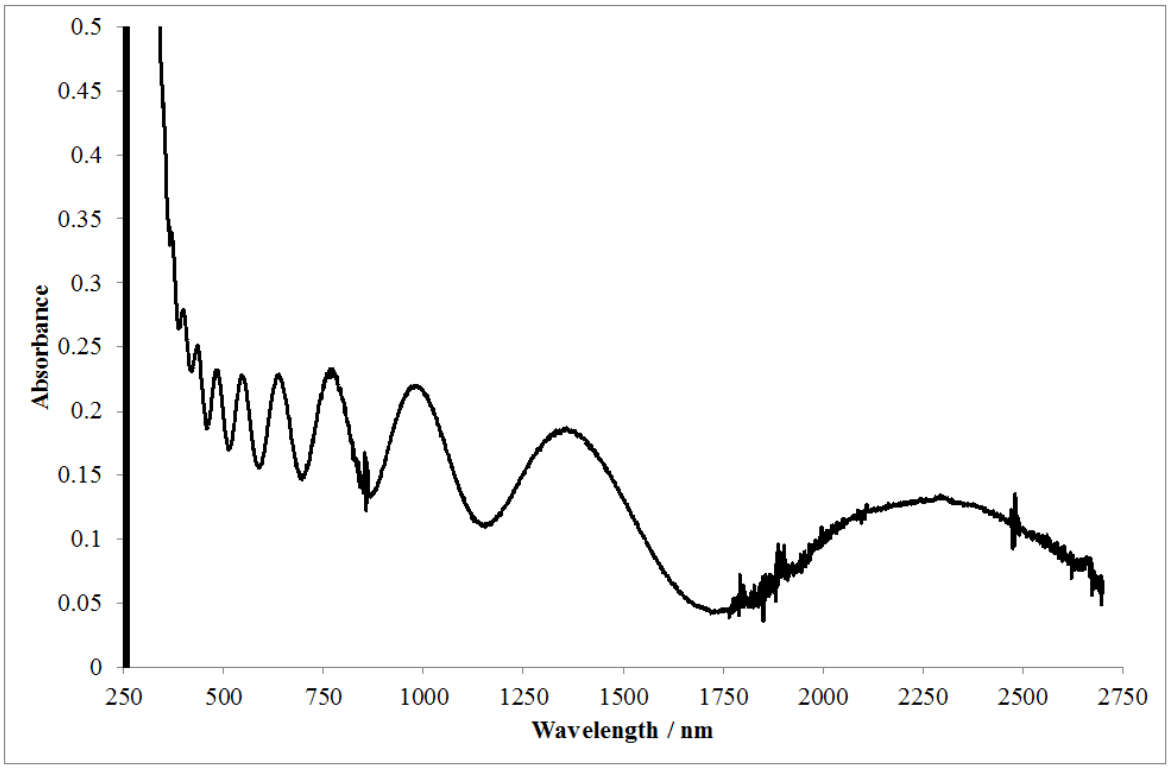

Figure 4-5 – UV-Vis-NIR spectrum of pseudo-brookite

4.3 Removal of Zinc Phases

Samples chosen for acid washing and hydrogen reduction were cut into four equal sizes. These samples are labelled A-D and are treated as follows.

A – No treatment, this sample was chosen to remain as the reference

B – The sample was allowed to soak for 1 hour in an aqueous HCl solution. The concentration of the acid solution is outlined for each sample. This step removes wurtzite ZnO from the sample by dissolution into the acid.

C – The sample was reduced in an atmosphere of H_2 (5% in N_2) at a temperature of 752 °C for 2 hours. This step further leaches the Zn present within zinc titanate compounds by reducing the zinc to its elemental state, volatising it and transporting it away from the hot zone of the reactor.

D – The sample was first soaked in the aqueous acid solution for 1 hour and then reduced in an atmosphere of H_2 (5% in N_2) at 752 °C for 2 hours.

4.4 Initial Reduction of Zinc Titanate Film

Due to the low melting point of float glass (c.a. 600 °C) the sample formed from the ratio of 2:1 ZnAc:TTiP was remade on quartz using the same conditions outlined above (see Initial Formation of Mixed Phase). The resulting sample was then cut into 4 equal sized pieces (c.a. 2 x 2.5 cm^2) and treated following the procedure outlined above (see Removal of Zinc Phases, page 118) using an aqueous HCl solution of concentration 2.0 mol dm^{-3}.

Upon treatment, X-ray diffraction patterns of the four samples were collected using a Rigaku Smartlab diffractometer. The data was processed using GSAS with refinement focusing on peak shape using a Gaussian profile, peak position as part of sample height alignment, lattice parameters and the preferred orientation as part of a spherical harmonic function. The patterns are shown below (Figure 4-6).

Once sample B had been removed from the acid solution, there was visible 'damage' to the film, it was apparent that the films along the edges of the substrate had been removed. It was decided that the acid solution was too concentrated and so subsequent reactions would employ a more dilute HCl solution. This reduction in film is supported by the lower intensity present in the sample treated with acid (Sample B) as opposed to the untreated sample (Sample A). The sample which had undergone the hydrogen reduction (Sample C) has been entirely converted to TiO_2 (anatase) with no visible signs of zinc containing species present within the X-ray diffraction pattern. Finally, the sample which had undergone both the acid washing and the hydrogen reduction (Sample D) showed no definitive evidence of crystalline species suggesting that the thin film had been completely removed from the substrate by a combination of the harsh acidic conditions and the hydrogen reduction. There is however, a small feature present in the pattern at approximately $2\theta = 25$, this could be a peak caused by the presence of a small quantity of TiO_2 in the anatase phase, however, due to the low intensity and the absence of any other peaks, this cannot be confirmed.

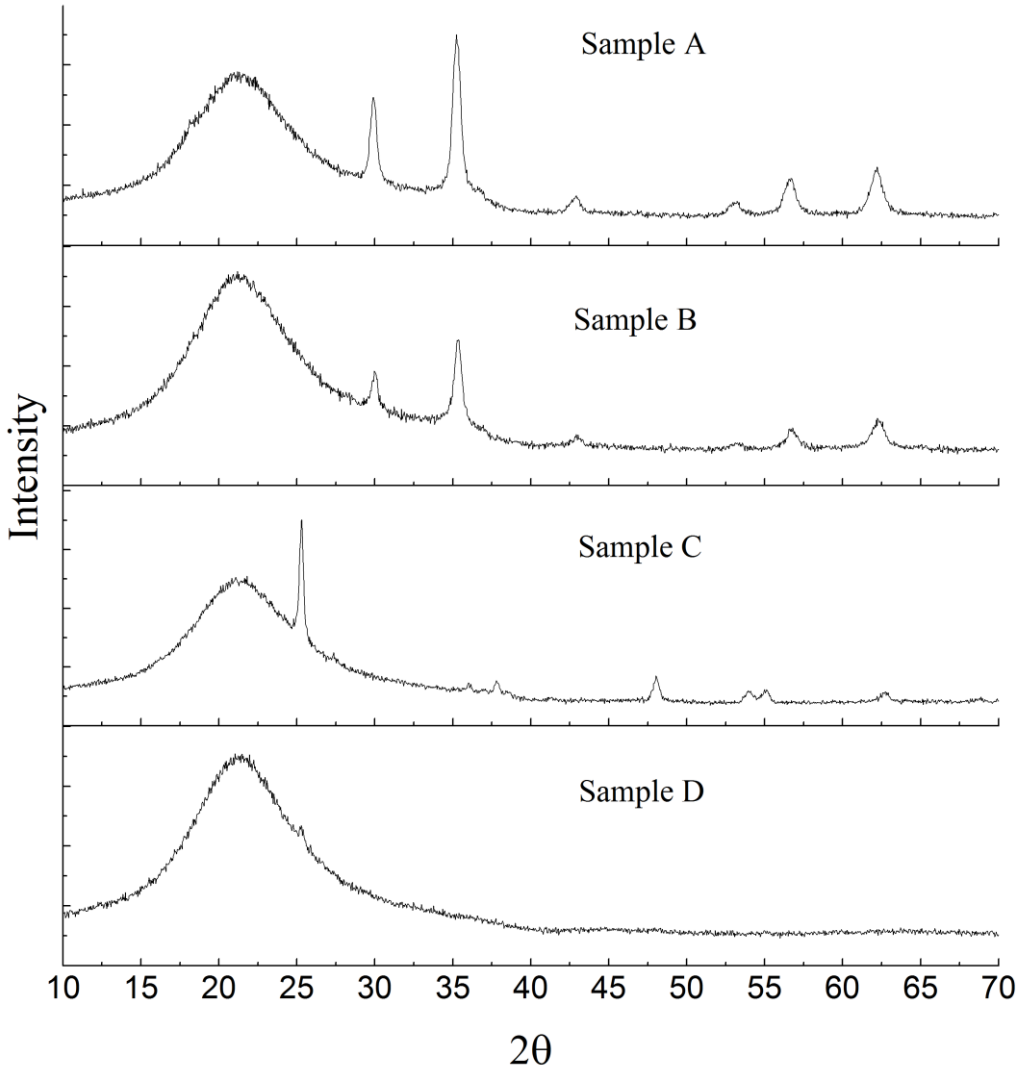

Figure 4-6 – X-ray diffraction patterns of the four sections of the sample synthesised from 2:1 mixture of ZnAc:TTiP after each treatment. A – no treatment, B – after acid treatment, C – after hydrogen reduction and D – after acid treatment and hydrogen reduction.

The samples were analysed using scanning electron microscopy to determine how the treatment affected the surface morphology (Figure 4-7). The sample of solely Zn_2TiO_4 which has not been treated (Sample A) shows rounded crystalline powders forming elongated clusters. These clusters are evenly distributed and appear to be randomly orientated across the surface. The sample which has been treated in the aqueous acid bath (Sample B) appears to have changed slightly. The top of the sample appears to be smoother, with the crystallites appearing to be flatter. Sample C, which has been reduced in a hydrogen containing environment shows potential porosity. The surface is composed of small crystallites (< 10 nm) arranged in small islands separated by fissures within the surface. These fissures potentially provide the material with porosity and could therefore increase the surface area of the resulting titania film. The fissures are likely caused by the liberation of zinc vapour. Finally, the sample which has been treated by both acid washing and reduction (Sample D) shows a layered film. The bottom layer appears to be composed of small crystallites (< 10 nm)

arranged uniformly across the surface. The top layer is similar in composition to that of Sample C. It is composed of small crystallites arranged in tight clusters, separated by fissures in the surface. These could potentially increase the porosity and therefore the surface area of the film.

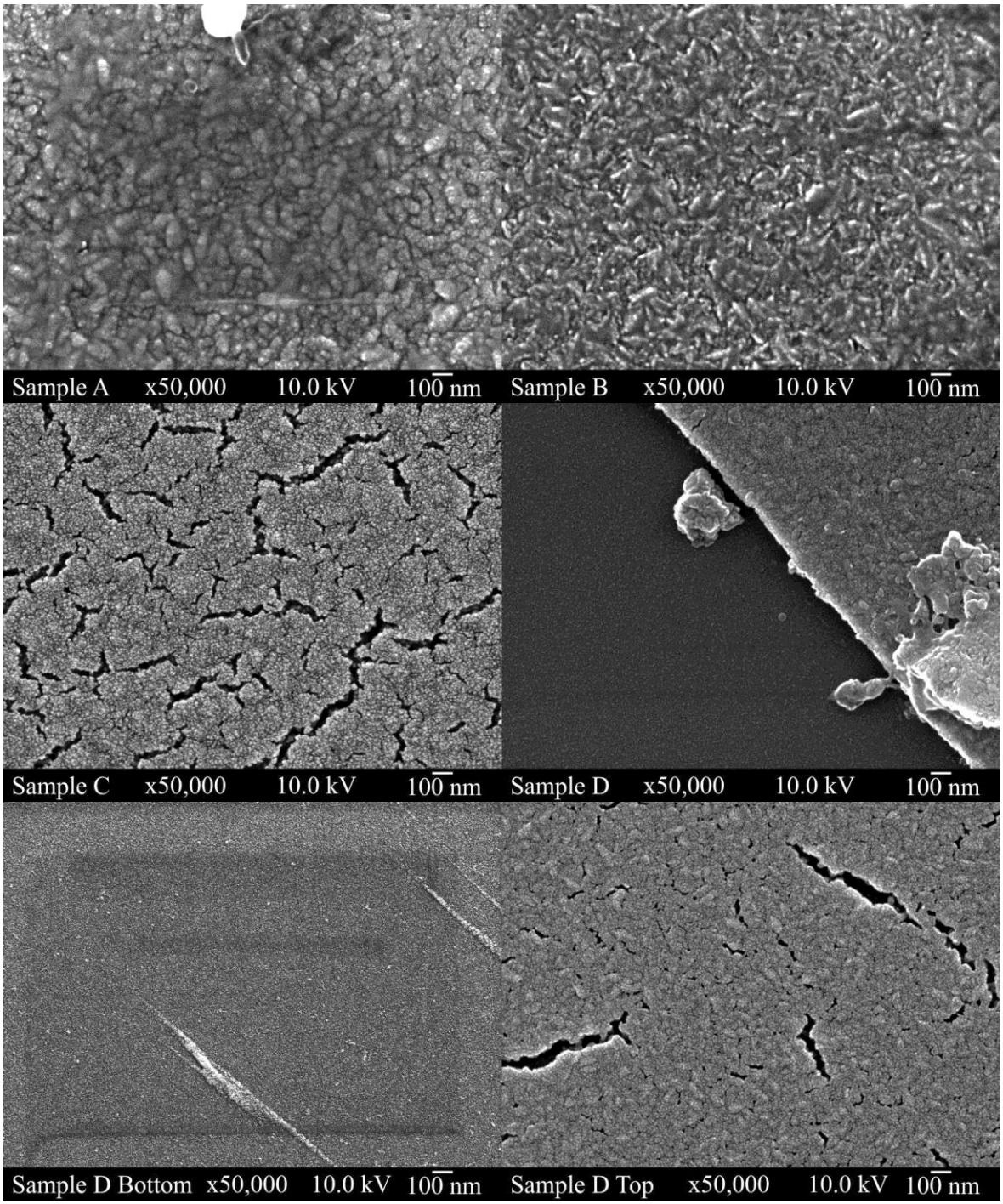

Figure 4-7 – SEM images of the 2:1 ZnAc:TTiP samples after treatment. A – no treatment (top left), B – soaked in dilute acid (top right), C – hydrogen reduced (middle left), D – both acid washed and hydrogen reduced (middle right). Bottom layer of sample D (bottom left), top layer of sample D (bottom right).

4.5 Further Investigation into the Ratios of Zinc and Titanium Precursors in the Formation of Thin Films of Zinc Titanate

Further depositions were carried out in an attempt to refine the synthesis of thin films of zinc titanate which could then be treated to remove zinc, leaving solely titanium dioxide which could potentially be hierarchically porous. Depositions were carried out following the method outlined above (see Experimental, page 8) using the tube furnace at a temperature of 450 °C, using an argon flow rate of 0.5 l min^{-1}. These samples were formed onto float glass (15 x 2.5 cm^2). Some samples were coated with a layer of titanium dioxide prior to introduction of the zinc titanate precursor solution. This base layer was deposited from a solution of titanium isopropoxide (0.25 g / 0.916 mmol) in ethanol (10 cm^3) at a temperature of 450 °C and an argon flow rate of 0.5 l min^{-1}. Each precursor solution was composed of TTiP (0.25 cm^3 / 0.916 mmol) in methanol (40 cm^3) with varying quantities of zinc acetate; this is outlined in the table below (Table 4-3)

Table 4-3 – Quantity of zinc acetate used in each film formed in the further investigation into zinc titanate formation

Sample	Base Layer	Zinc Acetate / g	Zinc Acetate / mmol
1B	Yes	0.1936	1.055
1N	No	0.1936	1.055
2B	Yes	0.17	0.926
2N	No	0.17	0.926
3B	Yes	0.15	0.817
3N	No	0.15	0.817

X-ray diffraction data for each sample was collected at varying positions across the surface of the substrate, taking the leading edge to be point 0 mm. The data collected was refined using the GSAS software, focusing on the peak shape using a Gaussian profile, peak position related to sample height, lattice parameters, preferred orientation as part of a Spherical Harmonic function and finally, the phase fractions to obtain weight fractions of the phases present. The results for the refinement are outlined in the table below (Table 4-4).

Table 4-4 – Summary of the X-ray diffraction results obtained for the zinc titanate synthesis

Run	Position /mm	Phase 1	wt %	Phase 2	wt %	Phase 3	wt %
1B	15	Zn_2TiO_4 (Cubic)	39	Anatase	14	ZnO	47
	55	Zn_2TiO_4 (Cubic)	55	Anatase	35	$ZnTiO_3$	10
	100	Anatase	67	Rutile	33		
1N	10	Zn_2TiO_4 (Cubic)	56	Zn_2TiO_4 (Tetra)	27	$ZnTiO_3$	17
	70	Rutile	21	$ZnTiO_3$	79		
2B	50	Anatase	69	Rutile	31		
2N	30	Zn_2TiO_4 (Cubic)	85	Zn_2TiO_4 (Tetra)	15		
	90	Rutile	100				
3B	60	Anatase	67	Rutile	33		
3N	30	Zn_2TiO_4 (Cubic)	65	Zn_2TiO_4 (Tetra)	35		
	70	Rutile	100				

To form hierarchically porous films of titanium dioxide, it was decided that a film with a mixture of ZnO, TiO_2 and zinc titanate phases would be ideal. Using this criteria, the films formed using 0.1936 g of ZnO were remade on quartz substrates so that they could be reduced at 752 °C. These films were synthesised following the procedure outlined above (see Experimental, page 8) at a temperature of 450 °C using the tube furnace and an argon flow rate of 0.5 l min^{-1}. Three small squares of quartz (2.5 x 2.5 cm^2) were positioned on a steel block (2.5 x 15 cm^3) at 0 mm, 45 mm and 95 mm on the substrate in relation to the leading edge for each deposition. Two depositions were carried out, one of which was carried out with an initial base layer of TiO_2 deposited from TTiP (0.25 cm^3) in ethanol (10 cm^3) using the above conditions. The precursor solution used for each deposition was ZnAc (0.1936 g / 1.055 mmol) and TTiP (0.25 cm^3 / 0.916 mmol). The two depositions are labelled as follows:

QB – Sample formed on quartz with a base layer of TiO_2

QN – Sample formed directly onto the quartz substrate

X-ray diffraction data was collected on a Rigaku Smartlab diffractometer. Due to peak broadness within the samples, full refinement was not possible. However, the quartz sample QN at 45 mm (referred to as QN45) shows evidence of the presence of titanium dioxide as well as mixed phases of zinc titanate, therefore this sample was chosen as the principle sample to undergo acid treatment and hydrogen reduction.

4.6 Reduction of Zinc Titanate Films

Three samples were chosen as candidates for acid treatment and hydrogen reduction, these samples were 1B (2 x 2 cm^2 section taken from position 50 mm away from leading edge of substrate), 1N (2 x 2 cm^2 section taken from leading edge of substrate) and QN45. Each of these samples was cut into 4 equal squares and given the additional letters A-D. The samples on quartz are treated according to the procedures outlined above (see Removal of Zinc Phases, page 118). Due to the lower melting point of the float glass the samples deposited on this substrate are reduced under H_2 (5% in N_2) at the lower temperature of 600 °C. The concentration of the HCl solution used was 0.1 mol dm^{-3}.

After treatment, X-ray diffraction patterns were collected of each sample. The patterns were refined using GSAS with the main focus being on the phase fractions so as to obtain weight fractions of each phase present within the samples. Other parameters which were refined were the peak shape as part of a Gaussian function; peak position caused by sample height alignment, lattice parameters, and preferred orientation as part of a Spherical Harmonic function. The weight fractions of the phases present are summarised in the table below along with goodness of fit index χ^2.

Table 4-5 – Table outlining the weight fractions of phases present in the samples after different steps of treatment

		Zn_2TiO_4 (Cubic)	Zn_2TiO_4 (Tetragonal)	TiO_2 (Anatase)	TiO_2 (Rutile)	Zinc Oxide	$ZnTiO_3$	$Zn_2Ti_3O_8$	χ^2
QN45	**A**				23.4%		9.2%	67.3%	1.5
	B							100.0%	1.7
	C			66.4%	33.6%				1.1
	D			66.8%	33.2%				1.2
1N	**A**	69.2%		17.8%		13.0%			1.2
	B	85.3%		14.7%					1.3
	C			100.0%					1.1
	D			100.0%					1.1
1B	**A**	4.6%	23.2%	63.2%			9.0%		1.4
	B	25.7%	20.6%	34.4%			19.3%		1.3
	C			35.9%	26.3%			37.8%	1.8
	D			44.5%	10.1%			45.4%	1.5

An exemplar set of X-ray diffraction patterns are shown below (). As the X-ray data shows, for the sample on quartz (QN45) and the float glass sample with no base layer of TiO_2 (1B) all of the zinc species present within the film are removed during the hydrogen reduction to leave behind films composed entirely of titanium dioxide, most of which is anatase. Upon treatment with acid, sample 1B shows that all of the zinc oxide present in the sample previously has been removed, however, this is mitigated by a relative increase in weight fraction of Zn_2TiO_4. However, this could be an

artefact of the overlap between peaks of Zn_2TiO_4 and TiO_2 rather than being a significant result. There is still some zinc titanate present in sample 1B after hydrogen reduction, the reason for this is unclear, however, there has been some conversion of phases as well as an overall relative increase in weight fraction of TiO_2, suggesting that the zinc is being removed in this sample, it is just occurring at a slower rate than is observed in the other samples. The cause of this is unclear; however, there could be some stabilising effect from the base layer of titanium dioxide.

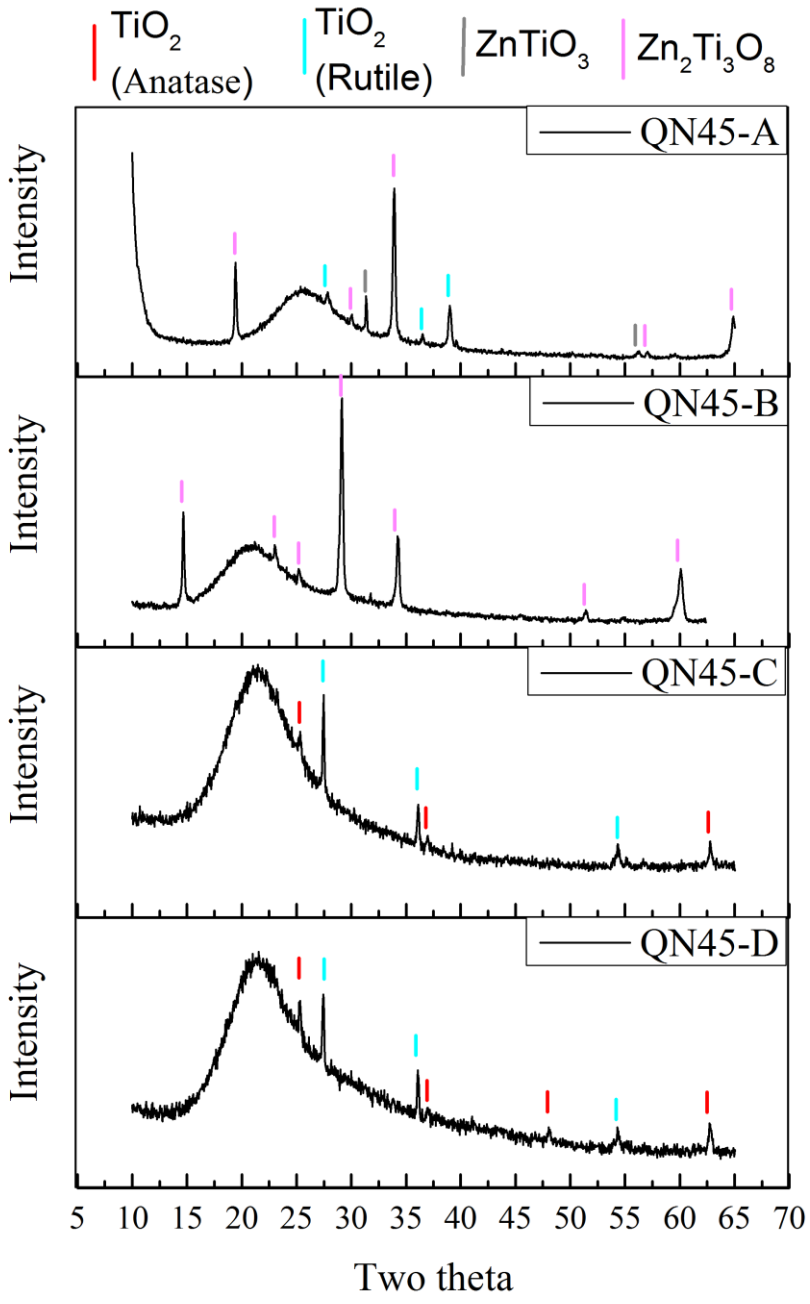

Figure 4-8 – Exemplar set of X-ray diffraction patterns for a sequence of zinc titanate reductions. Data shown represents sample QN45 with phase peaks identified with tick marks.

4.6.1 Photocatalytic Testing of Reduced Films

To test the photocatalytic activity of the films, a Rank Brothers oxygen electrode was set up as shown in the diagram below (Figure 4-9). The apparatus consists of a 50 mm diameter glass chamber with a water cooled jacket. At the base of the chamber is a Clark cell, this is composed of a platinum electrode and a silver/silver chloride reference counter electrode. This cell is separated from the bulk reaction solution by a gas permeable, ion impermeable membrane so as to only allow dissolved O_2 to pass through to the electrode. The water jacket was connected to the water mains and held the system at a constant temperature of 12.5 °C. Before the UV-lamp (6 W, 356 nm) was switched on, the electrolyte solution was degassed by bubbling argon through the solution for c.a. 30 min. The electrolyte solution used is outlined below and the solvent used was deionised water. Plots of the voltage vs time were made. Due to the direct correlation between measured voltage and dissolved oxygen, the gradient of these plots is representative of the rate of oxygen formation in the system.

NaOH – 0.1mol dm^{-3}
$Na_2S_2O_8$ – 0.01 mol dm^{-3}

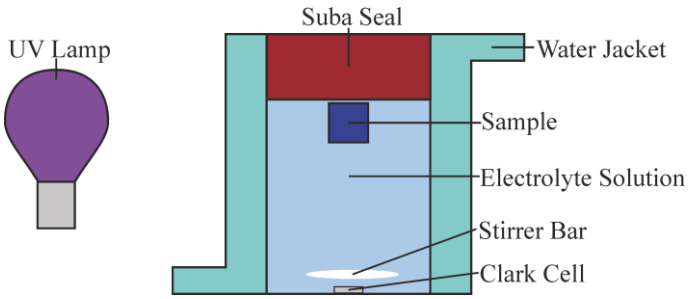

Figure 4-9 – Diagram showing the setup of the oxygen electrode

The samples which were analysed were QN45-D and 1N-D, each sample was a square of 1 cm^2. A 4 cm^2 sample of a thin film of TiO_2 was also used to act as a comparison. The reference sample of TiO_2 was synthesised using the method outlined above (see Experimental, page 8) at 450 °C with an argon flow rate of 0.5 l min^{-1} and a precursor solution of TTiP (0.25 cm^3 / 0.916 mmol) in ethanol (10 cm^3). A final reference of Degussa P25 powder (20 mg) was analysed using the system.

The sample of 1N-D and the reference TiO_2 exhibited negative gradients; this suggests that the rate of oxygen consumption at the electrode is greater than the rate of oxygen formation via water splitting on the sample. Once the reference sample of TiO_2 was removed from the chamber, it was noted that a small amount of delamination of the film was occurring around the edges of the substrate. This is likely a result of the caustic nature of the solution and therefore steps were taken to limit the exposure time of the future samples to the solution. Plots generated for QN45-D and the Degussa P25 powder exhibited positive gradients (Figure 4-10), therefore the rate of oxygen generation can be calculated.

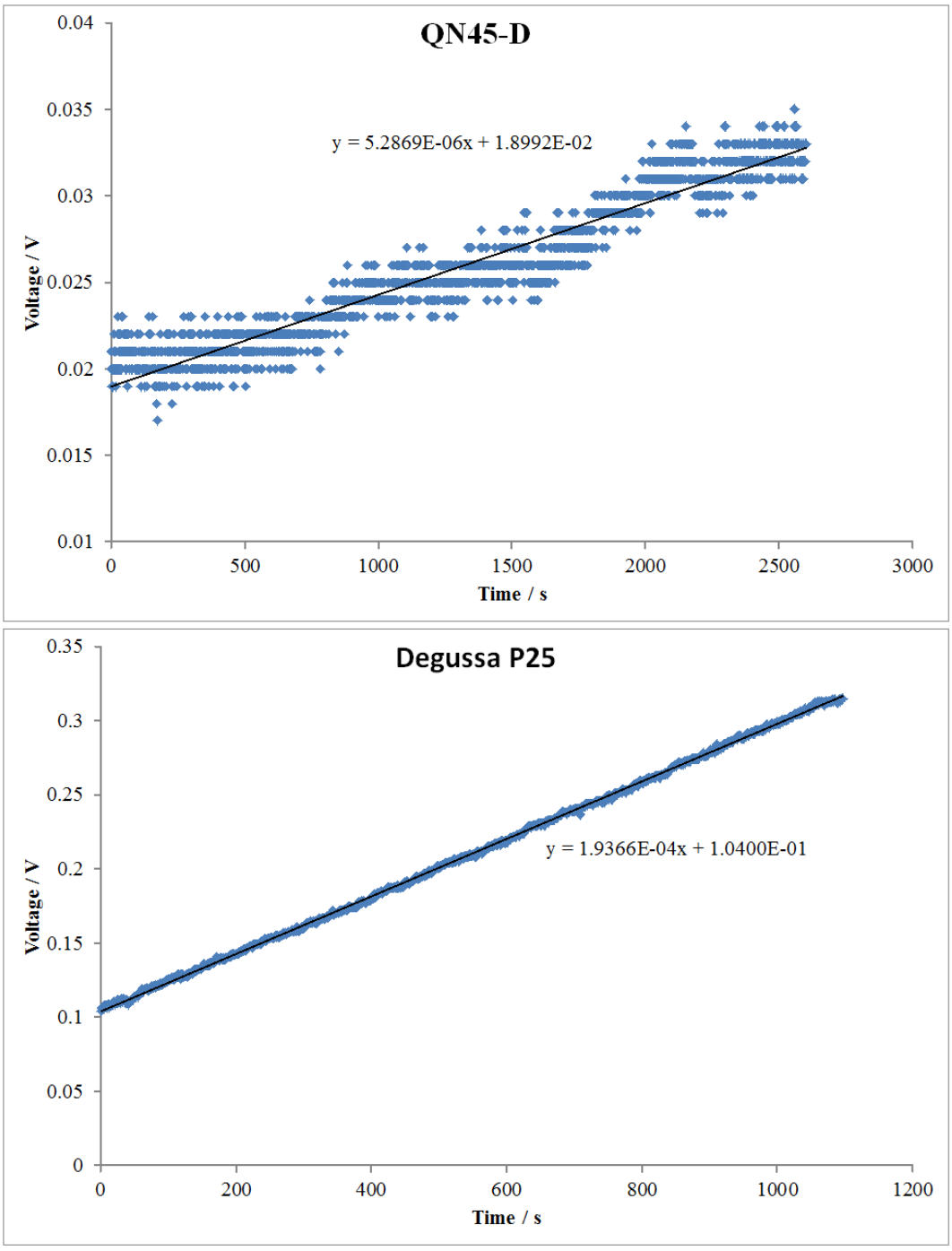

Figure 4-10 – Plots of voltage vs time using Rank Brothers oxygen electrode. QN45-D (top) and Degussa P25 powder (bottom).

The concentration of oxygen in water in equilibrium with air at 12.5 °C is 334.9 μmol dm^{-3}; this corresponds to a voltage of 1.284 V. This can be used to calculate the rate of oxygen formation. The results are shown below:

QN45-D – 4.137×10^{-5} mol min^{-1} m^{-2}
Degussa P25 powder – 0.126 μmol $s^{-1} g^{-1}$

The results show that the reduced titania film QN45-D outperforms the reference sample of a TiO_2 thin film in terms of water splitting using this method, however, without analysing the entire

sequence no conclusions can be made with respect to the change in photocatalytic activity as the films are reduced. A direct comparison of the film to Degussa P25 powder cannot be made without first knowing the mass of the thin film. A comparison can be made to titanium dioxide thin films deposited on glass by Hyett *et al*.[7] In their work, they deposited thin films of titanium dioxide with carefully controlled thicknesses onto glass substrates and analysed their photocatalytic activity using the same conditions and Clark cell as outlined above. The key difference between the equipment used was the intensity of the UV-lamp used, in the work by Hyett *et al* they used a 16 W, 365 nm UV lamp which is more intense than the lamp used in this work (6 W, 365 nm), therefore the results are not directly comparable and require a correction factor. This correction factor can be determined from the results for Degussa P25 powder. Hyett *et al* determined the photocatalytic activity of Degussa P25 to be 0.4 μmol s^{-1} g^{-1}. By comparing to the result obtained in this work a scale factor can be determined which can then be used to correct the result for Q45-D so that a direct comparison can be made.

QN45-D (after correction) – 13.13×10^{-5} mol min^{-1} m^{-2}

The results for anatase films deposited on float glass obtained by Hyett et al range from 0.6 - 4.7 x 10^{-5} mol min^{-1} m^{-2}, suggesting that the porous titania film QN45-D synthesised during this investigation is more effective as a photocatalyst than dense titania films deposited on the same substrates.

4.6.2 Scanning Electron Microscopy of Reduced Zinc Titanate Films

To analyse the change in microstructure of the reduced zinc titanate films they were analysed using scanning electron microscopy. The collected images are shown below (Figure 4-11, Figure 4-12 and Figure 4-13). The SEM images in this chapter (5.6.2) were collected by Dr Alex Kulak at the University of Leeds.

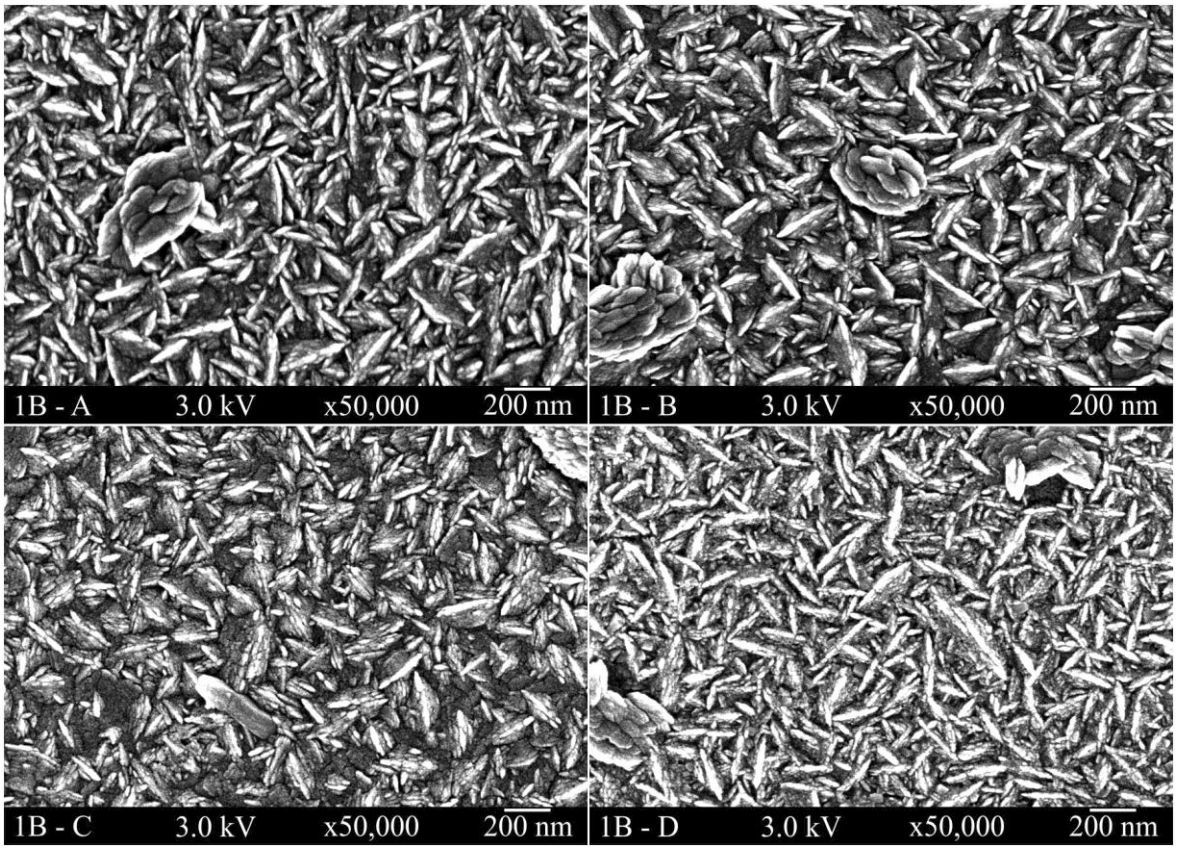

Figure 4-11 – SEM images for sample 1B at varying stages during treatment. A – no treatment (top left), B – acid wash (top right), C – hydrogen reduction (bottom left) and D – acid wash then hydrogen reduction (bottom right).

The SEM images show very little difference in the microstructure for the sample of formed with a base layer of TiO_2 on float glass (Figure 4-11). In each example, the crystallites are forming plates between c.a. 100 – 400 nm in diameter with random orientation.

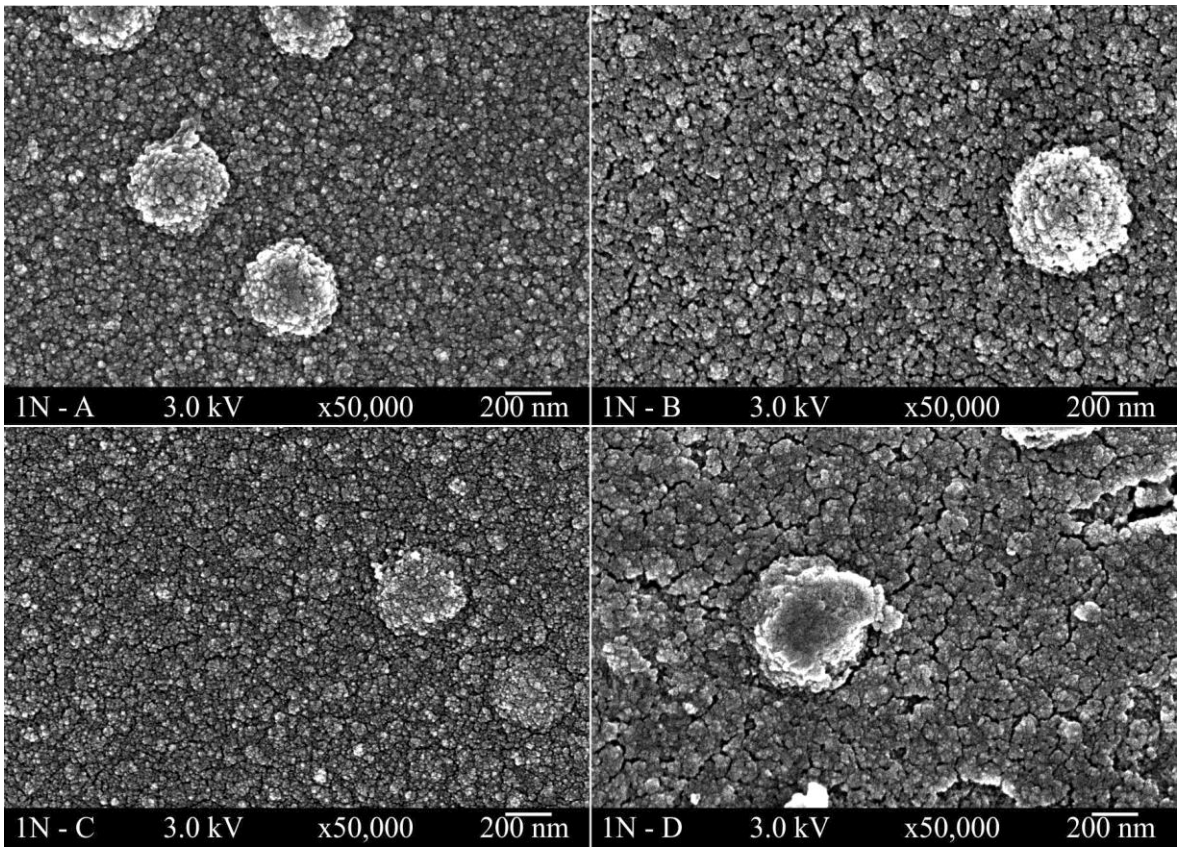

Figure 4-12 – SEM images for sample 1N at varying stages during treatment. A – no treatment (top left), B – acid wash (top right), C – hydrogen reduction (bottom left) and D – acid wash then hydrogen reduction (bottom right).

As was the case with sample 1B, there is very little change in the microstructure between each sample (Figure 4-12). In each sample the crystallites are growing in irregular shaped clusters c.a. 30 nm in diameter with an even distribution across the surface of the substrate. However, for samples 1N-B and 1N-D, the sections which have been treated in acid, there appears to be an increase in potential porosity as the spacing between clusters appears to be larger. This is likely caused by the dissolution of the ZnO present in the initial sample, resulting in macroporosity within the sample. This increase is more pronounced in sample 1N-D with fissures appearing across the surface. This could possibly increase the surface area of the sample.

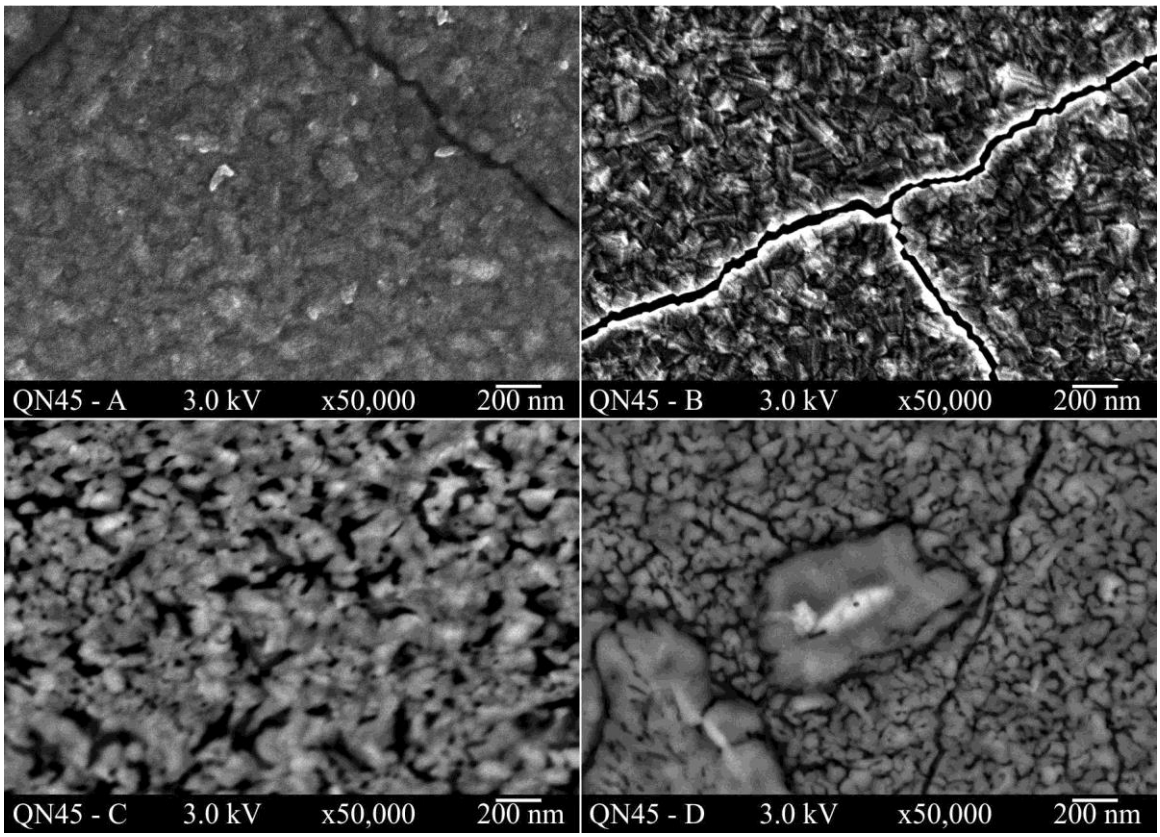

Figure 4-13 – SEM images for sample 1N at varying stages during treatment. A – no treatment (top left), B – acid wash (top right), C – hydrogen reduction (bottom left) and D – acid wash then hydrogen reduction (bottom right).

The untreated sample (QN45-A) shows a densely packed arrangement of crystallites forming plates separated by fissures (Figure 4-13). These fissures are potentially caused by the thin film shrinking during the cooling process after being synthesised and are present on each quartz sample analysed. After treatment in the acid wash (QN45-B) the sample exhibits increased edge effects, this reveals that the crystallites are growing in very angular plates with uniform distribution, random orientation and remain densely packed. On the other hand, after being hydrogen reduced at 752 °C (QN45-C and QN45-D) the microstructure changes to being composed of more rounded crystallites with poor edge effects. The crystallites also appear to be less densely packed with gaps appearing between the clusters. Along with the X-ray diffraction data, this suggests that the removal of the zinc species has indeed resulted in porous thin films of titania. This increase in porosity will potentially increase the available surface area of the titanium dioxide material, with could increase the photocatalytic activity of the film.

4.7 Conclusions

This chapter has demonstrated that it is possible to deposit a mixed phase film of zinc oxide, titanium dioxide and various zinc titanate phases. These films can then be washed in acid to remove zinc oxide and then further reduced using hydrogen (5% in N_2) to remove the remaining zinc containing species, leaving behind TiO_2 as the sole species. The sample deposited on quartz (QN45) is an example of being able to form a porous thin film of titanium dioxide using this method.

The photocatalytic tests shows that after acid washing and reducing in hydrogen the sample on quartz (QN45-D) outperforms a thin film of pure titanium dioxide deposited using aerosol assisted chemical vapour deposition. This could potentially be a result of the increased porosity of the thin film. However, without analysing the entire range of films deposited to determine how this photocatalytic activity changed as the samples were treated, it is impossible to determine whether the increased surface area is the sole factor in the increased activity.

The SEM images obtained for 1N potentially show that it is possible to form a porous film of TiO_2 using this method, however, the porosity does not appear to be visually as high as that attained by the sample on quartz (QN45). The reason for this unclear, but could be a result of the lower temperature used to reduce the samples on float glass as opposed to quartz.

4.8 References

(1) Djerdj, I.; Tonejc, A. M. *J. Alloys Compd.* **2006**, *413*, 159.

(2) Tobaldi, D. M.; Tucci, A.; Škapin, A. S.; Esposito, L. *J. Eur. Ceram. Soc.* **2010**, *30*, 2481.

(3) Meagher, E. P.; Lager, G. A. *Can. Mineral.* **1979**, *17*, 77.

(4) Herrmann, J.-M. *Catal. Today* **1999**, *53*, 115.

(5) Kafizas, A.; Carmalt, C. J.; Parkin, I. P. *Chem. Eur. J.* **2012**, *18*, 13048.

(6) López, R.; Gómez, R. *J. Sol-Gel Sci. Technol.* **2012**, *61*, 1.

(7) Hyett, G.; Darr, J. A.; Mills, A.; Parkin, I. P. *Chem. Eur. J.* **2010**, *16*, 10546.

(8) Parkin, I. P.; Palgrave, R. G. *J. Mater. Chem.* **2005**, *15*, 1689.

(9) Euvananont, C.; Junin, C.; Inpor, K.; Limthongkul, P.; Thanachayanont, C. *Ceram. Int.* **2008**, *34*, 1067.

(10) Dumitriu, D.; Bally, A. R.; Ballif, C.; Hones, P.; Schmid, P. E.; Sanjinés, R.; Lévy, F.; Pârvulescu, V. I. *Appl. Catal., B* **2000**, *25*, 83.

(11) Mills, A.; McGrady, M. *J. Photochem. Photobiol., A* **2008**, *193*, 228.

(12) Garzella, C.; Comini, E.; Tempesti, E.; Frigeri, C.; Sberveglieri, G. *Sens. Actuators, B* **2000**, *68*, 189.

(13) Kim, R.; Kim, Y.; Park, J.-W. *J Mater Sci* **2001**, *36*, 1469.

(14) Weinberger, B. R.; Garber, R. B. *Appl. Phys. Lett.* **1995**, *66*, 2409.

(15) Gupta, S. K.; Singh, J.; Anbalagan, K.; Kothari, P.; Bhatia, R. R.; Mishra, P. K.; Manjuladevi, V.; Gupta, R. K.; Akhtar, J. *Appl. Surf. Sci.* **2013**, *264*, 737.

(16) Sung, Y.-M.; Kim, H.-J. *Thin Solid Films* **2007**, *515*, 4996.

(17) Yang, W.; Wolden, C. A. *Thin Solid Films* **2006**, *515*, 1708.

(18) Lim, S. P.; Huang, N. M.; Lim, H. N.; Mazhar, M. *Ceram. Int.* **2014**, *40*, 8045.

(19) Saadoun, L.; Ayllón, J. A.; Jiménez-Becerril, J.; Peral, J.; Domènech, X.; Rodríguez-Clemente, R. *Appl. Catal., B* **1999**, *21*, 269.

(20) Huang, W.; Lei, M.; Huang, H.; Chen, J.; Chen, H. *Surf. Coat. Technol.* **2010**, *204*, 3954.

(21) Huang, S.-C.; Lin, T.-F.; Lu, S.-Y.; Chou, K.-S. *J Mater Sci* **1999**, *34*, 4293.

(22) Lei, L.; Chu, H. P.; Hu, X.; Yue, P.-L. *Ind. Eng. Chem. Res.* **1999**, *38*, 3381.

(23) Toberer, E. S.; Epping, J. D.; Chmelka, B. F.; Seshadri, R. *Chem. Mater.* **2006**, *18*, 6345.

(24) Sattler, K. D. *Handbook of Nanophysics: Nanotubes and Nanowires*; CRC Press, 2010.

(25) Müller-Buschbaum, H.; Waburg, M. *Monatsh. Chem.*, *114*, 21.

(26) Perry, N. H.; Stevanovic, V.; Lim, L. Y.; Mason, T. O. *Dalton Trans.* **2016**, *45*, 1572.

Chapter 5: Titanium Nitride Formation

5.1 Introduction

Titanium nitride is a material which is implemented as a coating for cutting tools as a way to extend the life of the equipment.[1,2] The reasons for this are numerous and include the materials resistance to high temperatures, the hardness values and the low coefficient to friction which can reduce wear and increase the lifespan of coated tools. It is also highly inert chemically and has a remarkable adhesion to substrates.[2] One of the other reasons why titanium nitride is a favourable material coating is purely for aesthetic value due to a pure titanium nitride coating imparting a golden-yellow reflective surface to the tool. Titanium nitride is also used as a diffusion barrier in electronic systems. It is effective within the aluminium/silicon system,[3] which is a simple eutectic system composed of face-centred cubic aluminium and diamond silicon.[4]

Titanium nitride can be formed in many different ways, for instance, via atmospheric pressure chemical vapour deposition using titanium (IV) chloride in the presence of nitrogen and hydrogen. These reactions are generally carried out at high temperatures between 900 and 1200 °C.[5,6] This temperature can be lowered if low pressure and ammonia is used in the place of nitrogen gas, with deposition occurring as low as 480 °C.[7] In 1986, Mayr and Stock demonstrated the formation of TiN on steel substrates using plasma assisted chemical vapour deposition using titanium (IV) chloride, nitrogen, hydrogen and argon. Using this method, they were able to deposit films as low as 500 °C.[8] Finally, metallo-organic precursors such as tetrakis (diethylamido) titanium (IV) and tetrakis (dimethylamido) titanium (IV) can be used to deposit thin films of TiN. For instance, in 1996, Wang *et al* reported the use of tetrakis (dimethylamido) titanium as a precursor during PECVD in the presence of nitrogen gas to deposit thin films of titanium nitride.[9]

Titanium nitride exists in a rock salt structure in the space group $Fm\bar{3}m$ and has a unit cell length of a = 4.235 Å (Figure 5-1).[10,11] One of the challenges facing the characterisation of titanium nitride films is the similarity in crystal structure between TiN, TiC and TiO. All three of the phases adopt a rock salt structure which is represented by the same peaks in X-ray diffraction patterns. The key difference lies in the position of these peaks. Due to the slight variations in unit cell size, the peaks are all situated in slightly different positions within the diffraction patterns (Figure 5-2).[12-14] These three phases are also infinitely soluble in each other, further complicating the characterisation as alloys of the materials will exhibit X-ray diffraction patterns with peak positions which lie in between the values for the pure samples.

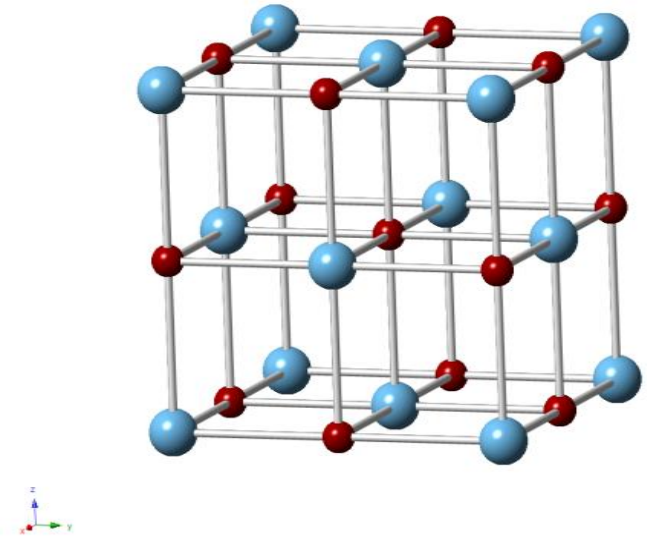

Figure 5-1 – Crystal structure of TiN

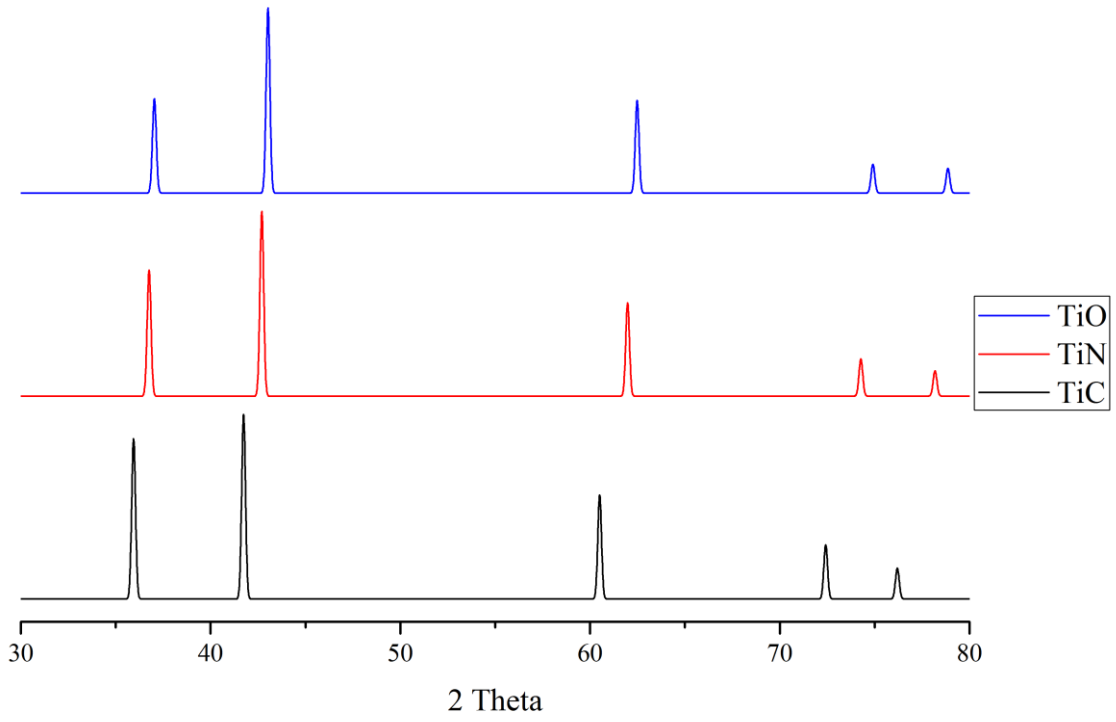

Figure 5-2 – Figure of powder X-ray diffraction patterns for rock salt structures of TiO, TiC and TiN

There has been a great deal of interest in titanium oxynitrides thin films, particularly those with a tuneable N:O ratio.[15] Using a reactive sputtering method Chappé *et al* produced a range of films with varying N:O ratios.[16] Their results showed that as the oxygen level increases, the properties of the material transition from those of titanium nitride to those of titanium dioxide.

Physical vapour deposition is a convenient method in forming titanium oxynitride films, for instance, Martin *et al* used direct current magnetron sputtering to deposit thin films of titanium oxynitride, of the formula TiO_xN_y, from titanium metal in an oxygen and nitrogen environment.[17]

Recent computational studies carried out by Wu *et al* analysed a multitude of various nitrides and oxynitrides to determine their potential application as water-splitting photocatalysts.[18] Among them, they identified three which are possibly synthesisable and have the potential to outperform contemporary oxynitride based photocatalysts. One of the compounds identified is $Ti_3O_3N_2$. Further work carried out by Wu and Ceder proposed that the solid solution of Ta_3N_5:$Ti_3O_3N_2$ is a promising water splitting catalyst with a band gap of 2.0 eV.[19]

As a result of the computational work carried out by Wu *et al*, the main aim of this project was to attempt to synthesise the titanium oxynitride $Ti_3O_3N_2$. This was carried out by using a metallo-organic titanium precursor during aerosol assisted chemical vapour deposition to initially deposit thin films of titanium nitride. Once accomplished, small quantities of an oxygen source was introduced in an attempt to deposit films of titanium oxynitride, with the goal being to tune the quantities to form the desired compound.

5.2 Formation of Titanium Nitride Precursor

The material chosen to be the titanium nitride precursor was tetrakis (diethylamido) titanium (IV) (TDEAT). Synthesis was carried out according to the report by Bradley and Thomas[20] with a few minor adjustments. Toluene was replaced by hexane as the solvent and hexyllithium was used as opposed to n-butyllithium. Before the reaction was begun, all glassware was dried in an oven (c.a. 70 °C) for at least 2 hours. The reaction was carried out in a Schlenk with a PTFE stirrer bar. All equipment was purged under vacuum and refilled with argon three times to ensure that the system was free of both water and oxygen.

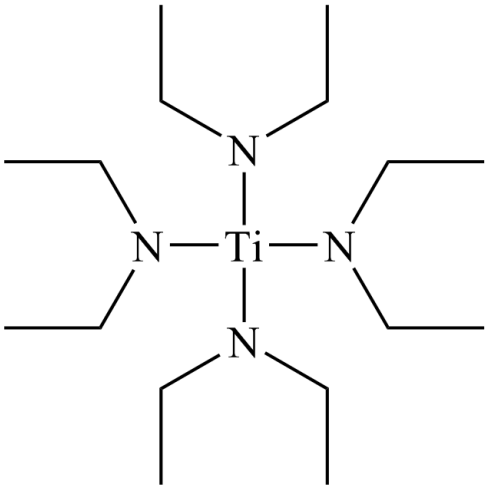

Figure 5-3 – Structure of TDEAT

Dry hexane (10 cm^3) was added to the Schlenk using a syringe and needle through a suba seal. To this, diethylamine (1 cm^3 / 9.66 mmol) was added to form an amine solution in hexane. Hexyllithium (2.6 M in hexane) was added (4.0 cm^3 / 10.4 mmol). A slight excess of hexyllithium was used to ensure that all of the available amine is deprotonated to form lithium amides. Titanium (IV) chloride (0.25 cm^3 / 2.28 mmol) was added to the solution slowly and the mixture was left to stir under a positive pressure of argon for c.a. 1 hour. The resulting solution was deep orange in colour with a colourless precipitate. The mixture was the filtered using a filter Schlenk to separate the solution and precipitate. The reaction occurs via the following steps (Equation 5-1).

$$HNEt_2 + LiCH_2(CH_2)_4CH_3 \rightarrow LiNEt_2 + CH_3(CH_2)_4CH_3 \qquad (1)$$

$$TiCl_4 + 4LiNEt_2 \rightarrow Ti(NEt_2)_4 + 4LiCl \qquad (2)$$

Equation 5-1 – Equations outlining the reaction steps in the formation of TDEAT. Equation 1 shows the deprotonation of diethylamine using hexyllithium. Equation 2 shows the formation of the titanium amide compound along with the formation of lithium chloride.

5.3 Deposition of Titanium Nitride

5.3.1 Initial Trial of Tetrakis (Diethylamido) Titanium (IV)

A deposition was carried out using the solution synthesised above (see Formation of Titanium Nitride Precursor, page 138). The experiment was carried out following the procedure outlined above (see Experimental, page 8) at 550 °C using an argon flow rate of 0.25 l min^{-1}. The dispersion chamber was set at a height of 20 mm above the tip of the piezoelectric humidifier. The TDEAT solution was used directly in the deposition without any further treatment. The resulting film was opaque but reflective and was copper coloured across the entire substrate (Figure 5-4). Analysis was carried out by X-ray diffraction (Rigaku Smartlab) and is shown below (Figure 5-5).

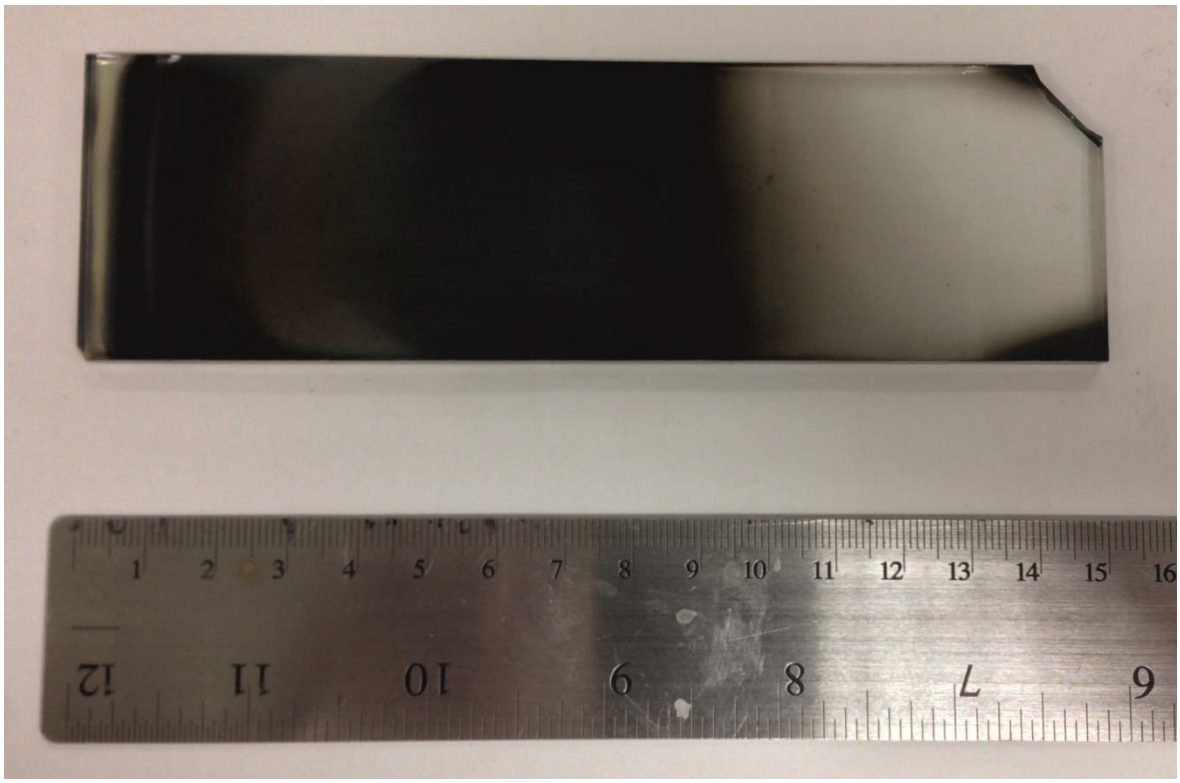

Figure 5-4 – Picture of the initial film formed using TDEAT as a precursor

The X-ray diffraction pattern shows that the film formed is potentially titanium nitride; however, the crystallinity is poor, with the peaks being both very broad and low in intensity. The data was refined focusing on peak shape using a Gaussian profile, peak position, preferred orientation as part of a spherical harmonic model and unit cell parameters. The goodness of fit index $\chi^2 = 1.2$ with wRp = 4.7%. After refinement the unit cell lengths were calculated to be a = 4.360 Å. This value is higher than the literature value of 4.235 Å.[10] There are various reasons why this could be the case, one explanation is that crystal strain caused by growth on a substrate. Another reason is that the film is a composite of TiN and titanium carbide (TiC). Both compounds exist in the same rock salt structure. Composite materials of these will exhibit X-ray diffraction patterns partway between the

two pure phases with peak positions laying at 2θ values in between those of the pure phases as a result of the lattice parameters which are also intermediate values between TiN (4.235 Å) and TiC (4.328 Å). A third possibility is the formation of titanium nitride with a deficiency in either titanium or nitrogen, these also have the rock salt structure in the space group $Fm\bar{3}m$ and so exhibit the same diffraction pattern with slight differences in peak position caused by variations in unit cell size. Examples of the potential phases are shown in the table below (Table 5-1). The similar structure of the other phases will make characterisation of the titanium nitride films challenging, however, due to the structure of the desired titanium oxynitride being different, X-ray diffraction is the most convenient analytical technique for initial characterisation.

The small artefact in the pattern at c.a. 25° 2θ could be a result of trace amounts of TiO_2 (anatase) present within the sample.

Table 5-1 – Table showing potential rock salt phases. Pure titanium nitride,[10] pure titanium carbide,[12] pure titanium monoxide,[13] nitrogen deficient titanium nitride,[12] titanium deficient titanium nitride[21] and $(TiN)_{0.96}$,[22]

Phase	**Unit Cell a / Å**	**Phase**	**Unit Cell a / Å**
TiN	4.235	$TiN_{0.9}$	4.239
TiO	4.204	$Ti_{0.76}N$	4.235
TiC	4.328	$(TiN)_{0.96}$	4.242

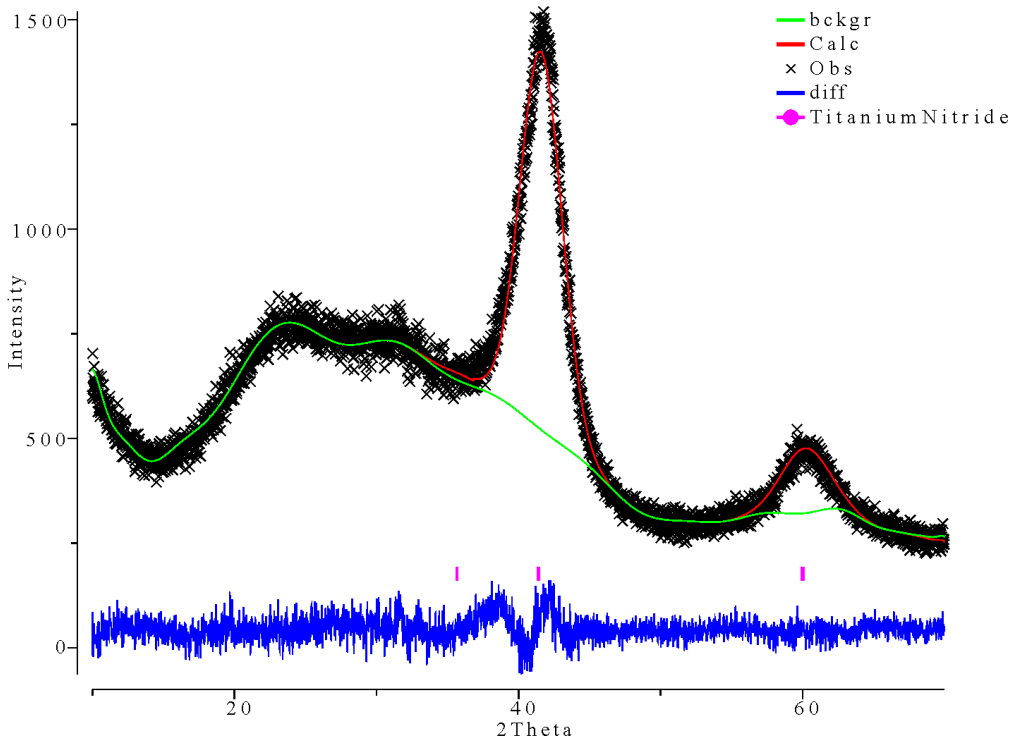

Figure 5-5 – X-ray diffraction pattern of initial TiN film

5.3.2 Further Formation of Titanium Nitride from Tetrakis (Diethylamido) Titanium (IV)

A solution of TDEAT was made following the procedure outlined above (see Formation of Titanium Nitride Precursor, page 138). Once synthesised, the solution was put under vacuum to remove the hexane. The resulting product was an orange oil. This oil was used during a sequence of experiments in which the deposition conditions were refined.

Depositions were carried out as outlined above (see Experimental, page 8) at 550 °C. Argon flow rates and volumes of solvent are outlined in the table below (Table 5-2). In each deposition, TDEAT (0.25 cm^3, 1.06 mmol) was used. The position of the dispersion chamber was set so that it was positioned 0 mm above the tip of the piezoelectric humidifier.

Table 5-2 – Table outlining the conditions for TiN formation from synthesised TDEAT

Run	**Hexane / cm^3**	**Argon Flow Rate / l min^{-1}**	**Dispersion Chamber**	**Result**
1	10	0.25	Dispersion Flask	Deposition in first c.a. 3 cm of substrate, heavy delamination
2	10	0.50	Dispersion Flask	Deposition in first c.a. 3 cm of substrate, heavy delamination
3	10	0.34	3-Neck RB Flask (100 cm^3)	Deposition in first c.a. 3 cm of substrate, heavy delamination
4	30	0.34	3-Neck RB Flask (100 cm^3)	Deposition in first c.a. 3 cm of substrate, heavy delamination

The deposition within the initial 3 cm of the substrate on Run 1 demonstrates that the precursor is decomposing within the leading section of the reaction chamber. To try to account for this, the flow rate was doubled for Run 2 in an attempt to cause the precursor to be further through the chamber before decomposition occurs. This had no influence on the deposition. After this point the deposition flask was changed to a 3-neck round bottom flask (100 cm^3). The flow rate used was slightly higher than that used in Run 1; however, for both Run 3 and Run 4, the result was the same, all of the deposition occurred within the initial 3 cm of the substrate and the film was heavily delaminating, with most of the film being removed from the surface of the substrate. The reason for the dramatic change between the initial formation and the subsequent depositions is unclear. The main difference between the experiments is the smaller quantity of precursor used in this set, however, this does not account for the increased delamination observed in this sequence.

5.3.3 Use of Commercial Tetrakis (Diethylamido) Titanium (IV)

Further investigation into TiN formation utilised commercial TDEAT as opposed to in-lab synthesised. The reason for this is due to the challenges involved in scaling up the reaction and purification of the final product. A sequence of depositions was carried out following the procedure outlined above (see Experimental, page 8) using a 3 neck round bottom flask (100 cm^3) as the dispersion chamber and an argon flow rate of 0.4 l min^{-1}, the temperature was changed for each reaction in an attempt to maximise coverage on the substrate and minimise the amount of delamination which is occurring. A solution of TDEAT (0.25 cm^3 / 1.06 mmol) in hexane (10 cm^3) was used for each deposition. The following table outlines the temperature and the results of the depositions in this sequence (Table 5-3).

Table 5-3 – Table outlining the change in temperature using commercial TDEAT

Run	Temperature / °C	Result
1	550	Deposition occurred all in initial section of the substrate (c.a. 3 cm) with large amount of delamination
2	450	Deposition occurred all in initial section of the substrate (c.a. 3 cm) with large amount of delamination
3	350	Deposition occurred across initial c.a. 10 cm of substrate with no visible delamination

At 450 and 550 °C both reactions showed depositions at the initial edge of the substrate with large amount of delamination occurring. However, at 350 °C, the coating covered the initial c.a. 10 cm^3 and had no visible delamination. The X-ray diffraction pattern for run 3 (Figure 5-6) showed the formation of a crystalline TiX compound (where X = N, C or O) with unit cell length of 4.281 Å and a goodness of fit index $\chi^2 = 1.7$.

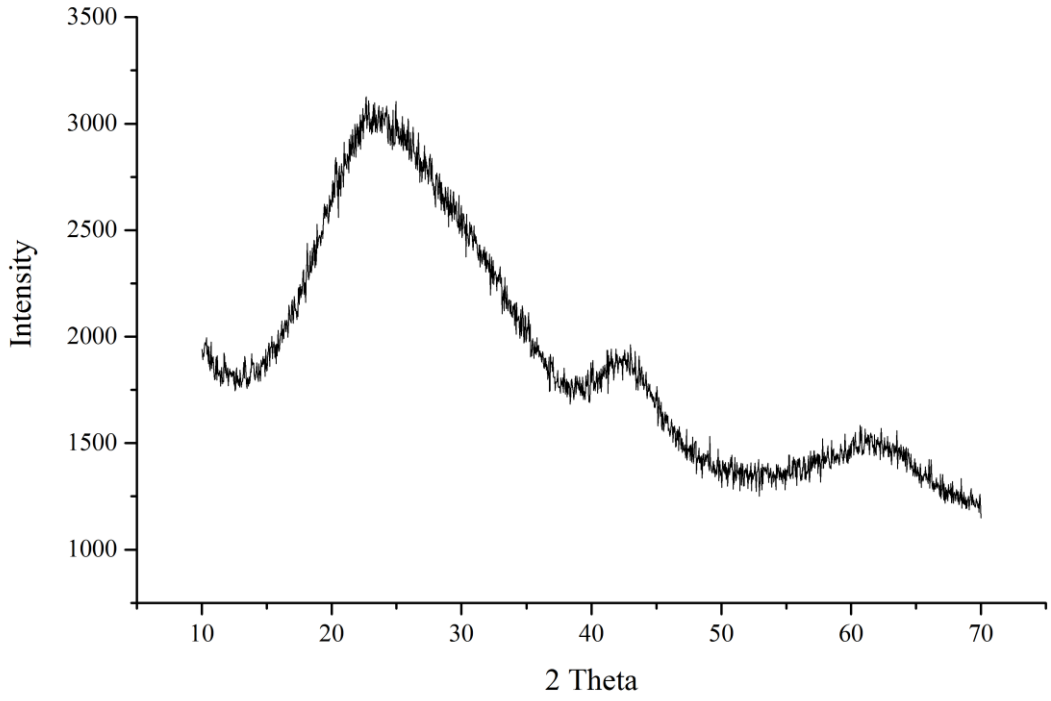

Figure 5-6 - X-ray diffraction pattern of TiX deposited from run 3

5.4 Introduction of an Oxygen Source

5.4.1 Initial Attempt at Formation of Titanium Oxynitride

Oxygen was introduced into the system by adding small amounts of ethyl acetate (EtAc) to the reaction solution. A sequence of depositions was carried out using differing quantities of ethyl acetate. The experiments were performed as outlined above (see Experimental, page 8) at a temperature of 350 °C, with an argon flow rate of 0.34 l min^{-1}. A solution of TDEAT (0.25 cm^3 / 1.06 mmol) in hexane (10 cm^3) was used each time with quantities of ethyl acetate as shown in the table below (Table 5-4).

Table 5-4 – Table showing differing amounts of EtAc used during initial attempt at titanium oxynitride formation

Run	EtAc / cm^3	EtAc / mmol	Temperature / °C	Visible Result	X-Ray Diffraction
1	0.1	1.02	350	Transparent yellow-brown film with interference effects	No peaks
2	0.05	0.51	350	Transparent yellow-brown film with interference effects	No peaks
3	0.05	0.51	400	Transparent yellow-brown film with interference effects	No peaks

Each film formed was yellow-brown in appearance and was transparent. Upon collection of X-ray diffraction data, it was discovered that the films were poorly crystalline as no peaks were visible in any of the patterns. The temperature was increased to 400 °C for run 3 in an attempt to deposit a more crystalline film; however, there was no observable difference in either the visible appearance or the X-ray diffraction pattern. A small section of Run 2 was taken and annealed at 600 °C under argon for 2 hours. The resulting film was now darker in colour, and when analysed on an X-ray diffractometer, it displayed peaks characteristic of TiO_2 (anatase), however, the peaks were of low intensity and very broad, preventing full characterisation of the sample. The change in appearance of the films suggests that the ethyl acetate is having the desired effect of introducing oxygen into the system; however, steps need to be taken to improve crystallinity of the resulting films before characterisation can take place.

5.4.2 Improving the crystallinity of the Resulting Films

In an attempt to improve crystallinity, a new sequence of experiments was carried out following the procedure outlined above (see Experimental, page 8) using a temperature of 400 °C, an argon flow rate of 1.0 l min^{-1} and a three neck round bottom flask (100 cm^3). A solution of TDEAT (0.25 cm^3 / 1.06 mmol) in dry toluene (10 cm^3) was used in each deposition with a quantity of ethyl acetate as outlined in the following table (Table 5-5). Toluene was chosen in favour of hexane as it has a higher viscosity and so transmission of the ultrasound will be lower resulting in slower aerosol generation than a solution in hexane.

Table 5-5 – Table outlining the quantity of EtAc used and summary of results from attempting to improve the crystallinity of thin films of titanium nitride

Run	**EtAc / cm^3**	**EtAc / mmol**	**Visible Result**	**a / Å**	**χ^2**
1	0.0	0.00	Initial 5 cm of substrate opaque brown and reflective with delamination. Middle 5 cm of substrate yellow-brown and transparent	4.300	2.3
2 (Back)	0.2	2.04	Remaining substrate transparent yellow-brown coating	4.212	1.6
2 (Front)			Initial c.a. 2 cm transparent blue coating.	TiO_2 (Anatase)	1.9
3	0.1	1.02	Transparent yellow-brown coating	4.352	1.1

The results from the X-ray diffraction (Figure 5-7) show that in the presence of 2 mole equivalents of ethyl acetate, the resulting film begins to form TiO_2 (anatase) in favour of TiN. However, the influence of the ethyl acetate mostly occurs within the initial 2 cm of the substrate. After this point there is a phase change to a rock salt TiX compound (where X = N, C or O) with a unit cell of a = 4.212 Å. The unit cell suggests that the compound is predominantly TiO or a deficient form of titanium nitride.

With one mole equivalent of ethyl acetate, there is no visible phase change and the X-ray diffraction patterns show the formation of crystalline TiX compound with the rock salt structure. The unit cell size (4.352 Å) suggests that the phase is at least partly TiN. However, the physical appearance is different to films formed from TDEAT in the absence of EtAc, instead of being opaque and reflective; it is yellow-brown and transparent. The transparency could be a result a thinner coating and smaller crystallites; however, without quantitative data of the elemental composition of the film it is not possible to confirm the possibilities.

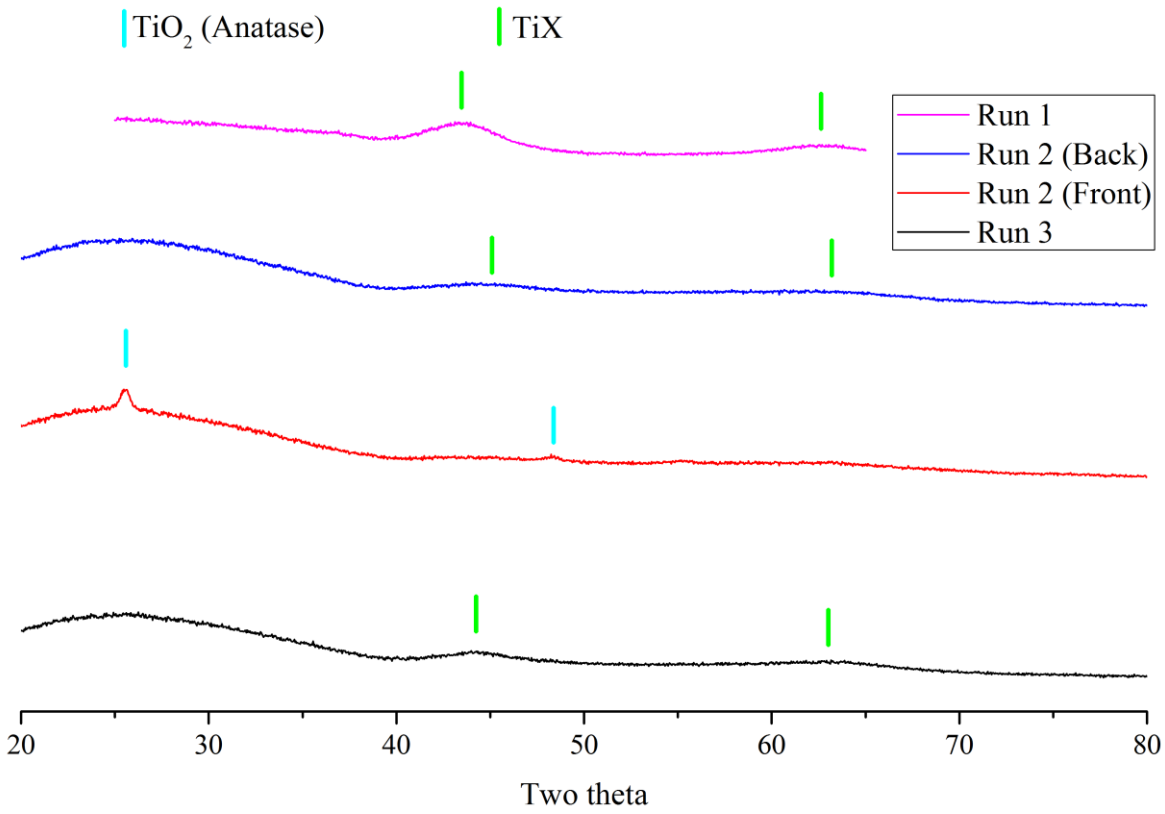

Figure 5-7 – X-ray diffraction patterns of TiX films deposited from TDEAT solutions in toluene in the presence of ethyl acetate

5.5 Conclusions

The experiments carried out have confirmed that it is possible to deposit thin films of titanium nitride using tetrakis (diethylamido) titanium (IV) as a precursor via aerosol assisted chemical vapour deposition. However, due to the abundance of related titanium compounds which exist in the same rock salt structure, powder X-ray diffraction cannot be used to fully characterise the films formed.

The formation of TiO_2 in the deposition from TDEAT in the presence of ethyl acetate has confirmed that this is a viable method of introducing oxygen into this system. By carrying out more depositions using a larger range of mole equivalents it will be possible to determine whether it is possible to deposit crystalline films of titanium oxynitride using this technique.

Another suggestion for future work in this area is the investigation into the use of other titanium amide precursors, for instance, tetrakis (dimethylamido) titanium (IV) or bis(N,N'-dimethyl-1,3-propanediamido) titanium (IV). Different titanium amides will have slightly different decomposition temperatures and decompositional pathways; it will be interesting to see how this influences the deposition.

One of the challenges facing the formation of titanium oxynitride using this method is the abundance of organic compounds which decompose under these conditions. This decomposition opens the door for potential carbon contamination with could cause the formation of oxocarbonitrides instead. However, this is an issue which is difficult to address, as most common solvents are organic, and most inorganic solvents are unsuitable for use in this system. A potential solution if carbon contamination becomes an issue is to lower the temperature of the reaction. This could work by preventing complete decomposition of the organic fragments, reducing the quantity of carbon available to be incorporated into the resulting thin film.

5.6 References

(1) Egland, K. M.; Mazumder, J. 1996; Vol. 2703, p 552.

(2) Zhang, S.; Zhu, W. *J. Mater. Process. Technol.* **1993**, *39*, 165.

(3) Hyatt, S. O.; Chao, B. S.; Yamauchi, H. *Vacuum* **1993**, *44*, 1025.

(4) Murray, J. L.; McAlister, A. J. *Bull. Alloy Phase Diagrams* **1984**, *5*, 74.

(5) Glejbol, K.; Pryds, N. H.; Thölén, A. R. *J. Mater. Res.* **1993**, *8*, 2239.

(6) Bhat, D. G. *Proc. - Electrochem. Soc.* **1990**, *90-12*, 648.

(7) Sherman, A.; Raaijmakers, I. J. *Proc. - Electrochem. Soc.* **1990**, *90-12*, 374.

(8) Mayr, P.; Stock, H. R. *J. Vac. Sci. Technol., A* **1986**, *4*, 2726.

(9) Chin-Kun, W.; Lu-Min, L.; Marvin, L.; Huang-Chung, C.; Mou-Shiung, L. *Jpn. J. Appl. Phys.* **1996**, *35*, 4274.

(10) Hasegawa, M.; Yagi, T. *J. Alloys Compd.* **2005**, *403*, 131.

(11) Pierson, H. O. *Handbook of Chemical Vapor Deposition*; 2nd Ed. ed.; William Andrew Publishing/Noyes, 1999.

(12) Noerlund Christensen, A. *Acta Chem. Scand., Ser. A* **1978**, *A32*, 89.

(13) Bartkowski, S.; Neumann, M.; Kurmaev, E. Z.; Fedorenko, V. V.; Shamin, S. N.; Cherkashenko, V. M.; Nemnonov, S. N.; Winiarski, A.; Rubie, D. C. *Phys. Rev. B: Condens. Matter Mater. Phys.* **1997**, *56*, 10656.

(14) Becker, K.; Ebert, F. *Z. Phys.* **1925**, *31*, 268.

(15) Chappé, J.-M.; Martin, N.; Lintymer, J.; Sthal, F.; Terwagne, G.; Takadoum, J. *Appl. Surf. Sci.* **2007**, *253*, 5312.

(16) Chappé, J.-M.; Martin, N.; Terwagne, G.; Lintymer, J.; Gavoille, J.; Takadoum, J. *Thin Solid Films* **2003**, *440*, 66.

(17) Martin, N.; Banakh, O.; Santo, A. M. E.; Springer, S.; Sanjinés, R.; Takadoum, J.; Lévy, F. *Appl. Surf. Sci.* **2001**, *185*, 123.

(18) Wu, Y.; Lazic, P.; Hautier, G.; Persson, K.; Ceder, G. *Energy Environ. Sci.* **2013**, *6*, 157.

(19) Wu, Y.; Ceder, G. *J. Phys. Chem. C* **2013**, *117*, 24710.

(20) Bradley, D. C.; Thomas, I. M. *J. Chem. Soc.* **1960**, 3857.

(21) Christensen, A. N. *Acta Chem. Scand., Ser. A* **1975**, *A29*, 563.

(22) Matthew W, M. In *Searching the Chemical Literature*; American Chemical Society: 1961; Vol. 4, p 132.

Appendix A Experimental Materials

ααα-Trifluorotoluene – Sigma-Aldrich, ≥99.9%

Ammonium Fluoride – Alfa Aesar, 96%

Aluminium (III) Nitrate Nonahydrate – Aldrich, 99.997%

Brilliant Blue G – Acros Organics, pure

Cetyltrimethylammonium Bromide – Acros Organics, 99+%

Cyanamide – Aldrich, 99%

Decyldimethylammonium Bromide – Aldrich, ≥98.0%

Dichloroindophenol Sodium Salt – Acros Organics, 98+%

Didodecyldimethylammonium Bromide – Aldrich, 98%

Dry Hexane – Hexane (supplied by Fisher), distilled over sodium

Ethanol – Fisher Scientific, Technical Grade

Ethyl Acetate – Fisher Scientific, Laboratory Reagent Grade, dried over molecular sieves (4 Å)

Hexyllithium 2.3M Solution in Hexane –Sigma-Aldrich

Methanol – Fisher Scientific, Technical Grade

Methyl Sulphate Sodium Salt – Aldrich

Potassium Fluoride – Sigma, ≥99.5% BioUltra

Sodium Dodecyl Sulphate – Sigma-Aldrich, ACS Reagent, ≥99.0%

Sodium 1-Heptanesulphonate – Sigma Aldrich

Sodium 1-Pentanesulphonate – Sigma-Aldrich, ≥95%

Sodium 1-Propanesulphonate – Aldrich, ≥99%

Tetrabutylammonium Bromide – Sigma-Aldrich, ReagentPlus ≥99.0%

Tetrakis(diethylamido) Titanium (IV) – Acros Organics 99%

Tetraethylammonium Bromide – Sigma-Aldrich, ReagentPlus 99%

Appendix A

Tetrahexylammonium Bromide – Aldrich, 99%

Tetramethylammonium Bromide – Acros Organics 98%

Tetraoctylammonium Bromide –Aldrich, 98%

Titanium (IV) Chloride – Sigma-Aldrich, ReagentPlus 99.9% trace metals basis

Titanium (IV) Isopropoxide – Aldrich, 97%

Toluene – Fisher, dried over molecular sieves (4 Å) degassed under vacuum

Urea – Alfa Aesar, 99.3%

Zinc Acetate –Aldrich, 99.99%

Appendix B Experimental Data

See attached media.